CALIFORNIA INSTITUTE OF TECHNOLOGY

SOIL MECHANICS LABORATORY

APPLICATIONS OF PLASTICITY THEORY TO SELECTED PROBLEMS IN SOIL MECHANICS

by

Mohsen Mohamed Baligh

1972

APPLICATIONS OF PLASTICITY THEORY TO SELECTED PROBLEMS IN SOIL MECHANICS

Thesis by

Mohsen Mohamed Baligh

In Partial Fulfillment of the Requirements

For the Degree of

Doctor of Philosophy

California Institute of Technology

Pasadena, California

1972

(Submitted May 15, 1972)

ACKNOWLEDGMENT

The author wishes to express his appreciation and sincere gratitude to his advisor, Professor R. F. Scott, for his inspiring guidance and constant encouragement. He is also grateful to Professor G. W. Housner for helpful discussions.

The author is grateful for the research assistantships and tuition scholarships granted by the California Institute of Technology and for the financial support received from the National Science Foundation during the course of this work.

ABSTRACT

Two topics in plane strain perfect plasticity are studied using the method of characteristics. The first is the steady-state indentation of an infinite medium by either a rigid wedge having a triangular cross section or a smooth plate inclined to the direction of motion. Solutions are exact and results include deformation patterns and forces of resistance; the latter are also applicable for the case of incipient failure. Experiments on sharp wedges in clay, where forces and deformations are recorded, showed a good agreement with the mechanism of cutting assumed by the theory; on the other hand the indentation process for blunt wedges transforms into that of compression with a rigid part of clay moving with the wedge. Finite element solutions, for a bilinear material model, were obtained to establish a correspondence between the response of the plane strain wedge and its axi-symmetric counterpart, the cone. Results of the study afford a better understanding of the process of indentation of soils by penetrometers and piles as well as the mechanism of failure of deep foundations (piles and anchor plates).

The second topic concerns the plane strain steady-state free rolling of a rigid roller on clays. The problem is solved approximately for small loads by getting the exact solution of two problems that encompass the one of interest; the first is a steady-state with a geometry that approximates the one of the roller and the second is an instantaneous solution of the rolling process but is not a steady-state. Deformations and rolling resistance are derived. When compared with existing empirical formulae the latter was found to agree closely.

TABLE OF CONTENTS

LIST OF FIGURES

LIST OF TABLES

NOMENCLATURE

B	breadth of indenters
$\underset{\sim}{c}$	fourth order elasticity tensor
E	Young's modulus of elasticity
e	deviatoric strain
e^*	deviatoric strain of yield
$\underset{\sim}{e}_i$	unit vector in direction of coordinate axis x_i
$\underset{\sim}{e}_n$	unit normal vector to a surface
$\underset{\sim}{e}_t$	unit tangent vector to a surface
$\underset{\sim}{f}$	body force vector field
G	shear modulus
J	jump in velocity
k	yield shear strength
ℓ	length
L	length of side
L_R	rear length
p	interface normal pressure
p_{av}	average interface normal pressure
R	radius of cylinder
R	region
r	radial distance in cylindrical coordinates
s	deviatoric stress
s^*	deviatoric stress at yield
s_ν	normal component of surface traction
s_t	shearing component of surface traction

U	translation velocity of indenters
$\underset{\sim}{u}$	displacement vector field
u	velocity along α-line
v	velocity along β-line
$\overline{v}$	velocity
v_o	velocity
W_e	power expended by external loading
W_i	internal power of dissipation
W_{id}	power dissipated in producing deformation
W_{ih}	power dissipated in producing heat
X	frame of reference
x	coordinate
Y	yield strength in uniaxial testing
y	coordinate
z	coordinate
α	direction of first slip line
β	direction of second slip line
Γ	curve
γ	angle
$\overline{\gamma}$	angle
γ_{ij}	component of strain tensor in frame X
$\underset{\sim}{\gamma}$	strain tensor
γ_i	principal values of the strain tensor
Δs_i	error in element i of a finite element mesh
$\overline{\Delta s}$	average error in field

$\dot{\epsilon}_{ij}$ components of strain-rate tensor field in frame X

ζ angle

θ angle, slope

ϑ angle

μ coefficient of solid or rolling friction

μ_o minimum coefficient of friction

δ deformation, settlement

ν Poisson's ratio

λ Lamé modulus

σ compressive hydrostatic stress

σ_{ij} components of stress tensor in frame X

$\underset{\sim}{\sigma}$ stress tensor

σ_i principle values of stress tensor

σ_n normal stress

σ_r radial stress in cylindrical coordinates

σ_θ tangential stress in cylindrical coordinates

τ_n shearing stress

Σ summation

Σ curve

Φ angle

Ψ angle

CHAPTER I

THEORETICAL PRELIMINARIES AND FUNDAMENTAL CONCEPTS

I-1. Introduction, problems treated

Two topics are treated in this text. The first concerns the plane strain steady-state motion of rigid indenters in an infinite space, Fig. I-1. The indenters are either a wedge with a triangular cross section, Fig. I-1-a, or a plate inclined to the direction of motion, Fig. I-1-b. The solution of these problems is given in chapter II for a rigid-perfectly plastic infinite medium using the method of characteristics. Results of experiments simulating the wedge problem are also given in chapter II as well as results of finite element solutions that extend results of the plane strain wedge to its axi-symmetric counterpart, the cone.

The second topic is on the theory of rolling; it is covered in chapters III and IV. In chapter III the solutions of two problems in perfect plasticity are obtained. The first is the ironing plate problem shown in Fig. I-2-a, it is that of an inclined rigid smooth plate moving steadily parallel to the surface of a rigid-perfectly plastic half-space. Ahead of the plate, a heap is present; the shape of the heap must be found such that the steady-state condition is satisfied. The second problem is the instantaneous solution of the rolling problem , Fig. I-2-b; it is the incipient failure of a wedge (or half-space) indented by a smooth rigid roller. The wedge is made of a rigid-perfectly plastic material and has the upper surface

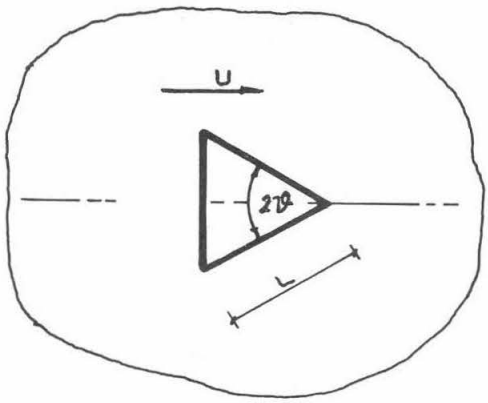

(a) Rigid wedge

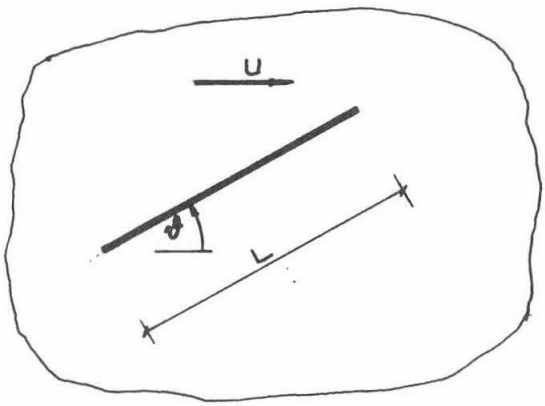

(b) Smooth inclined plate

Fig. I-1. Steady-state motion of rigid indenters in an infinite space, the problems treated in Chapter II.

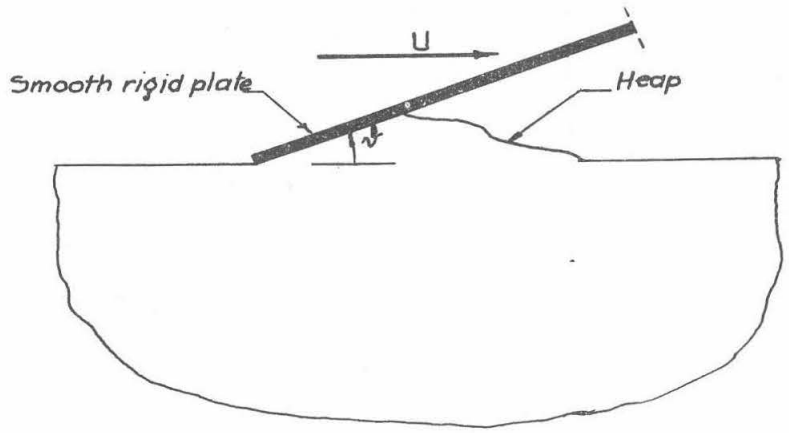

(a) The ironing plate problem

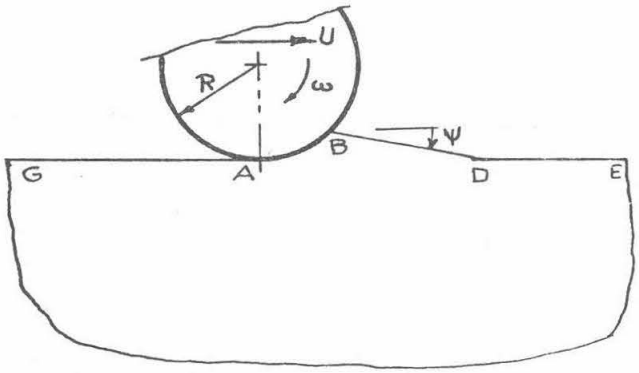

(b) Instantaneous solution

Fig. I-2. Fundamental solutions for the plane strain rolling; the problems treated in Chapter III.

GABDE as shown in Fig. I-2-b. The roller is fitted such that AB is the arc of contact and then an instantaneous horizontal velocity U and an angular rotational velocity ω are given to the roller. The results of the above two problems represent the fundamental solution of the rolling theory formulated in Chapter IV.

In chapter IV the general formulation of the steady-state free rolling of a rigid cylinder is first presented. A discussion of why the rigid-perfectly plastic material was chosen to idealize the half-space material follows. Finally using the results of chapter III expressions for the rolling resistance are derived and compared with existing empirical formulae.

Chapter I is devoted to the main theoretical preliminaries and fundamental concepts used subsequently. First, the theory of plane strain ideal plasticity is briefly presented; definitions and notations follow the lines of Hill [1]* apart from some concepts that are special to our steady-state solutions. Next the apparatus used for plane strain testing of clay is described. It allows the measurement of deformations on a plane of symmetry instead of at the walls of a container as previous investigators have done [2,3]. Finally the fundamentals of Wilson's finite element technique [8] of solving for a bilinear material are presented as well as the modifications made in it to suit our problems.

---

*Numbers in brackets refer to the bibliography at the end of the chapter.

I-2. Definitions and notations in perfect plasticity

The following part is intended to outline the notations used subsequently rather than to present a rigorous and complete treatment of the theory of ideal plasticity as discussed in Hill [1] or Prager [4].

I-2-1. The rigid-perfectly plastic material

For plasticity solutions in the following section, the deformable material will be taken to be a homogeneous, isotropic, massless, rigid-perfectly plastic, and incompressible with a yield criterion independent of the hydrostatic pressure. This material is often described as "rigid-perfectly plastic" and for convenience will be called "rigid-plastic" or "plastic" herein whenever no confusion is caused.

The formulation of problems dealing with this material can either be analytical or graphic; the latter method will be used here for its simplicity and convenience of representation. Knowing the graphical solution of a problem enables its analytical counterpart to be derived.

I-2-2. The plastic state

In plane strain problems, as considered here, a material point is said to be in a plastic state if:

$$\left(\frac{\sigma_{11} - \sigma_{22}}{2}\right)^2 + \sigma_{12}^2 = k^2 \qquad (1)$$

where σ_{11} and σ_{22} are the normal components of the stress tensor in the right-handed orthogonal cartesian frame X. Unless otherwise mentioned X will be taken as

in Fig. I-3-a.

σ_{12} is the shearing component of the stress tensor in X.

k is a material constant

$= Y/2$ for a Tresca material

$= Y/\sqrt{3}$ for a Von Mises material, where

Y is the major principal stress at yield in simple axial extension.

Equation (1) can be represented in a Mohr diagram, Fig. I-3-b, where the radius of the circle, describing the state of stress at the material point, has a radius equal to k. Material points in a "rigid" or unyielding state have corresponding Mohr circles with radii less than k. Referring to Fig. I-3

σ is the compressive hydrostatic stress at the point.

σ_n is the normal stress on a plane with outward normal $\underset{\sim}{e}_n$, taken to be positive when tensile.

τ_n is the shearing stress on the plane with outward normal $\underset{\sim}{e}_n$ taken to be positive if it acts in the direction of $\underset{\sim}{e}_t$, where $\underset{\sim}{e}_t$, $\underset{\sim}{e}_n$ form a right-handed orthogonal system.

The pole P is the point on the circle through which a straight line drawn parallel to $\underset{\sim}{e}_t$ will intersect the circle at a point with co-ordinates equal to the stresses acting on a plane whose normal is $\underset{\sim}{e}_n$. The α and β directions are the directions of the planes on which maximum shearing stresses occur at the material point and thus form

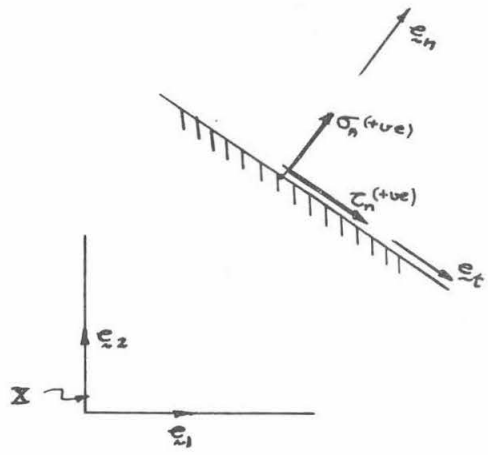

(a) Sign convention in the physical plane

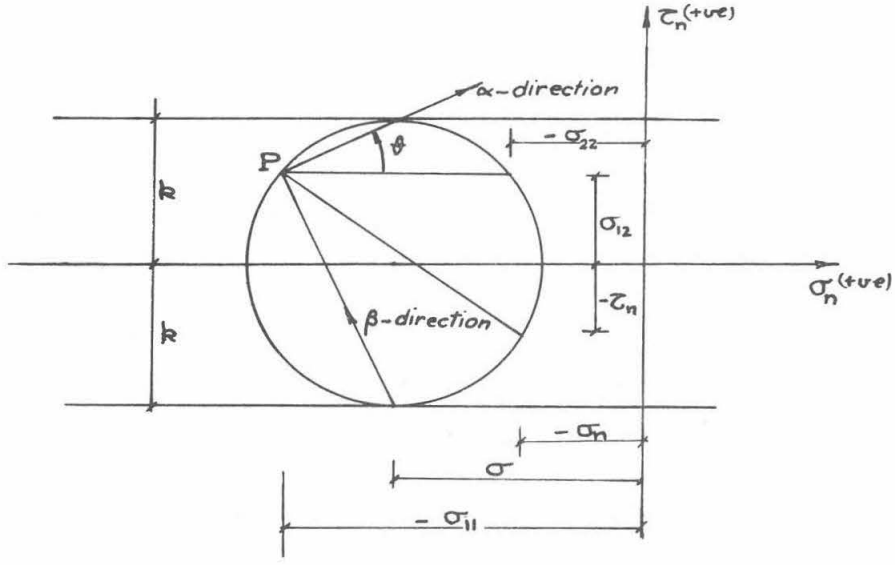

(b) Mohr Diagram

Fig. I-3. The stress space showing Mohr circle for a material point in a plastic state.

a right-handed orthogonal frame (in that order). The α-line makes an angle θ with the horizontal, being measured counterclockwise. The principal stress directions thus make angles of $45^{\circ} \pm \theta$ with the horizontal. In a yielding domain two sets of curves will be formed by lines parallel to α- and β-directions; they will be called the "α-family" and the "β-family" respectively.

It is thus clear that if a point is at a plastic state, given the pole P the state of stress at this point is fully determined. In this sense we can regard the stress plane, or Mohr diagram, as a mapping of the stress state at every point in the physical plane into its corresponding pole location in Mohr diagram and thus describe the stress field in a plastic domain.

I-2-3. The conjugate problem

Since we consider massless materials exclusively, the problem of a rigid indenter moving in a rigid-plastic material with a constant velocity $+U$ (to the right) is statically identical to the one in which the material is moving with a velocity $-U$ (to the left) with respect to a fixed indenter. The latter case, which is equivalent to taking the coordinate axes fixed to the indenter, will be referred to as the conjugate problem. The kinematics of a conjugate problem are such that its velocity field is equal to the velocity field of the initial problem superimposed on a constant field of magnitude $-U$.

I-2-4. Field equations, characteristics and slip lines

Substituting from (1) in the equilibrium equations to eliminate

derivatives of σ_{12} we get a quasi-linear system of hyperbolic equations in σ_{11} and σ_{22}. The characteristics, which are the curves across which discontinuities of field variables may exist, are thus real and are found to coincide with the α and β directions at every point in the plastic domain.

"Slip lines" at a point are defined as the planes on which the maximum shear strain rate occurs; isotropy of the material implies that they must also coincide with the α and β directions at any point in a plastic state. Invoking isotropy again, we can show that the slip lines are the characteristics of the velocity field.

We thus conclude that for the material considered, the α and β lines form an orthogonal net that coincides with the slip lines which are also the characteristic directions of both stress and velocity fields.

Using the graphical method of solution developed by Prager [4], we need to draw the following three diagrams for each problem:

(a) Field of characteristics or the physical plane

The field of characteristics in a massless domain in a plastic state needs to satisfy the "Hencky-Prandtl" net requirements. These restrictions, which are implied by equilibrium, are: (1) the angle between two characteristics of one family, where they are cut by a characteristic of the other family, must be constant along their length, i.e., independent of the particular intersecting member of the other family; (2) along a characteristic, the radius of curvature of each characteristic of the other family at its point of intersection must

change in proportion to the distance travelled.

(b) The stress plane

Writing the equilibrium equations in terms of σ and θ along the characteristics, one can show that the image of a characteristic must trace a cycloid in Mohr diagram; moreover infinitesimal sections of this characteristic in physical space must be orthogonal to their images on the cycloid.

(c) The velocity plane or the hodograph

The velocity of every material point in the physical plane can be mapped into a point in a hodograph. The position vector of the latter, with respect to some origin, is defined to be the velocity vector of the material point.

To satisfy the requirement of incompressibility of the material, corresponding line segments in the physical plane and the hodograph, along slip lines, must be orthogonal.

I-2-5. Discontinuities and singular points

The two mappings described above from the physical plane into the stress plane and the hodograph are one to one and smooth except in special cases that we now point out in some detail.

From the Hencky-Prandtl mesh requirements, the discontinuities in curvature of a member of one family of slip lines can only occur at its intersection with a member of the other family. Discontinuities in stresses may occur across any plane through a point in a plastic domain except on directions parallel to the slip lines. This becomes clear by looking at Fig. I-4. Suppose P_- and C_-

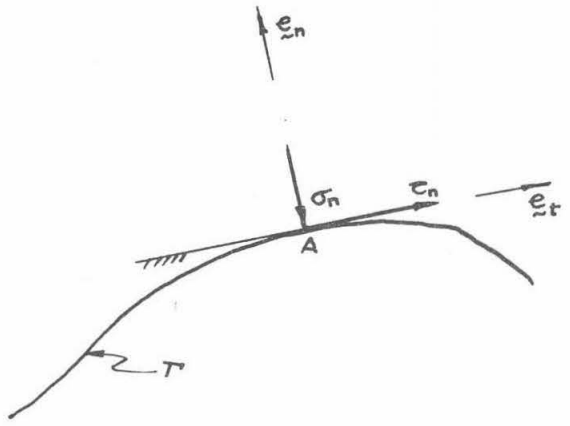

(a) Physical plane

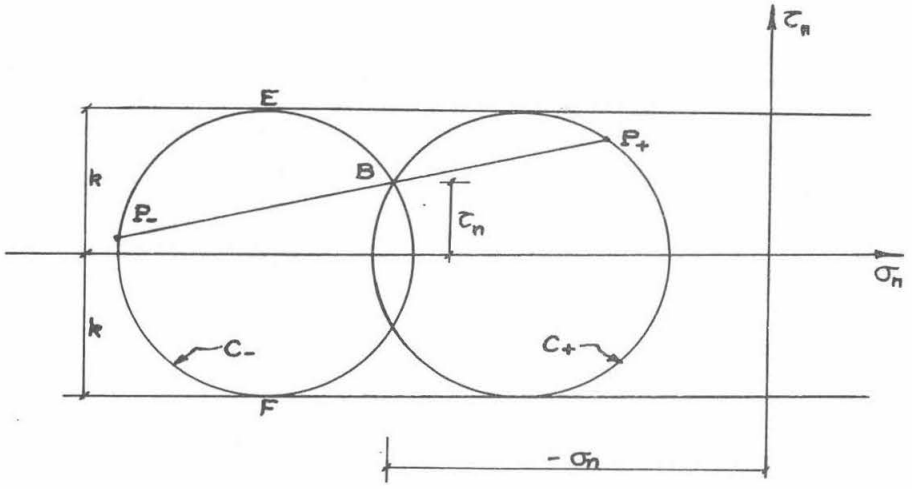

(b) Stress plane

Fig. I-4. Discontinuity in the stress field.

are the pole and the circle of stress corresponding to the stress state at physical point A, lying on a curve Γ (Γ is not a physical boundary) when approached from below. Also let PB be parallel to the tangent to Γ at A. Clearly σ_n and τ_n, at A are as shown in Fig. I-4. Now if the stress field undergoes a discontinuity across Γ, so that P_+ and C_+ are the location of the pole and the circle when A is approached from above, then equilibrium across Γ implies that the location of P_+ and C_+ are determined uniquely as shown in Fig. I-4. In the case where P_+ coincides with E or F, no discontinuity can exist.

The orthogonality between a line segment of a characteristic and its image in the stress plane and the hodograph implies the following conditions:

(1) If one characteristic is a straight line, which also implies that its family is straight lines, its image in the stress plane is a point. Its image in the hodograph can however be either a straight line or a point.

(2) If a family of characteristics meet at a point, a singularity of stresses and velocity is implied and the point has an infinite number of image points; it must therefore be excluded from the domain.

Velocity discontinuities may exist either inside a plastic domain or at the boundary between plastic and rigid domains. By looking at a jump in velocity as the limit of a rapid change of a continuous velocity in a layer whose thickness tends to zero, we can directly deduce that the discontinuity must be in the tangential velocity component across a slip line. A point on this slip line will

have two image points in the hodograph, one corresponding to each side from which this point is approached; the vector joining the two images is called a "jump" and will be represented by a heavy line in the hodograph. At the boundary between a plastic zone and a smooth surface, a velocity discontinuity may also exist. This also is represented by a jump in the hodograph.

I-2-6. Boundaries of a plastic domain, free, smooth and rough

A "free surface" is a boundary of a plastic domain along which the normal and shearing tractions vanish.

A "free surface fixed in space" is a free surface with a fixed position in space for all time. If a boundary of a domain in a plastic state is a free surface fixed in space, it thus follows that the normal component of velocity at points in the plastic domain, in the neighborhood of the surface, will vanish.

A "smooth surface" is a boundary along which the shearing component of the surface traction vanishes. Moreover, the normal component of the relative velocity with respect to this surface of adjacent points on the boundary and within the plastic region must vanish.

A "rough surface" with coefficient of friction μ is a boundary along which points in the plastic domain adjacent to the boundary have no normal relative velocity with respect to this surface. In case there exists a relative tangential velocity between the surface and adjacent points, the ratio of shearing to normal stresses at this point is given by μ. If, on the other hand, no relative tangential velocity

exists at this point, then the stress ratio is less than or equal to μ.

From the previous definitions, it is clear that:

(a) For free and smooth surfaces, the slip lines at a point on the surface makes an angle equal to $\pm\frac{\pi}{4}$ with the normal to the surface.

(b) For rough surfaces, there do not exist perfectly rough or imperfectly rough surfaces as are often mentioned in the literature [5] and [6], i.e., there exists one degree of roughness which is completely defined by specifying the parameter μ which is a property of the two bodies in contact (solid friction). On the other hand the definition, being only applicable to points adjacent to the boundary, does not rule out the possibility of having any permissible velocity field within the plastic domain which may or may not have velocity discontinuities.

As an example, let us consider the rough surface Γ with coefficient of friction μ shown in Fig. I-5. Let Γ be fixed in space and the plastic material below it occupy regions D_1 and D_2. Let D_1 and D_2 be separated by a characteristic Σ which is taken, for simplicity, to be a straight line. Suppose that a permissible plastic state exists in D_1 and D_2, such that at any arbitrary point A on Γ the ratio of tangential to normal stresses does not exceed μ. It is clear that along Γ the definition of a rough surface is satisfied if D_1 is fixed in space, while D_2 may or may not be moving (e.g. parallel to Σ as a rigid body). Note: In fact D_1 may be in a rigid state and the same mode of deformation would still occur. However such generalizations will not be needed herein.

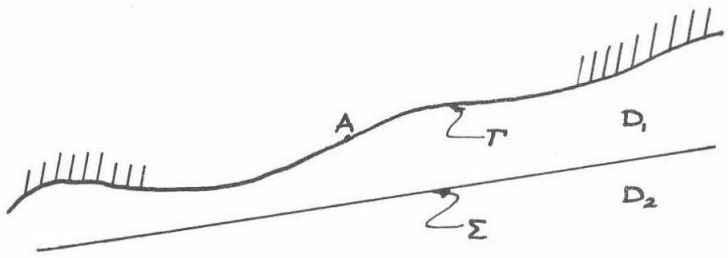

Fig. I-5. Example of a permissible velocity field solution in the vicinity of a rough surface Γ.

I-2-7. Assumed steady free surfaces; uniqueness of solutions

All the rigid indenters treated here (smooth or rough) will provide us with well-defined boundary conditions for at least part of the total boundary of the plastic domain. To find a steady-state solution to some of the problems of interest here requires the existence of a free surface which will have to be assumed. This type of surface will now be discussed in some detail since it is critical to the solutions obtained.

The two-dimensional symmetric rigid wedge in Fig. II-1 is an illustration. It has a smooth surface and is moving with constant velocity $+U$ in a full space of a rigid-perfectly plastic material. Along the front boundary ABC of the plastic domain, we have a smooth surface with properties previously defined. Now for the rear part we have two alternatives:

(1) Require that the rigid-plastic material extend over the full space and in particular to remain in contact with surface AC. This approach is physically attractive because, if we begin with the wedge embedded in a full space of an incompressible material, as a reasonable initial condition, the volume of material should remain constant after any subsequent deformation; that is, the material should fill the space apart from the wedge entirely. However, with the ideal material model of perfect plasticity, solutions under those restrictions could not be obtained.

(2) Allow the existence of a free surface behind the wedge at all times (air gap) ADC in Fig. II-1 and look for the shape of this surface that would satisfy a steady-state condition. It is easier at

this stage to consider the conjugate problem where the rigid-plastic material moves past the indenter with a velocity - U. To satisfy the condition of steady-state, the assumed free surface needs to be a free surface fixed in space, i.e., the velocity of any point on the surface must be parallel to the tangent to the surface at this point.

The main advantage of the second technique, which will be used in this text, is that it allowed us to reach solutions by means of the relatively simple theory of perfect plasticity. These solutions are exact if the motion is begun with the free surface having the assumed shape. On the other hand if motion is started with the wedge completely in contact with the full space one needs to study the unsteady transition from the initial configuration to the steady-state motion. This method which requires changes in the model of the deformable medium, for example, the introduction of compressibility, was not done.

After assuming the location of part of the boundary, no uniqueness proof could be obtained. For this reason we will rely on experiments to show how close is the assumption to real steady-states.

I-3. Apparatus for plane strain testing

Before actually solving the indentation problems described in the introduction and since the object of this chapter is to give a theoretical background for subsequent work, we now present the idea behind the apparatus used in plane strain testing.

After the theoretical solution of an indentation problem had been obtained using the rigid-perfectly plastic model, it was felt that an experiment on a real material exhibiting properties similar, but not identical, to the one in the theory would be useful in understanding how differences in properties affect the results. Moreover in cases where part of the boundary had been assumed in the theoretical solution, the experiment would represent a check on this assumption. To this end, a special box was constructed which when filled with clay afforded plane strain testing with particular emphasis on the pattern of deformation.

I-3-1. Clay, the plastic material

A modelling clay was chosen to simulate the rigid-perfectly plastic material; our choice was made because of the following reasons:

(a) Convenience in handling

The clay, having been mixed with oil during its manufacture, is sensitive to temperature. At 60° C it is in a near fluid state, while at room temperature (26° C) it is in a solid state. This allows the relatively convenient casting and molding of the clay into the required geometry at 60° C, before performing all tests at room

temperature.

The changes in strength due to room temperature fluctuations were measured after each test, using a vane test [7] and found negligible.

(b) The stress-strain behavior of the clay

The results of a set of one-dimensional compression tests on this clay, performed at room temperature, are shown in Fig. I-6. In these tests, the increments of load were added at equal time intervals and the strains were recorded before each increment. The test specimens were cylindrical with both diameter and height approximately equal to 3.5 cms. No correction was made for the change in geometry due to straining. No brittle fracture occurred in any of the tests.

In Fig. I-6, it can be seen that the clay behaves as a rigid-plastic material with respect to:

(1) Rate of loading: comparing curves A and B, Fig. I-6-a, the rate of loading has a negligible effect up to 5% strain, while for 20% strain, an increase in rate of 400% changes the stress by less than 15%.

(2) Unloading: the clay has virtually no elastic recovery upon unloading, Fig. I-6-b, and in this respect is similar to the ideal material. Along the first portion of the unloading curve, the strain is still increasing while the stress is being decreased; this behavior is believed to be caused by the time-dependent properties of clay.

On the other hand the clay behaves quite differently from the

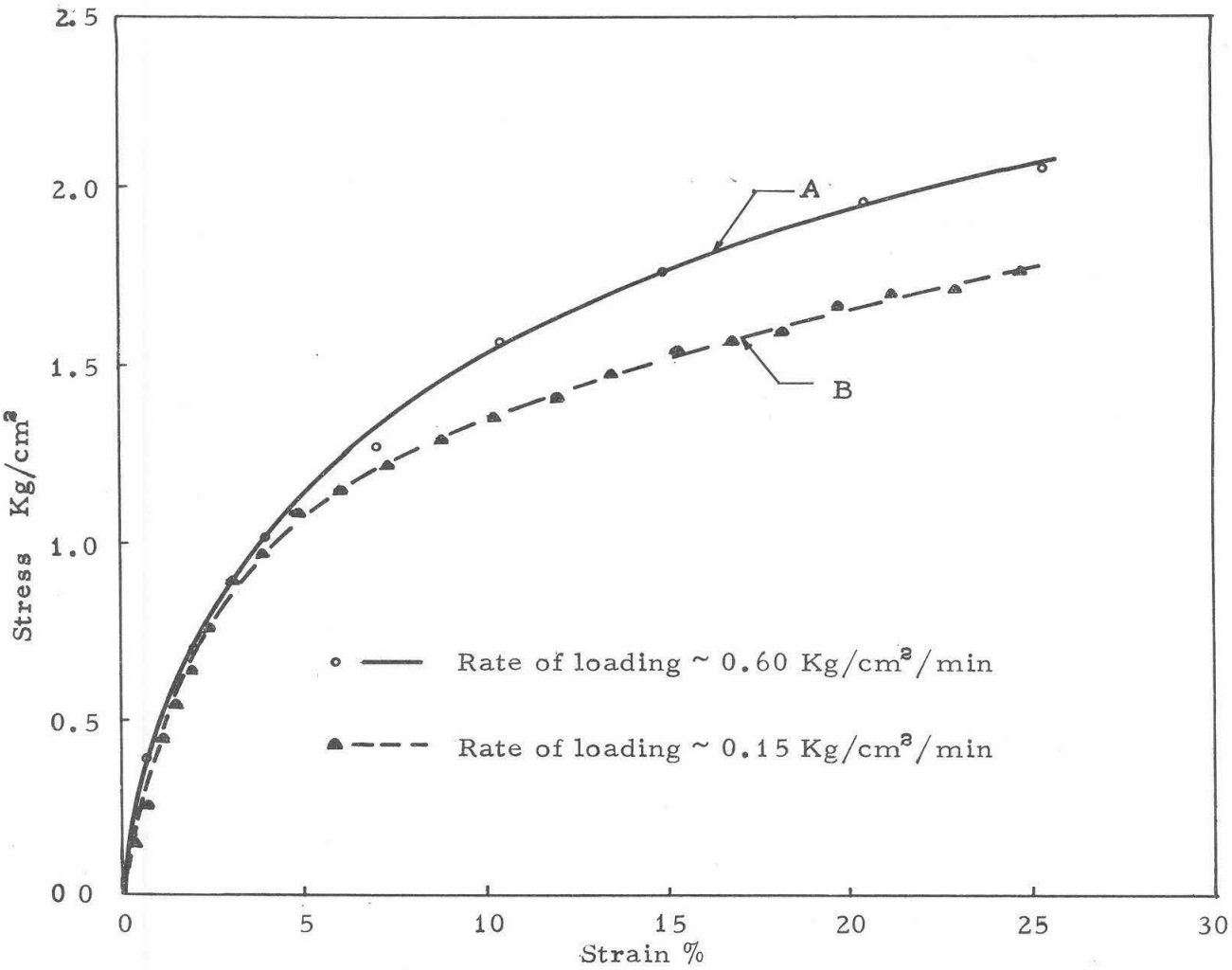

Fig. I-6-a. Effect of rate of loading on modeling clay behavior.

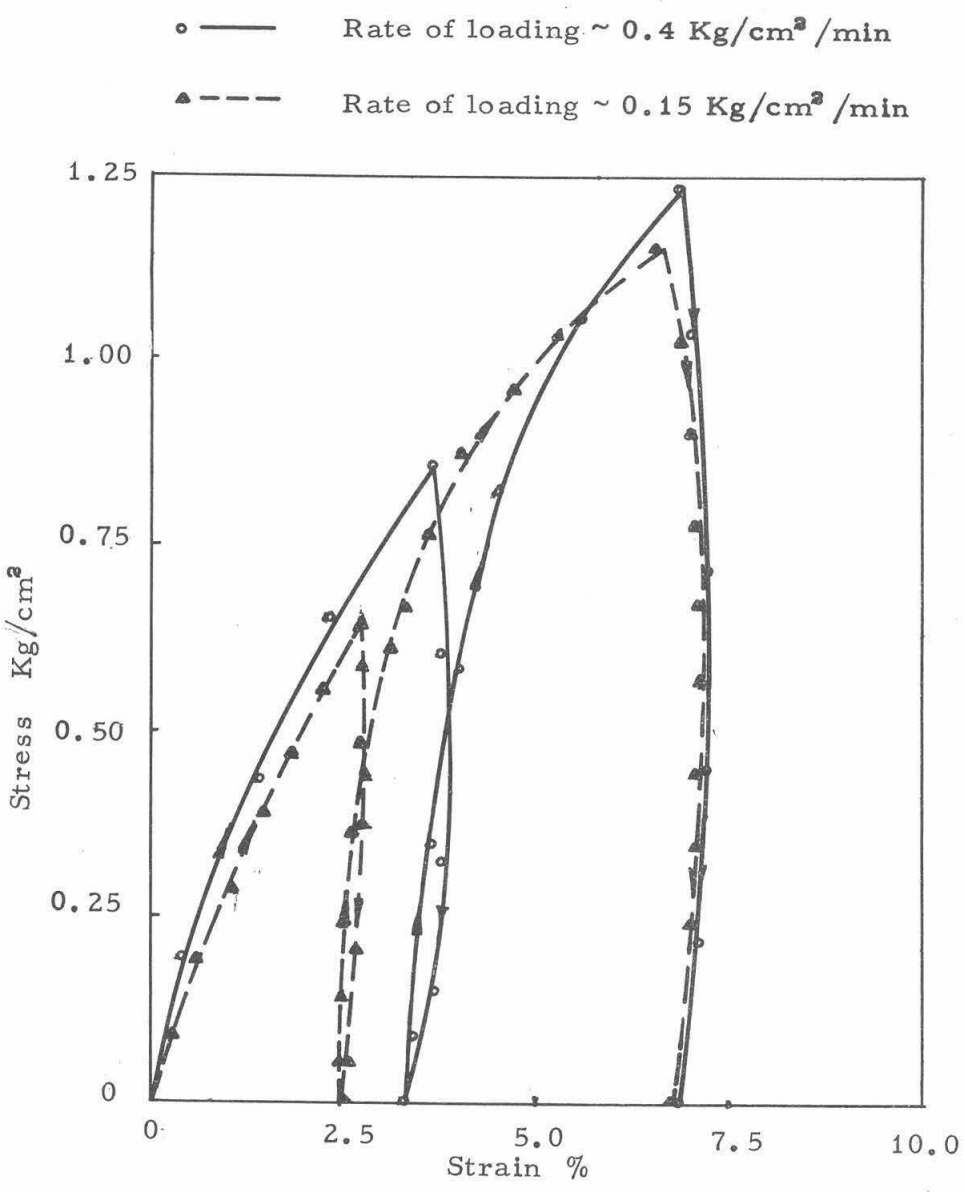

Fig. I-6-b. Unloading curves for modeling clay.

rigid-plastic material in the loading part of the curve. It has a near-parabolic shape and no definite yield stress can be seen. This fact makes our tests more interesting, since most clays behave in this manner and an estimate of how close the theory can get to real test behavior is of prime importance.

I-3-2. Apparatus

Since the main object of the experiments was to determine the pattern and mode of deformations in plane strain problems, a special box was designed to suit that purpose. Instead of recording deformations at the walls of the container as most previous experimenters have done [2], [3], we make use of the symmetry about the center plane to reduce the effect of boundary shearing stress unaccounted for in the theory.

The box is shown in Fig. I-7-a and its dimensions given in Fig. I-7-b; the enclosed space, where the clay is to be fitted, is $40 \times 40 \times 10$ cm . The basic components of the box are four parts A and two sliders B. Each two of the parts A can be assembled separately to form half the box; we are interested in having each half on either side of the center plane, to behave as a unit. Such a half is shown in Fig. I-7-c. The two halves can then be held together by means of bolts and nuts to form the static part in the experiment. Sliders B are held together at both ends by means of aluminum blocks D. The surfaces of the sliders in contact with A are covered with teflon to minimize friction. Part C fits in a cut made in the slider B; it has properly spaced holes to allow the fixation of the

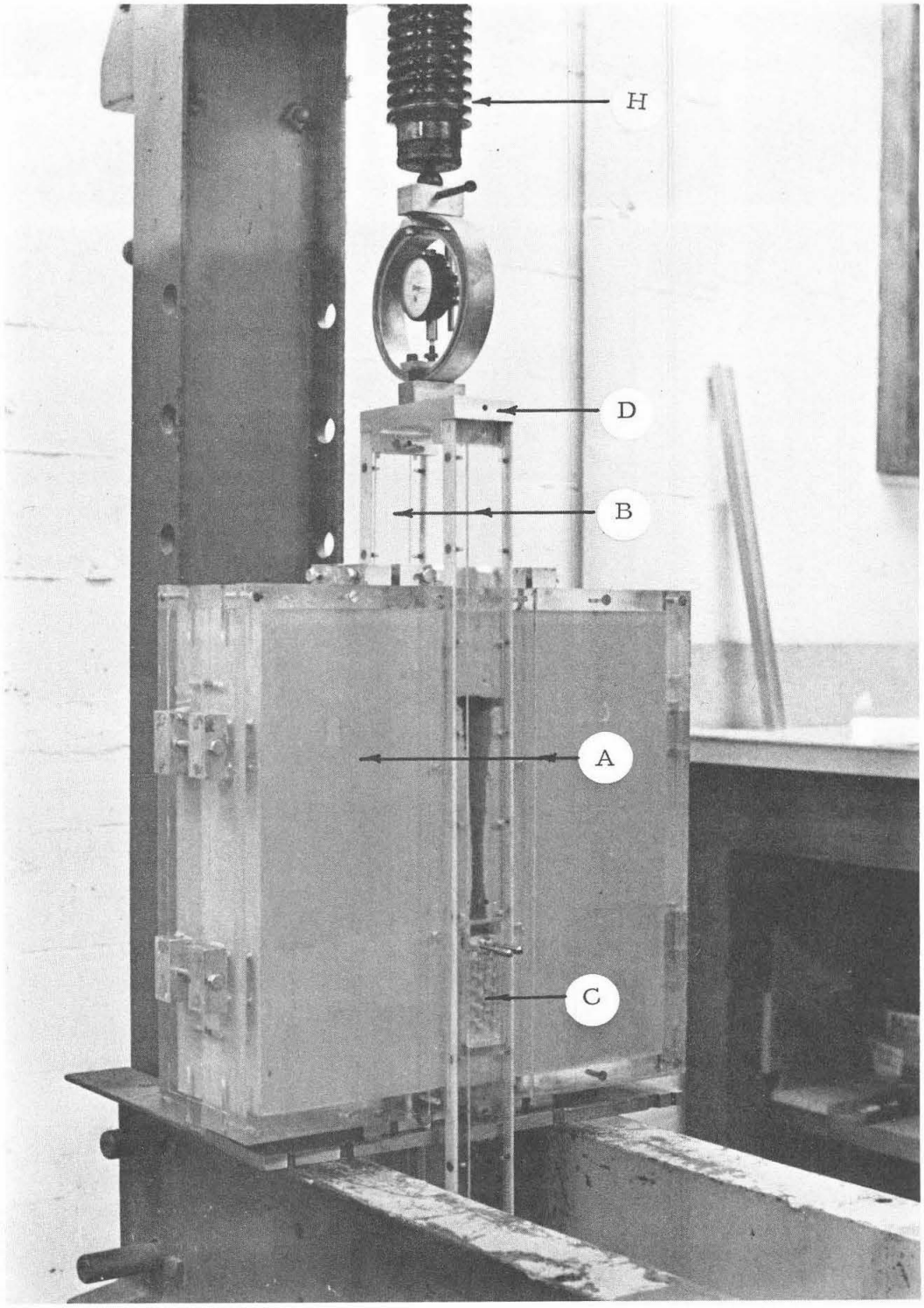

Fig. I-7-a Apparatus for plane strain testing.

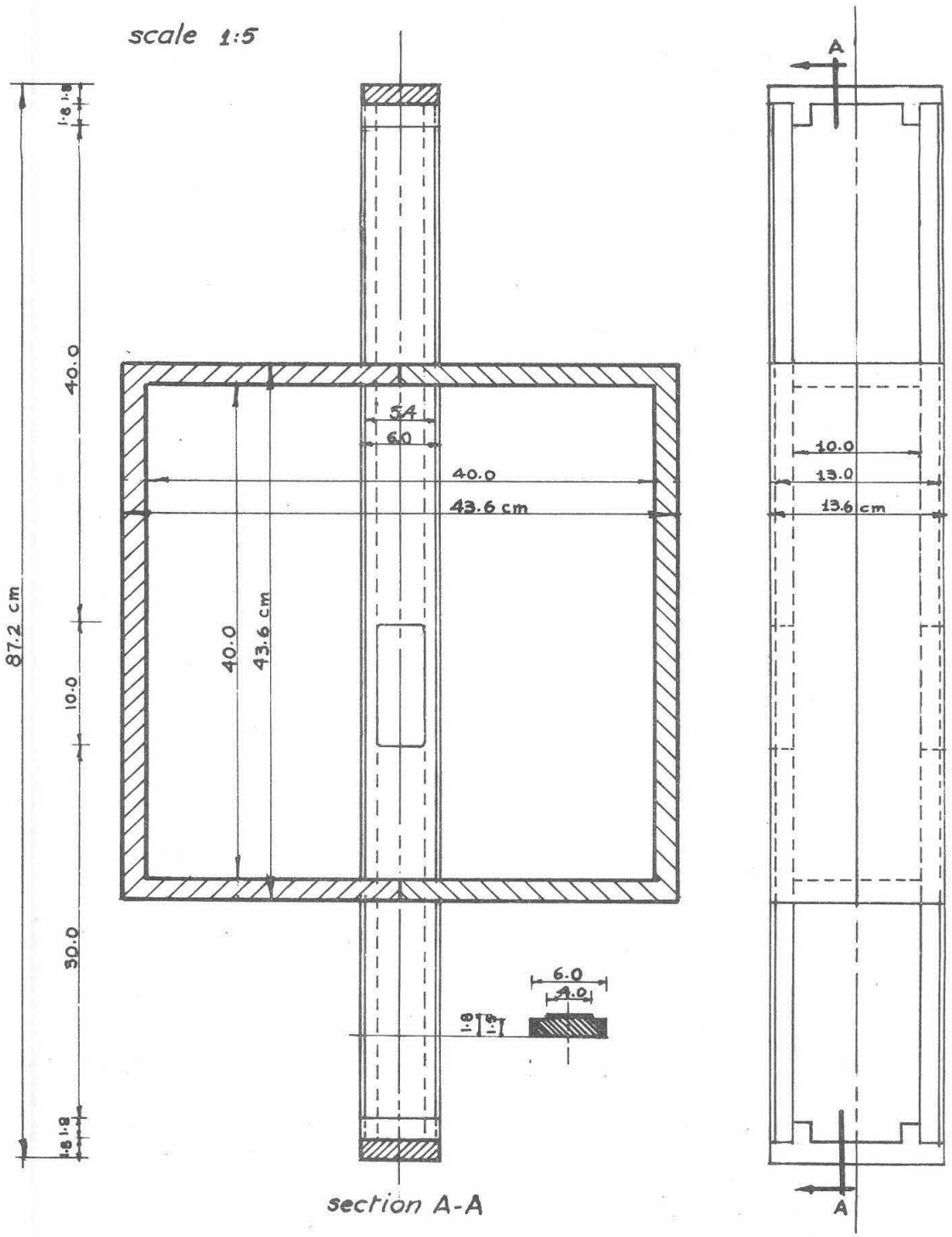

Fig. I-7-b. Dimensions of box used in plain strain testing.

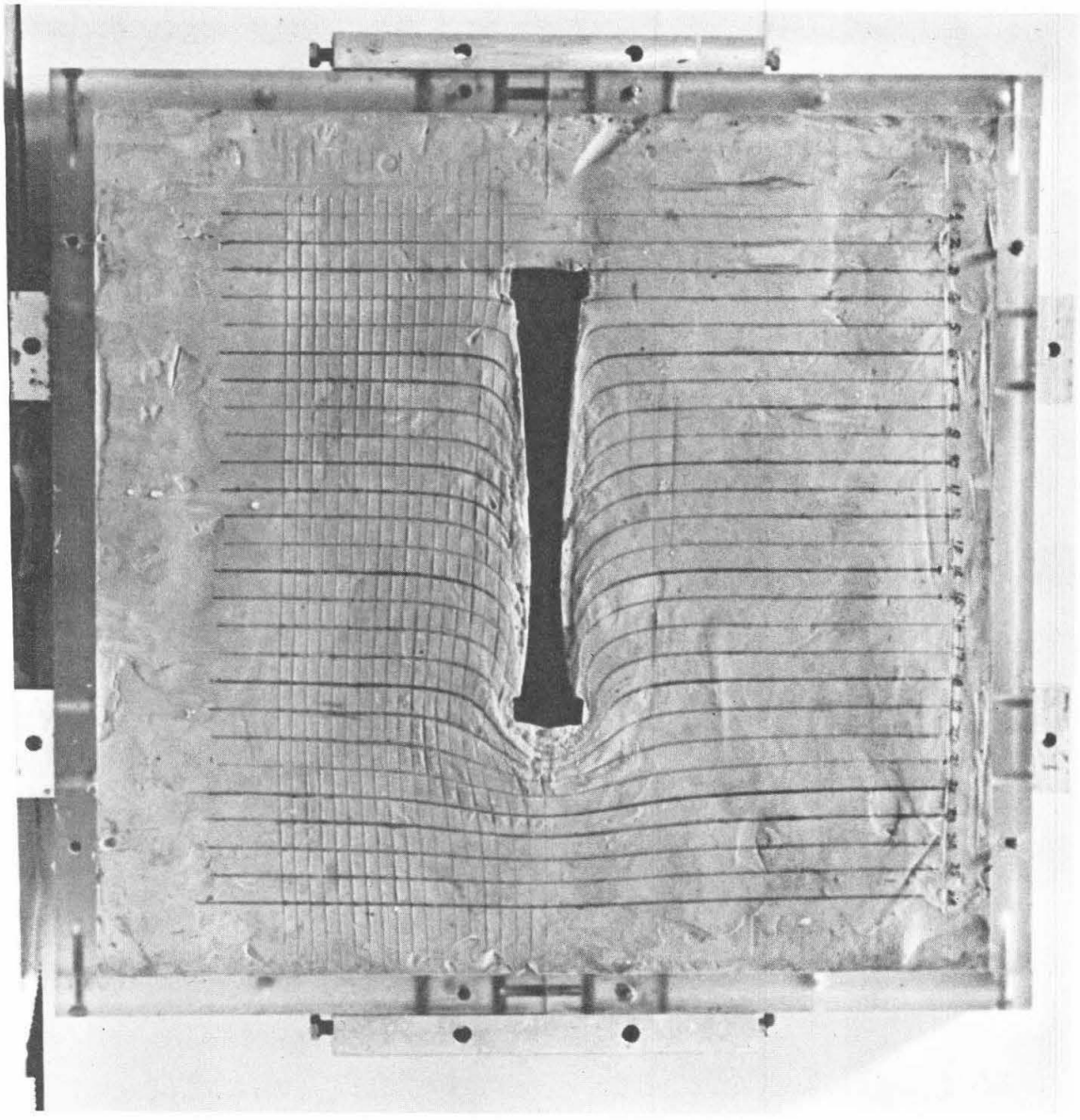

Fig. I-7-c Half the box on one side of the center plane.

indenter E to the sliders by means of screws. The cut in the slider is necessary to insert and adjust the indenter into its proper position. The movable part of the experiment which includes B, C, D and E is shown in Fig. I-7-d.

I-3-3. Plane strain testing

a. Specimen preparation

A test specimen representing an infinite medium is made by filling the box with clay. This is done as follows:

The clay is heated to 60°C and poured into each half of the box on both sides of the center plane separately. At this stage, each slider B is attached to half of the box and the indenter secured in the proper position to start a test. After the clay has solidified at room temperature, an orthogonal grid is drawn on the surface of the clay which represents the center plane. One set of lines is drawn parallel to the direction of motion of the sliders. It was found that securing the indenters in position before pouring the clay is more convenient and accurate than cutting a hole in the hardened clay and then inserting the indenter; this however requires having two identical indenters to attach each to one half of the box during clay preparation.

b. Testing

After 48 hours of cooling, the two halves of the box are brought together, and blocks D and the indenter fixed to the sliders. To avoid buckling of the sliders two stiffening U channels were added; the test set up is shown in Fig. I-7-e.

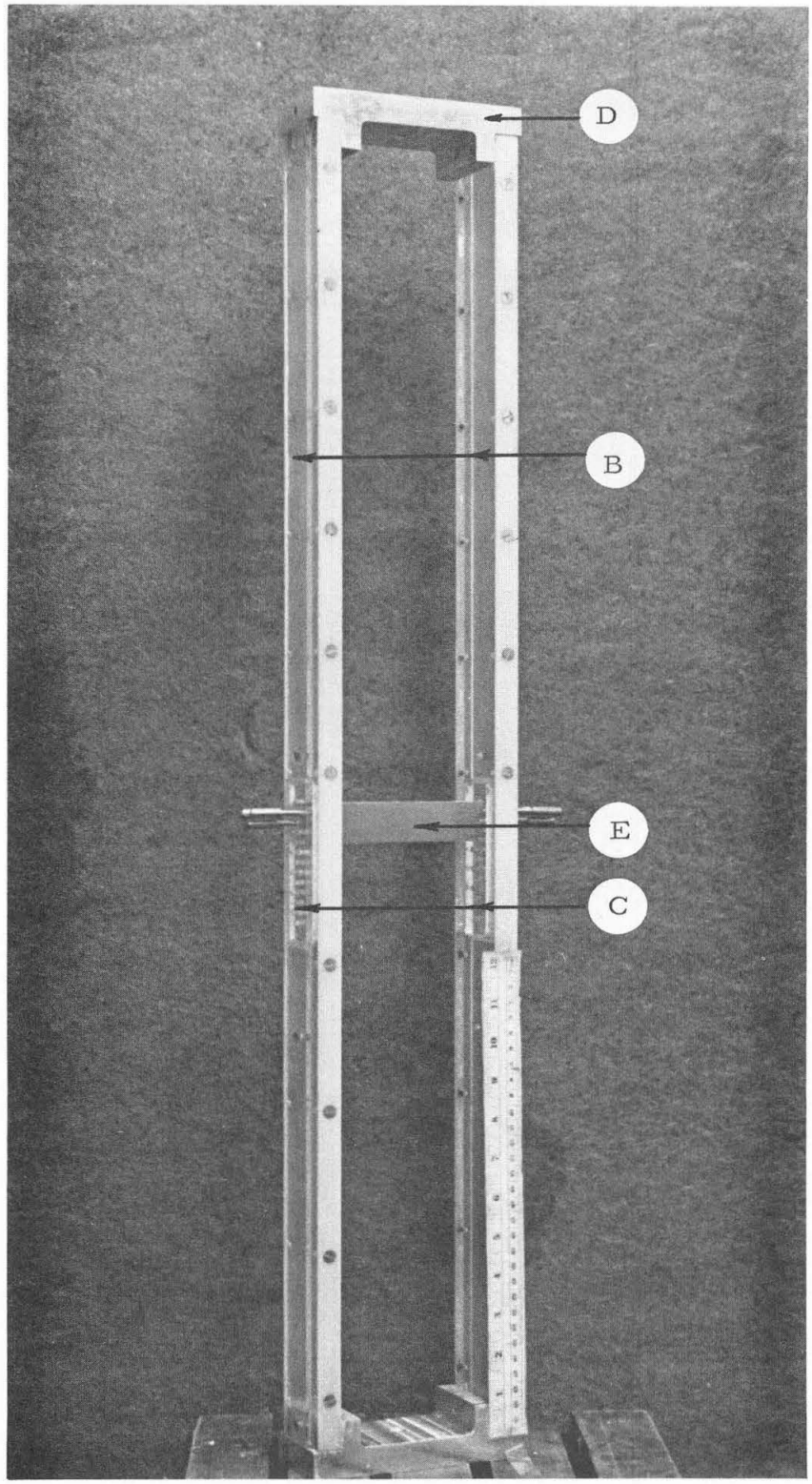

Fig. I-7-d Movable parts in plane strain testing.

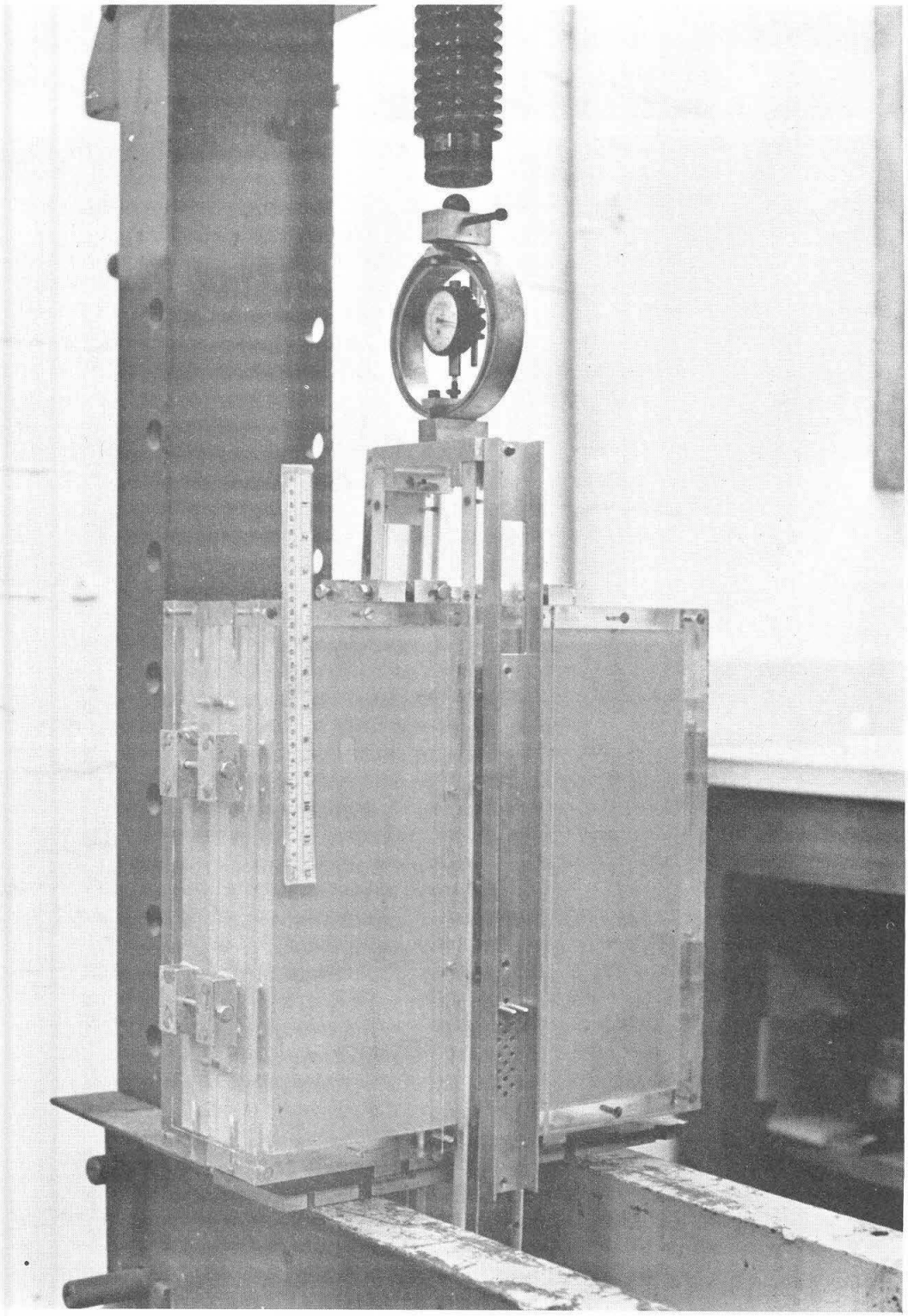

Fig. I-7-e Test setup

The box is rested on two parallel I beams of a 10-ton capactity compression machine spaced with a sufficiently large gap for the sliders to move between them. To measure the load, a proving ring is inserted between the upper block D and the head of the machine H which can be driven by an electric motor to move downwards at a constant speed of 1.36 mm /sec. The indenter is driven through the clay by the motion of the driving head of the machine.

In this setting, we take readings of the load as the testing proceeds. During the motion of the indenter a deformation pattern is recorded at the center plane by the distortion of the grid. After the test, when the two halves are separated, the distortions can be measured on the grid.

I-4. Finite element solutions, the bilinear technique

Besides the experimental verification on perfect plasticity solutions a second check will be made using the finite element technique, the essentials of which now follow. Let curve B in Fig. I-8-a represent the stress-strain deviatoric behavior of the modelling clay used in testing. When this type of behavior, which is typical of a wide class of saturated clays, is incorporated into the field equations, it makes the solution of general problems impossible; to obtain solutions requires further simplifications. If a piecewise linear curve is used to approximate curve B, solutions can be found either theoretically or through numerical techniques depending on how the idealization has been made.

A first step in idealizing curve B is through the rigid-perfectly plastic behavior, curve A, Fig. I-8-a. Theoretical solutions now can be found and generalizations are easy to make because of the relative simplicity of describing the material. On the other hand although such an approximation may be acceptable in some problems, it may not be for others and a more accurate description is necessary.

A better idealization may be achieved through the bilinear curve C. Theoretical solutions are no longer possible and numerical techniques must be introduced. Out of these techniques we chose the finite element method developed by Wilson [8] with corrections and modifications. In addition to filling the gap between ideal plasticity and real material behavior, the finite-element method gives insight into the deformation and stress fields. Furthermore, once plane-strain solutions have been found and compared with ideal plasticity

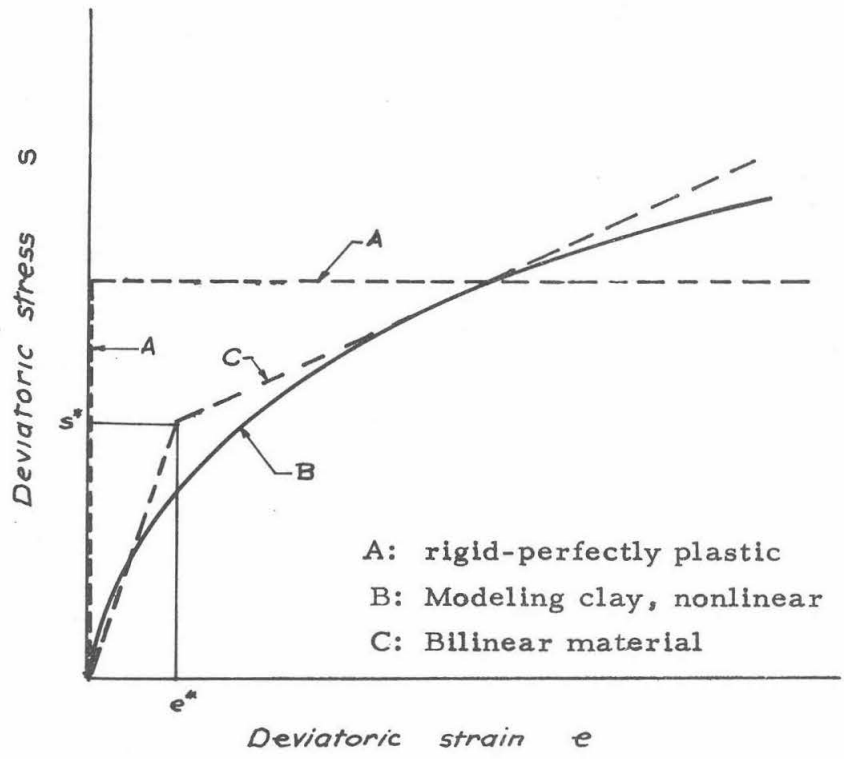

Fig. I-8-a. Different idealization methods for a nonlinear material.

and test results, the extension to axi-symmetric problems is not difficult and requires a new meaning and credibility.

Finally we wish to make it clear that since bilinear solutions rely on solving successive infinitesimal elasticity problems, as will be seen shortly, the technique as usually employed does not allow for the large deformations associated with steady state problems. In that respect, the finite element solutions apply for incipient failure while ideal plasticity covers the steady state.

I-4-1. Definitions and notations

The following definitions apply only to the discussion of finite element solutions in the rest of this chapter as well as in Appendix A; they were simplified to cover the discussion of the problem at the price of generality. The basics of finite element theory can be found in Zienkiewicz [9] while the elasticity terminology is that described by Turteltaub [10].

(1) Elastostatic state

Let R be a bounded regular region (see Kellog [11]) in Euclidean 3-space. We call the ordered array of functions $\mathcal{S} = [\underset{\sim}{u}, \underset{\sim}{\gamma}, \underset{\sim}{\sigma}]$ an elastostatic state on R with the vector-valued displacement field $\underset{\sim}{u}$, the 2-tensor strain field $\underset{\sim}{\gamma}$ and the 2-tensor stress field $\underset{\sim}{\sigma}$ corresponding to the 4-tensor elasticity tensor field $\underset{\sim}{c}$ and the vector-valued body-force density field $\underset{\sim}{f}$, provided:

(a) Continuity conditions

$$\left.\begin{array}{c} \underset{\sim}{u} \in c^2(\dot{R}) \cap c(R), \quad \underset{\sim}{\gamma} \in c^1(\dot{R}) \cap c(R), \quad \underset{\sim}{\sigma} \in c^1(\dot{R}) \cap c(R) \\ \underset{\sim}{c} \in c(R) \quad \text{and invertible}, \quad \underset{\sim}{f} \in c(R) \end{array}\right\} \quad (2)$$

(b) field equations (3), (4) and (5) hold on $\dot{R}$

$$\gamma_{ij} = \frac{1}{2}(u_{i,j} + u_{j,i}) \tag{3}$$

$$\sigma_{ij} = C_{ijk\ell}\gamma_{k\ell}, \qquad C_{ijk\ell} = C_{jik\ell} = C_{k\ell ij} \tag{4}$$

$$\sigma_{ij,j} + f_i = 0 \tag{5}$$

$i,j,k,\ell = 1,2,3$ with summation convention implied

For the special case when $\underset{\sim}{c}$ is isotropic, i.e. in the form

$$c_{ijk\ell} = \lambda\delta_{ij}\delta_{k\ell} + G(\delta_{ik}\delta_{j\ell} + \delta_{i\ell}\delta_{jk})$$

This amounts to replacing (4) by (4'), where:

$$\gamma_{ij} = \frac{1}{E}\left[(1+\nu)\sigma_{ij} - \nu\sigma_{kk}\delta_{ij}\right] \tag{4'}$$

where

Young's modulus E

Poisson's ratio ν

The shear modulus $G = \dfrac{E}{2(1+\nu)}$

Lamé modulus $\lambda = \dfrac{\nu E}{(1+\nu)(1-2\nu)}$

(2) A deviatoric state

We call the ordered array (s,e) a deviatoric state with scalar fields s and e associated with the elastostatic state $\mathcal{S}$ provided:

$$\left.\begin{aligned} \text{the deviatoric stress } \quad s &= \frac{1}{\sqrt{2}}\sqrt{(\sigma_1-\sigma_2)^2+(\sigma_2-\sigma_3)^2+(\sigma_3-\sigma_1)^2} \\ \text{and the deviatoric strain } \quad e &= \frac{1}{\sqrt{2}}\sqrt{(\gamma_1-\gamma_2)^2+(\gamma_2-\gamma_3)^2+(\gamma_3-\gamma_1)^2} \end{aligned}\right\} \quad (6)$$

where σ_i and γ_i are the principal values of the 2-tensor fields $\underset{\sim}{\sigma}$ and $\underset{\sim}{\gamma}$ respectively.

Notes.

(a) The invariance of s, under rotation of the frame of reference, and subsequently of e can easily be proved (see [12]) which makes the definition of a deviatoric state meaningful.

(b) For an isotropic material upon substitution from (4') into (6) we get

$$s = 2Ge \quad (7)$$

(3) Bilinear material

By a bilinear material we mean a linear isotropic material, with elastic modulii G and ν, for values of s less than a particular value of s^*. For s larger than s^* its shear modulus becomes nG.

The $s-e$ relationship for the material is thus given by:

$$\left.\begin{aligned} s &= 2Ge && \text{for } s \leq s^* \\ s &= 2G[e^* + n(e-e^*)] && \text{for } s \geq s^* \end{aligned}\right\} \quad (7')$$

where the deviatoric yield strain $e^* = s^*/2G$, the deviatoric yield stress is s^* and the ratio of plastic to initial modulii is n.

This material is defined through G, ν, s^* and n in a graph which is given by curve C in Fig. I-8-a.

According to (6) substituting $\sigma_1 = Y$ and $\sigma_2 = \sigma_3 = 0$ and calling the corresponding $s = s^*$, we get

$$s^* = Y \tag{8}$$

This relation describes the yield condition for a uniaxial stress testing with Y as the one-dimensional yield stress.

(4) The error and the average error.

Associated with an (s,e) state and a bilinear material in the element i, we define an error Δs_i as the ratio of the difference between s and the deviatoric stress s', corresponding to e on the bilinear curve, to s^*, i.e.

$$\Delta s_i = \frac{s - s'}{s^*}$$

An example of $s^*(\Delta s)$ is shown in Fig. I-8-b, it is represented by the vertical distance $\overline{34}$.

The average error $\overline{\Delta s}$ is defined as

$$\overline{\Delta s} = \left[\sum_{i=1}^{m} (\Delta s_i)^2 \right] / m \tag{9}$$

where m is the total number of elements in a F.E. mesh.

I-4-2. Wilson's technique

Suppose we have a well-posed problem in elastostatics within the framework of infinitesimal elasticity. Let the elastic material be isotropic with G and ν the elastic shear modulus and Poisson's

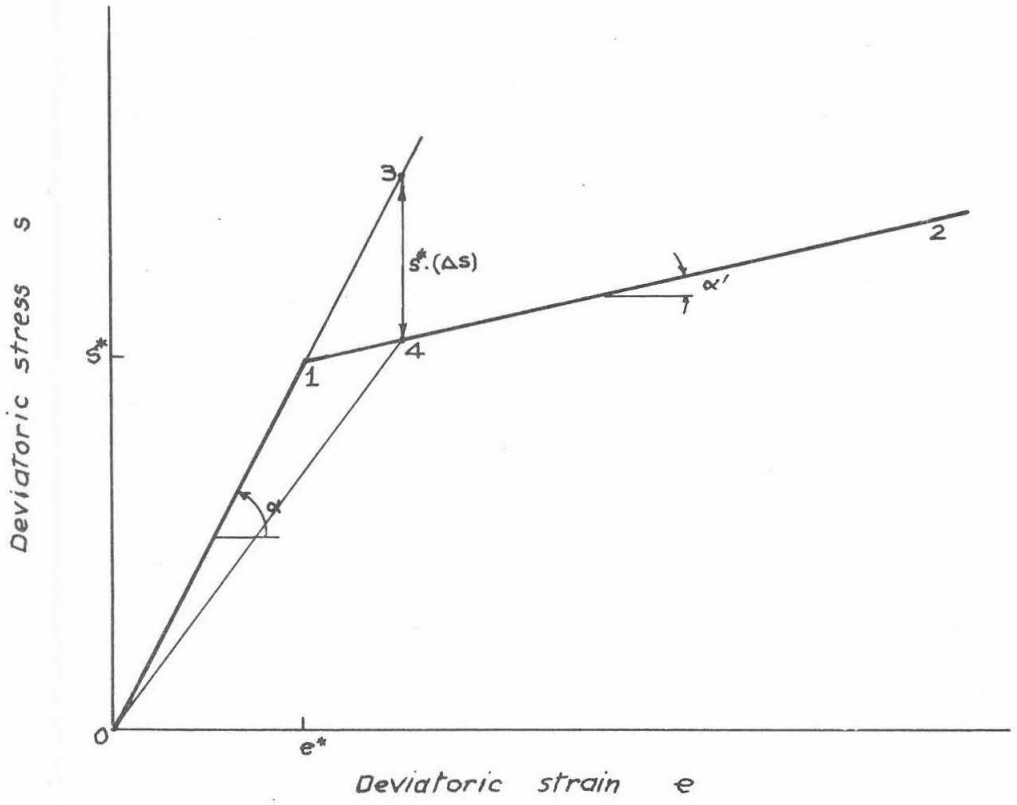

Fig. I-8-b. Wilson's technique of solution for a bilinear material.

ratio describing it. Now keeping all other properties the same, let it be bilinear in deviator behavior, i.e., its s-e diagram is 012 Fig. I-8-b instead of 013. By a solution to this problem we mean that it is required to find a state $\mathcal{S} = (\underset{\sim}{u}, \underset{\sim}{\gamma}, \underset{\sim}{\sigma})$ in which every point in the field has an (s,e) state lying on 012 instead of 013.

Wilson's technique was developed to achieve this goal by solving the same problem several times, each solution being called an approximation. At every element in the field the rigidity is changed according to the (s,e) state at this element in the previous approximation. The technique thus amounts to solving several inhomogeneous linear elasticity problems.

In a more systematic manner, this is done as follows:

(1) The first approximation is the solution for a linearly elastic material with a rigidity equal to the initial part of the curve 01 Fig. I-8-b.

(2) Let point 3 be the (s,e) state within a certain element; point 3 lies on the straight line 013. Let point 4 be directly below 3, but on line 12, i.e. points 3 and 4 are two deviatoric states having the same strain e. Then for this element, in the second approximation, the s-e line will be taken to be 04.

(3) Repeating the same procedure for all elements in the field, the second approximation will thus be the solution of a nonhomogeneous linearly elastic material.

(4) The subsequent approximations are carried out in a similar manner until the (s,e) state at every element lies close enough to line 012 to be considered satisfactory. The method that

will reach such a state in the least number of approximations is considered superior because of the cost of computations.

I-4-3. Modifications made on Wilson's technique

The successful convergence of the (s,e) states to line 012 by successively changing the stiffness of each element hinges on the following assumption.

Let the (s,e) state of a point in an elastostatic field subject to certain boundary conditions be represented by point 3, Fig. I-8-c; point 3 lies on line A representing the stiffness of the elastic material. Then a change in the stiffness of every point in the field, under the same boundary conditions, will change the (s,e) state at that point from 3 to 5 or 7. Point 5 which lies in the second quadrant on line B corresponds to an increase in stiffness, and point 7 which lies in the fourth quadrant on line C corresponds to a decrease in the stiffness. Repeating the same argument, for other lines such as D, E and F we get a "convergence curve" which represent the locus of the (s,e) states at a point in a problem when its rigidity varies. The assumption of the technique is that the slope of the convergence curve is non-positive.

The assumption is certainly true for homogeneous elasticity fields ($\underset{\sim}{c}$ is constant on R) when all points have the same stiffness. On the other hand, for the general case, when the material is inhomogeneous the assumption neglects the effect of the variation of the stiffness of other points on the (s,e) state at a particular one. It is for this reason that Wilson's convergence technique was not proved,

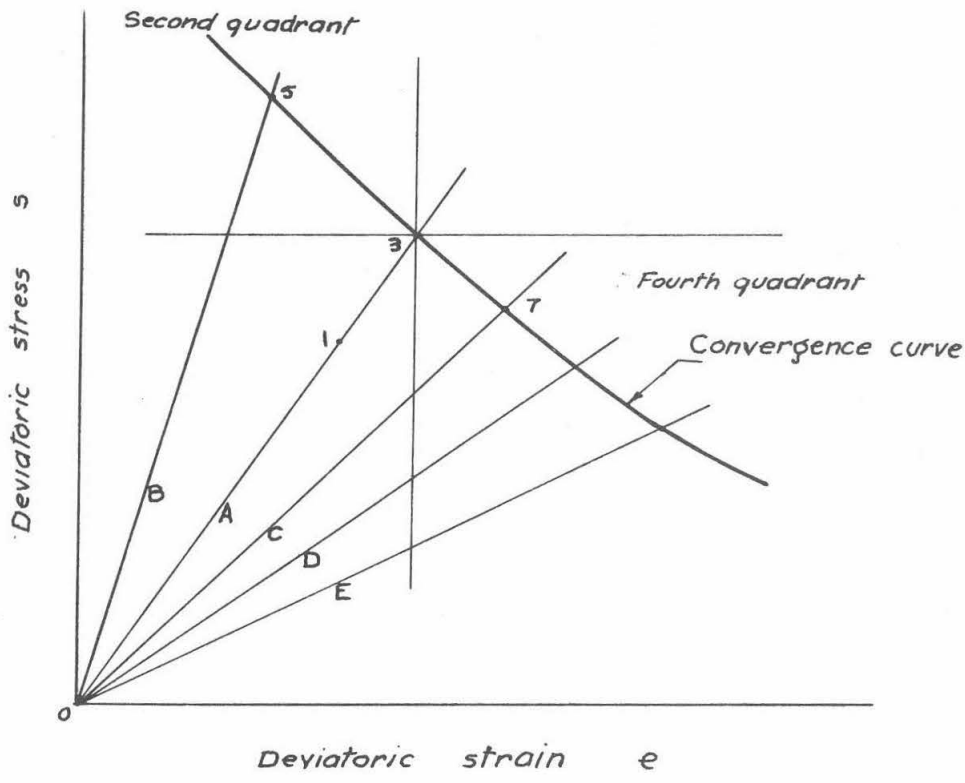

Fig. I-8-c. Construction of the convergence curve.

as pointed out by Clough [13] and checked by solving different problems, simply because the assumption on which it relies is not always true. However by trying the technique on a variety of problems, we found that, depending on the problem, one can reach a satisfactory degree of accuracy by changing the method of selection of the rigidity of an element after each approximation. Here we now give the main modifications made on Wilson's code. Some examples of how to make these changes are given in Appendix A.

(1) From equation (6), the slope of the (s,e) line is 2G. In Wilson's code this value was taken as E such that instead of converging to the correct bilinear line $\overline{012}$, Fig. I-8-d, the solution converges to the dotted line in the same figure which does not have a particular meaning.

(2) Since the intersection of the convergence curve with the line 012 is the solution to the problem, point B in Fig. I-8-d, a technique that would reach that point in a smaller number of approximations will certainly be better. With line 012 known and the convergence curve having a non-positive slope let us investigate special cases of the convergence curve.

Suppose we have a uniform field of stresses or strains. For a first type boundary value problem, where the displacements are specified along the boundary, the strains at every point will be constant for any value of stiffness of the material; hence the convergence curve will be given by the vertical line $\overline{34}$ where 4 is the intersection required. Similarly for a second type of boundary value problem, where the surface tractions are specified along the boundary,

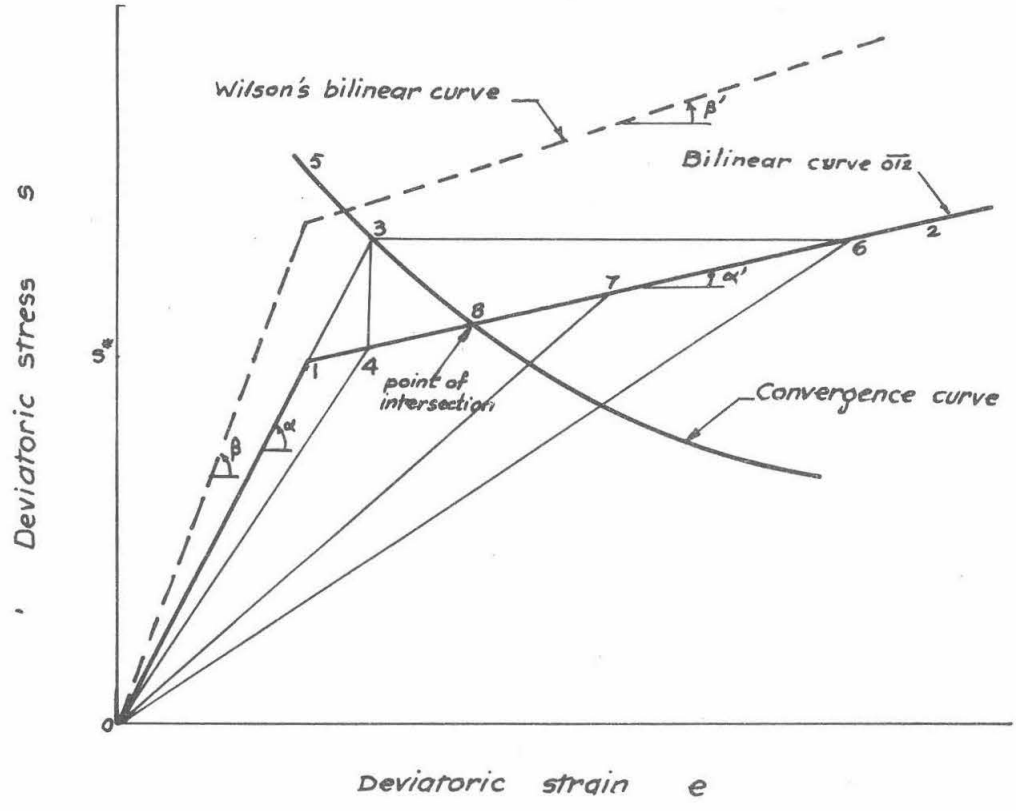

Fig. I-8-d. Modified Wilson's technique to solve problems of bilinear material by finite element.

the stresses at every point will be independent of the stiffness of the material; hence the convergence will be given by the horizontal line $\overline{36}$ where 6 is the intersection required.

In general problems when the fields of stresses and strains are non-uniform, it was found by solving a variety of problems that the intersection is close to either of points 4 or 6 depending on how close the problem is to being of the first or second type. The computer program was thus modified to perform one of three convergence methods after any approximation:

(a) The first method which we call the "strain controlled method" is Wilson's; it uses line $\overline{04}$, Fig. I-8-d. It is suitable for problems close to being of the first type.

(b) The second method we call the "stress controlled method," it uses line $\overline{06}$. It is appropriate to problems close to being of the second type.

(c) The third method we call the "average method" uses line $\overline{07}$, point 7 being at mid-length between 4 and 6 along line $\overline{12}$. It is suitable for mixed problems.

The choice between the three methods is left either to intuition or to experience and trial. In our rigid indenter problems which are of a mixed-mixed type, the fastest convergence was achieved by using the average method for the second approximation and the strain-controlled method for the following ones.

REFERENCES OF CHAPTER I

1. Hill, R., The Mathematical Theory of Plasticity, Oxford University Press, 1950.

2. Mohan, D., Murthy, V. N. S. and Jain, G. S., "Design and Construction of Multi-under-reamed Piles," Proceedings of the 7th Int. Conf. on Soil Mech. and Foundation Engineering, Mexico, Vol. II, 1969, p. 183.

3. Szechy, C., "Some Experimental Observations Relative to the Magnitude and Distribution of Settlements," Proceedings of the 7th Int. Conf. on Soil Mech. and Foundation Engineering, Mexico, Vol. II, 1969, p. 247.

4. Prager, W., An Introduction to Plasticity, Addison-Wesley Pub. Co., 1959.

5. Meyerhof, G. G., "Influence of Roughness of Base and Groundwater Conditions on the Ultimate Bearing Capacity of Foundations," Geotechnique Vol. 5, 1955, p. 227.

6. Meyerhof, G. G., "The Ultimate Bearing Capacity of Wedge-shaped Foundations," Proceedings of the 5th Int. Conf. on Soil Mech. and Foundation Engineering, Vol. II, 1961, p. 105.

7. Lambe, T. W. and Whitman, R. V., Soil Mechanics, John Wiley and Sons, Inc., 1969, p. 79.

8. Wilson, E. L., "Finite Element Analysis of Two-Dimensional Structures," Thesis presented to the University of California at Berkeley, California in Partial Fulfillment of the Requirements for the Degree of Doctor of Engineering, 1963.

9. Zienkiewicz, O. C., The Finite Element Method in Engineering Science, McGraw-Hill, 1971.

10. Turteltaub, M. J. and Sternberg, E., "On Concentrated Loads and Green's Functions in Elastostatics," Archive for Rational Mechanics and Analysis, Vol. 20, No. 3, 1968, p. 193.

11. Kellog, O. D., Foundations of Potential Theory, Dover Publications, 1953.

12. Fung, Y. C., Foundations of Solid Mechanics, Prentice Hall, 1965, p. 80.

13. Clough, R. W., "The Finite Element Method in Structural Mechanics," Chapter 7 in Stress Analysis, Zienkiewicz, O.C., and Holister, G. S., eds., John Wiley, Inc., N.Y., 1965.

CHAPTER II

PLANE STRAIN STEADY-STATE INDENTATION OF AN INFINITE MEDIUM

In this chapter two problems in the plane strain steady-state motion of rigid indenters in an infinite medium are treated. The first is for a symmetric wedge, Fig. II-1-a, with a surface either smooth or rough; the second is for a smooth rigid plate inclined to the direction of motion Fig. II-31. Solutions are obtained using the method of characteristics when the infinite medium is rigid-perfectly plastic. Furthermore, the wedge solution is checked by experiments and finite element analysis.

II-1. Indentation by a rigid symmetric wedge

II-1-1. The problem and its applications

Let us consider the plane strain problem of the rigid symmetric wedge shown in Fig. II-1-a. The semi-angle of the wedge is δ, $0 < \delta < \frac{\pi}{2}$, and the length of the side $\overline{AB}$ is L. The wedge is made of a rigid material with its surface either smooth or rough. In case it is rough, we assume its coefficient of friction with respect to the surrounding material μ to be larger than a particular value μ_o which depends on δ ($0 < \mu_o \leq 0.175$ for the range of δ considered); this condition will prove necessary in subsequent analysis.

It is required to find a steady-state solution to the problem when the wedge is moving at a constant velocity U, to the right, in an entire space of a deformable medium.

The solution to this problem is useful in connection with pile foundations since it gives insight into the mechanism of pile driving and pile resistance under axial and lateral loading. In particular, questions like the extent of disturbance due to driving and its relation to the shape of the pile tip, the effect of the compressibility and strain-hardening properties of the supporting clay, may be answered at least qualitatively.

Another application of the wedge problem is in connection with the standard cone penetrometer used in determining soil properties at depth. However, to do so one must assume or develop a correspondence between the plain strain case of the wedge and the axially symmetric cone. This correspondence is recognized from solutions and experiments on related problems; some examples include:

a. The indentation of a half-space by a rigid indenter

For the indentation of a rigid-plastic half-space by a rigid smooth flat ended punch, plane strain solutions by Prandtl [1]* and Hill [2] for different modes of failure (velocity fields), give the same contact pressure at yield. The latter is 10% smaller than the one obtained by Shield [3] in the case of a circular punch.

When the indenter is a smooth wedge and the half-space is rigid-plastic, Hill et al. [4] obtained the plane strain solution. It was later checked and extended to various degrees of roughness by Grunzweig et al. [5]. When compared with the smooth cone solution by Lockett [6], the plane strain solution was found to give indentation pressure consistently lower by 10 to 14 per cent depending on the half-angle β in the range $\pi/2 \geq \beta \geq \pi/3$. When β is less than 52.5° Lockett's solution ceases to hold (because the assumed plastic field is no longer valid) and no comparison can be made. For blunt wedges (β larger than $\pi/4$ say) and for materials with low E/Y ratio (E is Young's modulus and Y the uniaxial yield strength) the measured deformations in experiments of Dugdale [7, 8, 9], Samuels et al. [10], Hirst et al. [11], Atkins et al. [12] showed that the deformation mode is

*Numbers in brackets refer to the bibliography at the end of the chapter.

more of a compression nature than the cutting assumed by perfect plasticity and which was experimentally verified for small δ.

Along suggestions by Bishop et al. [13], March [14] applied Hill's theory for the expansion of a spherical cavity in a semi-infinite elastic-plastic medium to Vicker's hardness test. The same idea of using the results of the expansion of a cylindrical and a spherical cavity in a half-space to simulate the indentation by a blunt wedge and a pyramid was later used by Johnson [15]. The results in both cases compare favorably with test results by previous investigatiors. The contact pressure in the axially symmetric case is larger than plane strain by zero to 14 per cent depending on the parameter $a = \frac{E}{Y} \cot \delta$ in the range $7 \leq a \leq 100$. (δ enters the analysis by determining the geometry of the expanding cavity.)

b. Expansion of cavities in an infinite medium and the point resistance of piles

On parallel lines as in the case of the half-space, and initiated by Bishop et al. [13], the point resistance of deep foundations has been interpreted in terms of the pressure required to expand a spherical or cylindrical cavity in an infinite medium. In this context the succession of work done by Gibson [16], Chadwick [17], Skempton et al. [18] led to the most general formulation

of the problem by Vesic [19]. It allows for the infinite medium to behave in an elastic-plastic manner, have internal friction and be compressible when in a plastic stage. For materials with no internal friction and incompressible in a plastic state, the comparison between the pressure required to expand both spherical and cylindrical cavities shows that the axi-symmetric pressure is roughly 33% more when G/Y lies between 2.5 and 250 (G is the shear modulus). Moreover, while the effect of compressibility (in the plastic stage) on the difference between plane strain and axial symmetry pressures is small, the effect of internal friction is considerable [19].

c. The bearing capacity of shallow and deep foundations

On the basis of intuition, experiments, and less rigorous solutions, the analogy between axial symmetry and plane strain has been recognized or simply used by earlier investigators (Terzaghi [20] and Meyerhof [21]). Empirical factors were used to determine the bearing capacity of axially symmetric foundations from analysis of plane strain problems.

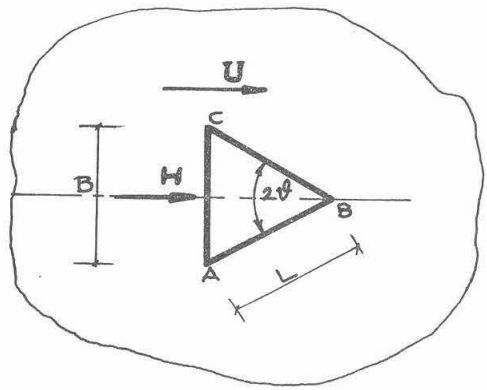

(a) Problem identification

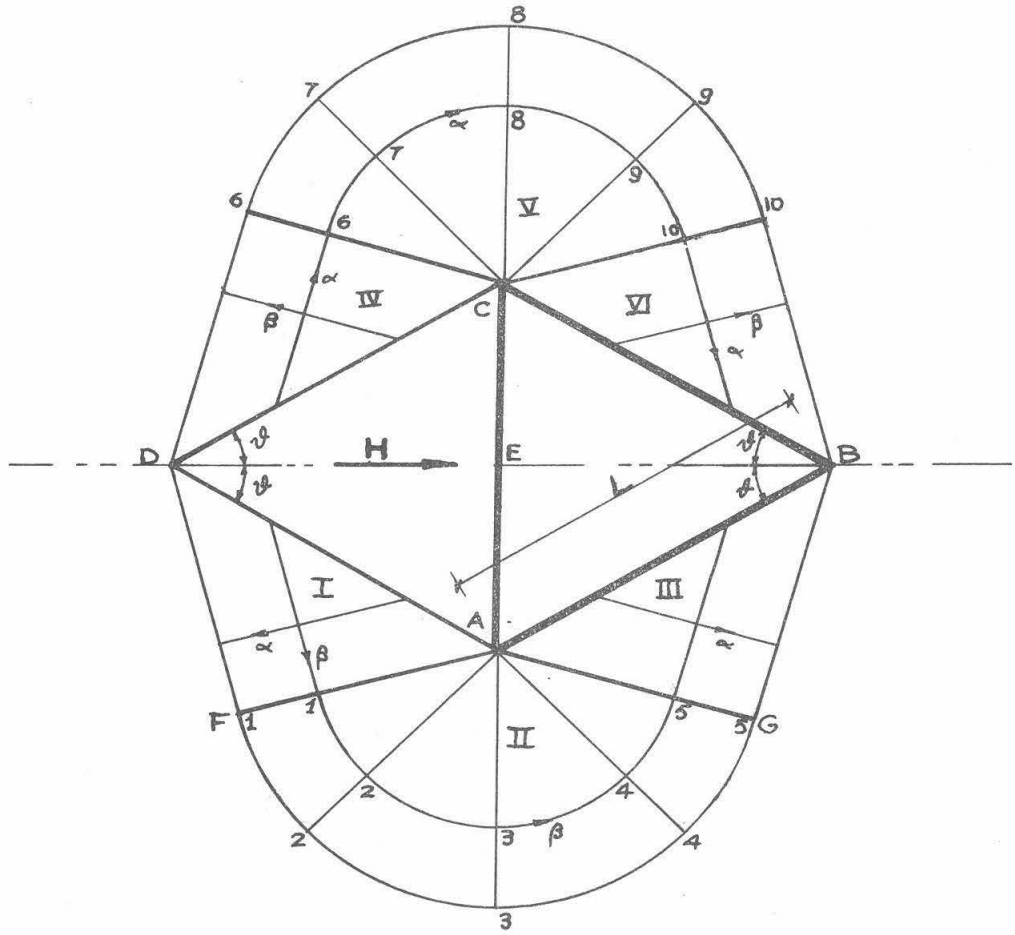

(b) Physical plane for a smooth wedge

Fig. II-1. Steady-state motion of a rigid symmetric wedge in a rigid-perfectly plastic full space

Here we will use the finite element technique to extend the plane strain solution to the axially symmetric cone.

Finally the solution to the wedge problem is needed in the design of a scoop that will pick up mineral balls imbedded and scattered along a clayey ocean floor. The scoop consists of steel fingers at some distance apart each having a cross section given by the wedge described above. When the fingers are pushed into the clay a distance h, where $\frac{L}{h} \ll 1$, and moved parallel to the ocean floor, a condition of plane strain steady state is reasonably satisfied.

In the following part we first solve the wedge problem when the full-space material is rigid-plastic using the method of characteristics of perfect plasticity. Test results are then presented and compared with the theory. Finally we use the finite element method to solve the problem when the full-space material is bilinear in deviatoric behavior. The solution is then extended to the problem of the axi-symmetric cone.

II-1-2. Solution by ideal plasticity

Let us assume that the deformable material surrounding the wedge Fig. II-1-a is rigid-perfectly plastic. For a solution it is required to find a stress field and a velocity field in the rigid-plastic material that would comply with the field equations proper to the material, and satisfy the boundary conditions when the wedge is moving with velocity U.

a. Smooth wedge

Along the front part of the wedge, AB and BC, the boundaries are well defined as being smooth and rigid. The part behind the wedge can either have a zone of separation as in Fig. II-1-b or not. We will assume that there exists a separation zone (air gap) and hence AD and DC are free surfaces. Furthermore, when the angles ADE and CDE are equal to δ and AD and CD are straight lines, we will show that these assumptions produce a permissible steady state.

The physical plane is shown in Fig. II-1-b. Under the previous assumptions, the symmetry about DB is clear and we need only discuss one symmetrical half of the solution. Considering the part below DB, in the solution shown, the domain in a plastic state occupies the following three zones:

Zone I : determined by the triangular ADF in which both families of characteristics are straight and the distance AD = L.

Zone II : determined by the circular fan FAG in which the characteristics are straight and the β-lines consist of circular arcs.

Zone III: determined by the triangle ABG in which both families are straight and the distance AB = L.

The field satisfies the "Hencky-Prandtl" net requirements and is thus permissible.

The stress plane is shown in Fig. II-2. The upper diagram is the mapping of the upper half of the physical plane (above DB) and the lower diagram is the mapping of the lower half. Considering the latter, we can see that Zones I and III map into their corresponding

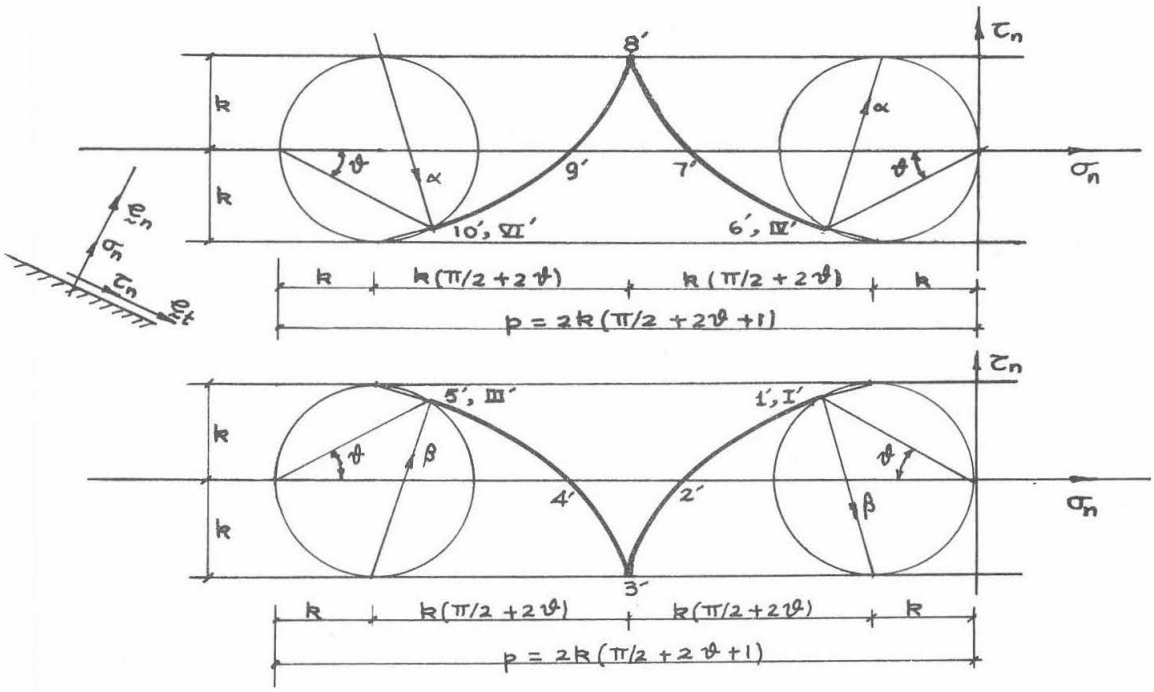

Fig. II-2. Stress plane for a smooth wedge.

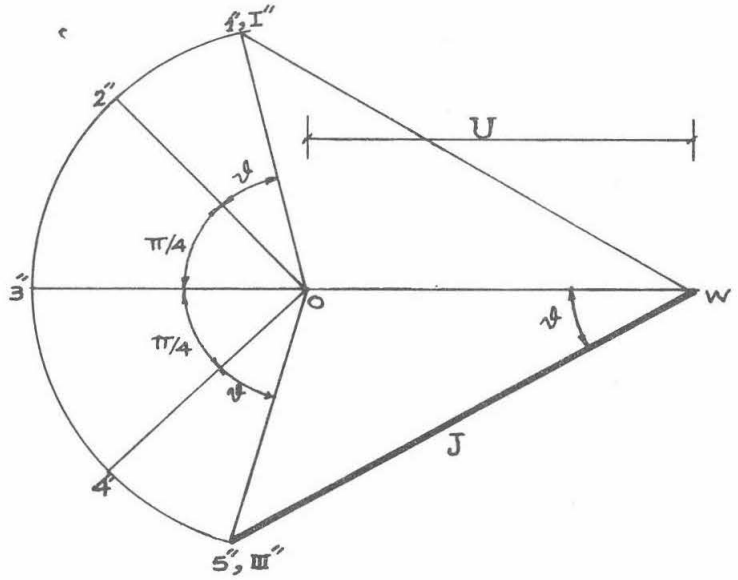

Fig. II-3. Hodograph for a smooth wedge.

image points I' and III'. In Zone II since the radial α-lines are straight, the image of each is a point; the β-lines are mapped into the cycloid which satisfies the orthogonality requirement.

The normal stress p at the interface is found to be:

$$p = k(\pi + 4\delta + 2) \tag{2}$$

The shearing stresses at the interface, by the definition of a smooth surface, vanish. Integrating the known stresses at the interface, and noting the symmetry of the problem, it follows that the resulting force, H, required to drive the wedge is horizontal and given by:

$$H = 2Lk \sin\delta[\pi + 4\delta + 2] \tag{3}$$

A graph of H as a function of δ is shown in Fig. II-8.

The hodograph is shown in Fig. II-3 with the origin at O. The rigid part of the full space outside the plastic domain, which is fixed in space, is mapped into O. The rigid wedge is mapped into point W at a distance U to the right of O. In Zones I and III both families of characteristics are straight, and the Zones move as rigid bodies with their corresponding images occurring at the two points I" and III" whose location is still unknown.

Zone III moves parallel to BG and Zone I moves parallel to FD, and the directions of $\overline{OI''}$ and $\overline{OIII''}$ must be at $\pm(\frac{\pi}{4} + \delta)$ with the horizontal. Since interface AB is smooth, a jump between the indenter velocity and the velocity of adjacent points in Zone III, parallel to AB, is permissible. The jump J is assumed to exist, and thus point III" lies on a line through W making an angle δ

with the horizontal. The location of III" is now fully determined.

In Zone II the radial α-lines are straight. As the outside rigid domain is static, the velocity at any point can only be in a tangential direction, i.e. parallel to the β-line through the point. Now applying the orthogonality condition, the image of each α-line is a point and the image of any β-line such as 54321 is the curve 5"4"3"2"1" which must be an arc of a circle centered at O.

From the previous treatment, the proposed fields of stress and velocity are instantaneously satisfied. It remains however to prove continuity, in the sense that for an observer moving with the wedge this velocity field yields a solution that will maintain the geometry of deformation unaltered at any time. For this it is necessary and sufficient to show that in the conjugate problem, AD is a free surface fixed in space.

The conjugate problem is, by definition, the same as the original problem treated above but with the origin of the hodograph at W instead of O. From the symmetry of the hodograph, it is clear that $\overline{WI"}$ makes an angle δ with the horizontal which means that points adjacent to AD move parallel to it and the surface is a free surface fixed in space as required.

Now that the problem is solved, the distortion of elements of the medium near the indenter can be computed; however this will not be done here but will be treated later for the case of a rough wedge.

b. Rough wedge

Consider a rigid symmetric wedge identical to the one in the previous problem and shown in Fig. II-4. In this case however, the

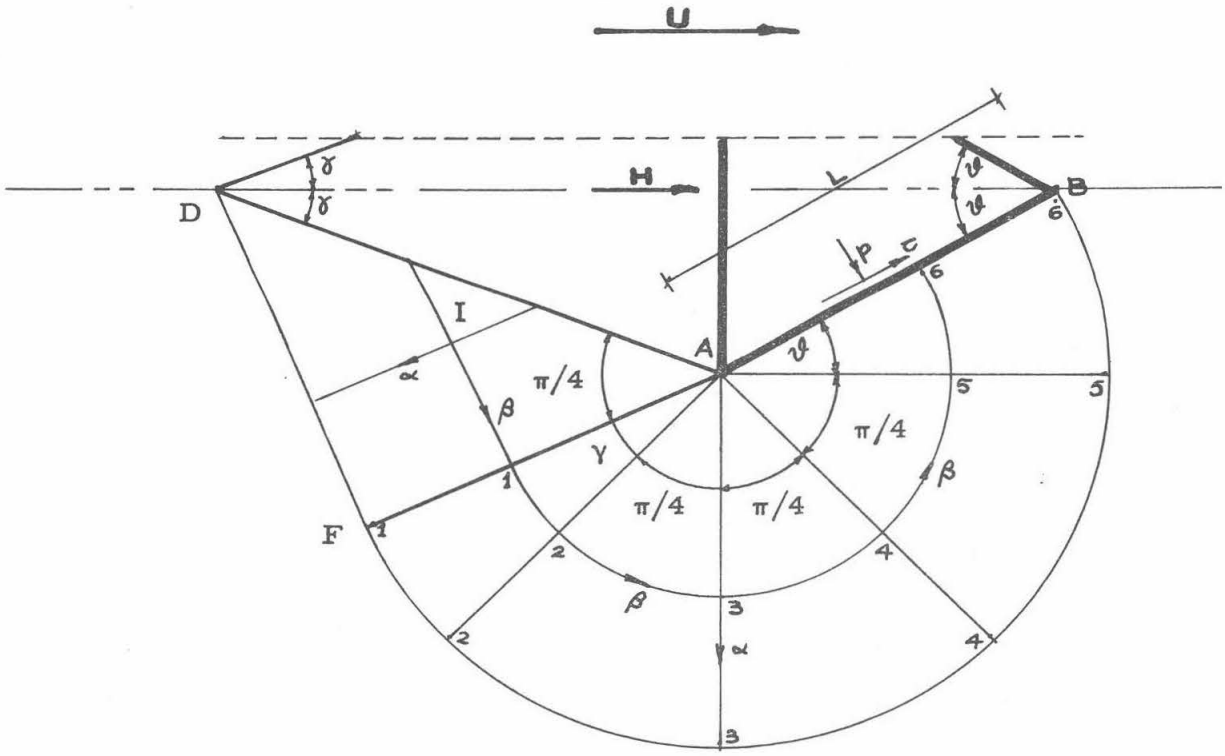

Fig. II-4. Physical plane for a rough wedge ($\mu > \mu_o$).

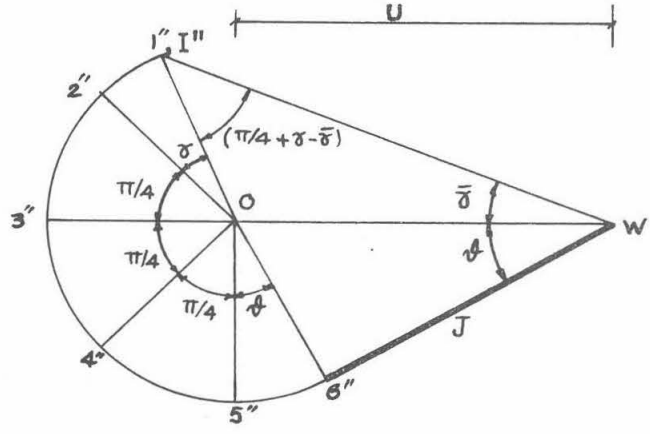

Fig. II-6. Hodograph for a rough wedge.

surface of the wedge is taken to be rough with a coefficient of friction μ larger or equal to $\mu_o(\delta)$. This restriction on μ will prove to be necessary for the following solutions to hold; hence values of $\mu_o(\delta)$, later derived, are now presented as conditions identifying the problem.

$$\mu_o(\delta) = \frac{1}{3\pi/2 + 1 + 2(\delta + \gamma(\delta))} \tag{4}$$

where $\gamma(\delta)$ is given by

$$\gamma(\delta) = \text{arc sin}\left(\frac{\sin \delta}{\sqrt{2}}\right) \tag{5}$$

Graphs of $\gamma(\delta)$ and $\mu_o(\delta)$ are shown in Fig. II-7 in which we note that for the range of definition of δ, $0 < \delta < \frac{\pi}{2}$, the value of μ_o is less than 0.175.

If μ is indeed equal to or larger than $\mu_o(\delta)$, which is a condition frequently satisfied in practice, the solution to this problem is taken to be symmetrical about DB and follows the same lines as for the case of a smooth wedge.

The following assumptions are made: (1) the plastic material adjacent to the interface is taken to be sticking to the wedge and moves with it. At an infinitesimal distance along the normal to AB, (Fig. II-4) in the plastic domain, a characteristic parallel to AB is assumed to exist. This amounts to considering AB as a characteristic of the plastic domain; (2) to be able to satisfy the steady-state requirements, the free surface AD is assumed to be straight and at an angle γ, given by Equation (5), with the horizontal.

The physical plane given in Fig. II-4 is similar to that for the

smooth wedge but in which Zone III disappears and angle BAF is now equal to $\frac{3\pi}{4} + \delta + \gamma$.

The stress plane in Fig. II-5 describes the stress field in the plastic domain. From it, the normal stresses at the interface are found to be

$$p = k\left[\frac{3\pi}{2} + 1 + 2(\delta + \gamma)\right] \tag{6}$$

The shearing stress at the interface is given by

$$\tau = k \tag{7}$$

The total force acting on the wedge is again horizontal and is given by

$$H = 2Lk\left\{\left[\frac{3\pi}{2} + 1 + 2(\delta + \gamma)\right]\sin\delta + \cos\delta\right\} \tag{8}$$

A graph of H as a function of δ is given in Fig. II-8.

The hodograph in Fig. II-6 is analogous to the one in Fig. II-3. The origin at O is the image of the static material outside the plastic domain. The rigid wedge is mapped into W which lies at a distance U to the right of O. A jump J between the plastic material sticking to the wedge and the material at an infinitesimal distance from AB is permissible and is assumed to exist. It thus follows that point 6", the image of the point 6 in the plastic Zone (Fig. II-4) just below AB, lies on a line through W making an angle δ to the horizontal. Furthermore, as the component of velocity at 6 along the α-line is zero, the line $\overline{O6''}$ must be at an angle δ to the vertical, i.e. is perpendicular to $\overline{W6''}$. The location of 6" is now determined and $\overline{O6''} = U \sin\delta$.

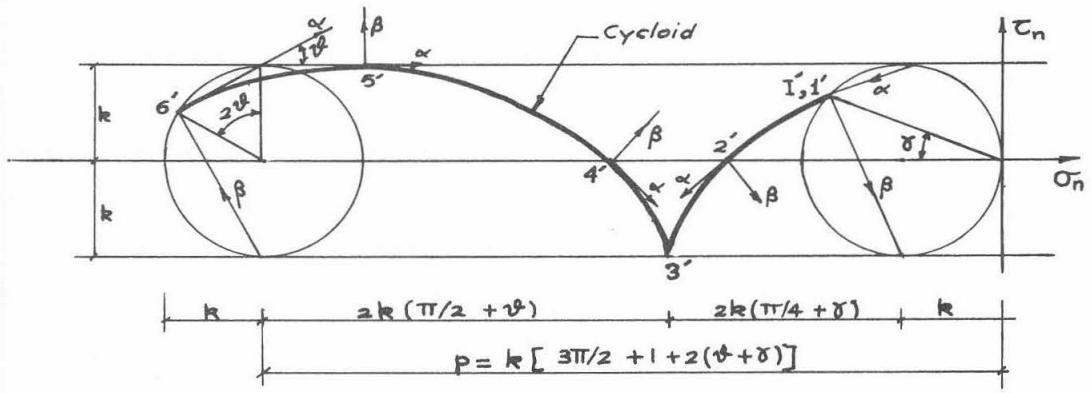

Fig. II-5. Stress plane for a rough wedge.

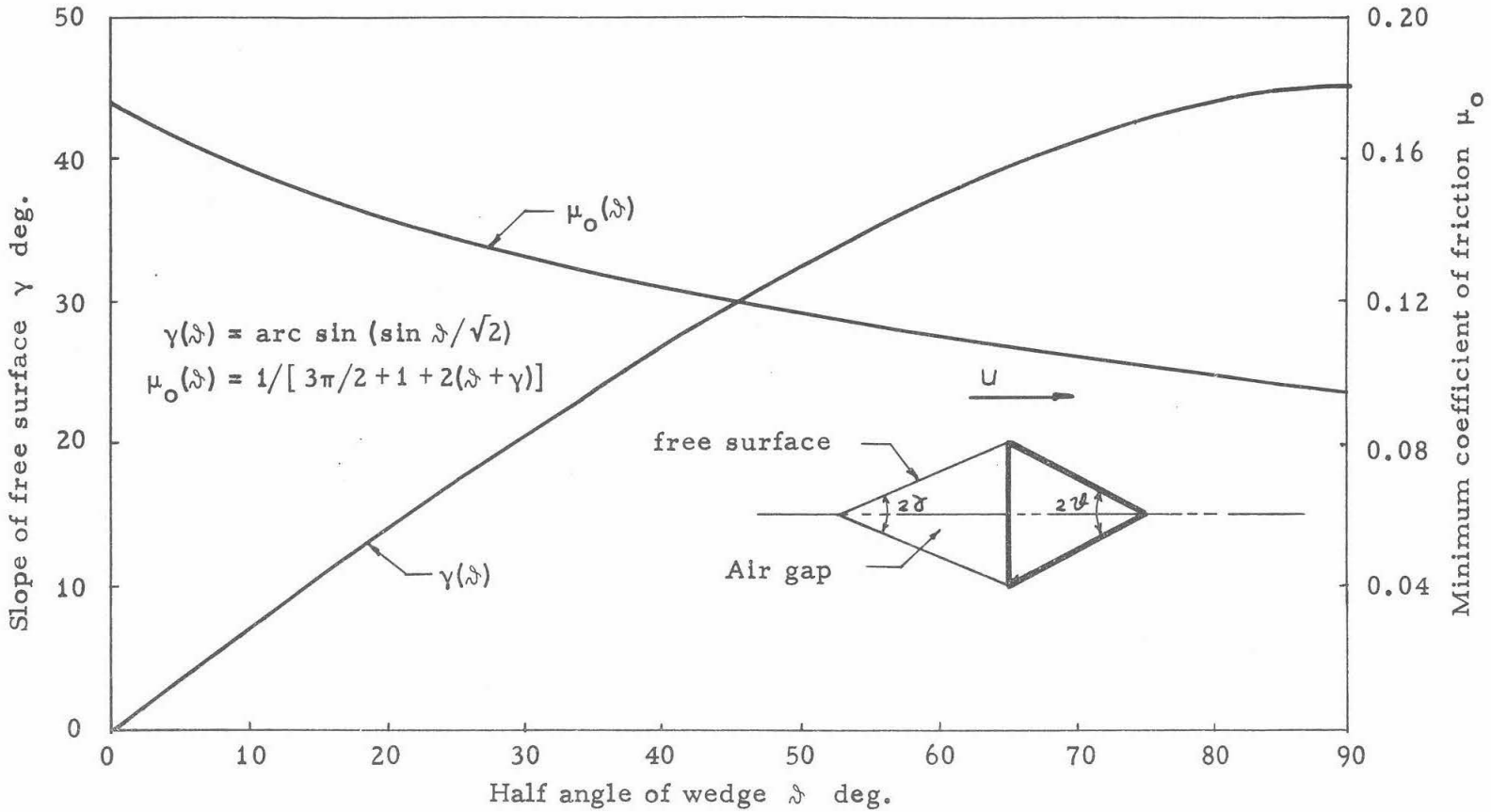

Fig. II-7. Slope γ of the free surface behind the wedge and minimum coefficient of friction μ_o for a rough rigid wedge moving in a steady state in a rigid-plastic full space.

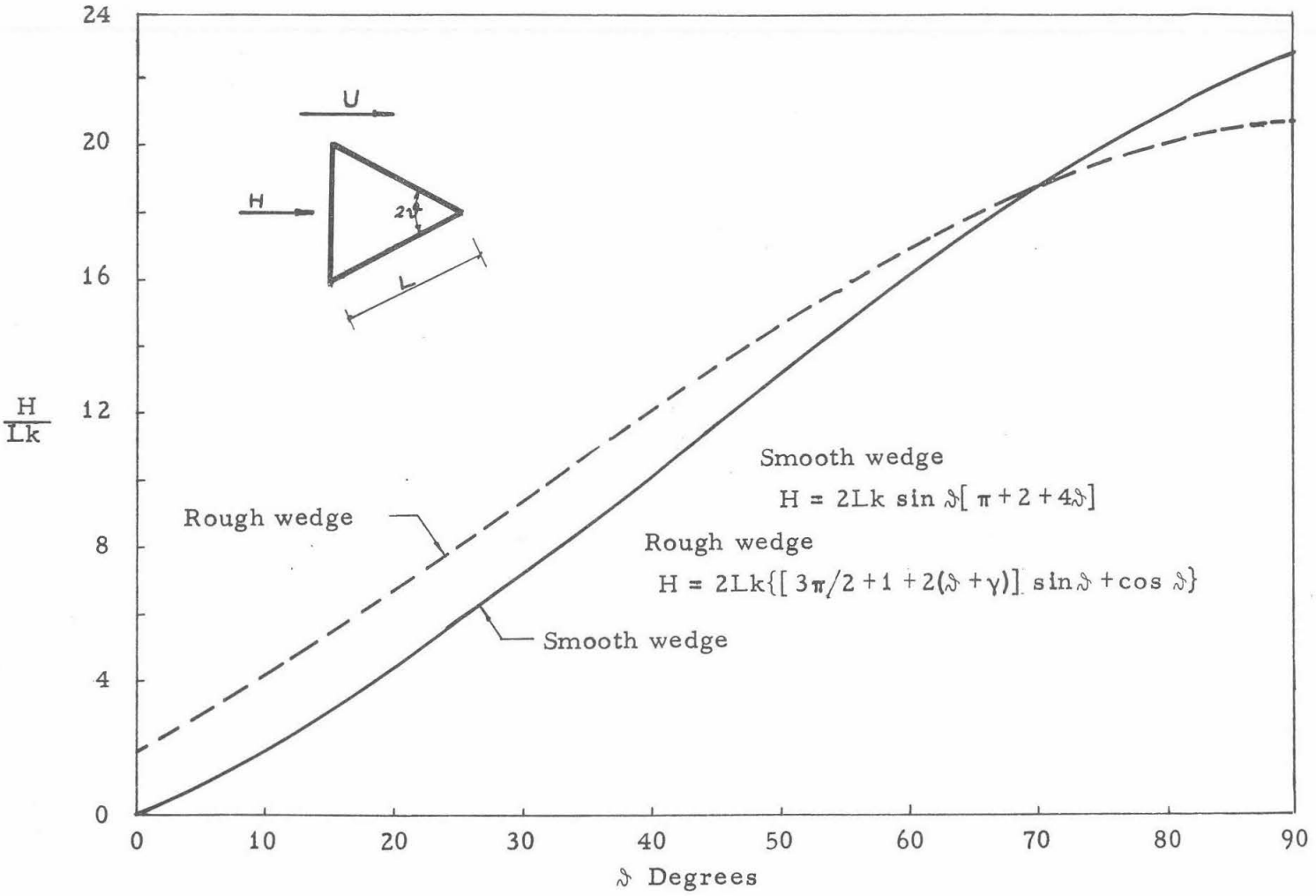

Fig. II-8. Force required to produce the steady-state motion of a rigid wedge in a rigid-perfectly plastic full space.

Since the curve 6"5"4"3"2"1", the image of any β-line 654321, is a circular arc centered at O, and knowing that the velocity of Zone I must be at an angle $(45 + \gamma)$ to the horizontal, then $\overline{OI''}$ is equal to $U \sin \delta$ and is at an angle $45 + \gamma$ to the horizontal. Calling $\overline{\gamma}$ the angle OWI", then to satisfy the steady-state condition, we need to show that $\overline{\gamma} = \gamma$. This result is immediately obvious when we use eq. (5) and consider the triangle OWI" in the hodograph in which

$$\frac{U}{\sin(\pi/4 + \gamma - \overline{\gamma})} = \frac{U \sin \delta}{\sin \overline{\gamma}}$$

Now that the solution is complete, the distortion of a square grid can be carried out. This is done graphically using the hodograph for the conjugate problem. Knowing the direction of the velocity at points in the deformable medium as they move past the wedge, the stream lines are first obtained. Next the distortion of originally vertical lines is determined by following every point along a stream line as it approaches the wedge; the known magnitude of the velocity allows us to determine the location of the deformed vertical lines through a step-by-step procedure. Finally and as a check on both the hodograph and the accuracy of the distortion computation, the area inside each quadrilateral should remain the same; this is the expression of the incompressibility of the material.

The results of this calculation are shown in Figs. II-9, II-10 and II-11 for $\delta = 10^{\circ}$, 30° and 45° respectively. The accuracy of the curves in these figures depends, of course, on the graphical integration technique employed; it is sufficiently accurate for engineer-

ing purposes. With regards to the distorted mesh in any one of the three figures, we note:

(1) The distortions occur only within the plastic domain. This is due to the assumption that the material is rigid below yield stresses.

(2) The slope of the stream lines undergoes a discontinuity at the boundary between the rigid and the plastic domains. This is due to the jump in velocity that exists across the boundary.

(3) The horizontal lines are horizontal and at the same level after passing through the plastic domain. This is a result of the incompressibility of the material.

(4) The distorted vertical lines have a slope that changes from negative to positive as one approaches the centerline of the wedge. Physically this means that some material is pushed backwards as the wedge is moved forward. This phenomenon arises because the material is incompressible and the plastic zone is finite and small.

Comparing the three figures II-9, II-10, and II-11 to see the effect of γ on the distorted mesh we note that for a constant wedge thickness B:

(1) The plastic zone decreases in size as γ increases.

(2) The curvature of the stream lines, in the conjugate problem, increases as γ increases.

(3) The slope of the distorted vertical lines becomes larger as γ increases.

Points (2) and (3) above mean that for a constant indentation velocity U the rate of straining and the intensity of straining become larger as γ increases.

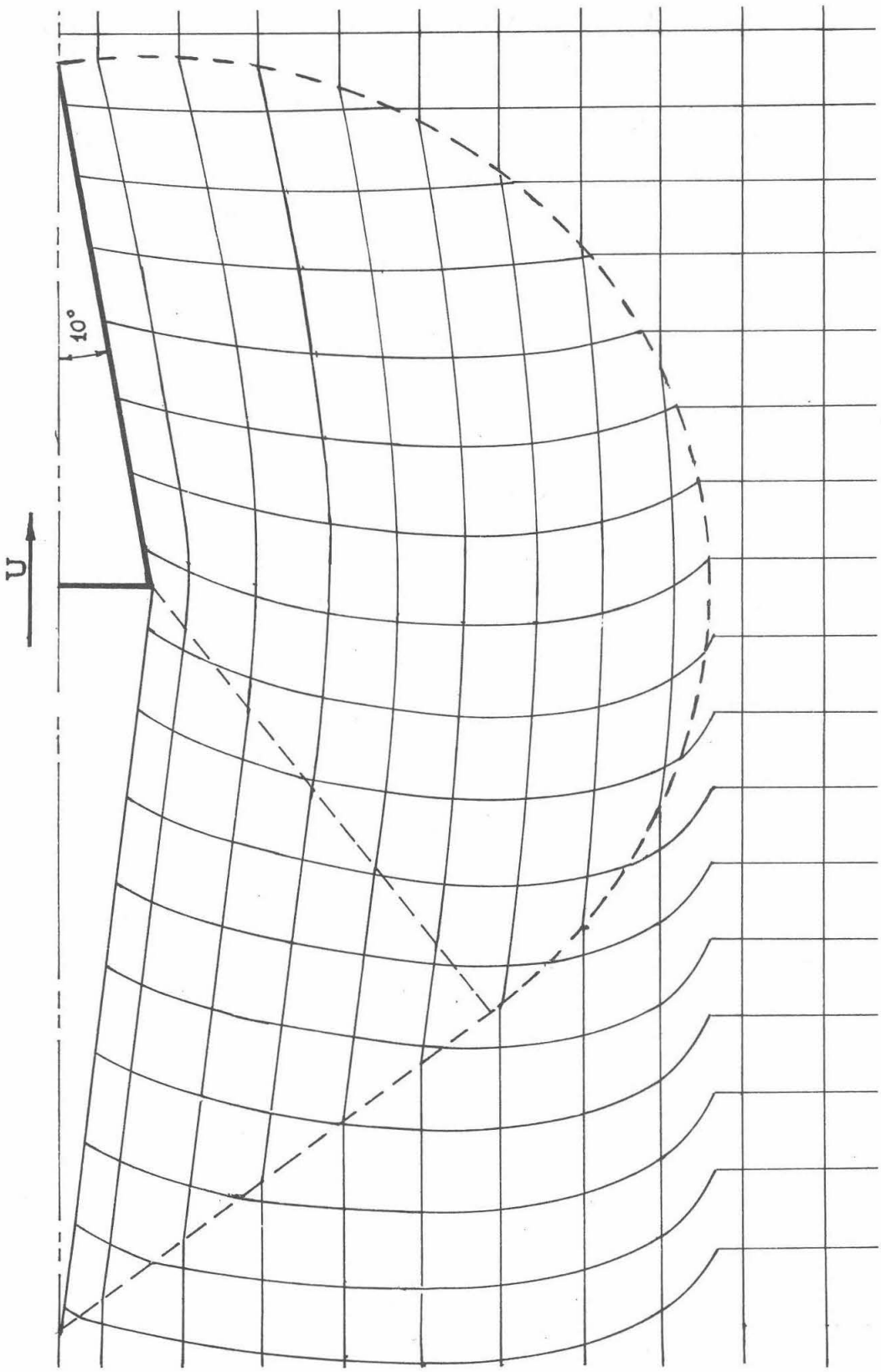

Fig. II-9. Distortion of a square grid for $\delta = 10^{\circ}$.

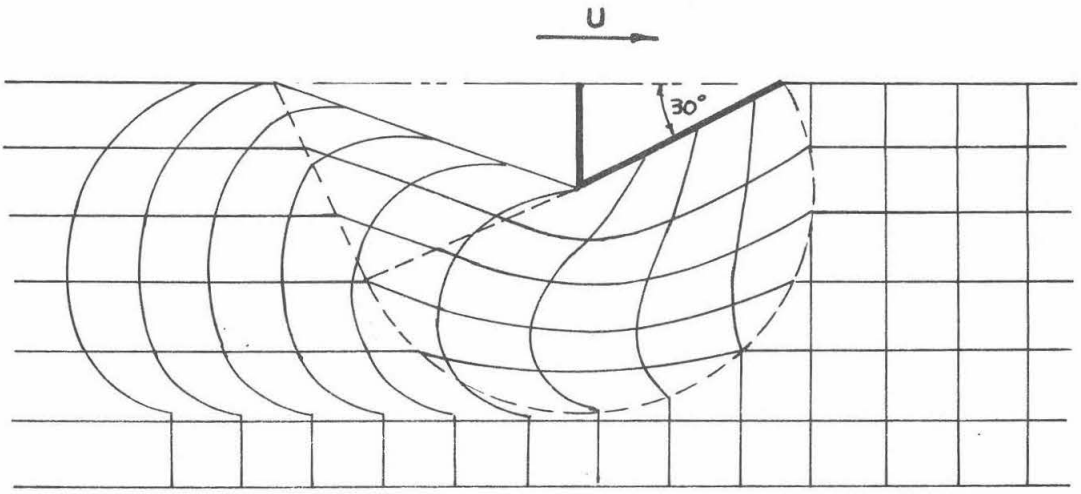

Fig. II-10. Distortion of a square grid for $\vartheta = 30^{\circ}$.

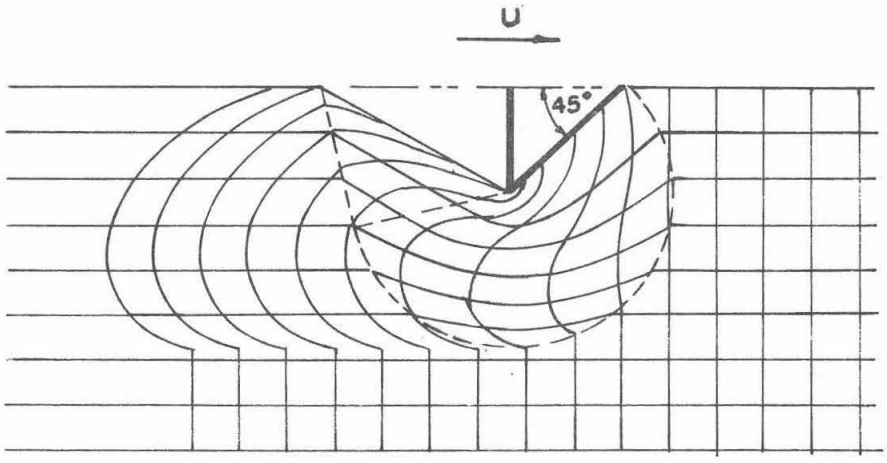

Fig. II-11. Distortion of a square grid for $\vartheta = 45^{\circ}$.

II-1-3. Summary of theoretical results and their implications

The problems of a rigid smooth and rough wedge moving with constant velocity in a full space of a rigid-perfectly plastic material have been solved assuming the existence of a free surface behind the wedge. To satisfy the steady-state condition, the free surface behind the wedge was taken to be a straight line with a specified slope γ to the horizontal. Values of γ are given in Fig. II-7 for different values of the semi-wedge angle δ. The geometry associated with this surface was the only one found to satisfy the steady-state condition.

The total force to drive the wedge H is given as a function of δ in Figs. II-8. An interesting result may be deduced from this figure, namely that the curves corresponding to rough and smooth wedges intersect at $\delta = 68.7^{\circ}$. According to this result, if we were to carry out a test using a wedge of this angle to determine the shear strength of a rigid-plastic material, the state of surface roughness of the wedge would be immaterial. The value of k is directly given by

$$k \simeq \frac{H}{18.52\, L}$$

where H is the force per unit length of the wedge at right angles to its direction of motion.

For values of δ larger than 68.7° the force required to drive a smooth wedge is larger than the rough one. This unexpected result is a consequence of the assumed free surface behind the wedges and the associated plastic fields. A detailed discussion of this result

will be carried out in connection with Fig. II-12 where the variation of H/Bk with δ is plotted rather than H/Lk. The reason behind studying this relationship is that, in practice, the question of the resistance of a wedge (or cone) is usually presented as follows: Given a certain plastic material with yield shear strength k and a rigid wedge with width B (or a cone with diameter B) what is the relationship between the resisting force and the wedge angle? To answer this question we consider Fig. II-12. For materials used in practice, unless continuous lubrication at the interface is supplied, the coefficient of friction between the wedge and the plastic material exceeds 0.175, and thus falls in the range for which our solution for rough wedges holds.

The dotted curve abc in Fig. II-12 corresponding to a rough wedge indicates that:

(1) The resistance force H per unit width has a minimum (point b on the graph). This minimum is reached at $\delta = 33.6^{\circ}$ and is given by $H = 9.194\,Bk$.

(2) From curve abc of Fig. II-12 when δ lies between 15° and 90°, the value of H/Bk is bounded between 10.5 and this minimum value 9.194. Thus over a wide range of wedge angle 2δ, the value of H/Bk changes only slightly (less than 15%). This weak dependence of H/Bk on δ has been experimentally observed in soil mechanics tests [22]. Some previous observations in this regard, as found in a number of references [23][24] are:

   a. The value of H/Bk for a wedge (H is the load per unit width) is roughly the same as for a cone (H is the total

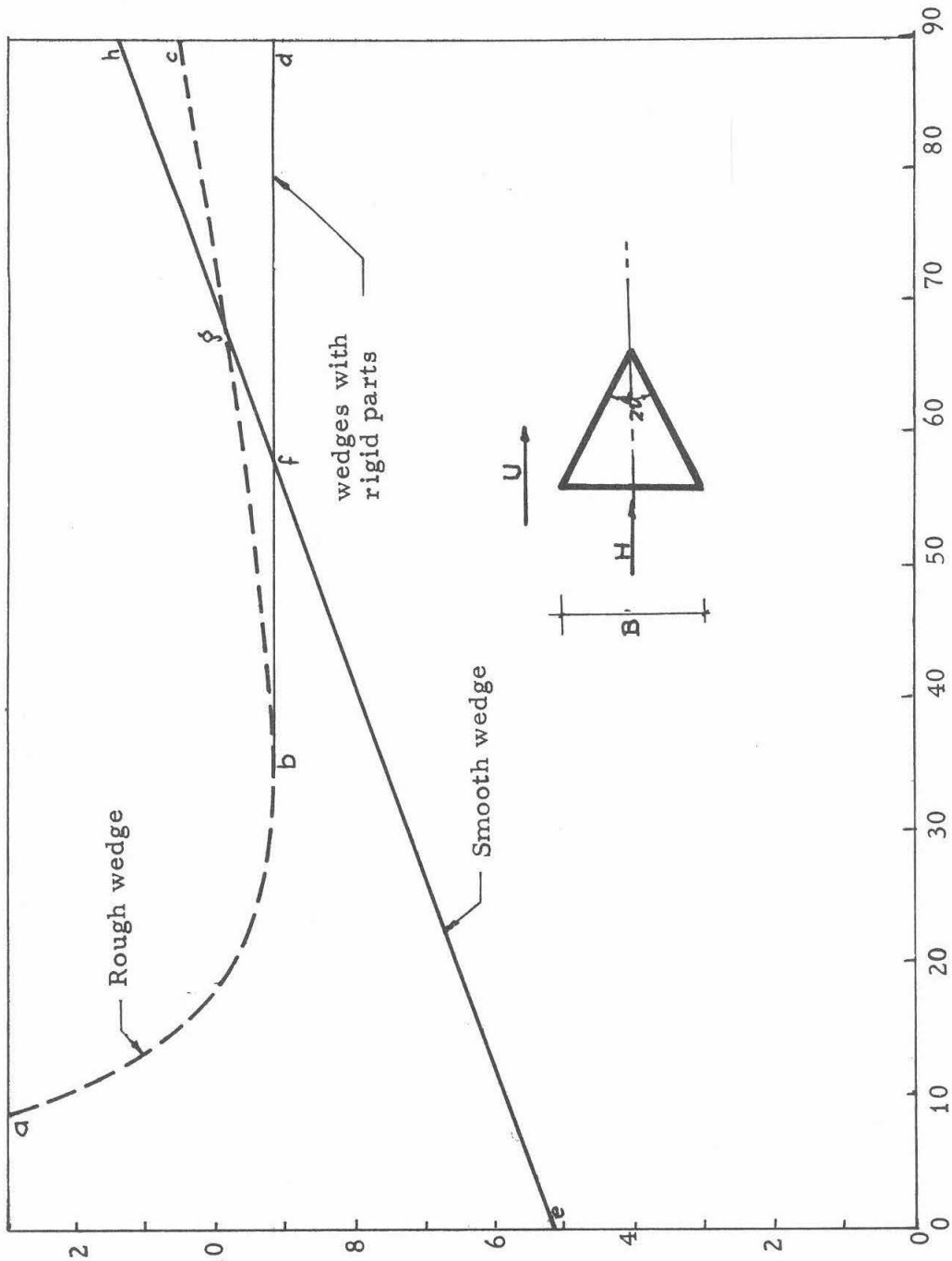

Fig. II-12. Values of H/Bk as a function of δ.

load and B is the projected area of the cone). This value is about 9. This is the reason that the results of plane strain solutions are used in connection with the axi-symmetric point resistence of piles (Terzaghi [20], Meyerhof [21], Berezantzev [25], Skempton [26]).

b. The effect of δ on H/Bk for a cone is negligibly small for a range of practical values of δ (say $15^\circ < \delta < 90^\circ$). This leads to the use of the cone penetrometer test ($\delta = 30^\circ$) to estimate pile resistance where, in piles, $60^\circ < \delta < 90^\circ$, see [27].

(3) For small δ, ($\delta < 10^\circ$) the value of H/Bk rises sharply as δ decreases. This is due to the substantial effect of the interface shearing stresses s_t. As an example, when $\delta = 1^\circ$, the value of H/Bk is 63.06 of which 91% is due to s_t.

It is interesting to compare the results of the present solution, for small δ, with the indentation of a rigid-plastic half-space by a rigid rough infinite wedge, Grunzweig et al. [5]. The latter is the plane strain counterpart of the driven, axially loaded, tapered pile. When the coefficient of interface friction μ is larger than 0.39, a condition frequently met in applications, both solutions hold and are thus comparable. The mechanism of failure is similar; specifically the interface shearing stress s_t is equal to k (the cohesion of the clay) in both cases. For $\delta = 1^\circ$ Grunzweig's solution gives a value of H/Bk less than 10% lower than the present solution. Since the main difference between the two problems is in the location of the free surface this result means that, for small δ, the geometry of the

plastic material has only a small effect on the indentation force. Moreover, when Grunzweig's problem was checked experimentally [11], his failure mechanism proved correct for small δ. Other experiments with cones and pyramids [12], [14] have shown similar results and proved the plane strain solution to be a good start to interpreting the more complicated case.

In this perspective one may now look at the problem of axial loading of straight piles, so far unresolved, as a limit of tapered ones when δ tends to zero. The case of $\delta = 0$, though by far the most widely used, is particularly difficult to solve because of the ambiguity associated with its mechanism of resistance and in turn with the boundary condition needed to start any rational solution. For example materials that compress during indentation will induce smaller normal loads s_n on the shaft than the relatively incompressible ones. Hence the interface shearing stress s_t is no longer equal to k but is probably dependent on the normal stress s_n and μ. Such unaccounted-for factors like the compressibility no doubt lie behind the wide scatter in the experimental literature [28]. The influence of such factors however is believed to be reduced by tapering of piles which will force a Grunsweig's mechanism of failure to come into play. In a medium to stiff clay where experiments [29] have shown that for a straight pile ($\delta = 0$) the value of s_t/k is small (around 0.5) tapering is expected to increase this value. The amount of tapering required to produce $s_t/k \simeq 1$ depends on the compressibility of the material. On the other hand for soft clays where experiments [30] have shown that straight piles have a high value of s_t/k

(near 1) tapering will naturally have little effect.

The above interpretation of tapering effect is in line with the current estimates of s_t/k values (see Scott et al. [31]). Recommended values between 0.6 and 0.9 for straight piles are increased to lie between 0.7 and 1.0 for tapered ones; the differences within each class depend on the type of clay, and the pile-placing technique.

Let us now return to Fig. II-12 and compare the behavior of both the smooth wedge (straight line eh) and the rough one (curve abc). As mentioned earlier, for values of ϑ larger than 68.7°, the force required to drive a smooth wedge is higher than the rough one. This unexpected result is a consequence of the assumed failure mechanisms. The associated solutions, though satisfying all field equations, were not proven unique; hence failure modes including a dead zone ahead of the wedges, when ϑ becomes large ($\vartheta > 45^\circ$ say), is what will probably occur. Such mechanisms of failure whereby, for large ϑ, an inert zone of the deformable material moves with the wedge is supported by: 1 - the requirement that yield should not be reached in the rigid part outside the plastic domain. This consideration, which so far was neglected because of the weak dependence of H on ϑ, restricts the given solution for a rough wedge to $\vartheta \leq 45^\circ$ (see ref. 30 in chapter IV). 2- The presence of the inert zone was experimentally observed in the indentation of a half-space by a rigid wedge [15]. From the symmetry of the problem, a dead zone, if present, will also be symmetric. A first attempt to incorporate it in the solution is to assume that it has straight boundaries; in which case the solution is readily available and is given by the rough wedge

results. Now, however, ϑ represents the half-angle of the dead zone.

Suppose that the criterion governing the motion of wedges is that the energy dissipated in the indentation process is a minimum. The previously mentioned dead zones develop if necessary in order to meet this condition. Assuming that dead zones have straight boundaries, a rough wedge with ϑ up to 33.6° will thus develop no dead zones and the value of H is given by curve ab in Fig. II-12; however, when ϑ exceeds 33.6°, a dead zone develops with half-angle equal to 33.6°. The result of this is a constant value of H equal to 9.194 Bk, this is represented by the straight horizontal line bd in Fig. II-12. On the other hand, a smooth wedge will develop no dead zones up to $\vartheta = 58.05^\circ$ and the value of H is given by straight line of Fig. II-12, however when ϑ exceeds 58.05°, a dead zone develops with half-angle equal to 33.6°. The result is a constant value of H equal to 9.194 Bk, which is represented by the straight horizontal line fd in Fig. II-12.

The above speculations with respect to the dead zones ahead of the wedges require either that they be in a plastic state but moving with a constant velocity U or that the yield criterion is not reached anywhere. A theoretical study of the existence and geometry of the dead zones is difficult to conceive and we will have to rely on experiments. The prime target of those experiments will be to determine the pattern of deformation as a function of ϑ because the measurement of indentation forces alone is expected to be inconclusive in view of their weak dependence on ϑ.

II-1-4. Experimental results

Together with the modeling clay and the apparatus described in chapter I, aluminum wedges were used, Fig. II-13. The coefficient of friction μ between the aluminum and the clay was determined from a classical solid friction experiment. The shearing force required to cause a cylinder to slide (parallel to its axis) over the surface of a sufficiently thick clay layer was determined for different values of normal forces. The value of μ was found to be 0.8 well above the lower limit 0.175 required by the theory; hence results of testing are to be compared with the previously obtained solutions for a rough interface.

After the modeling clay has been processed in the manner earlier described in chapter I, it fits into a rigid box and is divided by the center plane into two separate identical parts. An orthogonal grid is then drawn on one of the two halves of the clay mass; the lines parallel to the direction of motion (horizontal) consist of grooves made with a thin knife (0.6 mm) and are about 1 mm deep. The vertical lines were made with colored ink so that the distinction between the two sets of lines after deformation would be made easier.

All the aluminum wedges have a breadth of 3 cm and a width of 10 cm. which is the thickness of the clay in the box. To determine the effect of the wedge angle on the results, wedges with half angles $\beta = 10^{\circ}$, 30° and 45° were used. To reduce the friction between the sliding arms holding the wedges and the clay, they were lubricated with petroleum jelly. Moreover, after each test, the wedge was

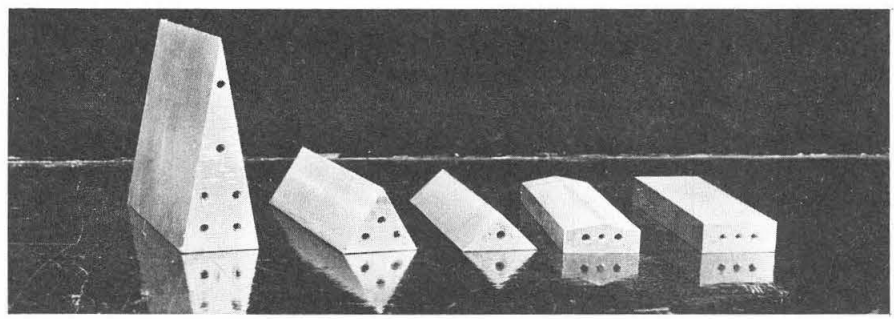

Fig. II-13. Wedges used in plane strain testing.

removed and the sliding arms pushed while recording the frictional load due to the mechanism. In no test did the friction exceed 5% of the total load.

A. Existence of a steady state and repeatability of experiments

The development of a steady state and its independence of the initial conditions were presumed by the perfect plasticity solution; this had to be checked first. Consequently two tests were carried out on a wedge with $\beta = 30^{\circ}$ having all parameters kept the same except for the initial geometry of the problem. The first test was started with the clay entirely surrounding the wedge, while the second was started with an air gap behind the wedge. The gap was made such that it had the same dimensions as the wedge, i.e. an initial condition as represented in Fig. II-1-b.

Comparing the results of the two tests, it was found that:

(1) In both tests a steady state, with respect to load and deformation, was reached after a distance $\ell \sim 2L$.

(2) The load required to produce a steady state in the first test was found to be 5% larger than that of the second test. This difference is believed to be caused by test imperfections (friction between sliding arms and clay, specimen preparation, etc.) rather than the effect of the initial conditions.

(3) The deformation pattern in the two tests is nearly identical. The air gap behind the wedge has the same shape in both tests except for the cut initially present in the second test. This cut kept its shape without noticeable change. Fig.II-14.

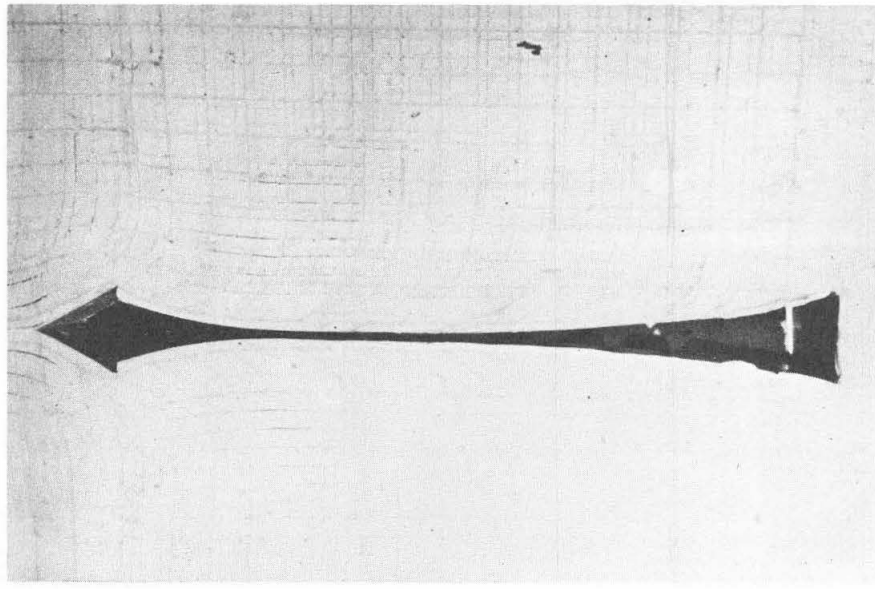

(a) Wedge initially surrounded by clay

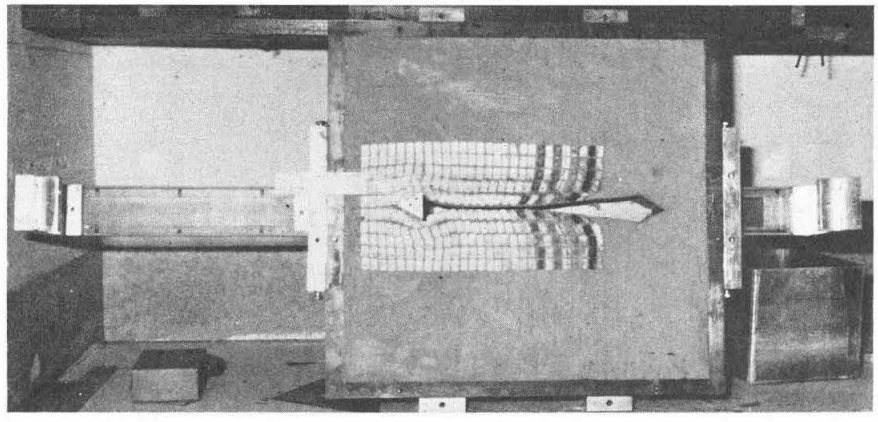

(b) Wedge initially has a gap behind it

Fig. II-14. Effect of initial conditions.

We conclude that the steady state for the wedge problem is indeed developed and is independent of the initial geometry. Furthermore the deformation patterns proved to be stable and repeatable.

B. Deformation patterns

The deformed shape of a square grid after a steady state has been reached is shown in Fig. II-15 for wedge angles of $\delta = 10^{\circ}$, 30° and 45°. All experimental wedges had a breadth B = 3 cms. The motion was started with the clay surrounding the wedge entirely and the pictures shown were taken after dismantling the box, i.e. about 30 minutes after the motion was stopped. Checking the deformed grid after a further 24 hours did not show any noticeable change in the deformation pattern. The grooves representing the originally horizontal lines cause the discontinuities seen in the deformed vertical lines; this effect is not related to the basic problem being studied.

Comparing the three patterns of deformations given in Fig. II-15, we note the following results that were predicted by perfect plasticity:

(1) The distortion of a line perpendicular to the direction of motion (vertical) increases as δ increases.

(2) The height of the distortion zone decreases as δ increases.

These results which might seem obvious are worth noting since they will be used in the discussion of loads required to produce a steady state.

On the other hand, the discrepancies between the theoretical

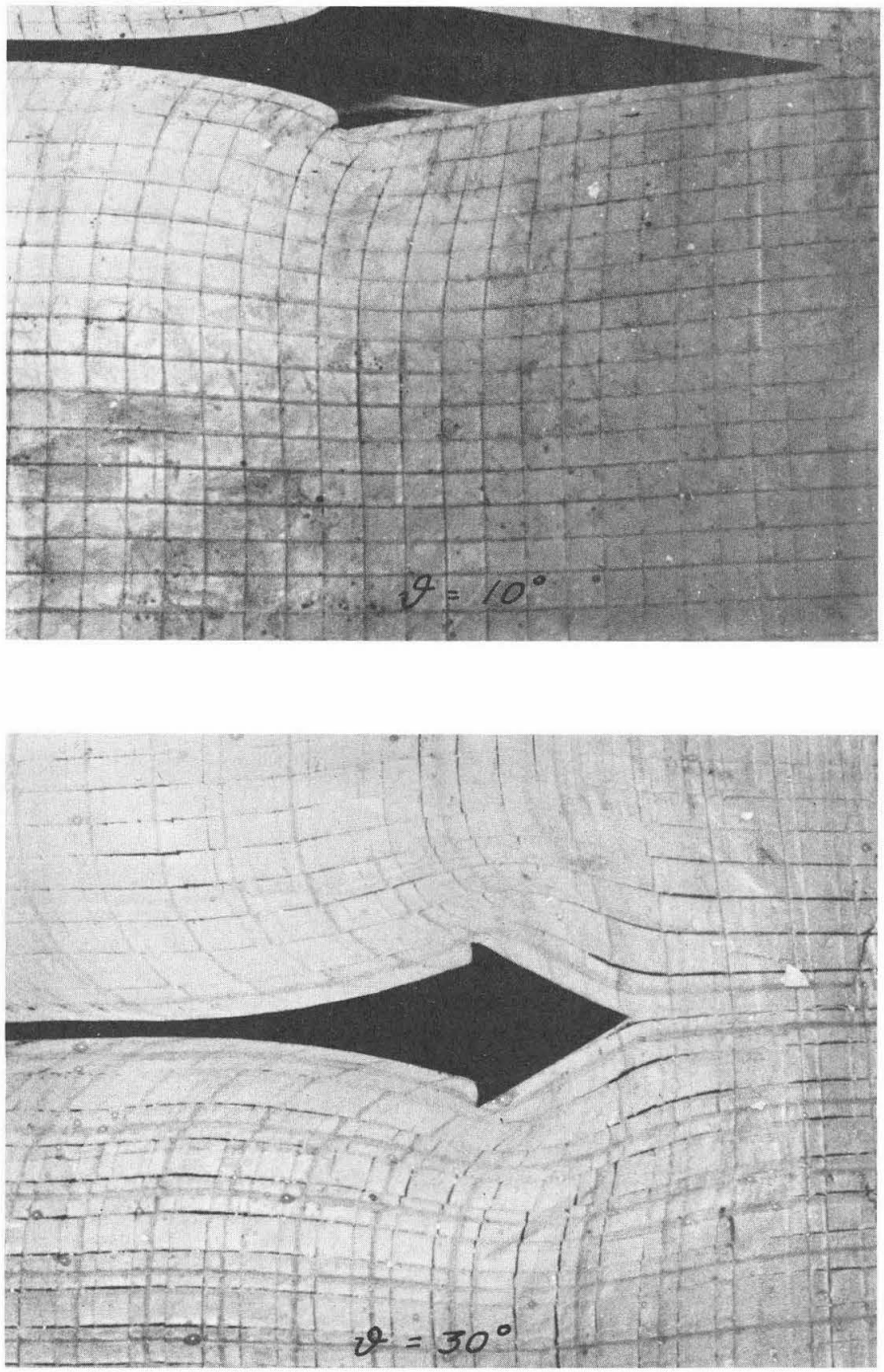

Fig. II-15. Deformation pattern in steady-state testing.

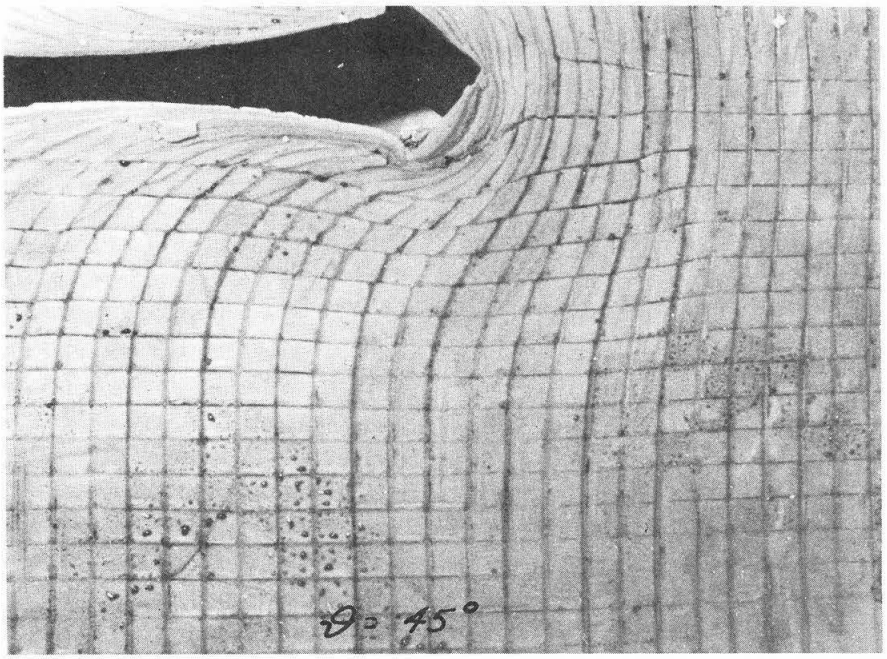

Fig. II-15. Deformation pattern in steady-state testing.

solutions and the test results become clear when comparing Figs. II-9, II-10, II-11 with II-15. They can be summarized as follows:

(1) The free surface behind the wedge which was assumed straight for plasticity solutions has instead a curved shape with a convexity towards the air gap. Moreover a definite area of contact with the back of the wedge is present in the test results.

(2) In plasticity solutions, the plastic domain, where deformations occur, is well defined by a boundary separating it from the rigid part. Along this boundary, discontinuities in velocity exist to produce a discontinuous slope of the deformed orthogonal grid. In the experiments however this plastic zone is not as clear, and deformations in the domain which is rigid in the theoretical solutions are noticeable. As a consequence, the field of deformation is smooth with no discontinuities.

For a better comparison, we plot the deformation pattern according to both theory and experiment to the same scale in Fig. II-16 and II-17 for $\beta = 10^{\circ}$ and 30° respectively. If the stream lines in both theory and experiment are reasonably close, the differences appear clearly in two aspects:

(a) The rigid domain ahead of the wedge which according to theory suffers no deformation actually deforms in in the test. The amount of deformation becomes more pronounced as β increases.

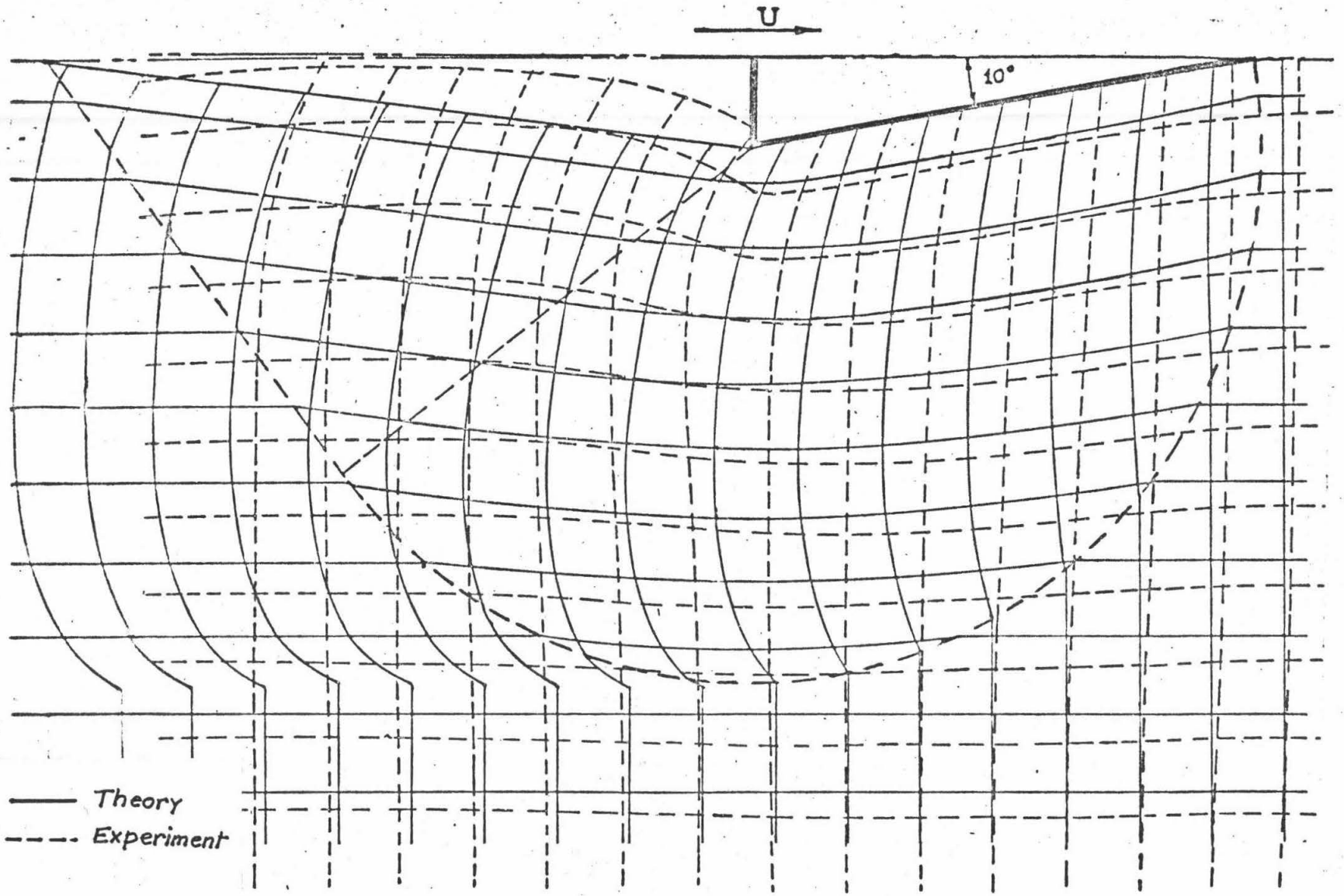

Fig. II-16. Distortion of a square grid for $\delta = 10^{o}$, comparison between theory and experiment.

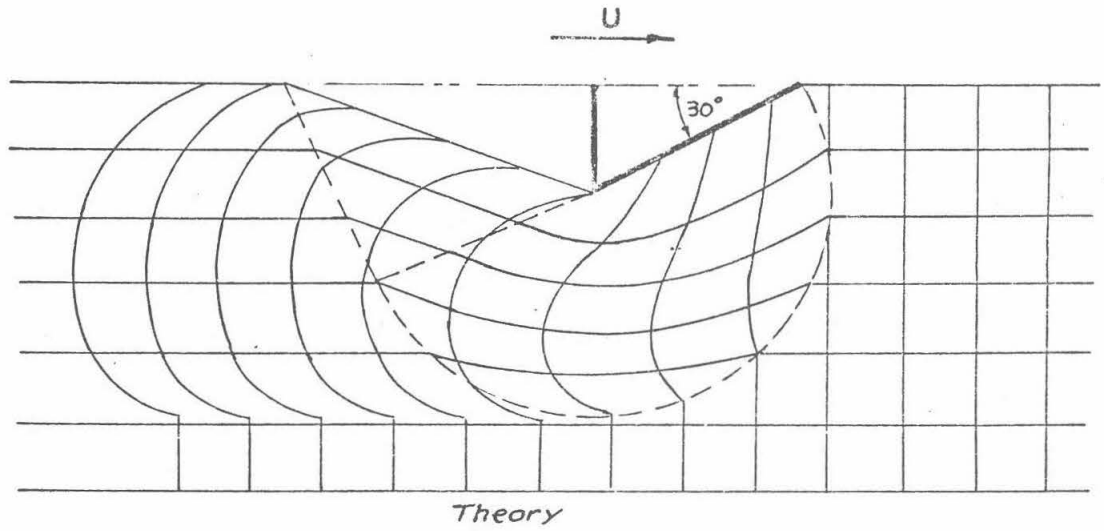

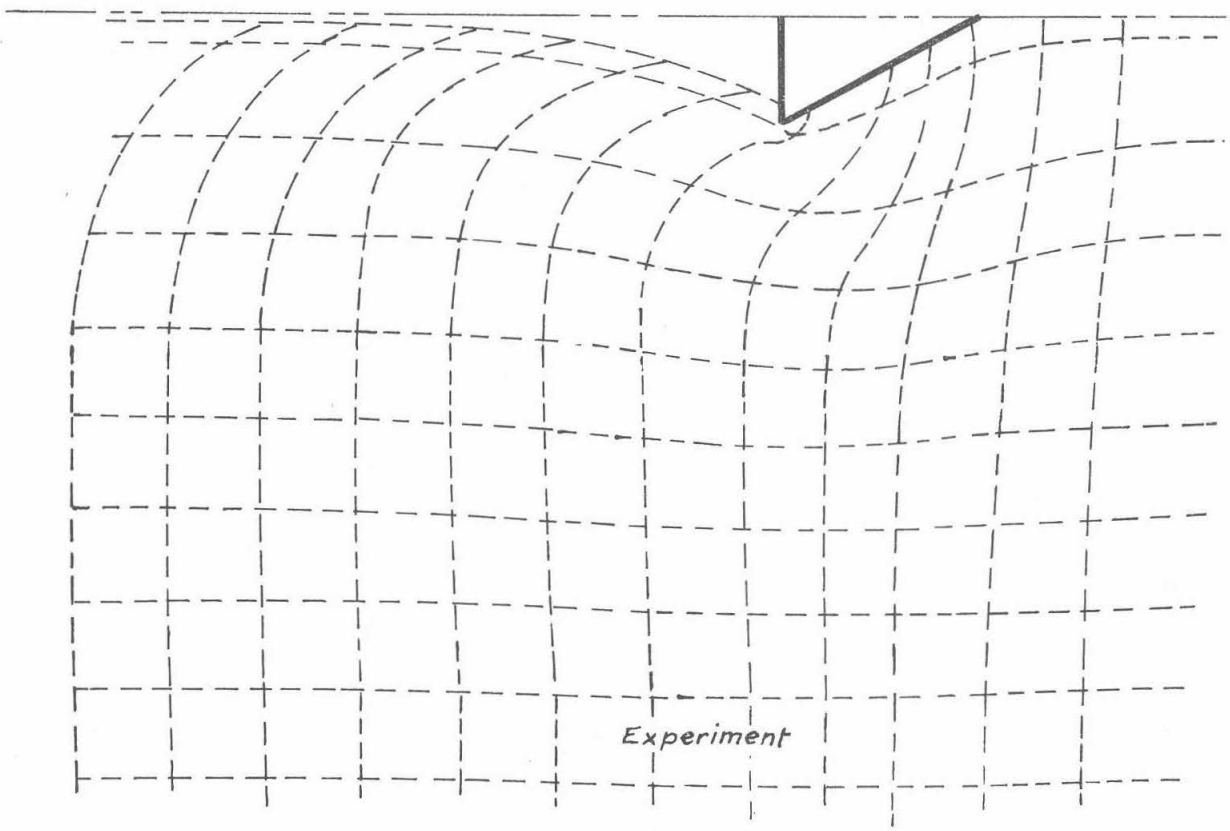

Fig. II-17. Distortion of a square grid for $\delta = 30^{\circ}$, comparison between theory and experiment.

(b) The slope of the deformed vertical lines, which according to the theory is discontinuous at the boundary between the rigid and plastic domains and changes direction from positive to negative, is found in the experiment to be smooth with virtually no change in sign, i.e., instead of having part of the deformed line move forward and the rest backwards, it displaces only backwards.

(3) The incompressibility of the material in perfect plasticity is not supported by the tests even at the relatively small stresses employed. Instead, the change in volume of the clay which is measured by the size of the air gap left behind the wedge seems to increase with increasing β.

Through two additional tests, we will now study the reasons behind the differences between theory and experiment with respect to:

(1) The free surface behind the wedge.

(2) The deformation zone and pattern.

The first test was carried out with a $\beta = 45^{\circ}$ wedge and the second with $\beta = 30^{\circ}$. In these tests the wedge was reinserted into position, 24 hours after the pictures of Fig. II-15 were taken and the test was continued. We call this testing in the second stage and the results are given in Figs. II-18 and II-19. The velocity of the wedge was kept constant throughout the second stage of Fig. II-18 with no halts. In Fig. II-19 ($\beta = 30^{\circ}$) the loading was stopped twice, each stop lasting for 30 seconds. The location where this was done is clear by the dents in the free surface. Moreover a fresh orthogonal grid

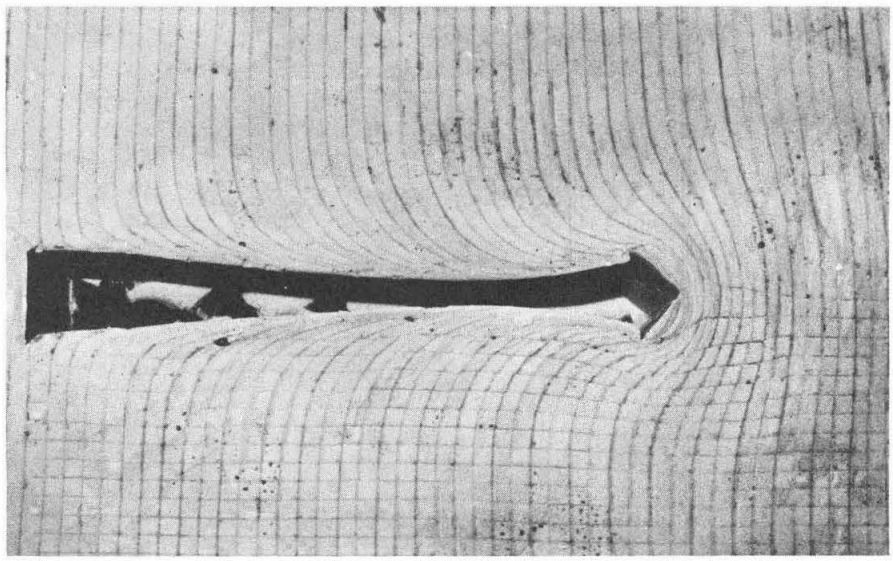

(a) End of first stage;
beginning of second stage

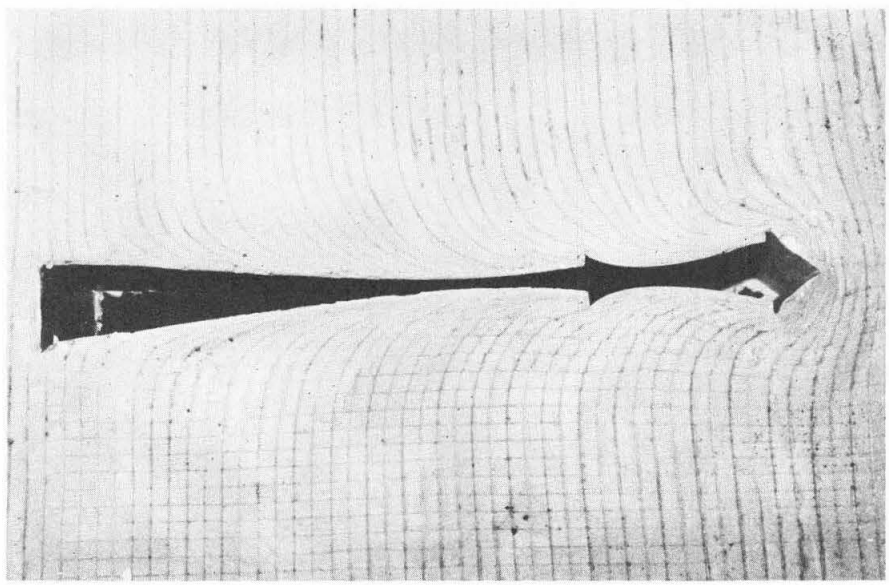

(b) End of second stage

Fig. II-18. Testing in the second stage with $\delta = 45^{\circ}$.

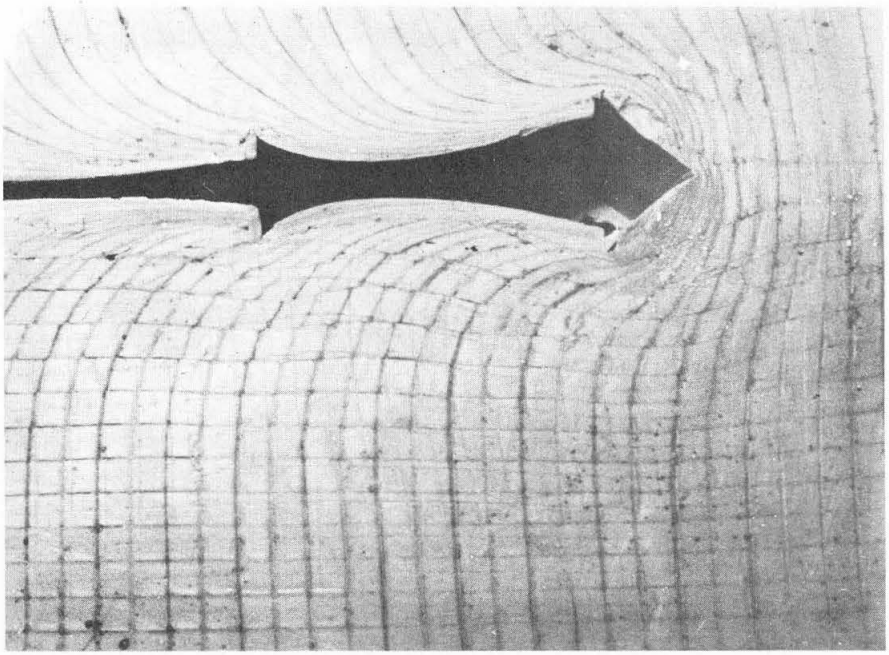

Fig. II-18. Testing in the second stage with $\delta = 45^{\circ}$.

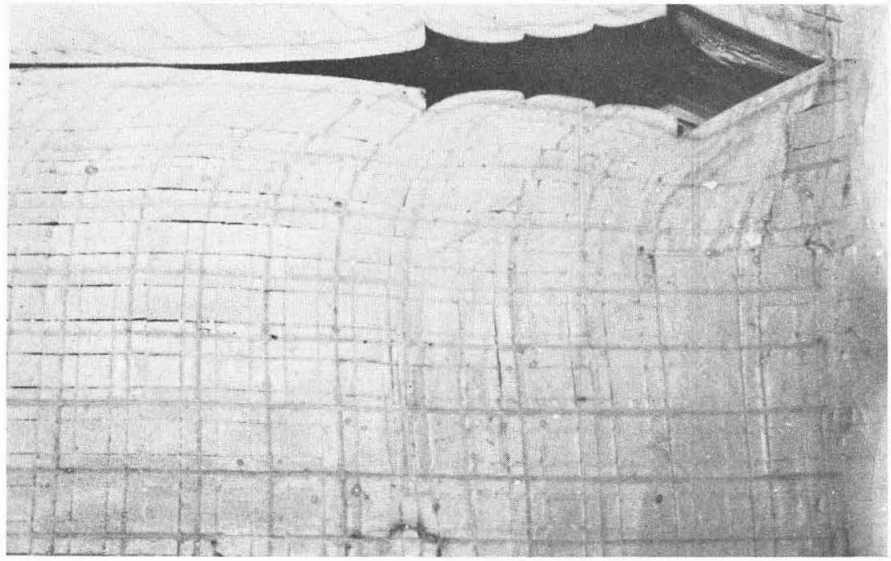

(a) Old grid drawn at the beginning of the first stage

(b) New grid drawn at the beginning of the second stage

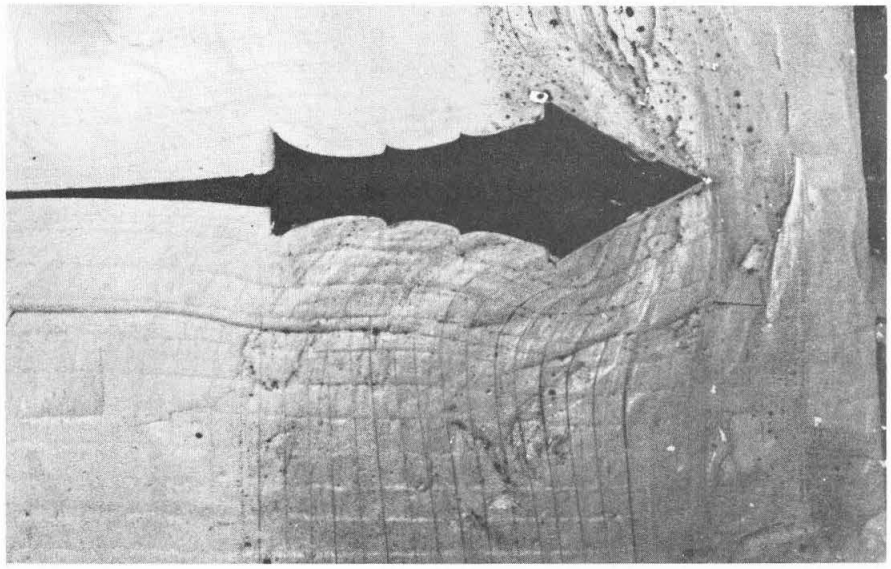

Fig. II-19. Testing in the second stage with $\delta = 30^{\circ}$.

drawn on the second half of the clay mass (the clay occupies the two halves of the box) before beginning the second stage deformed as shown in Fig. II-19-b. This distorted new grid is drawn together with the theoretical solution on Fig. II-20 .

Using Figs. II-18, II-19, II-20 it is concluded that:

(1) Concerning the free surface behind the wedge

Between the time the loading was halted and the picture taken, the free surface changed in shape by creep due to the time-dependent properties of the clay. The major part of this creep takes place during the 5 minutes required to dismantle the box. Moreover, by noting the sudden change of curvature of the stream lines near the corner of the wedge, Fig. II-15-a in particular, we believe that this is another effect of the creep. This suggests that the steady-state free surface behind the wedge is less convex than the pictures show it to be and instead, it is closer to the straight line shape assumed by the theory.

(2) The deformation zone and patterns

By eliminating in effect the distortion of the clay ahead of the wedge through redrawing the grid, the deformation of the fresh grid in Fig. II-20 improves the correspondence between theoretical and experimental deformation fields considerably. Moreover this distortion which masked the change of the slope in the distorted vertical lines from positive to negative in the first stage, now shows that the slope change indeed occurs in the test, confirming the

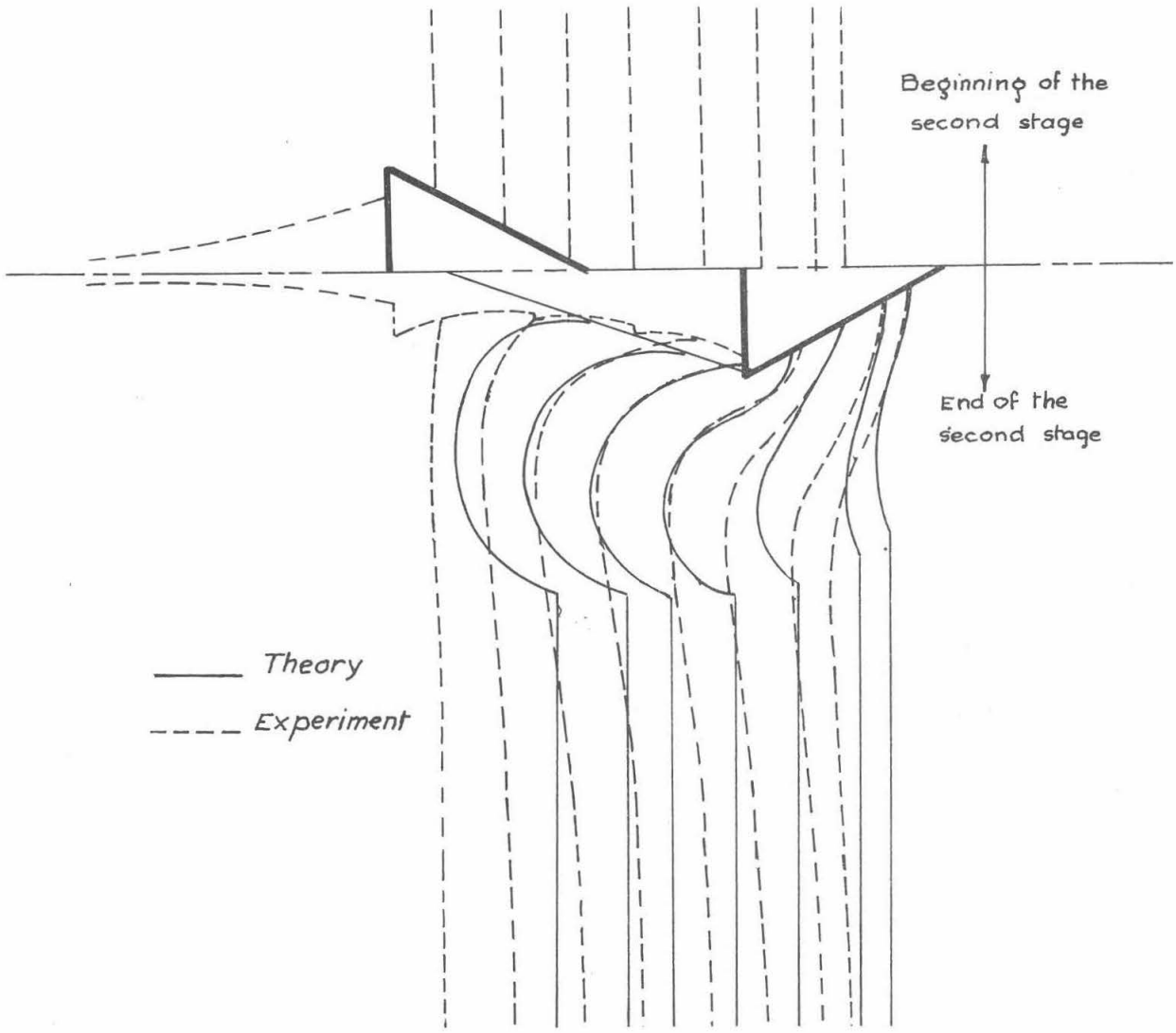

Fig. II-20. Distortion of vertical lines in the second stage for $\delta = 30^{\circ}$.

prediction of the theory in that respect.

C. Steady state loads

The loads required to produce a steady state were recorded for $\delta = 10^{o}$, 30^{o} and 45^{o} and the results, after subtracting frictional resistances, are plotted in Fig. II-21. On the same figure are also drawn curves representing the relationship between the loads and δ as given by the plasticity solution for rough wedges using a Tresca hypothesis for the yielding of the material. The uniaxial yield strength Y of the curve with higher resistance was chosen to be 1.25 Kg/cm^2 and the second corresponds to Y = 1.00 Kg/cm^2. These values of Y will give uniaxial stress-strain curves as shown by curves C and D on Fig. II-22. On the same figure are plotted the stress-strain curves of the modeling clay for rates of loading of 0.6 Kg/cm^2/min (A) and 0.15 Kg/cm^2/min (B) respectively. These curves are the same as the fitted experimental results previously given in Fig. I-6-a except that the stresses are now corrected for the change in area occurring during loading. To do this we assumed no volume change and that the cylindrical shape of the specimen is preserved at any load. Also under these assumptions we computed $\Delta\alpha$ the change in slope of a diagonal plane and used it as another measure for the strain to compare with the wedge results.

To be able to detect the effect of changes of the room temperature on the shearing strength, the cohesion of the clay at various locations was recorded after each test using the vane test. The cohesion varied due to inhomogeneity and vane test imperfections

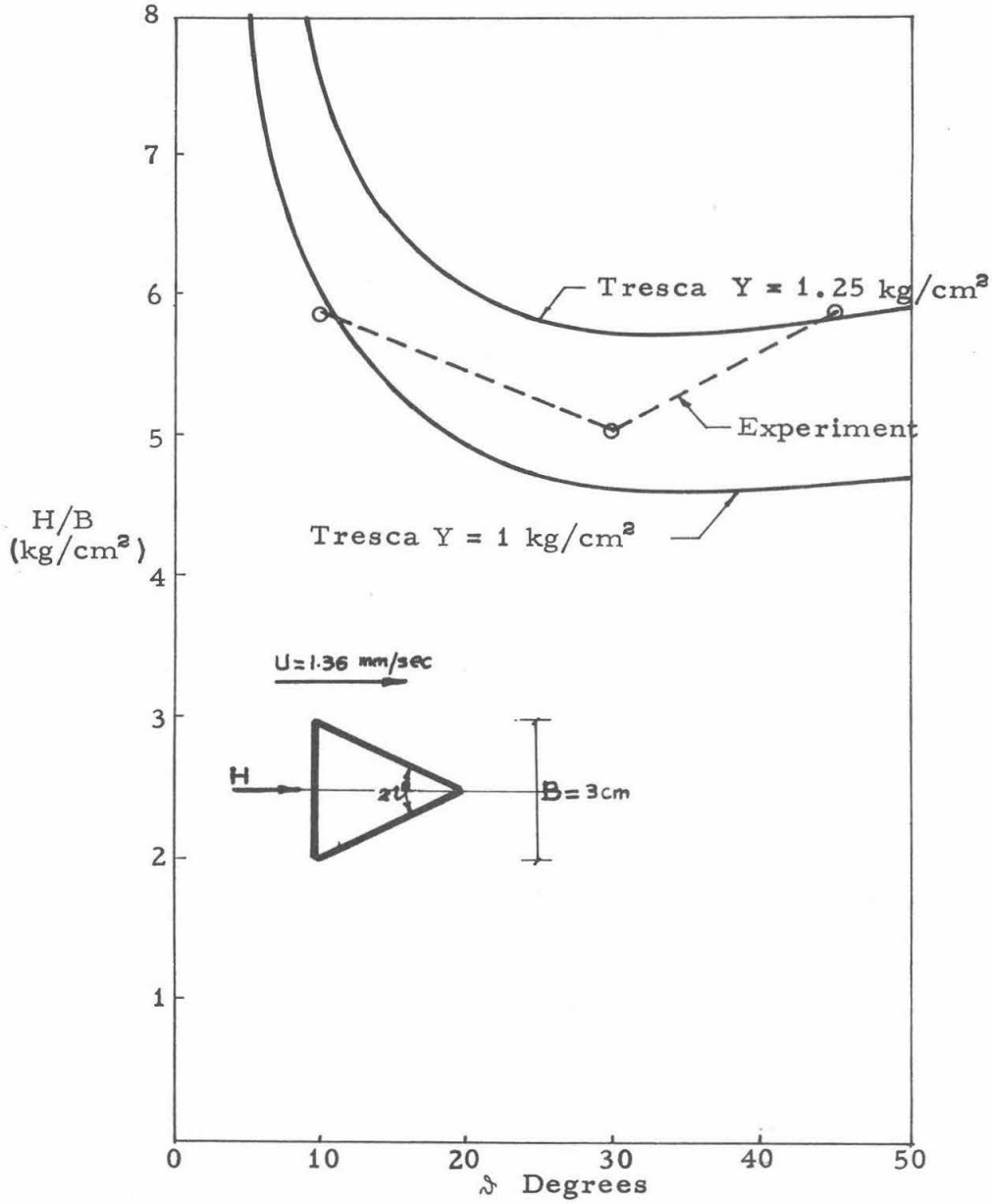

Fig. II-21. Indentation loads.
Comparison between perfect plasticity and experiment.

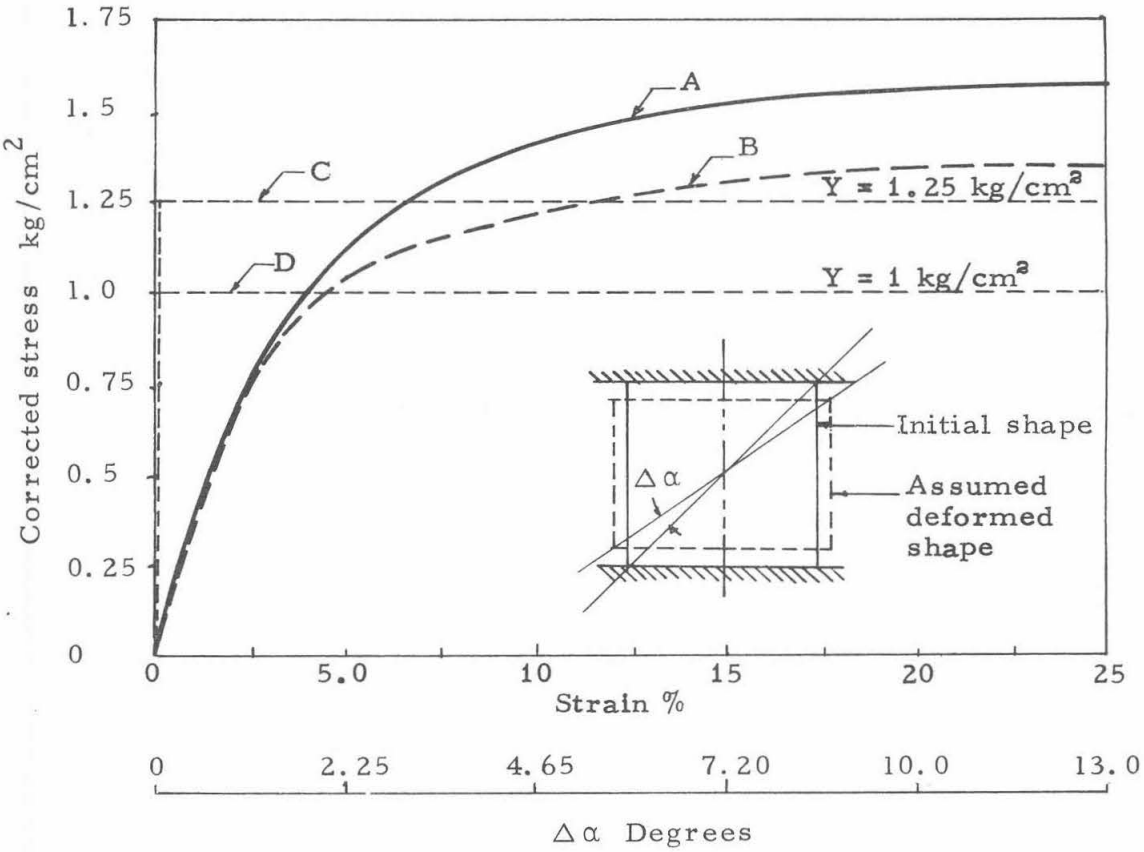

Fig. II-22. Corrected stress vs. strain in one dimensional compression of modeling clay.

from 0.58 to 0.62 Kg/cm^2 without noticeable variations from one test to another. This cohesive shear strength corresponds to a uniaxial strength of 1.16 to 1.24 Kg/cm^2.

In Fig. II-21 we note that by increasing ϑ, the value of the steady state experimental force H tends to approach the force predicted by the theory for a stronger material. This is believed to be caused by the deformation gradients as functions of ϑ. It is clear by comparing Fig. II-16 and II-17 that the gradients are larger for larger ϑ. This causes two properties of the clay, unaccounted for in the theoretical model, to come into play: the strain hardening effect and the rate of straining effect. Specifically what happens is:

(1) The slope of the distorted vertical lines which are a measure of the strains in the clay are larger for larger ϑ. This result is also predicted by the theory and implies that for our strain-hardening clay the larger ϑ is, the more resistance one would expect to develop, compared with the non-strain-hardening theoretical model, depending on the value assumed for the strength of the material in the theoretical solution.

(2) The curvature of the distorted horizontal lines increases by increasing ϑ. Since this curvature, for a constant wedge velocity U, is a measure of the straining rate, thus as ϑ increases the straining rate increases.

The combined effect of the above properties of the modeling clay makes us believe that if curve B Fig. II-22 represents the stress-strain curve for the clay, on the average, for $\vartheta = 10^{\circ}$ and is

idealized by D; then curve A better represents the higher straining rates in the $\delta = 45^{\circ}$ case; this is idealized by curve C.

D. Behavior of blunt wedges, the formation of a rigid part ahead of the wedge

From the previous study of the deformation patterns it was seen that as δ increases the test results deviate from the theoretical solutions. Consequently the direct comparison between theory and experiment made for $\delta = 10^{\circ}$ and 30° in Figs. II-16 and II-17 could not be made for the case of $\delta = 45^{\circ}$. In the latter case, the mesh near the wedge-clay interface is highly compressed and the horizontal streamline near the axis of the wedge which, according to the theory, should remain straight until it reaches the tip, bends from a considerable distance ahead of the wedge Fig. II-18. These, we believe, are indications of the existence of a rigid part of clay ahead of the wedge that moves with it. Such a mechanism involving a rigid part ahead of the wedge was reported in the indentation of a half space by a rigid wedge [15]. However to get a definite picture of how this rigid part looks like in such steady state problems, an additional test was performed with $\delta = 78^{\circ}$. The rigid part, if indeed present in the $\delta = 45^{\circ}$ case, should reveal itself better in this test.

To be able to attach the wedge to the sliding arms, the triangular cross section of the wedge had to be abandoned and the shape shown in Fig. II-23 was used. In the same figure the distorted mesh is shown; it bears a strong resemblance to that of the wedge with $\delta = 45^{\circ}$. In both cases, the gap behind the wedge is large

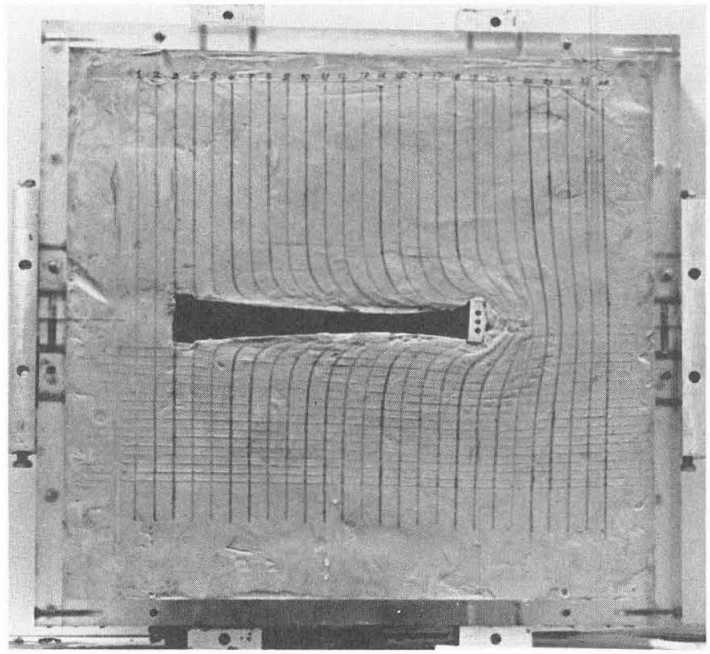

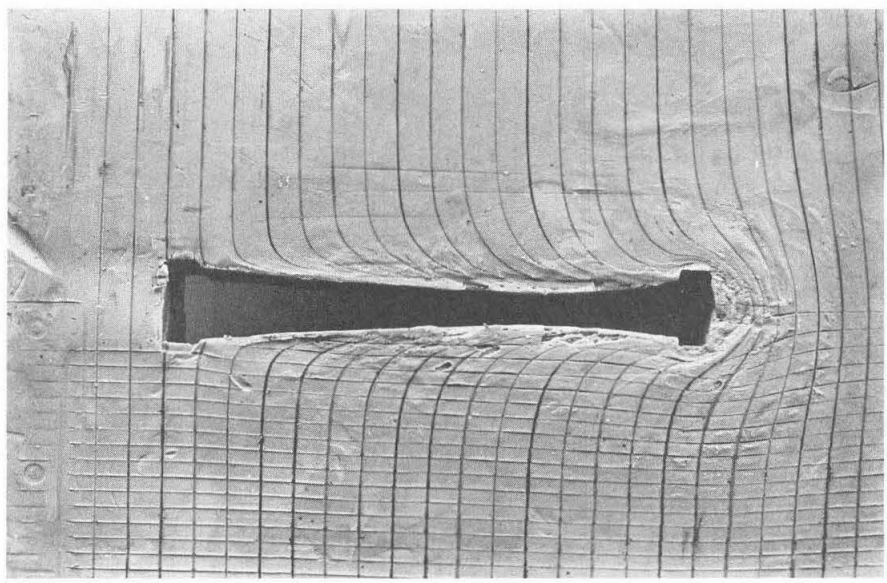

Fig. II-23. Distortion of an orthogonal grid ($\delta = 78^{\circ}$).

compared with that behind a sharp wedge thus showing that the clay undergoes a large compression during its indentation by a blunt wedge. Furthermore, the zone ahead of the wedge is heavily strained such that the distorted mesh can no longer be seen, this we believe is the indication of the existence of a rigid part.

We thus conclude that starting from a value of δ between 30 and 45^{o}, a rigid part of the clay is formed ahead of the wedge. The theoretical solution, presented earlier, which assumes a process of cutting to take place, whereby no such rigid part exists, ceases to describe the indentation process adequately. Until more tests have been made to determine the value of δ after which the rigid part starts to develop, it can reasonably be taken as the value $\delta = 33.6^{o}$ previously derived as the one giving the least resistance for a given width. Furthermore, as in the case of the indentation of a half space by a rough wedge, the indentation process of an entire space by blunt wedges becomes more of a compression nature than the cutting assumed by perfect plasticity.

II-1-5. Finite element solutions

Wilson's modified finite element technique (see chapter I) was used to solve the indentation problem for a bilinear material. The purpose of the solutions is twofold:

(1) To interpret the discrepancies between perfect plasticity solutions and the experiments. These are most obvious in the far field, i.e. at the boundary of the rigid domain with the plastic zone.

The use of the finite element method which relies on equations elliptic in character is expected to smooth out discontinuities given by plasticity theory and absent in the experiments. Furthermore, the finite element method allows us to control the properties of the model "material" closely.

(2) To extend and compare the plane strain solution to the axi-symmetric case of a cone.

The problems treated are a wedge and a cone both with semi-angle $\delta = 30^{\circ}$ as in the case of the Dutch cone penetrometer. The modeling clay properties were simulated by assigning the following values to the bilinear material of the finite element analysis: $E = 31.5\ Kg/cm^2$, $Y = 1.18\ Kg/cm^2$, and the moduli ratio $n = 0.035$. Poisson's ratio ν was taken equal to 0.45 and then changed to 0.35 to determine the effect of compressibility on the results. These material constants give an axial-compression stress-strain response shown by curve F in Fig. II-24. It clearly affords a better idealization of the clay (curve B), than the rigid-plastic material does (curve C or D), especially at small values of stresses and strains. On the other hand the relatively low rigidity of this particular clay is not best suited for the present F.E. technique because of the associated large strains and the resulting geometrical non-linearity. Since most clays encountered in engineering problems have a much higher rigidity (in the order of 10 times the modeling clay value), which will make the present technique more applicable, we will go ahead and use it, to get comparative and qualitative results. The

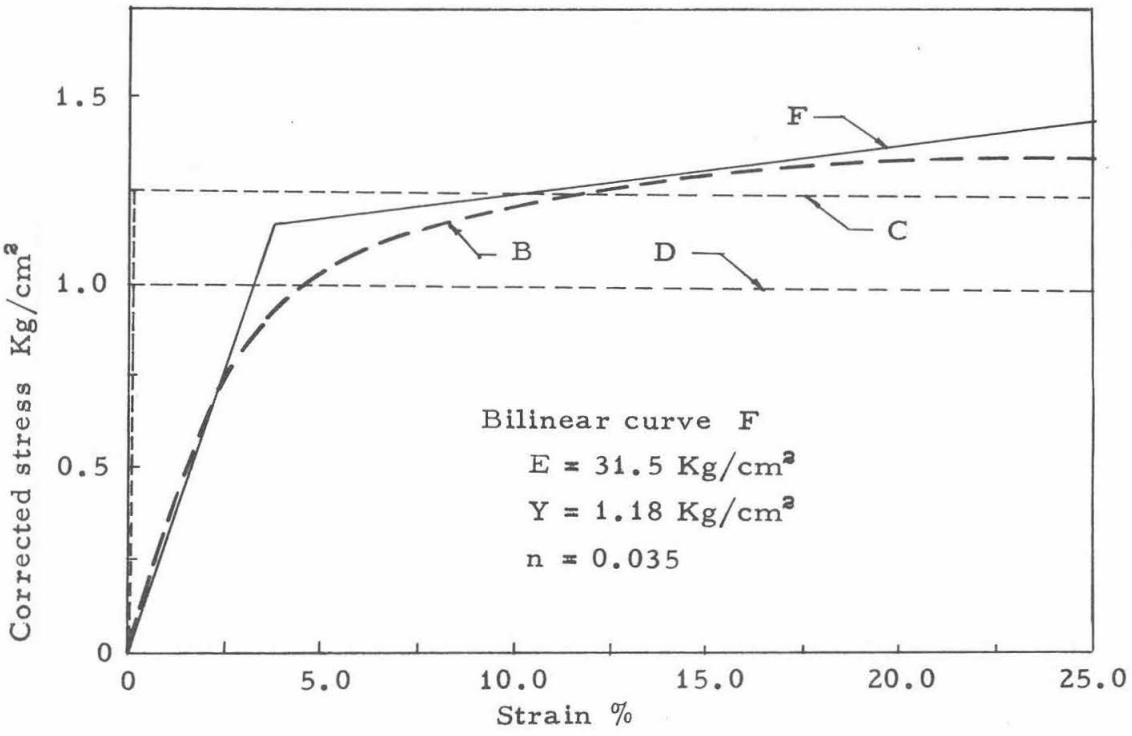

Fig. II-24. Corrected stress vs. strain in axial compression of modeling clay and various idealizations.

accuracy of the near field however, which includes large strains unaccounted for in this analysis, should be assessed in the light of this approximation.

The geometry, some of the boundary conditions and the F.E. ($\vartheta = 30^{\circ}$) mesh are shown in Fig. II-25. The symmetry about the z axis allows the consideration of only half the problem. The geometry of the free surface behind the wedge is taken from the ideal plasticity solution for a rough wedge ($\gamma = 20.7^{\circ}$). Along boundary $\overline{ab}$, nodes have a normal component of displacement $u_n = 0$ and a tangential component of traction $s_t = 0$. This is the symmetry condition. Along $\overline{bcdefg}$, the nodes have $u_n = u_t = 0$ representing the clay sticking to the box used in actual testing. Along $\overline{ghk}$ the boundary is stress-free representing the surface of the clay behind the indenter which in the tests did not close behind the wedge. For a closer look at the nodes inside circle Σ, we plot the grid again to a larger scale in Fig. II-26. The contact surface of the indenter with the clay is represented by $\overline{k\ell mn}$. Along this boundary we ideally want to specify the non-zero tangential tractions s_t for a rough interface, and the normal displacement $u_n \neq 0$. Denoting the forward displacement of the indenter by δ, we thus have $u_n = \delta \sin \vartheta$. To be able to specify s_t and u_n we face the following difficulties:

(1) The value of s_t is not only dependent on the frictional properties of the interface but also on δ and subsequently on u_n.

(2) The boundary conditions to be specified at the tip and at the edge of the indenter, i.e. at nodes n and k, Fig.

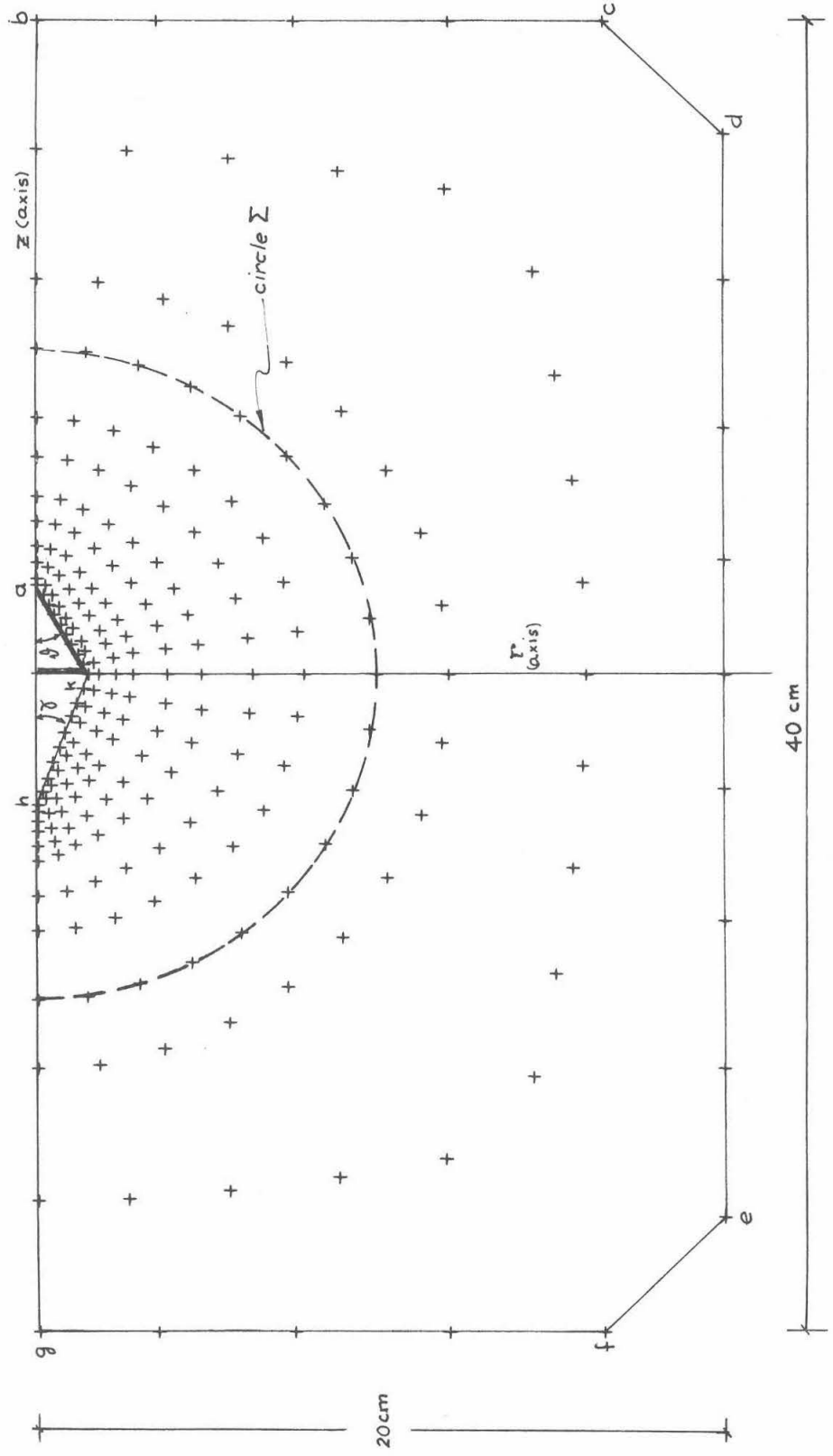

Fig. II-25. Node location in F.E. mesh and boundary conditions.

II-26. These are singular points and need a special consideration.

Other investigators, e.g. Ellison et al. [32], introduce elements of zero volume at the interface. When given a shear load versus displacement behavior they would simulate the frictional behavior of the interface. In this text such elements were not needed because of the relatively large values of displacement δ used. In addition the existence of slip at the interface coupled with the development of maximum shear resistance is presumed. This argument is based on one hand on solid friction load-displacement measurements by Bowden et al. [33] and on the other on load transfer measurements, of axially loaded piles by D'Appolonia et al. [34] and Whitaker et al. [35]. Their results show that full interface friction is developed at small displacements. It is thus assumed in the following solutions that $s_t = 0.6$ Kg/cm^2 along the boundary $\overline{k\ell mn}$. This is the yield shear strength of the clay corresponding to the value used in perfect plasticity.

As for the condition at both tip and edge of the indenter, the contribution of the elements at these points was minimized by reducing the node spacing near the interface without however eliminating the error involved in any boundary condition to be given to nodes n and k. Because of our greater interest in simulating the geometry of indentation, only the effect of the shearing stresses was given to nodes n and k in the form of a force component in the z direction. They were left free in the R direction. An alternative would have been to specify u_n and s_t as for the other interface

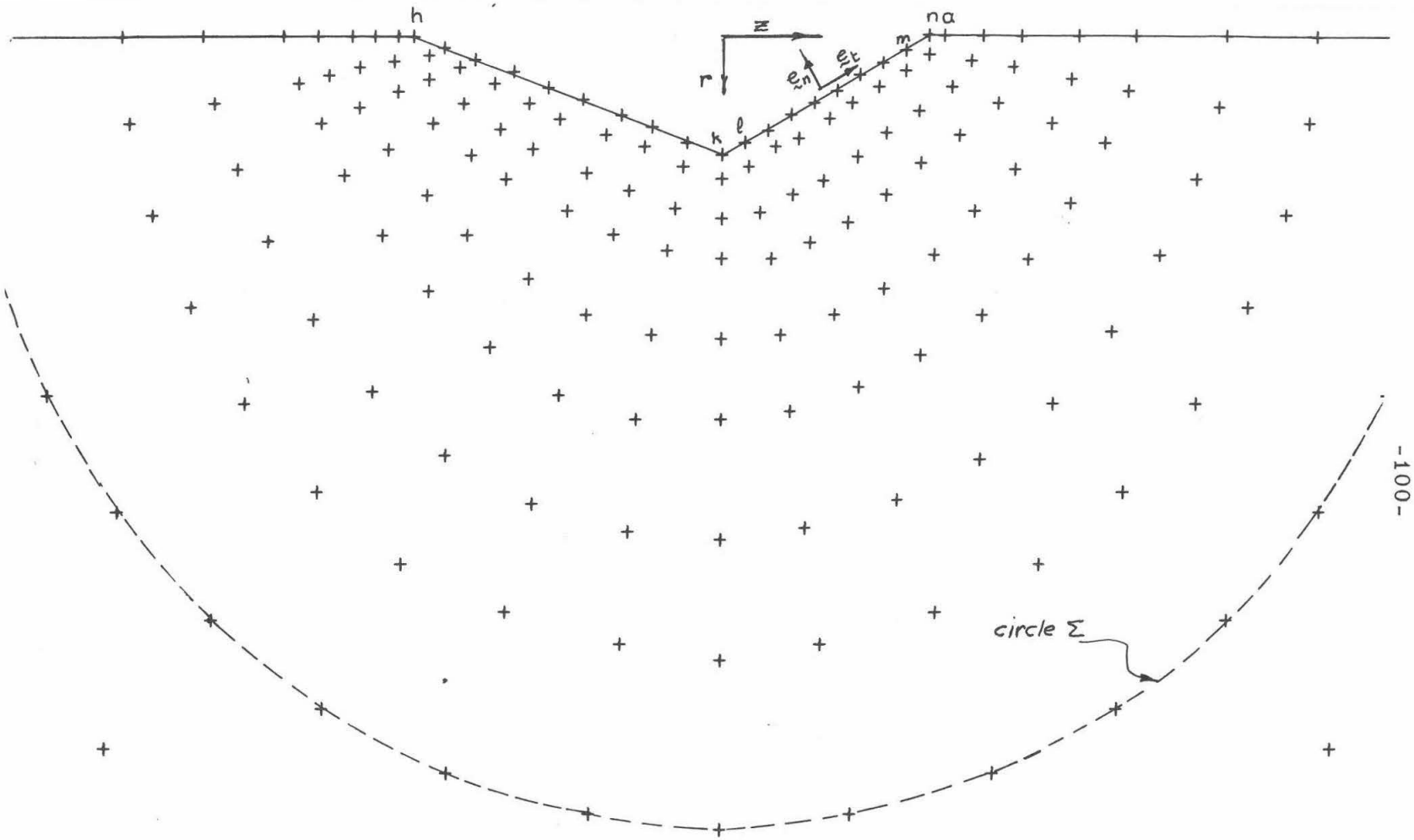

Fig. II-26. Finite element mesh and interface boundary conditions.

nodes. It might be argued that this approach will give more realistic indentation loads but on the other hand it will certainly represent a process of an expansion rather than indentation.

To avoid such difficulties other workers, e.g. Hoeg [36] prefer to specify the tractions along the interface. After solving the problem they determine an average value of displacement of the interface nodes and plot this value in a load-displacement type of curve. The stresses in this case are assumed uniform because no other distribution is more justified. The results are then referred to as "flexible foundations" solutions which have a very restricted use. We tried this concept but found the deformed interface taking a strongly concave shape which defied any averaging procedure and which exhibited no similarity with the indentation.

Finally the use in the model of two materials, a soft one for the clay and a rigid one for the indenter, showed that the oscillations in the displacement and stress fields near the interface were large. This phenomenon which often occurs near singularities when using the F.E. brought us back to the method previously described.

Improvement in the Finite Element technique to reduce the errors mentioned above can be achieved by:

(1) Reducing the size of the mesh.

(2) Using a step-by-step method in which each u_n increment would be small and the nodes displaced to their new location after deformation.

When estimated, the cost of such improvements did not justify their use in the comparative study presently conducted. It was

thus left for a more accurate quantitative research project.

The results obtained by the analysis of different problems are given in Fig. II-27 through II-30. In Fig. II-27 is shown a load-displacement plot for both a cone and wedge when $\nu = 0.45$. In each case three points were obtained at values of δ/B equal to 0.066, 0.1666, and 0.667, and joined by straight lines. The initial part of the curve in Fig. II-27 corresponds to the linear solution obtained (as a first approximation) in case of $\delta/B = 0.066$. The indentation loads were evaluated by integrating the stress components in the z-direction along circle Σ in Fig. II-25. The circle represents either a cylinder in the plane strain case, or a sphere in the axi-symmetric case. This affords a more reliable evaluation of the force away from the stress concentration near the interface. Comparing the graphs of the cone with that of the wedge, the former gives loads 10 to 25 per cent higher for δ/B between 0.1 and 0.65. Moreover, at $\delta/B = 0.667$ which is already too high to neglect geometrical nonlinearity in the near field, the value of H/Ak for a wedge is 6.95 which is still below the 9.21 value obtained by perfect plasticity. Such large values of displacements associated with this problem are caused by the low rigidity of the material used. However since the shape of the curves in Fig. II-27 indicates that higher loads are expected for larger δ, the steady-state predicted by plasticity is presumably reached for δ/B near the value 2 found in actual testing.

The development of the plastic zone as δ/B increases is shown in Fig. II-28. The black region is where the deviatoric straining is large and thus we call it the zone of substantial shearing. The ratio of the deviatoric stress to deviatoric strain $2G'$, within this

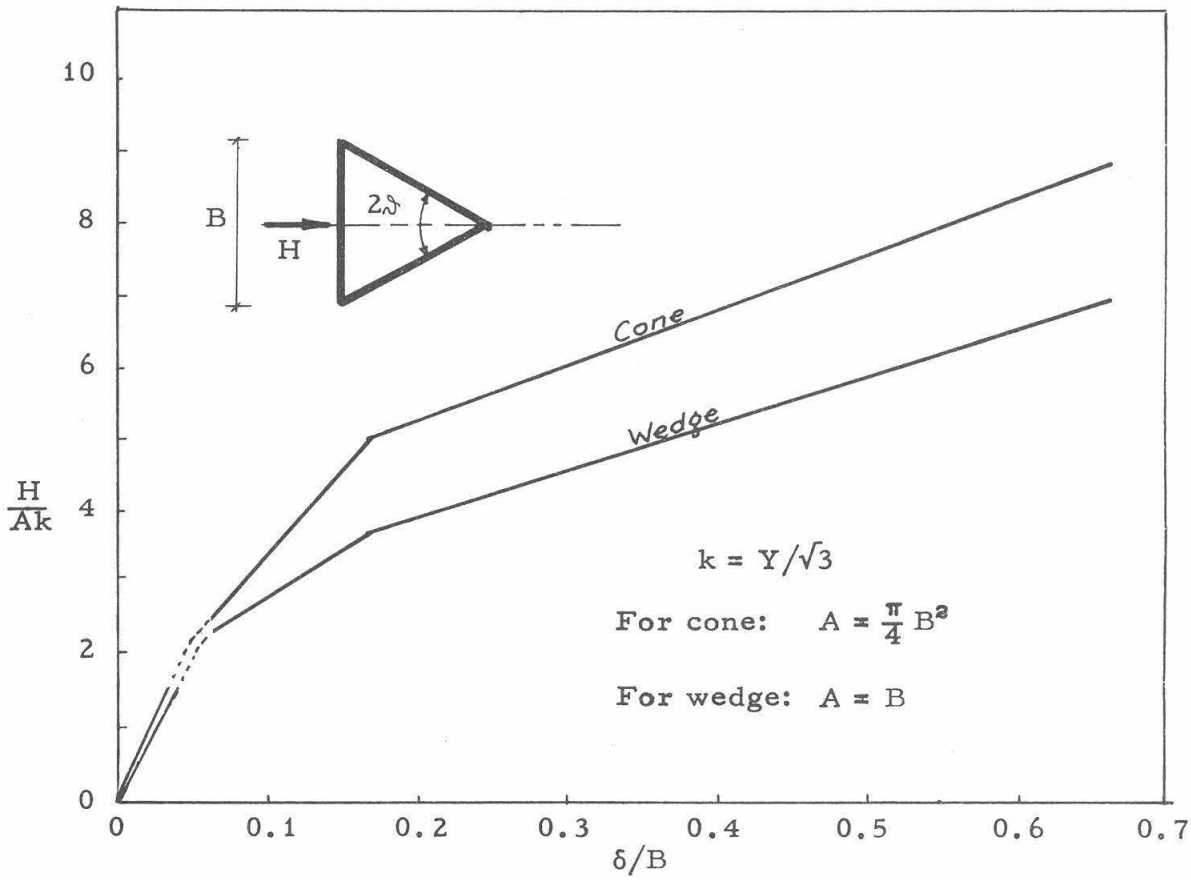

Fig. II-27. Load-displacement relationship for $\vartheta = 30^{\circ}$, solutions according to finite element for a bilinear material. ($E = 31.5$ Kg/cm^2, $Y = 1.18$ Kg/cm^2, $\nu = 0.45$, $n = 0.035$)

(a) Wedge

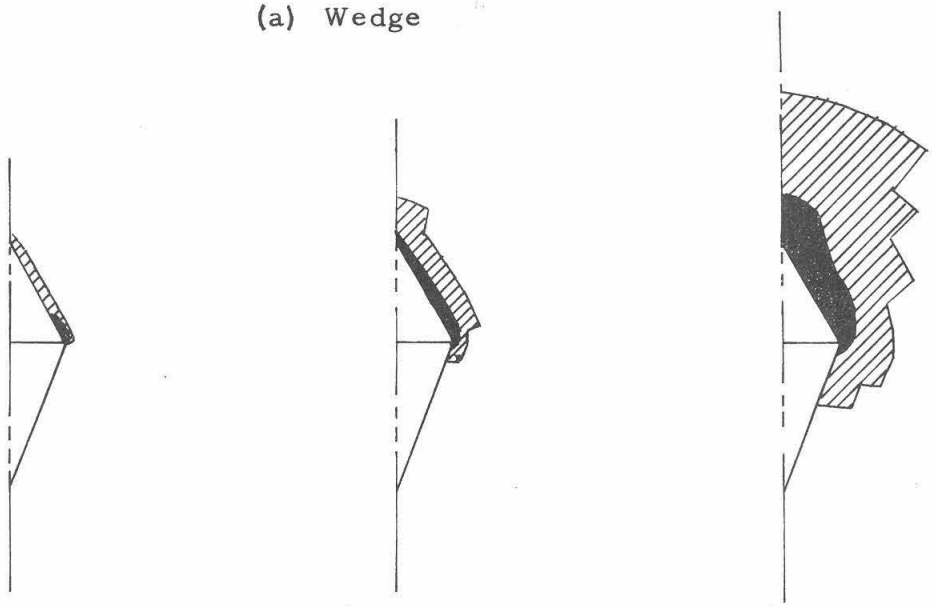

δ/B = 0.067 δ/B = 0.167 δ/B = 0.667

(b) Cone

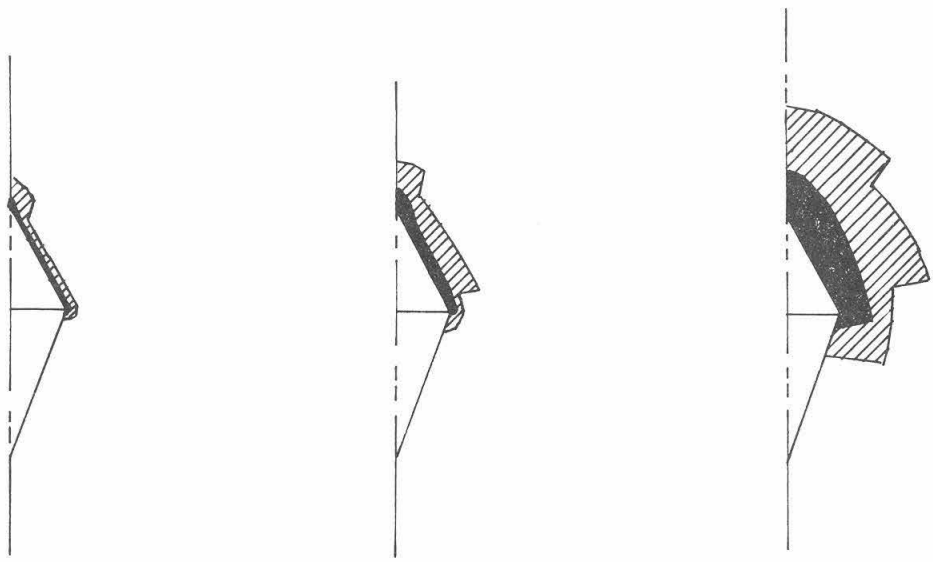

δ/B = 0.067 δ/B = 0.167 δ/B = 0.667

Fig. II-28. Development of the yielded zone.

region is less than 0.2G. The shaded region is a transition region between the zone of substantial shearing and that of the elastic zone where the stresses did not reach the yield stress. The similarity between the wedge and cone is clear by comparing (a) and (b) of Fig. II-28. Moreover the yielded zones lie mainly ahead of the indenter and do not extend as far behind it as perfect plasticity predicts. This phenomenon was also found in solving for the indentation of a half-space by a smooth circular punch described in the Appendix, using the same F.E. Technique. Other investigators using different numerical procedures have reached similar results, e.g. Ellison et al. [32] in their step-by-step finite element solutions for a pile with a flat toe.

The displacement field when $\delta/B = 16.67\%$ for both wedge and cone is given in Figs. II-29 and II-30. Comparing these two figures we note:

(1) The displacement patterns are similar. In the case of a cone however, the displacements are generally smaller and, as expected, die off faster as the distance from the interface increases. Moreover the deformation near the tip, in the case of a cone, simulates the indentation process better than the wedge.

(2) In both cases, the region ahead of the indenter is the most heavily distorted. Displacements are detectable up to a distance of about 3B for a wedge and 2B for a cone. (These distances vary of course with δ/B.)

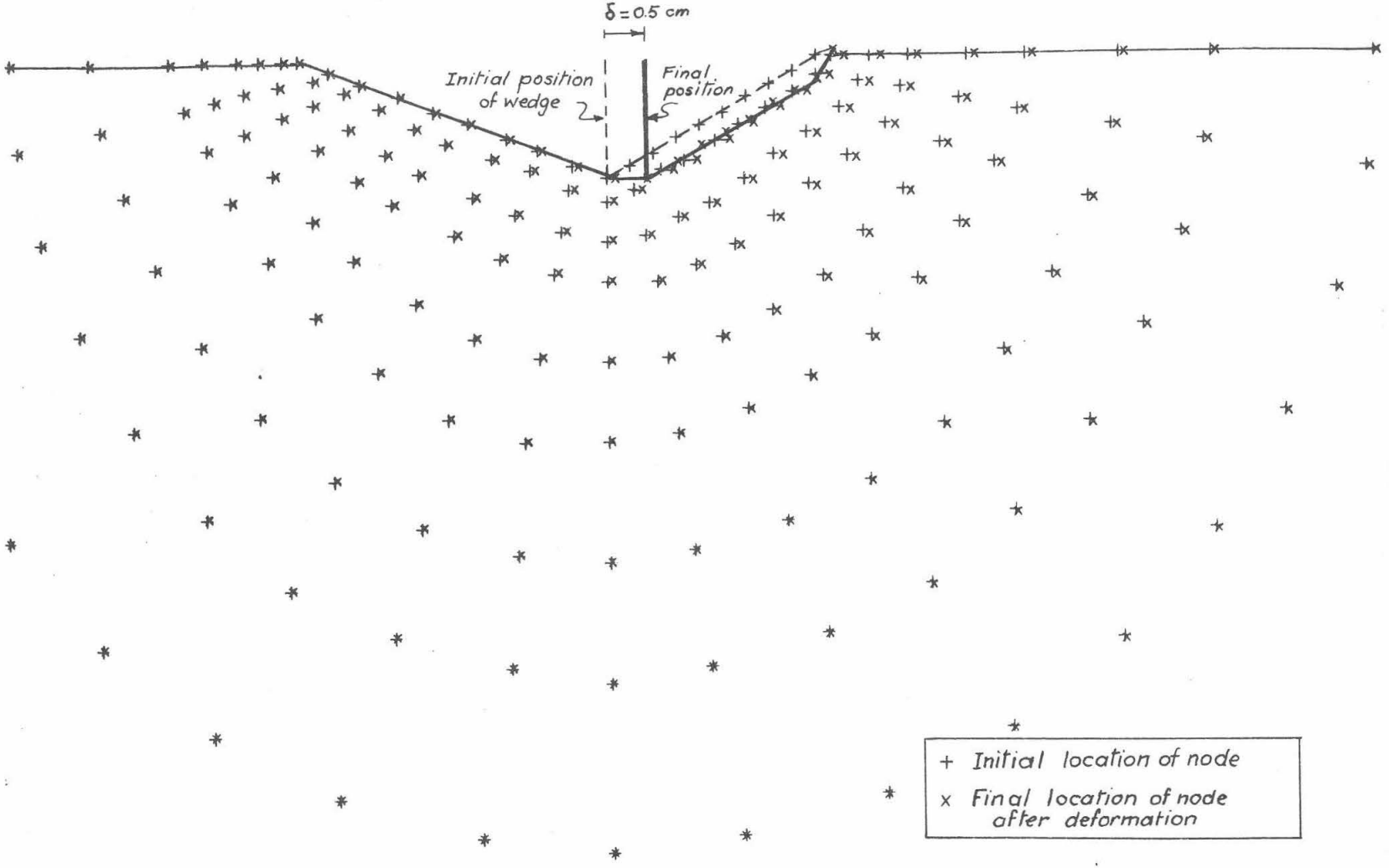

Fig. II-29. Displacement field for a rough wedge in a bilinear entire space when $\delta/B = 0.167$.

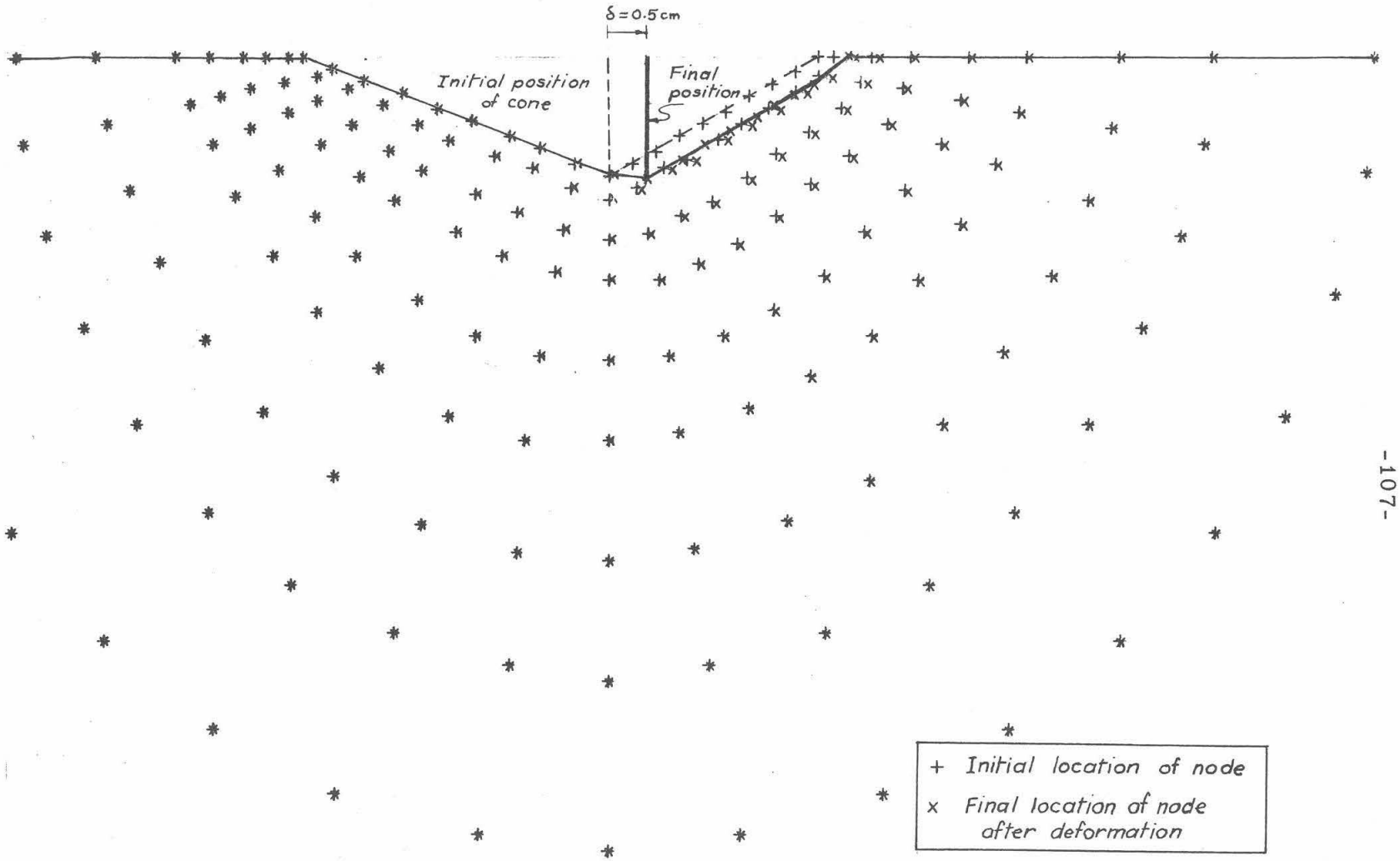

Fig. II-30. Displacement field for a rough cone in a bilinear entire space when $\delta/B = 0.167$.

(3) In both cases the displacement field is smoothly varying with no discontinuities in its gradient. This condition is found in actual testing and differs from the results of perfect-plasticity which assumes the existence of a rigid domain.

(4) The displacement field is predominantly in the z direction. However, within half the field, ahead of the indenter, the velocity vector may be considered to be radial. This would justify recent approaches to pile bearing capacity which assume that the process of pile resistance to axial loading can be idealized by that of the expansion of a cavity under condition of radial symmetry. On the other hand, the displacement field behind the indenter is clearly in the z direction which does not agree with the above mentioned approach.

Other results of interest are:

(1) When $\delta/B = 0.0667$, by computing the part of the load carried by the rear half of circle Σ, Fig. II -22, it was found to be 38% of the total load for a wedge and 46% in the case of a cone. Since these values are large, the early approach to bearing capacity of deep foundations in which a mechanism of failure is assumed in the front half only, and the half behind the base level is considered only as a surcharge (Terzaghi, Prandtl, Reissner, Caquot, see [37] and [38]) is by no means justified.

(2) To see the effect of compressibility, the wedge problem was repeated with $\nu = 0.35$ at $\delta/B = 0.166$; the load decreased by 16.5% as compared with the $\nu = 0.45$ case. The displacement field was virtually unaltered to the scale of Fig. II-29.

(3) When $\nu = 0.45$, the direction of the z component of displacement is positive except for points close to the boundary (r = 20 cms) at the level of the indenter ($|z|$ small). These points are not shown in either Fig. II-29 or II-30. The tendency to move in a direction opposite to that of the motion is more pronounced in the case of a wedge. It is believed to be caused by two factors:

a. The existence of the fixed boundary

b. The relative incompressibility of the material.

When ν was changed to 0.35, for $\delta/B = 16.65\%$, the region of negative z displacement component was eliminated. This result is of practical interest in pile driving since it is common while driving a pile in a relatively incompressible medium to cause predriven ones (simulated here by the fixed boundary) to move upwards. This is obviously due to the upward movement of the soil and the positive shearing stresses that develop due to the lateral restraint. It is interesting to note that even at a distance of about 7B, compared with the 3B common spacing between piles such a phenomenon is felt.

II-2. Indentation by an inclined smooth rigid plate

II-2-1. The problem and its applications

Let us consider the rigid smooth plate of length L shown in Fig. II-31. The plate moves in a rigid-perfectly plastic material, under a plane strain condition, with a constant velocity U (to the right). Its inclination δ to the horizontal is such that $0 < \delta \leq \pi/2$.

In Soil Mechanics applications the plate represents an anchor plate buried deeply under the surface of a clay layer. This is a suitable type of foundation for structures whose stability involves horizontal components of force, e.g. suspension bridges and sheet piles. Also in circumstances where the gravity effect is not efficient in resisting forces of pull (e.g. underwater structures subject to uplift forces) anchor plates are often found more economical to use than dead loads.

A previous solution to this problem has been obtained only for the special case of $\delta = \pi/2$ and for a particular failure pattern [39]. The following solution however is more general in the sense that:

(1) It applies for $0 < \delta \leq \pi/2$ which covers a wide range of forces of resistance. The knowledge of the variation of these forces with δ allows both an estimate of the effect of imperfect construction of an anchor plate and the use of δ in controlling the resistance force according to the particular application.

(2) The failure modes found are infinite in number. Of those modes only one is presently found in the literature [39].

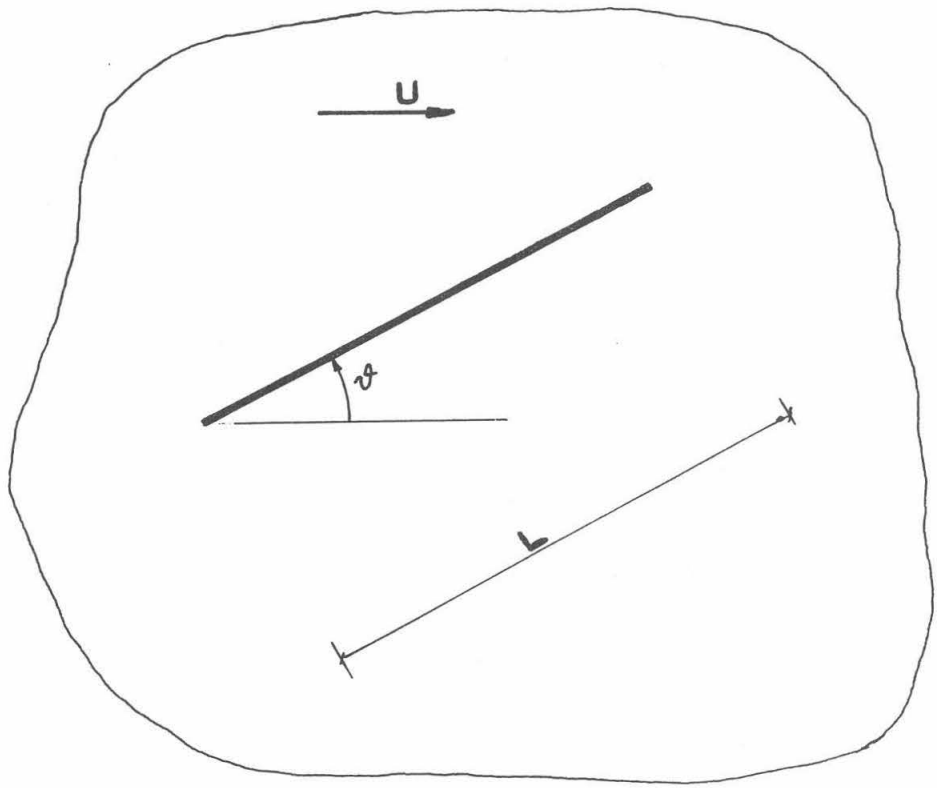

Fig. II-31. Plane strain steady-state motion of an inclined smooth rigid plate.

(3) The steady state solution applies for any value of velocity $U > 0$. In particular it thus covers the incipient failure case with a velocity field perfectly satisfied. The latter has only recently been considered by Soil Mechanics workers.

II-2-2. Perfect plasticity solution

As mentioned earlier the problem has an infinite number of possible solutions with regard to the shape of the plastic domain. However all these solutions give the same stresses at the interface, a fact that justifies considering a problem which would otherwise be practically meaningless. Each of the solutions has its proper velocity field and may be classified into one of two main types:

(1) The Hill-type of failure, Fig. II-32, where the plastic zone occupies two distinct domains with one singular point C in common. The point C lies between A and B, the distance AC is called L_R (the rear length) which can take any value in the range $0 \leq L_R \leq L$. The special cases of $L_R = 0$, the front failure; and $L_R = L$ the rear failure, are shown in Fig. II-33.

(2) The Prandtl-type failure is shown in Fig. II-34 and is the one given by Broms [39] for the special case of $\delta = \pi/2$.

In either type of failure no air gaps were introduced in the solution, i.e. the plate is completely embedded in the rigid-plastic space at all times.

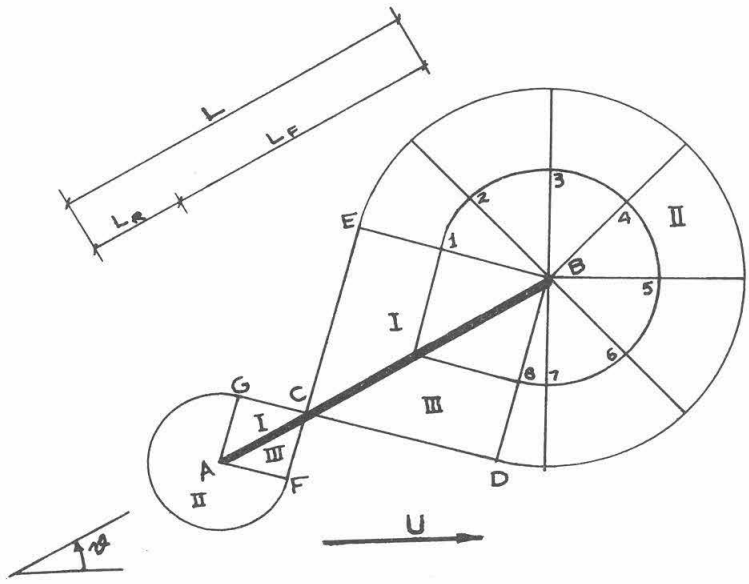

Fig. II-32. Physical plane in a Hill-type of failure mechanism.

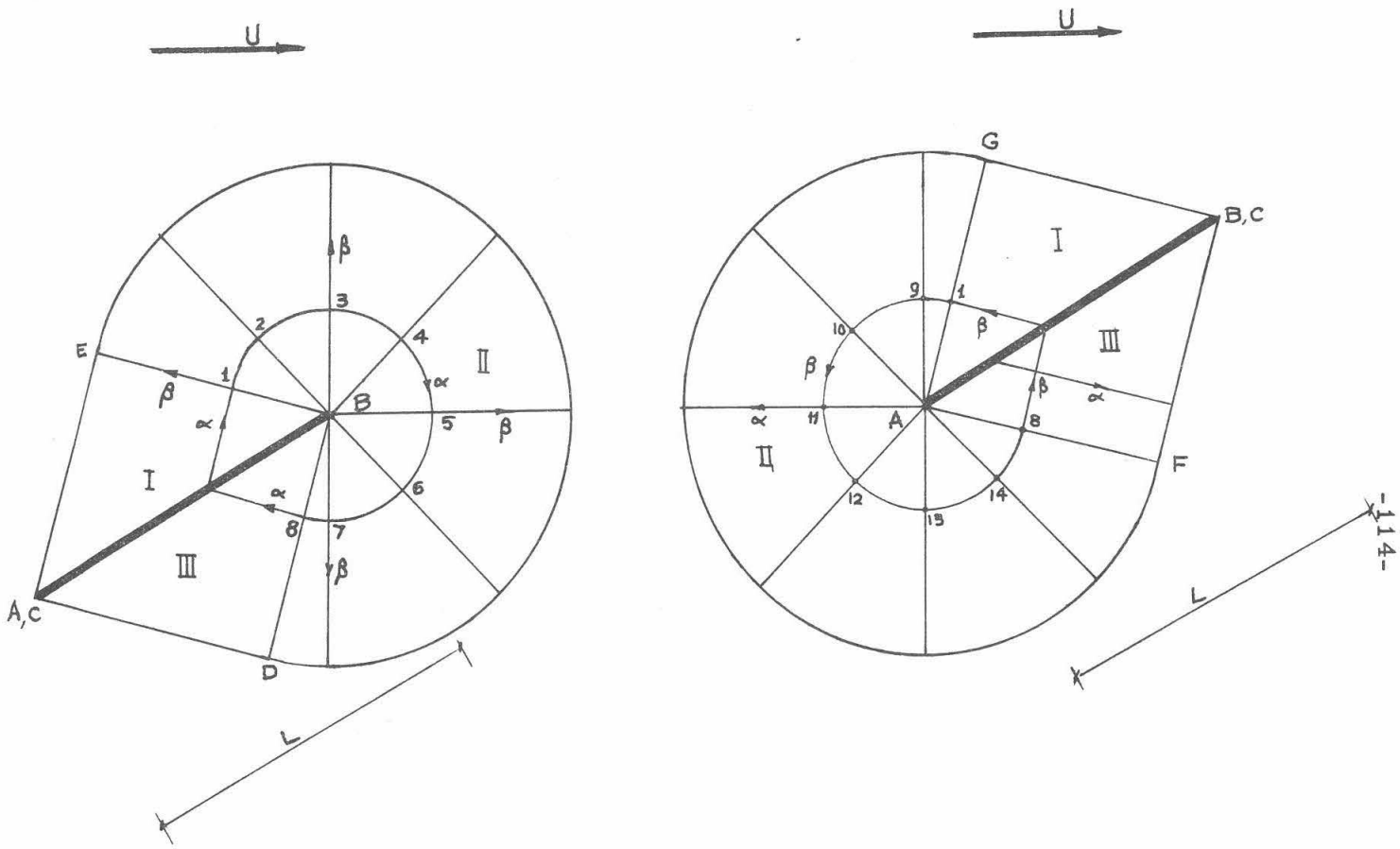

(a) Front failure, $L_R = 0$

(b) Rear failure, $L_R = L$

Fig. II-33. Special cases of a Hill-type of failure.

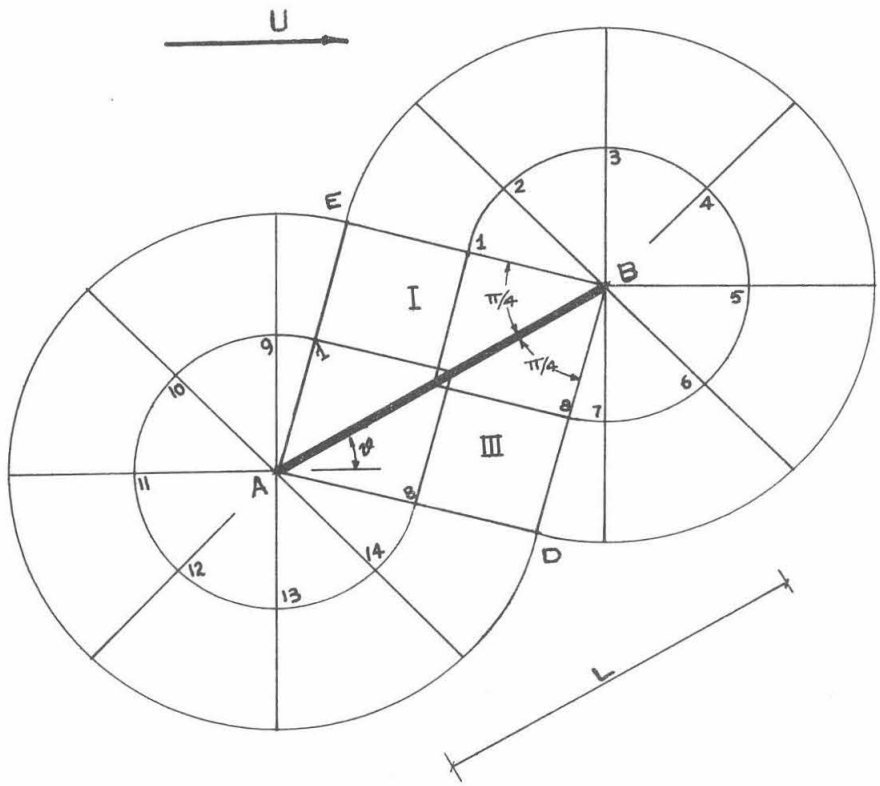

Fig. II-34. Physical plane in a Prandtl-type of failure mechanism.

The physical planes corresponding to each type of failure pattern are shown in Figs. II-32, II-33 and II-34. Each individual plastic domain consists of three distinct zones.

Zone I is a triangle in which both families of characteristics are straight. The hypotenuse of the triangle is equal to either L_R, $L - L_R$ or L depending on the type of failure.

Zone II is a circular fan centered either at A or B with a central angle equal to $3\pi/2$, i.e. the α-lines are radial and the β-lines are circular arcs or vice versa

Zone III is a triangle in which both families are straight; it is an image of zone I with respect to the plate.

The stress plane for all types of failure is shown in Fig. II-35. The upper diagram is the mapping of the front failure zone and the lower one the mapping of the rear failure zone. The origin of the Mohr diagram was located by assuming that the pressure along the back of the plate is zero. The orthogonality between any circular arc in Fig. II-33 such as 12345678, an α-line, and its cycloidal image 1'2'3'4'5'6'7'8' in Fig. II-35 is clearly satisfied. The normal stress along the surface of the plate was found to be:

$$p = 2k\left(\frac{3\pi}{2} + 1\right) \tag{9}$$

The shearing stresses along the interface, as assumed, are zero. Integrating the stresses along the length of the plate, the forces of drag (horizontal) and lift (vertical) acting on the plate are:

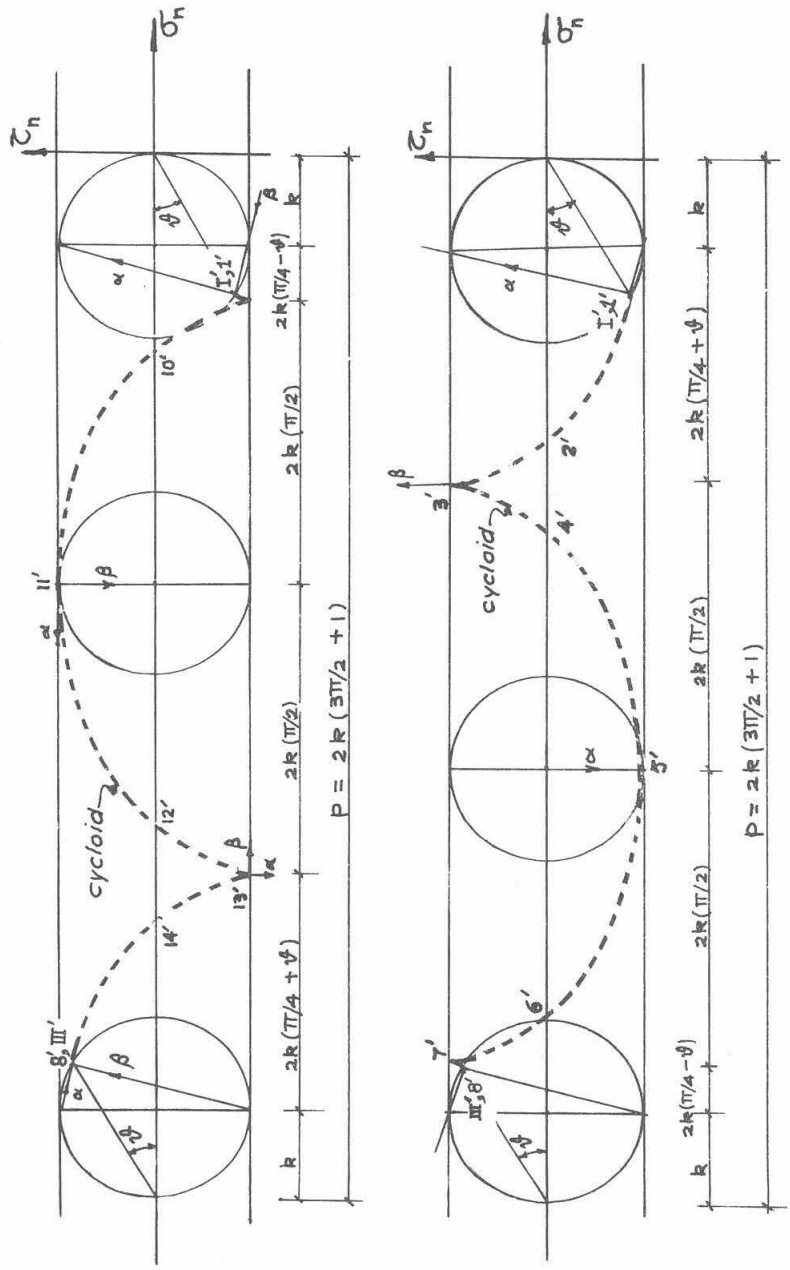

Fig. II-35. Stress plane for a smooth plate moving in an entire space.

$$\left.\begin{aligned} H &= (3\pi + 2)kL \sin \delta \\ P &= (3\pi + 2)kL \cos \delta \end{aligned}\right\} \qquad (10)$$

In case the pressure along the back of the plate is non-zero, it is not possible to deduce it from solutions of this type. However, equations (9) and (10) will still hold with p, H, P now being re-defined in terms of the difference between the front and back pressures on the plate; the quantities one would generally be interested in.

The hodographs are shown in Figs. II-36 and II-37. In both diagrams, the origin is taken at O, the image of the static space outside the plastic zone. The rigid plate moving with velocity U is mapped into P a distance U to the right of O. After choosing the numbering scheme shown in figures, the front and rear plastic zones map into the same points in the hodograph.

The velocity field of a Hill-type failure is shown in Fig. II-36. The main points in drawing the hodograph are:

(1) The smoothness of the plate allows a jump in the tangential velocity between the plate and the rigid parts I and III. It thus follows that I" and III" must lie on a line through P at an angle δ with the horizontal. Furthermore, due to the presence of the material in a rigid state outside the plastic domain, I and III can only move in directions of $(\frac{3\pi}{4} - \delta)$ and $(\frac{\pi}{4} - \delta)$ respectively with the horizontal. The location of I" and III" is thus determined.

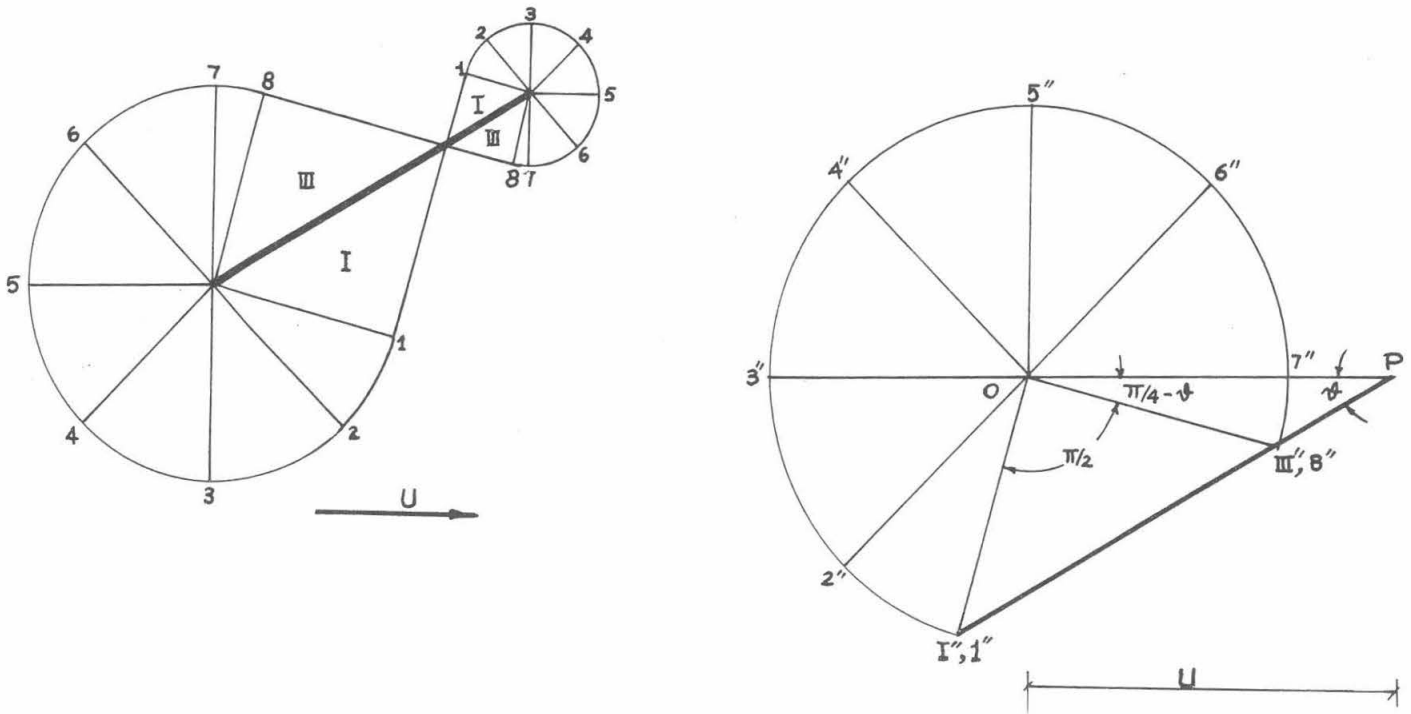

(a) Physical plane

(b) Hodograph

Fig. II-36. Velocity field in Hill-type failure mechanism.

(2) In zone II a circular arc with arbitrary radius such as 12345678, is mapped into the circular arc 1"2"3"4"5"6"7"8". Points 1" and 8" coincide with I" and III" respectively and the orthogonality condition is satisfied.

(3) To satisfy the condition of a steady state we only need to show that, in the conjugate problem, zones I and III move parallel to the plate, i.e. at an angle δ with the horizontal. It is immediately clear from the hodograph, with the origin now at P, that the segments $\overline{PI"}$ and $\overline{PIII"}$ satisfy this condition.

The velocity field for a Prandtl-type of failure is given by the hodograph in Fig. II-37; the main points for drawing the diagram are:

(1) Due to the smoothness of the plate, the points I" and III" lie on a line through P at an angle δ to the horizontal. The presence of the rigid static material outside the plastic domain implies that points 1 and 8, lying in zone II, must have velocities perpendicular to AD and BD (or BE and AE) respectively; i.e. $\overline{O1"}$ and $\overline{O8"}$ need make angles $(\frac{3\pi}{4} - \delta)$ and $(\frac{\pi}{4} - \delta)$ with the horizontal. Furthermore the jump of velocity between zone I and II, if present, needs to be parallel to a characteristic, which implies that $\overline{I"1"}$ and $\overline{I"8"}$ be parallel to $\overline{AD}$ and BD respectively, i.e. I"8" is orthogonal to O8" and $\overline{I"1"}$ is orthogonal to $\overline{O1"}$.

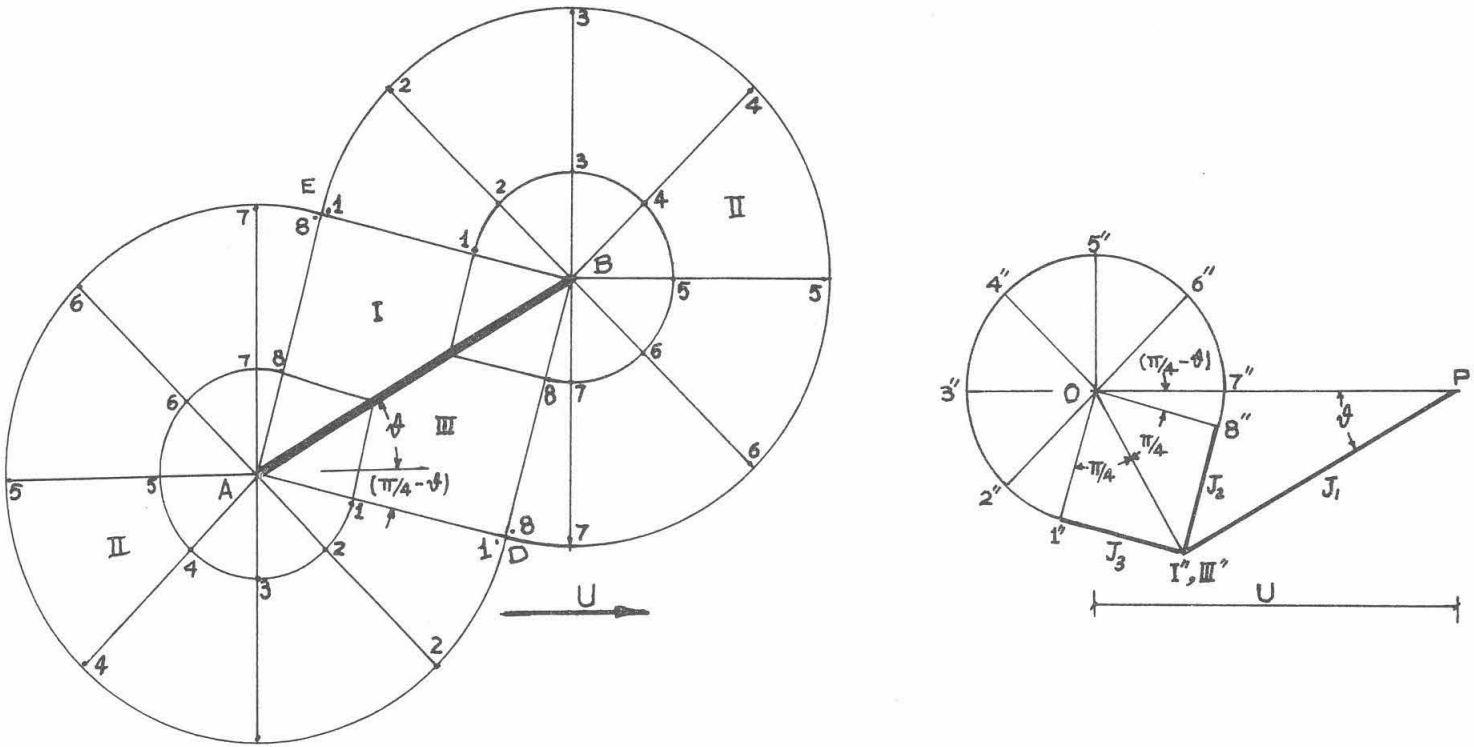

(a) Physical plane

(b) Hodograph

Fig. II-37. Velocity field in Prandtl-type failure mechanism.

To satisfy the above conditions points I", 1" and 8" are located uniquely as shown in Fig. II-37. A similar argument will show that III" must coincide with I".

(2) The orthogonality and the steady state conditions follow the same lines as for Hill-type of solution and are satisfied.

Now that the problem has been solved, one can easily get the stream lines of particles as they move past the plate in the conjugate problem. The stream lines will give a good idea of the process of deformation and are in many applications of crucial importance, e.g. in the study of heat transfer problems. The stream lines are shown in Figs. II-38, II-39 and II-40. Moreover, the distortion of vertical lines as they move past the plate are drawn in Fig. II-39. To draw all those diagrams, the graphical technique was used knowing the velocity at every point. Bearing this in mind, one should consider these figures as a rough indication of the deformation process to get an idea of the order of magnitude of the permanent deformation. It is not recommended that they be used to deduce results requiring accuracy such as the determination of the slopes of the distorted originally vertical lines.

To further study the permanent deformation in a Hill-type of failure for any value of L_R with the range $0 \leq L_R \leq L$, it is sufficient to consider the two special cases of $L_R = 0$ and $L_R = L$. This is because the permanent deformations of a plastic material going through two consecutive and separate plastic domains are additive. The incompressibility of the material and the continuity

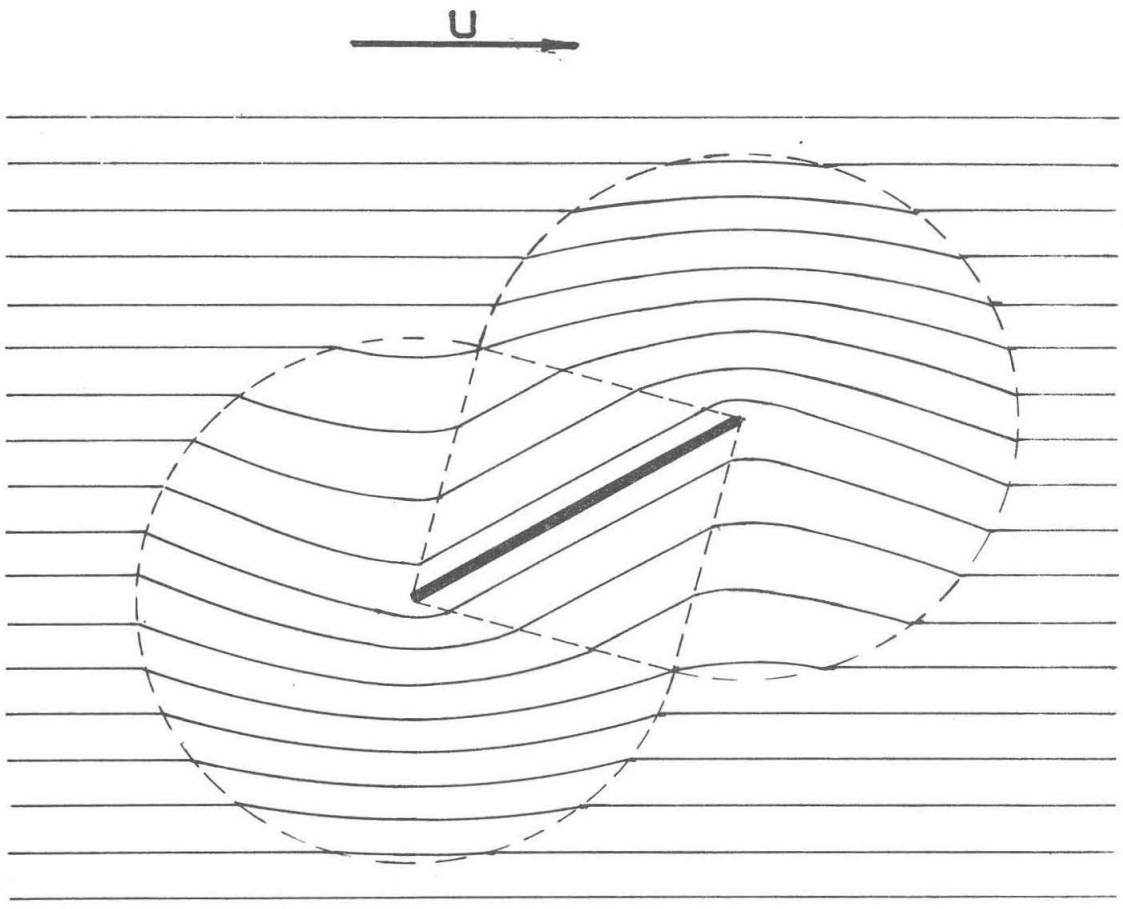

Fig. II-38. Stream lines in a Prandtl-type of failure.

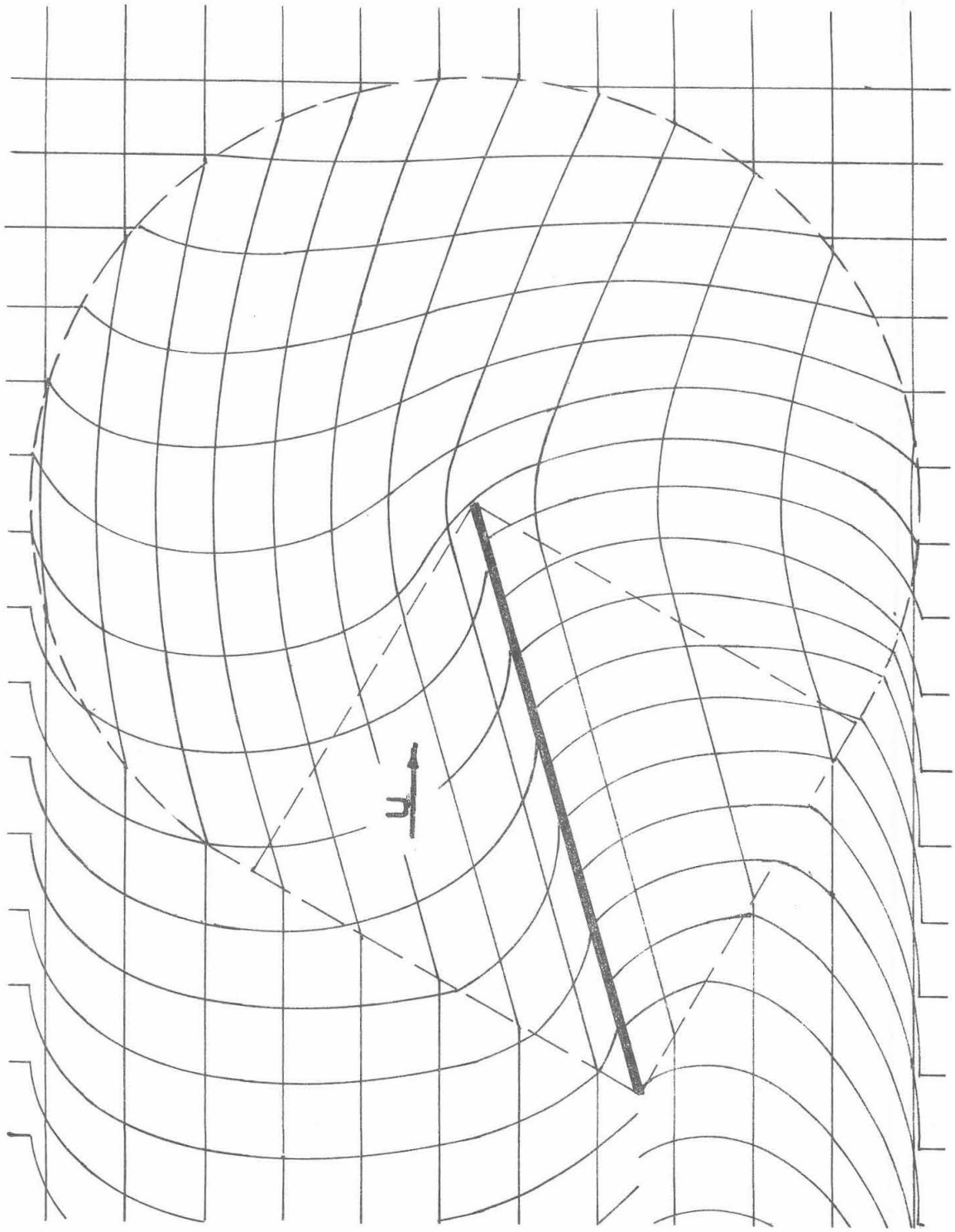

Fig. II-39. Distortion of a square grid in a front failure pattern.

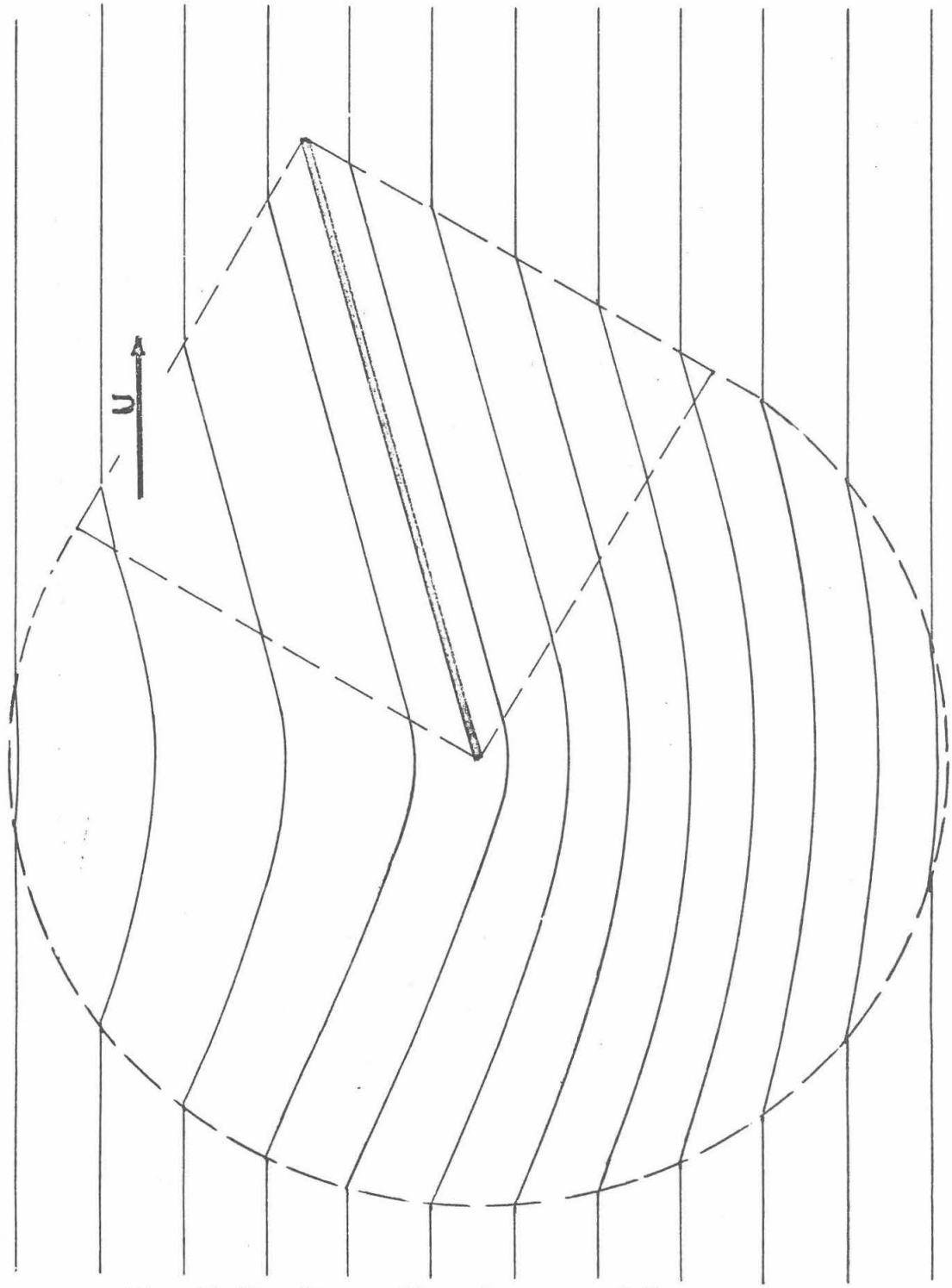

Fig. II-40. Stream lines in a rear failure pattern.

imply that the permanent vertical displacement must vanish. Let $\delta(y)$ be the permanent horizontal displacement, taken positive when in the direction of the velocity U, at a distance y above the mid-length of the plate. Fig. II-41 shows $\delta(y)$ for a plate inclined by an angle $\beta = 15^{o}$ to the direction of motion. Using the superposition of $\delta(y)$ caused by different plastic fields, and with the proper scaling, Fig. II-42 was drawn as an example for $L_R = 0.5L$.

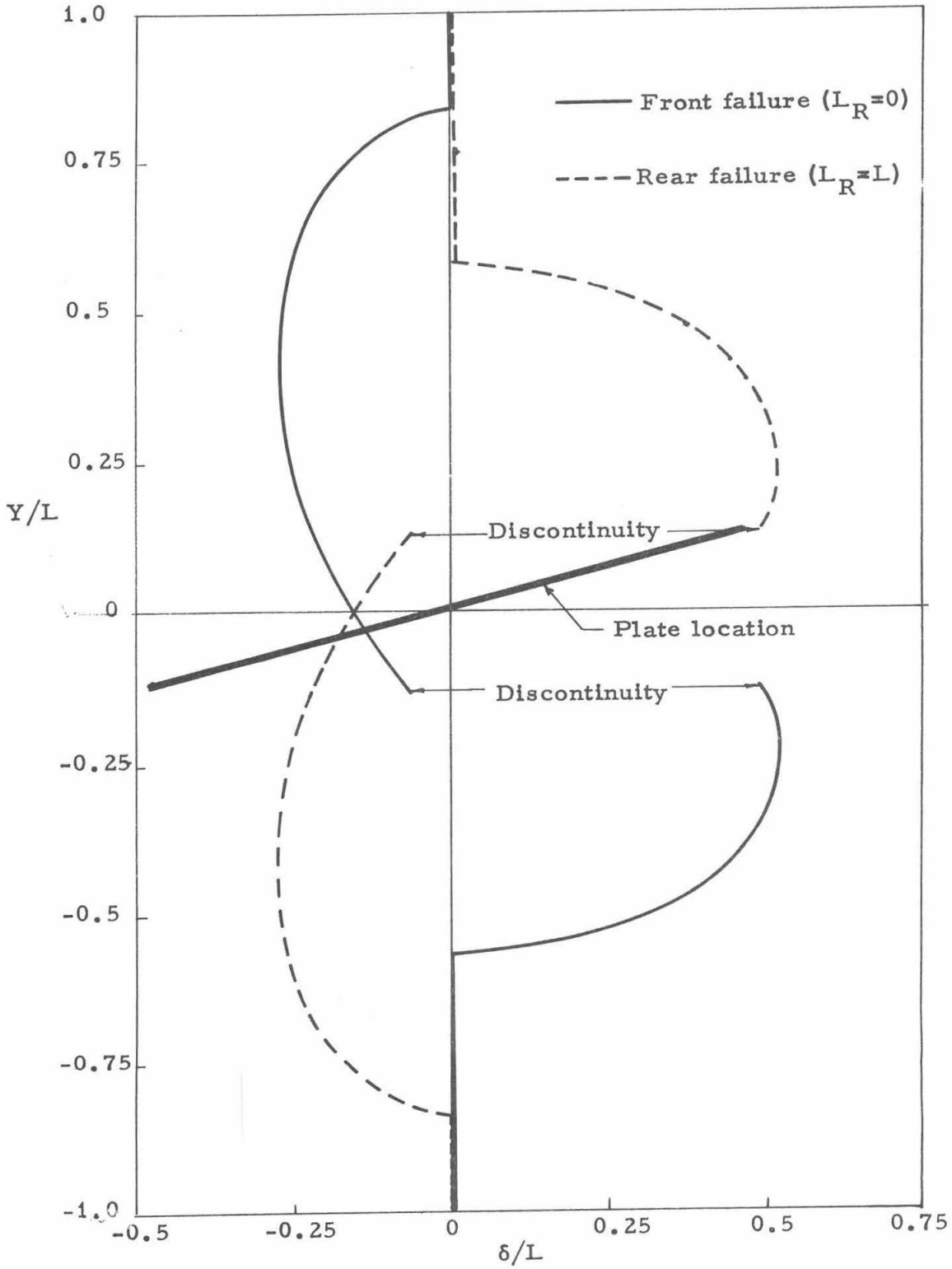

Fig. II-41. Permanent deformation of a vertical line in a Hill-type failure mechanism, $\delta = 15^{o}$.

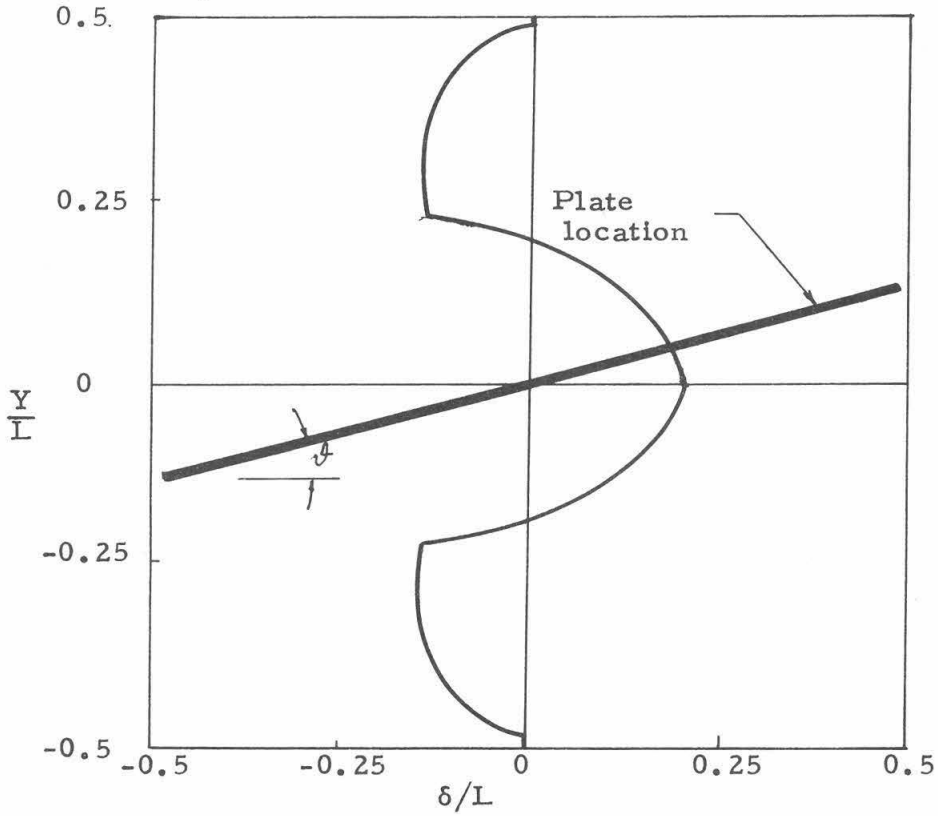

Fig. II-42. Permanent deformation of a vertical line in a Hill-type failure mechanism ($\vartheta = 15^{\circ}$ and $L_R = L/2$).

REFERENCES OF CHAPTER II

1. Prandtl, L., "Ueber die Haerte Plastischer Koerper," Goettinger Nachr., math.-phys. K1, 1920, p. 74.

2. Hill, R., The Mathematical Theory of Plasticity, Oxford University Press, 1950, p. 254.

3. Shield, R. T., "On the Plastic Flow of Metals under Conditions of Axial Symmetry," Proc. Roy. Soc. Lon. Series A, Vol. 233, 1955, p. 282.

4. Hill, R., Lee, E. H. and Tupper, S. J., "The Theory of Wedge Indentation of Ductile Materials," Proc. Roy. Soc. Lon. Series A, Vol. 188, 1947, p. 273.

5. Grunzweig, J., Longman, I. M., and Petch, N. J., "Calculations and Measurements on Wedge-indentation," Jour. Mech. Phys. Solids, Vol. 2, 1952, p. 81.

6. Lockett, F. J., "Indentation of a Rigid/Plastic Material by a Conical Indenter," Jour. Mech. Phys. Solids, Vol. 11, 1963, pp. 345-355.

7. Dugdale, D. S., "Wedge Indentation Experiments with Cold Worked Metals," Jour. Mech. Phys. Solids, Vol. 2, 1953, p. 14.

8. Dugdale, D. S., "Cone Indentation Experiments," Jour. Mech. Phys. Solids, Vol. 2, 1954, p. 265.

9. Dugdale, D. S., "Experiments with Pyramidal Indenters," Jour. Mech. Phys. Solids, Vol. 3, 1955, p. 197.

10. Samuels, L. E. and Mulhearn, T. O., "An Experimental Investigation of the Deformed Zone Associated with Indentation Hardness Impressions," Jour. Mech. Phys. Solids, Vol. 5, 1957, pp. 125-134.

11. Hirst, W. and Howse, M. G., "The Indentation of Materials by Wedges," Proc. Roy. Soc. Lon. Series A, Vol. 311, 1969, p. 429.

12. Atkins, A. G. and Tabor, D., "Plastic Indentation in Metals with Cones," Jour. Mech. Phys. Solids, Vol. 13, 1965, p. 149.

13. Bishop, R. F., Hill, R. and Mott, N. F., "The Theory of Indentation and Hardness Tests," Proc. Phys. Soc. Vol. 57, 1945, p. 147.

14. March, D. M., "Plastic Flow in Glass," Proc. Roy. Soc. Lon. Series A, Vol. 279, 1964, p. 420.

15. Johnson, K. L., "The Correlation of Indentation Experiments," Jour. Mech. Phys. Solids, Vol. 18, 1970, pp. 115-126.

16. Gibson, R. E., "Discussion," Jour. Institution of Civil Engineers, Vol. 34, 1950, p. 382.

17. Chadwick, P., "The Quasi-static Expansion of a Spherical Cavity in Metals and Ideal Soils," Quarterly Journal of Mechanics and Applied Mathematics, Vol. 12, Part 1, 1959, p. 52.

18. Skempton, A. W., Yassin, A. A. and Gibson, R. E., "Theorie de la force partante des pieux," Journeés de Mécamque des Sols, Annales du Botiment et des Travaux Publics de Belgique, Vol. 62, 1961, pp. 105-148, 365-406.

19. Vesic, A. S., "Expansion of Cavities in Infinite Soil Mass," Journal of the Soil Mechanics and Foundations Division, ASCE, Vol. 98, No. SM3, March 1972, p. 265.

20. Terzaghi, K., Theoretical Soil Mechanics, John Wiley and Sons, Inc., New York, 1943.

21. Meyerhof, G. G., "The Bearing Capacity of Foundations," Geotechnique Vol. 2, 1951, p. 301.

22. Eastwood, W. and Anagnostou, V., "The Effect of Base Shape on the End Bearing Capacity of Piles in Granular Soils," Civil Engineering and Public Works Review, Dec. 1967, p. 1543.

23. De Mello, V., "Foundations of Buildings in Clay," State of the Art Volume, Seventh Int. Conf. on Soil Mech. and Foundation Engineering, Mexico, 1969, p. 49.

24. Mensenbach, E., "The Determination of the Permissible Point-load of Piles by Means of Static Penetration Tests," Proceedings of the 5th Int. Conf. on Soil Mech. and Foundation Engineering, Vol. II, 1961, p. 99.

25. Berezantzev, V. G., "Design of Deep Foundations," Proceedings of the 6th Int. Conf. on Soil Mech. and Foundations Engineering, Vol. 2, 1965, p. 234.

26. Skempton, A. W., "The Bearing Capacity of Clays," Building Research Congress, London. The Inst. of Civil Eng. Div. I, 1951, p. 130.

27. DeBeer, E. E., "The Scale Effect in the Transposition of the Results of Deep-sounding Tests on the Ultimate Bearing Capacity of Piles and Caisson Foundations," Geotechnique, Vol. 13, No. 1, March 1963, p. 39.

28. Morgan, J. R. and Poulos, "Stability of Deep Foundations," Soil Mechanics, Selected Topics, Lee, I. K., Ed., Elsevier, N. Y., 1968, p. 578.

29. Tomlinson, H. J., "The adhesion of Piles Driven in Clay Soils," Proc. 4th Int. Conf. Soil Mech., Vol. 2, 1957, p. 66.

30. Sharman, F. A., "The Anticipated and Observed Penetration Resistance of Some Friction Piles in Clay," Proc. 5th Int. Conf. Soil Mech., Vol. 21, 1961, p. 135.

31. Scott, R. F. and Schoustra, J. J., Soil Mechanics and Engineering, McGraw Hill, Inc., 1968, p. 205.

32. Ellison, P. D., D'Appolonia, E., and Thiers, G. R., "Load Deformation Mechanism for Bored Piles," Journal of the Soil Mechanics and Foundations Division, ASCE, Vol. 98, April 1971, p. 661.

33. Bowden, F. and Tabor, D., The Friction and Lubrication of Solids, Clarendon Press, Oxford, 1964.

34. D'Appolonia, E. and Ronualdi, J. P., "Load Transfer in End-bearing Steel H-piles," Proc. Am. Soc. Civ. Eng. 89SM2, 1963, p. 1.

35. Whitaker, T. and Cooke, R. W., "An Investigation of the Shaft and Base Resistances of Large Bored Piles in London Clay," Proc. Symp. Large Bored Piles, London, 1966.

36. Hoëg, K., "Finite Element Analysis of Strain-Softening Clays," Journal of Soil Mechanics and Foundations Division, ASCE, Vol. 98, No. SM1, Jan. 72, p. 47.

37. Vesic, A. S., "A Study of Bearing Capacity of Deep Foundations," Georgia Inst. of Technology, Atlanta, March, 1967.

38. Vesic, A. S., "Ultimate Loads and Settlements of Deep Foundations in Sand," Proc. Symposium on Bearing Capacity and Settlement of Foundations, Duke Univ. Durham, N.C., 1967, p. 53.

39. Broms, B. B., "Lateral Resistance of Piles in Cohesive Soils," Journal of Soil Mechanics and Foundations Division, ASCE, Vol. 90, No. SM2, March 1964, p. 27.

CHAPTER III

PLANE STRAIN INDENTATION OF A RIGID-PERFECTLY PLASTIC HALF-SPACE

This chapter deals with two problems in plane strain perfect plasticity. The first we call the ironing plate is a steady state solution for a plate moving parallel to the surface of a half space. The second is the incipient failure solution of a cylinder indenting a wedge of a particular shape. The two problems, in addition to being examples in the use of perfect plasticity, are the fundamental solutions for the rolling theory treated in chapter IV.

III-1. The ironing plate problem

Consider the plane strain problem of a rigid smooth plate moving with a constant velocity U parallel to the surface of a rigid-perfectly plastic half space, Fig. III-1. The plate is inclined by an angle δ, $(0 < \delta < \pi/4)$, to the horizontal and its lowest point is at the same level of the surface of the half space. A heap ahead of the plate acts with the half space as a continuum and has a contact length L with the plate. It is required to find a steady-state solution to the problem, i.e. find the stress and velocity fields in the half space complying with the field equations and yielding a constant shape for the heap at all times.

In accordance with perfect plasticity techniques, the shape of the heap has first to be assumed and then the field equations checked. Several trials led to the symmetric shape in Fig. III-2; it will be shown to satisfy the steady-state conditions.

III-1-1. The stress field

In Fig. III-2 for $0 < \delta < 45^{\circ}$ a stress field is shown. The geometrical symmetry about the vertical through B is assumed, then AB = BE = L.

Zone I is determined by the triangle ABC - has both families of characteristics straight.

Zone II is determined by the triangle BDE - has both families of characteristics straight.

Zone III is determined by the circular fan CBD - has the β-lines straight and the α-lines consisting of circular

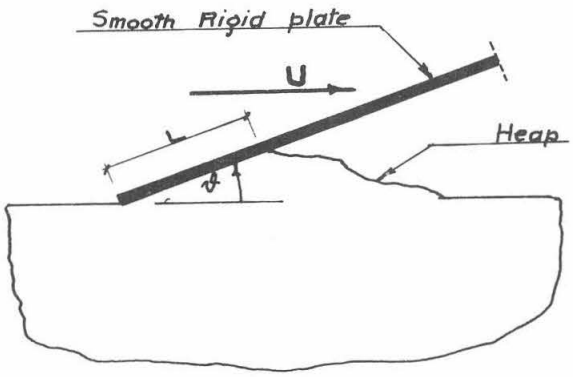

Fig. III-1. The ironing plate problem.

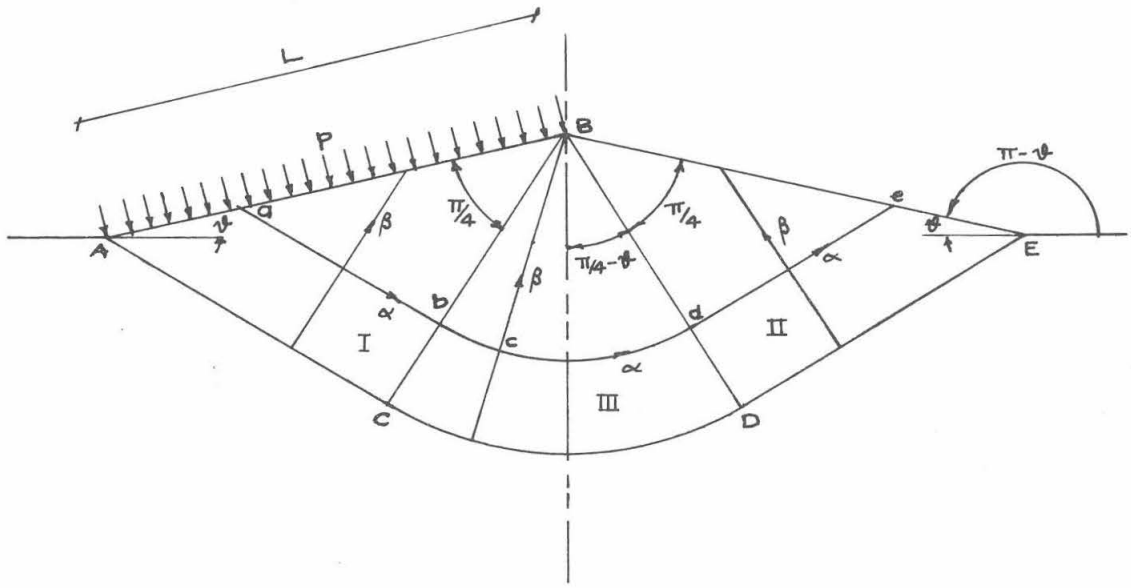

Fig. III-2. Physical plane for the ironing plate.

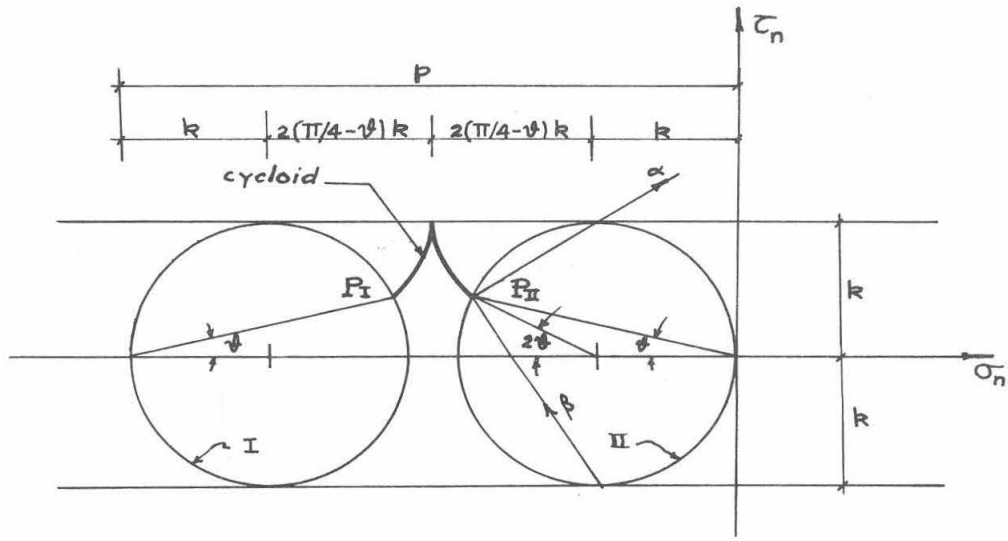

Fig. III-3. Stress plane for the ironing plate.

arcs.

The field satisfies the "Hencky-Prandtl" net requirements and is thus permissible. Since all β-lines are straight, then no variation of stresses along β-lines is present. In Zones I and II, the α-lines are also straight, thus the state of stress in both zones is constant. Knowing that the surface BE is stress free, and that the path of the pole is a cycloid in Mohr diagram, a graphical construction of the solution is given in Fig. III-3.

Let p be the contact pressure at the interface, ϑ the counterclockwise slope of the plate to the horizontal and k the yield stress in shear, then

$$p = (\pi + 2 - 4\vartheta)k \qquad (1)$$

III-1-2. The velocity field

Let the plate be moving to the right with a constant velocity U, Fig. III-4. The velocity field is fully described by the hodograph in Fig. III-5. The nonplastic zone outside ABEDC is at rest and thus located at the origin O of the hodograph. The plate being smooth, a jump in velocity J between the plate and the adjacent material is permissible and was assumed to exist.

To satisfy the requirement of incompressibility of the material, the hodograph should be such that along slip lines the images of corresponding points in the physical plane and the hodograph be orthogonal. This is easily checked by noting that

- Zones I and II which in Fig. III-4 have straight slip lines move as rigid bodies and thus have their corresponding

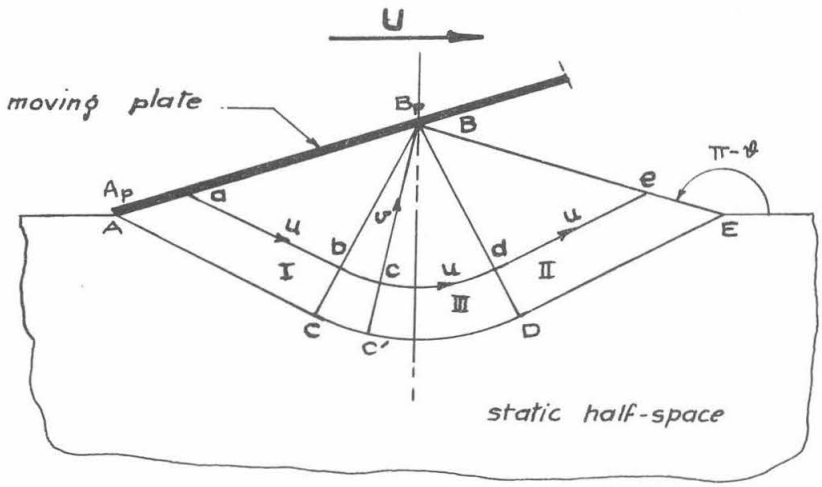

Fig. III-4. The velocity field for the ironing plate.

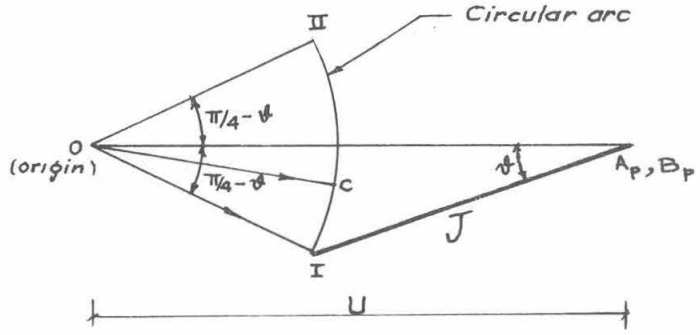

Fig. III-5. Hodograph for the ironing plate.

images at points I and II respectively, Fig. III-5. Zone I moves parallel to AC and Zone II parallel to DE thus directions O I and O II are determined.

- For Zone III we consider any α-line such as bcd with BC' the β-line through c. BC' being straight, then velocity v along β-line is constant; and since v at C' is zero, then all velocities in Zone III are tangential, i.e., along α lines. Moreover, the velocities u, along any α-line, are constant. Zone III is now fully determined by arc I - II centered at O in hodograph, the velocity at any point c along BC' is given by the vector OC in hodograph where OC is perpendicular to BC' and C lies on arc I - II.

The analytic derivation of the above statements is carried out in part III-1-3 where energy is treated). From the previous treatment, the proposed fields of stresses and velocities are instantaneously satisfied. Now it remains to prove continuity in the sense that this velocity field yields a solution that will maintain the geometry unaltered at any time. For this, a necessary and sufficient condition is that the free surface BE remains straight and at an angle $(\pi - \delta)$ with the horizontal. Necessity being clear from boundary changes and sufficiency by the use of incompressibility. It is difficult however in the present formulation to check continuity; for this and to calculate plastic deformations it is better to introduce an Eulerian frame of reference moving with the same velocity U as that of the plate. The new problem later referred to as the conjugate problem, is reduced to that of a moving half space with respect to a fixed rigid

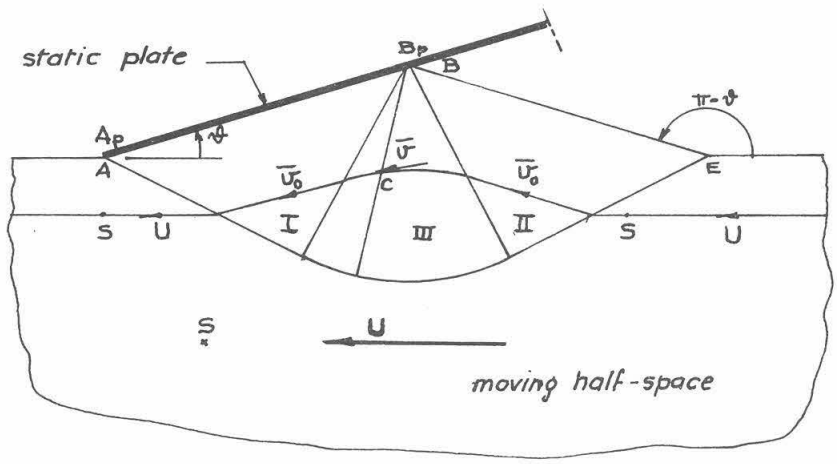

Fig. III-6. Velocity field for the conjugate ironing plate problem.

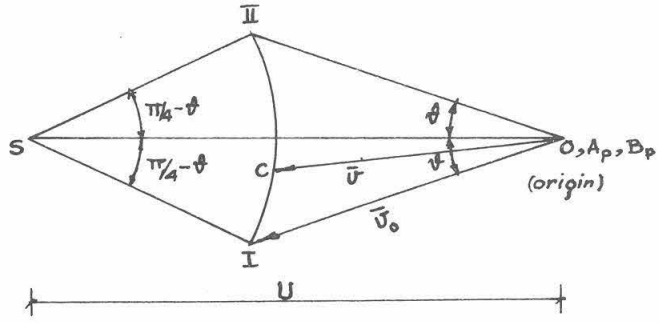

Fig. III-7. Hodograph for the conjugate ironing plate problem.

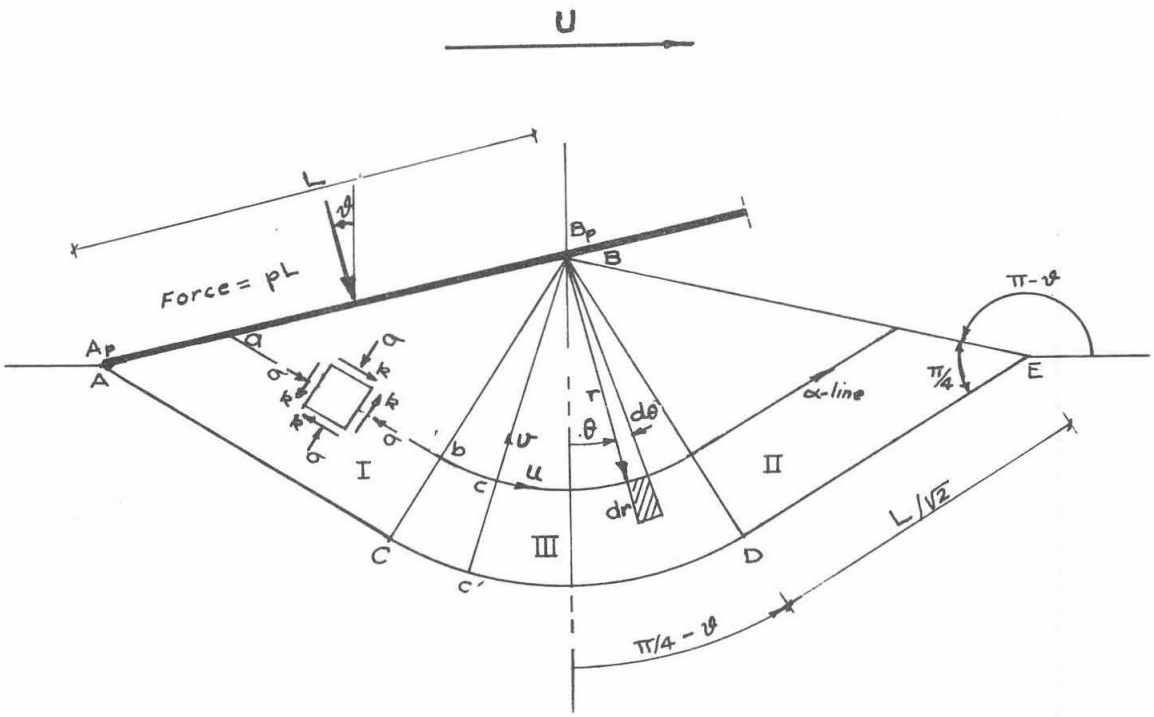

Fig. III-8. Variables for evaluating the energy dissipation.

smooth plate, and with the surface as shown in Fig. III-6. The stress field remains unchanged and is still given by Fig. III-3. The velocity field is given by Fig III-7 which differs from III-5 by a shift of the origin O by an amount U. Thus, in Fig. III-7, O, A_p, B_p coincide (A_p and B_p are points on the plate surface).

In this new setting with any point in Zone II moving parallel to BE at an angle $\pi - \delta$, to the horizontal, both conditions for continuity (BE remaining straight and at an angle $\pi - \delta$ to the horizontal) are clearly satisfied.

III-1-3. Energy considerations

We let

W_e = Power expended by external loading

W_i = Power dissipated in solid

W_{ih} = Power dissipated in solid in the form of heat

W_{id} = Power dissipated in solid in permanent distortion.

Thus,

$$W_i = W_{ih} + W_{id} \tag{2}$$

for power equilibrium

$$W_e = W_i \tag{3}$$

(1) External power

From Fig. III-8, we have

$$W_e = [pL \sin \delta] U$$

Using (1), then

$$W_e = kLU(\pi + 2 - 4\vartheta) \sin \vartheta \qquad (4)$$

(2) Internal power

1. Internal power of distortion

With u and v the velocities along α and β lines respectively, Fig. III-8, thus with θ being the counterclockwise angle between the α-line and the horizontal

$$\left.\begin{aligned} du &= v\, d\theta \text{ along } \alpha\text{-line} \\ dv &= -u\, d\theta \text{ along } \beta\text{-line} \end{aligned}\right\} \qquad (5)$$

In Zone I and II, we have

$$d\theta = 0, \text{ thus, using (5), } du = dv = 0;$$

which, in turn means that in both zones

$$W_{id} = \int_{vol} \sigma_{ij} \dot{\epsilon}_{ij}\, dV = 0$$

In Zone III

Along β lines $d\theta = 0$, then using (5) v = constant along β line and since v = 0 at C', then

$$v \equiv 0 \quad \text{in zone III.} \qquad (6)$$

(A result that directly follows from Fig. III-5).

Using (5), thus u = constant along α lines, and since u is constant along BC, then u = constant in zone III. (7)

Taking polar coordinates (r, θ) for region III as in Fig. III-8, then using (6) and (7)

$$\dot{\epsilon}_{rr} = \dot{\epsilon}_{\theta\theta} = \frac{\partial u}{\partial r} = \frac{\partial v}{\partial \theta} = 0$$

then (8)

$$\dot{\gamma}_{r\theta} = 2\dot{\epsilon}_{r\theta} = \frac{\partial u}{\partial r} + \frac{1}{r}\frac{\partial v}{\partial \theta} - \frac{u}{r} = -\frac{u}{r}$$

(The negative sign corresponds to negative shearing stresses).

From hodograph in Fig. III-5, we have

$$u = U\sqrt{2}\sin\vartheta \tag{9}$$

Using the condition of plane strain ($\epsilon_{zz} = 0$) together with (8) and (9)

$$\therefore \frac{\text{strain energy}}{\text{unit time}} \Big/ \text{unit volume} = \sigma_{ij}\dot{\epsilon}_{ij} = \sigma_{r\theta}\dot{\gamma}_{r\theta} = -k\dot{\gamma}_{r\theta}$$

$$= k\frac{U\sqrt{2}\sin\vartheta}{r}$$

$$W_{id} = \int_{vol} \sigma_{ij}\dot{\epsilon}_{ij}\, dv$$

$$= 2\int_0^1 \left[\int_0^{L/\sqrt{2}} \int_0^{\frac{\pi}{4}-\vartheta} \frac{kU\sqrt{2}\sin\vartheta}{r}\, r\, dr\, d\theta\right] dz$$

$$W_{id} = kLU\left(\frac{\pi}{2} - 2\vartheta\right)\sin\vartheta \tag{10}$$

2. Heat power of dissipation

The power released at discontinuities of velocity where shearing stresses are acting is considered to be dissipated in the form of heat.

In our problem, the discontinuities occur along the boundaries AB, AC, CD, DE. Along AB, the surface of the plate previously assumed to be smooth gives no energy dissipation.

Along the other boundaries which are an α-line, the shearing stresses are equal to k and the velocity is constant and equal to u.

Knowing that $AC = DE = \frac{L}{\sqrt{2}}$

and arc $CD = \frac{L}{\sqrt{2}} \left(\frac{\pi}{2} - 2\vartheta \right)$ (11)

and exterior material is static

then using (9) and (11):

$$W_{ih} = KLU \left[2 + \frac{\pi}{2} - 2\vartheta \right] \sin \vartheta \tag{12}$$

(2), (10) and (12) imply

$$W_i = kLU \left[\pi + 2 - 4\vartheta \right] \sin \vartheta \tag{13}$$

We note that (4) and (13) satisfy (3) and power is equilibrated. Dividing (10) by (13) and using (3), thus

$$\frac{W_{id}}{W_i} = \frac{W_{id}}{W_e} = \frac{\frac{\pi}{2} - 2\vartheta}{\pi + 2 - 4\vartheta}$$

For small ϑ, neglecting higher orders, thus

$$\frac{W_{id}}{W_e} \simeq \frac{\pi}{2(\pi + 2)} \simeq 0.306$$

i.e. the energy of distortion is about 30% of the total energy dissipated.

III-1-4. Distortion of a square grid

To evaluate the distortion of a square grid we shall compute the time $\frac{T}{2}(y)$ required for a particle at a height y above level $B'E'$,

in Fig. III-9, starting from the plane EE' (or $x = 0$) to reach BB' (or $x = L \cos \delta$) in the conjugate problem.

Using the symmetry of Figs. III-6 and III-7 we can directly deduce that

- No vertical distortion is present.
- The material below B'E' is left undisturbed, thus

$$T_o = T\big|_{y<0} = \frac{2L \cos \delta}{U} = \text{constant} \qquad \text{(i)}$$

- For δ denoting the total horizontal distortion of an originally vertical line in the direction of U (direction of -x in Fig. III-9). Then

$$\delta(y) = [\, T(y) - T_o \,] U$$

Using (i)

$$\delta(y) = \left[T(y) - \frac{2L \cos \delta}{U} \right] U \qquad \text{(ii)}$$

- From the hodograph Fig. III-10, the following velocity relations are deduced

$$\left(\frac{\overline{v}}{U}\right)^2 = 1 + 2 \sin^2 \delta - 2\sqrt{2} \sin \delta \cos \theta \qquad \text{(iii)}$$

where $\overline{v} \equiv \overline{v}(\theta) \equiv$ velocity of a particle at location θ in region BB'DB, Fig. III-9, for $\theta = 45 - \delta$, then specializing (iii):

$$\frac{\overline{v}_o}{U} = \cos \delta - \sin \delta \qquad \text{(iv)}$$

where $\overline{v}_o \equiv \overline{v}(45 - \delta) \equiv$ velocity of a particle in region DBED.

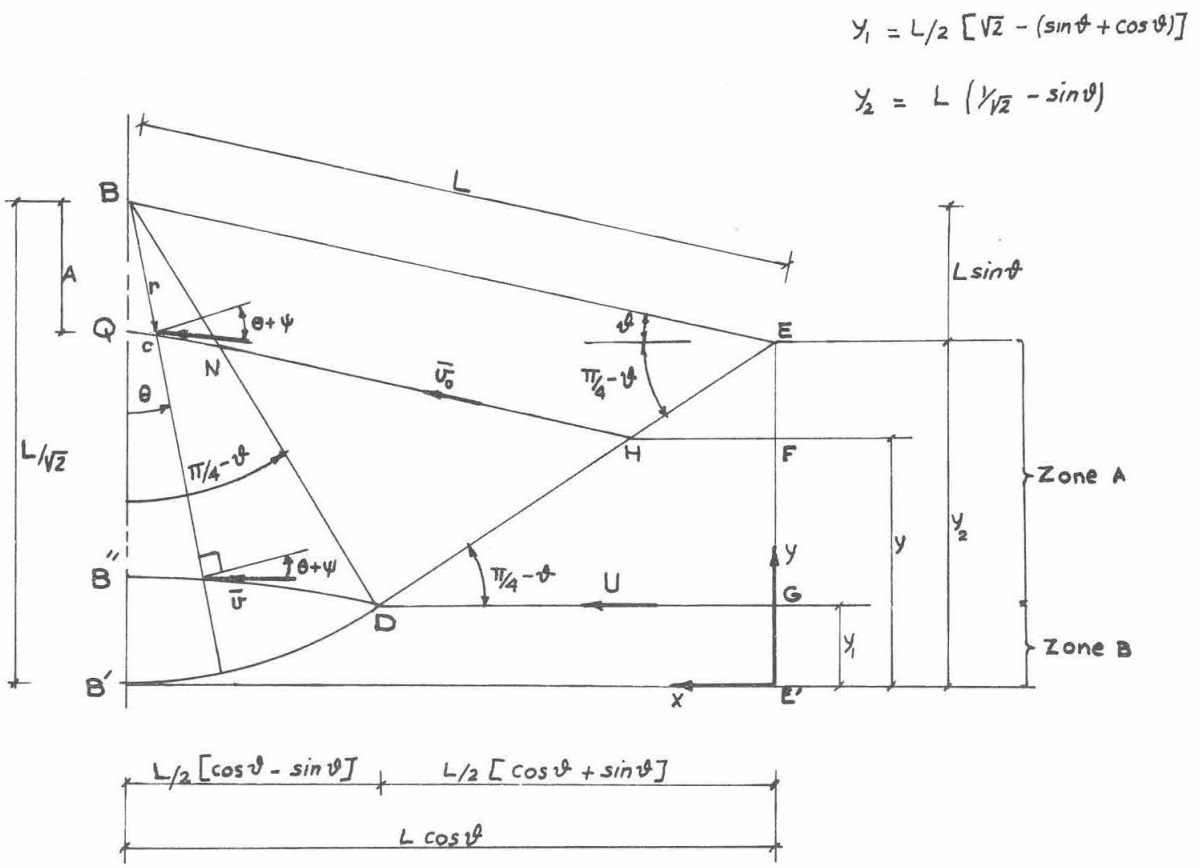

Fig. III-9. Variables for evaluating the distortion in zone A in the conjugate problem.

Also from Fig. III-10,

$$\bar{v}(\theta) \cos(\theta + \Psi) = U(\cos\theta - \sqrt{2}\sin\beta) \qquad (v)$$

where Ψ is the angle between the velocity direction and the positive x axis.

To get the particle path in region BB'DB, we note the independence of $\bar{v}$ on r; applying the incompressibility condition to Zone FHNCBE, with BC being the radial line at an angle θ, FHNC and BE are both stream lines and $\bar{v}$ makes an angle $(\theta + \Psi)$ to the normal to BC, then

$$\bar{v}(\theta) \cos(\theta + \Psi) \cdot r(y,\theta) = U\left[\frac{L}{2}(\sqrt{2} - 2\sin\beta) - y\right] \qquad (vi)$$

Using (v) in (vi), then

$$r(y,\theta) = \frac{\frac{L}{2}(\sqrt{2} - 2\sin\beta) - y}{\cos\theta - \sqrt{2}\sin\beta} \qquad (vii)$$

where $r(y,\theta) \equiv$ radial distance of a particle at an angle θ from BB' originally starting at a level y above B'E'.

From (vii) and with $y = y_1 = \frac{L}{2}[\sqrt{2} - (\sin\beta + \cos\beta)]$, we get the equation of B"D

$$r(\theta) = \frac{\frac{L}{2}(\cos\beta - \sin\beta)}{\cos\theta - \sqrt{2}\sin\beta} \qquad (viii)$$

Computation of T

Since particles follow two distinct types of paths we shall divide the region into two zones: Zone A, bounded by BB"GEB and Zone B, bounded by B"B'E'GB", Fig. III-9.

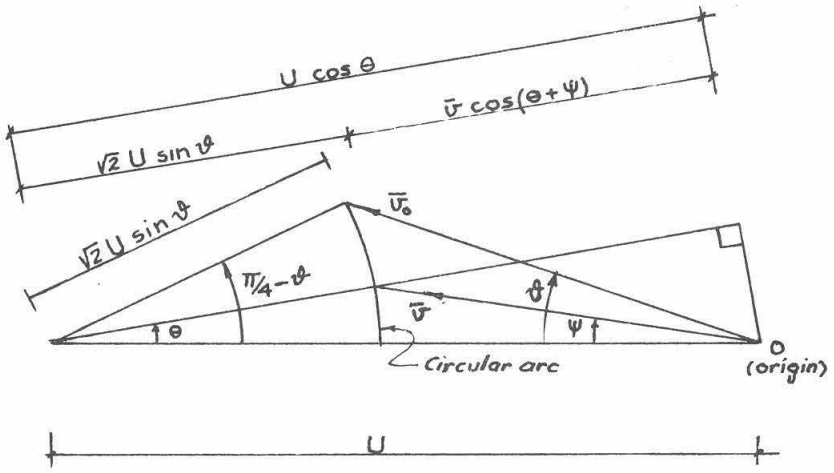

Fig. III-10. Geometric relationships in the hodograph.

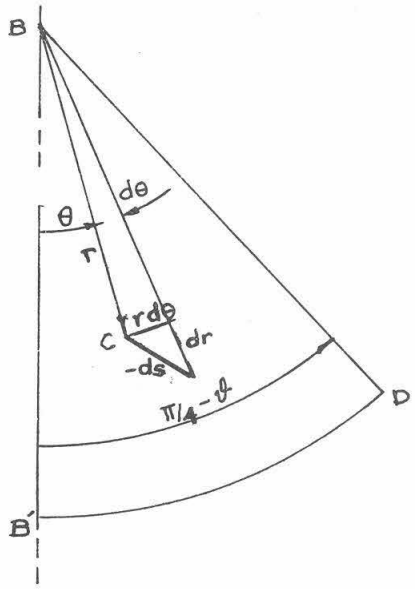

Fig. III-11. Infinitesimal length along a streamline.

Zone A: $y_1 < y < y_2$

Let s be the length along the path

Let t be the time

and for $t = 0$ we let the particle be at F with coordinates $(0, y)$, Fig. III-9,

for $t = \frac{T_1}{2}$ we let the particle be at H

for $t = \frac{T_2}{2}$ we let the particle be at N

for $t = \frac{T}{2}$ we let the particle be at Q

From F to H

the velocity is constant and equal to U and FH straight;

$$\therefore \frac{T_1}{2} = \frac{y_2 - y}{U} \cdot \frac{DG}{EG} = \frac{(y_2 - y)}{U} \tan (45 + \delta)$$

$$\therefore T_1 = \frac{2L}{U} \left[\frac{1}{\sqrt{2}} - \sin \delta - \frac{y}{L} \right] \frac{\cos \delta + \sin \delta}{\cos \delta - \sin \delta} \qquad \text{(ix)}$$

From H to N

the velocity is constant and equal to $\overline{v}_o$ and HN straight;

$$\therefore \frac{T_2 - T_1}{2} = \frac{NH}{\overline{v}_o} = \frac{L}{\overline{v}_o} \frac{\left[\cos \delta + \sin \delta + \frac{2y}{L} - \sqrt{2} \right]}{(\cos \delta - \sin \delta)}$$

using (iv) then

$$T_2 - T_1 = \frac{2L}{U} \frac{\left[\cos \delta + \sin \delta + \frac{2y}{L} - \sqrt{2} \right]}{(1 - \sin 2\delta)} \qquad \text{(x)}$$

From N to Q

the velocity is $\overline{v}(\theta)$ given by (iii) and the path by $r(y, \theta)$

in (vi). Consider y as constant (the original location of the particle at t = 0) and let

$$a = \sqrt{2} \sin \delta$$

$$A = r(y,0) = \frac{\frac{L}{2}(\sqrt{2} - 2\sin\delta) - y}{1 - \sqrt{2}\sin\delta} = \frac{\frac{L}{\sqrt{2}}(1 - a) - y}{1 - a} \quad \text{(xi)}$$

(xi) in (vi) →

$$r(\theta) = A(1 - a)\frac{1}{(\cos\theta - a)} \quad \text{(vi)'}$$

$$dr = A(1 - a)\frac{\sin\theta}{(\cos\theta - a)^2}\, d\theta \quad \text{(xii)}$$

From Fig. III-11, (vi)' and (xii) →

$$- ds = [dr^2 + r^2 d^2\theta]^{\frac{1}{2}}$$

Using (vi)' and (xii), we get

$$ds = - A(1 - a)\frac{[1 + a^2 - 2a\cos\theta]^{\frac{1}{2}}}{(\cos\theta - a)^2}\, d\theta \quad \text{(xiii)}$$

but $dt = \frac{ds}{v}$, by using (iii), (xi), (xii) we get

$$dt = -A(1-a)\frac{[1+a^2-2a\cos\theta]^{\frac{1}{2}}}{(\cos\theta - a)^2}\, d\theta \cdot \frac{1}{U[1+a^2 - 2a\cos\theta]^{\frac{1}{2}}}$$

$$\therefore\ dt = - \frac{A(1 - a)}{U}\frac{d\theta}{(\cos\theta - a)^2} \quad \text{(xiv)}$$

integrating both sides of (xiv)

$$\int_{T_2/2}^{T/2} dt = - \frac{A(1 - a)}{U}\int_{\theta=45-\delta}^{\theta=0} \frac{d\theta}{(\cos\theta - a)^2}$$

$$\text{i.e.} \quad T - T_2 = \frac{2A(1-a)}{U} \int_{\theta=0}^{\theta=45-\phi} \frac{d\theta}{(\cos\theta - a)^2}$$

Evaluating the integral and using (xi), we get

$$T - T_2 = \frac{2L}{U} \frac{\left[\frac{1}{\sqrt{2}} - \sin\phi - \frac{y}{L}\right]}{\cos 2\phi} B(\phi) \qquad \text{(xv)}$$

where $B(\phi) = 1 - \frac{2\sqrt{2}\sin\phi}{(\cos 2\phi)^{\frac{1}{2}}} \tanh^{-1}$

$$\left\{ - \frac{1+\sqrt{2}\sin\phi}{(\cos 2\phi)^{\frac{1}{2}}} \tan\left(\frac{45-\phi}{2}\right) \right\} \qquad \text{(xv')}$$

Adding (ix), (x) and (xv)

$$\therefore \quad T = \frac{2L}{U}\left\{\left(\frac{1}{\sqrt{2}} - \sin\phi - \frac{y}{L}\right)\left(\frac{\cos\phi + \sin\phi}{\cos\phi - \sin\phi} + \frac{B(\phi)}{\cos 2\phi}\right) + \frac{\cos\phi + \sin\phi - \sqrt{2} + \frac{2y}{L}}{1 - \sin 2\phi}\right\} \qquad \text{(xvi)}$$

where $B(\phi)$ is given by (xv)'

It is clear from (ii) and (xvi) that $\delta(y)$ is linear in Zone A. To describe the function completely it is sufficient to get values at end points $y = y_1$ and $y = y_2$.

For $y = y_2 = L\left(\frac{1}{\sqrt{2}} - \sin\phi\right)$, using (ii) and (xvi)

$$\delta(y_2) = \delta_{max} = 2L \frac{[\sin\phi \cos 2\phi]}{(1 - \sin 2\phi)} \qquad \text{(xvii)}$$

For $y = y_1 = \frac{L}{2}[\sqrt{2} - (\sin\phi + \cos\phi)]$

$$\therefore \quad \delta(y_1) = \delta_1 = L \frac{[B(\phi) - \cos 2\phi]}{[\cos\phi + \sin\phi]} \qquad \text{(xviii)}$$

Zone B: $0 < y < y_1$

Let MRS be the path of a particle at height y above B'E', Fig. III-12,

Let $t = 0$ for the particle at M

Let $t = \frac{T_1}{2}$ for the particle at R

Let $t = \frac{T}{2}$ for the particle at S

From M to R

The velocity is constant and equal to U and MR straight

$$\therefore \frac{T_1}{2} = \frac{\overline{MR}}{U}$$

$$\therefore T_1 = \sqrt{2}\,\frac{L}{U}\,[\sqrt{2}\cos\delta - \sin\Phi] \qquad \text{(xix)}$$

where Φ is the angle between BB' and BR, such that

$$y = \frac{L}{\sqrt{2}}\,(1 - \cos\Phi) \text{ or} \qquad \text{(xx)}$$

$$\Phi = \cos^{-1}\left(1 - \frac{\sqrt{2}\,y}{L}\right) \qquad \text{(xx)'}$$

From R to S

The path of the particle is defined by (vii) because the incompressibility condition used for Zone A still holds. Then (vi)' applies to path between R and S considering y (or Φ) as a constant, then using (xx)

$$r(\theta) = A(1 - a)\,\frac{1}{\cos\theta - a} \qquad \text{(vi)'bis}$$

where

$$a = \sqrt{2}\,\sin\delta$$

$$A = \frac{\frac{L}{\sqrt{2}}\,(1 - a) - y}{1 - a} = \frac{L}{\sqrt{2}}\,\frac{(\cos\Phi - a)}{(1 - a)} \qquad \text{(xi)'bis}$$

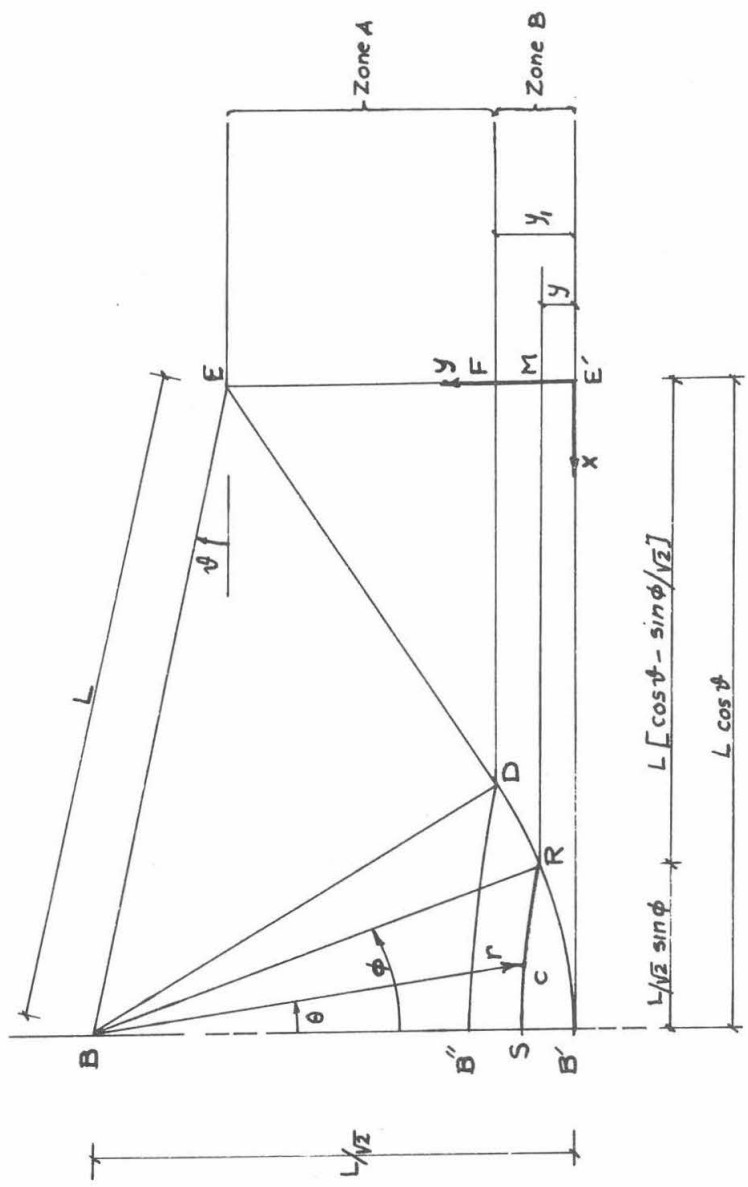

Fig. III-12. Variables for evaluating the distortion in zone B in the conjugate problem.

In a similar treatment as that of Zone A we get

$$dt = -\frac{A(1 - a)}{U} \frac{d\theta}{(\cos\theta - a)^2} \qquad \text{(xiv)bis}$$

Integrating both sides of (xiv) with their respective limits:

$$\int_{T_1/2}^{T/2} dt = -\frac{A(1 - a)}{U} \int_{\theta=\Phi}^{0} \frac{d\theta}{(\cos\theta - a)^2}$$

$$\therefore\ T - T_1 = \frac{2A(1 - a)}{U} \int_{0}^{\Phi} \frac{d\theta}{(\cos\theta - a)^2}$$

Evaluating the integral and using (xi)', we get

$$T - T_1 = \frac{\sqrt{2}\,L}{U\cos 2\vartheta}\left[\sin\Phi + \frac{2\sqrt{2}\sin\vartheta\,(\cos\Phi - \sqrt{2}\sin\vartheta)}{(\cos 2\vartheta)^{\frac{1}{2}}} \cdot \tanh^{-1}\left(\frac{1 + \sqrt{2}\sin\vartheta}{(\cos 2\vartheta)^{\frac{1}{2}}}\tan\frac{\Phi}{2}\right)\right] \qquad \text{(xxi)}$$

Adding (xix) and (xxi), we get

$$T = \frac{\sqrt{2}\,L}{U}\left\{\sqrt{2}\cos\vartheta - \sin\Phi + \frac{1}{\cos 2\vartheta}\left[\sin\Phi + \frac{2\sqrt{2}\sin\vartheta\,(\cos\Phi - \sqrt{2}\sin\vartheta)}{(\cos 2\vartheta)^{\frac{1}{2}}} \cdot \tanh^{-1}\left(\frac{1 + \sqrt{2}\sin\vartheta}{(\cos 2\vartheta)^{\frac{1}{2}}}\tan\frac{\Phi}{2}\right)\right]\right\} \qquad \text{(xxii)}$$

Using (ii) and (xxii), we get

$$\delta = \sqrt{2}\,L\left\{\left(\frac{1}{\cos 2\vartheta} - 1\right)\sin\Phi + \frac{2\sqrt{2}\sin\vartheta(\cos\Phi - \sqrt{2}\sin\vartheta)}{(\cos 2\vartheta)^{3/2}} \cdot \tanh^{-1}\left(\frac{1 + \sqrt{2}\sin\vartheta}{(\cos 2\vartheta)^{\frac{1}{2}}}\tan\frac{\Phi}{2}\right)\right\} \qquad \text{(xxiii)}$$

for $\Phi \to 0$ then $\delta \to 0$ i.e. no discontinuity at $y = 0$ (or $y \to 0$)

for $\Phi = 45 - \vartheta$ then $y = y_1 = \frac{L}{2}[\sqrt{2} - (\sin\vartheta + \cos\vartheta)]$

and

$$\delta(y_1) = L \frac{[B(\vartheta) - \cos 2\vartheta]}{(\cos\vartheta + \sin\vartheta)}$$

where $B(\vartheta)$ is given by (xv')

Comparing with (xviii) the function is continuous at $y = y_1$; from the above results it is clear that $\delta(y)$ is continuous for all ϑ in the considered range $(0 < \vartheta < \frac{\pi}{4})$

To get the slope of the curve $\delta(y)$ w.r.t. y, differentiate (xxiii) w.r.t. y, and use (xx)' in $\frac{d\delta}{dy} = \frac{d\delta}{d\Phi}\frac{d\Phi}{dy}$, we get

$$\frac{d\delta}{dy} = 2\left(\frac{1}{\cos 2\vartheta} - 1\right)\cot\Phi + \frac{4\sqrt{2}\sin\vartheta}{(\cos 2\vartheta)^{3/2}}$$

$$\times\left[\frac{(\cos\Phi - \sqrt{2}\sin\vartheta)(\cos 2\vartheta)^{\frac{1}{2}}(1 + \sqrt{2}\sin\vartheta)}{2\sin\Phi(\cos 2\vartheta - 2\sin^2\frac{\Phi}{2}(1 + \sqrt{2}\sin\vartheta)}\right.$$

$$\left.\frac{1 + \sqrt{2}\sin\vartheta}{(\cos 2\vartheta)^{\frac{1}{2}}}\tan\frac{\Phi}{2}\right] \qquad \text{(xxiv)}$$

for $\Phi \to 0$ (or $y \to 0$) then $\frac{d\delta}{dy} = O\left(\frac{1}{\Phi}\right) \to \infty$ for all ϑ (xxv)

Special case ϑ small

Writing

$$\sin\vartheta = \vartheta + O(\vartheta^3)$$

$$\cos\vartheta = 1 + O(\vartheta^2)$$

$$\tan\vartheta = \vartheta + O(\vartheta^3) \qquad \text{(xxvi)}$$

for $|\alpha| < 1$

$$\tanh^{-1}(\alpha + O(\vartheta)) = \alpha\left[1 + \frac{\alpha^2}{3} + \frac{\alpha^4}{5} + \text{——}\right] + O(\vartheta)$$

from (xv)' and (xxvi)

$$B(\mathfrak{H}) \simeq 1 + 1.2454\,\mathfrak{H} \qquad \text{(xxvii)}$$

in Zone A: $y_1 \leq y \leq y_2$

(xxvi) in (xvii) yield

$$\delta_{max} \simeq 2L\mathfrak{H} \qquad \text{(xvii)'}$$

(xxvi) and (xxvii) in (xviii) yield

$$\delta(y_1) = \delta_1 \simeq L\,\frac{[1 + 1.2454\mathfrak{H} - 1]}{1 + \mathfrak{H}}$$

$$\therefore \delta_1 \simeq 1.2454\,L\mathfrak{H} \qquad \text{(xviii)'}$$

$$\text{slope of } \delta(y) \text{ line} = \frac{\delta_{max} - \delta_1}{y_2 - y_1} \simeq \frac{0.7546\,L\mathfrak{H}}{L/2} \simeq 1.51\mathfrak{H} \qquad \text{(xxviii)}$$

in Zone B: $0 \leq y \leq y_1$ (or $0 \leq \Phi \leq 45 - \mathfrak{H}$)

(xxvi) in (xxiii) yield

$$\delta \simeq \sqrt{2}\,L\left\{2\sqrt{2}\,\mathfrak{H}\,\cos\Phi\,\tanh^{-1}\left((1 + \sqrt{2}\,\mathfrak{H})\tan\frac{\Phi}{2}\right)\right\}$$

$$\simeq 4L\mathfrak{H}\cos\Phi\,\tanh^{-1}\left(\tan\frac{\Phi}{2}\right)$$

$$\therefore \delta \simeq 4L\mathfrak{H}\cos\Phi\,\tan\frac{\Phi}{2}\left[1 + \frac{\left(\tan\frac{\Phi}{2}\right)^2}{3} + \frac{\left(\tan\frac{\Phi}{2}\right)^4}{5} + \cdots\right] \qquad \text{(xxiii)'}$$

(xxvi) in (xxiv) yield

$$\frac{d\delta}{dy} \simeq 4\sqrt{2}\,\mathfrak{H}\left[\frac{1}{2\sin\Phi} - \tanh^{-1}\left(\tan\frac{\Phi}{2}\right)\right]$$

for $\Phi = 45 - \mathfrak{H}$

$$\therefore \frac{d\delta}{dy} \simeq 4\sqrt{2}\,\delta\left[\frac{1}{\sqrt{2}} - 0.4142\left(1 + \frac{(0.4142)^2}{3} + \frac{(0.4142)^4}{5} + \text{——}\right)\right]$$

$$\simeq 4\sqrt{2}\,\delta\left[\frac{1}{\sqrt{2}} - 0.4142(1.063)\right]$$

$$\simeq 1.51\,\delta \qquad \text{(xxix)}$$

Compare (xxviii) and (xxix), it is clear that $\frac{d\delta}{dy}$ is continuous everywhere.

III-1-5. Summary of results

The ironing plate problem has been solved assuming that the heap ahead of the plate is an isosceles triangle, Fig. III-2. This shape of the heap was the only one found to satisfy the steady-state requirements; however, without a proof of uniqueness, other shapes cannot be ruled out.

The main results of the solution are:

(1) The slip line field of Fig. III-2 gives a uniform normal stress at the interface p equal to

$$p = (\pi + 2 - 4\delta)k \qquad \text{(1)bis}$$

The shearing stresses at the interface being zero by definition of a smooth plate, the resultant force thus acts at an angle δ to the vertical and is given by

$$P = (\pi + 2 - 2\delta)kL \qquad (14)$$

(2) After one plate traversal, the permanent deformations are in the same direction as that of the motion (horizontal) with no vertical displacements.

For small values of ϑ ($0 < \vartheta < 10^{\circ}$ say), which is the range of interest in applications to the rolling theory of Chapter IV, a summary of the dimensions and permanent horizontal deformation δ is given in Fig. III-13. We can see that the distribution of δ at different heights y can be divided into two zones: An upper zone A ($y_1 \leq y \leq y_2$) where δ is linear and a lower one B ($0 < y < y_1$) where it is curved. For depths larger than y_2, ($y < 0$) δ is zero. Moreover the slope of $\delta(y)$ is continuous everywhere except at $y = 0$. For a more detailed graph of the curved part in zone B, Fig. III-14 was drawn. Noting the difference in scale between the two coordinates in this figure the curve is thus very flat with an infinite slope at $y = 0$.

For large values of ϑ ($10^{\circ} < \vartheta < 45^{\circ}$) second order terms may not be neglected and need to be used. The pattern of deformation δ is still the same as for small ϑ however y_1 and y_2 are now given by:

$$y_1 = \frac{L}{2}[\sqrt{2} - (\sin\vartheta + \cos\vartheta)] \qquad (15)$$

$$y_2 = L\left(\frac{1}{\sqrt{2}} - \sin\vartheta\right) \qquad (16)$$

δ_{max} and δ_1 describing the linear variation of δ in zone A are given by equation (xvii) and (xviii) respectively.

$\delta(y)$ in zone B is given by equation (xxiii).

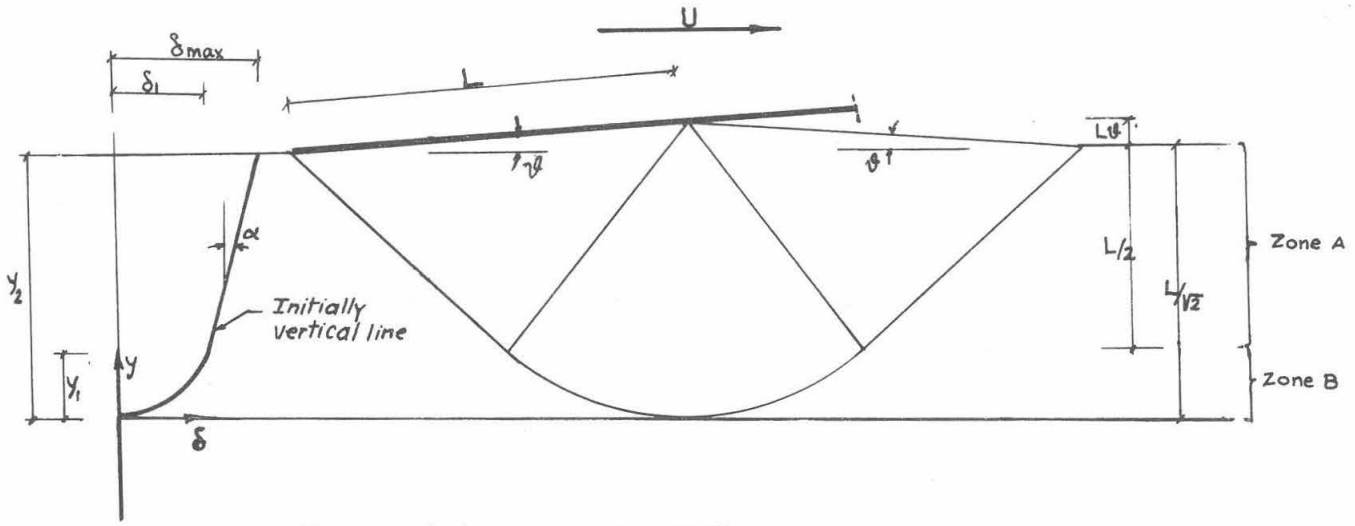

For small ϑ:

$\alpha \simeq 1.51\,\vartheta$

$y_1 \simeq 0.207\,L$ $\qquad \delta_1 \simeq 1.245\,L\vartheta$

$y_2 \simeq 0.707\,L$ $\qquad \delta_{max} \simeq 2\,L\vartheta$

Fig. III-13. Summary of the computed distortion of a square grid for small values of ϑ.

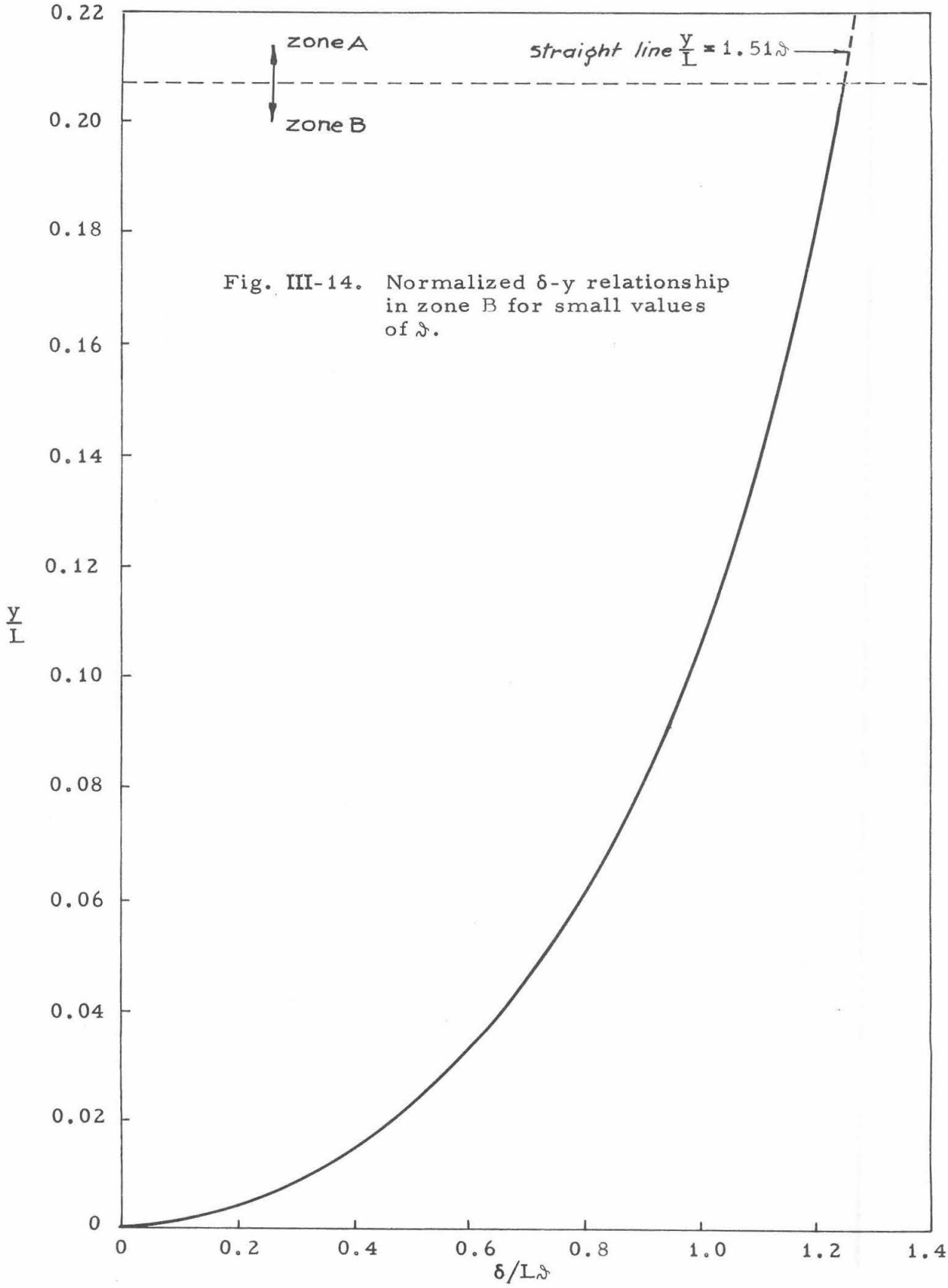

Fig. III-14. Normalized δ-y relationship in zone B for small values of δ.

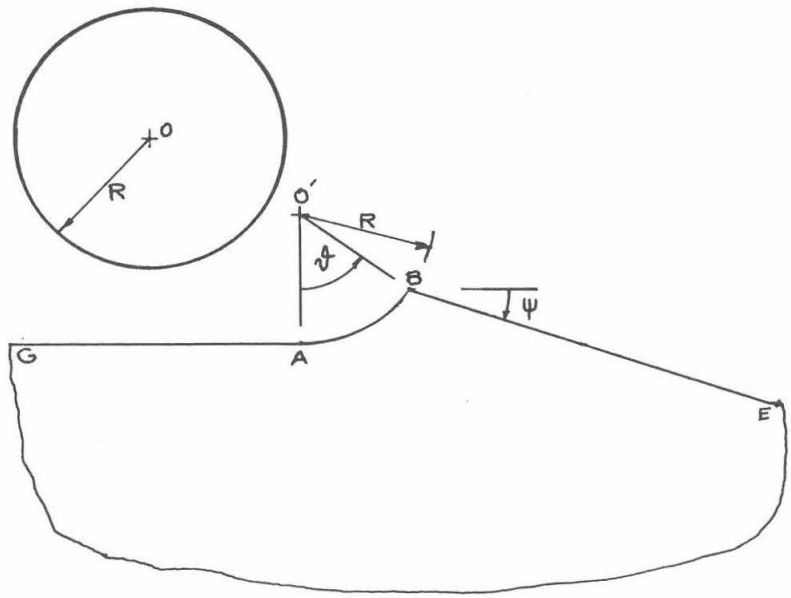

(a)

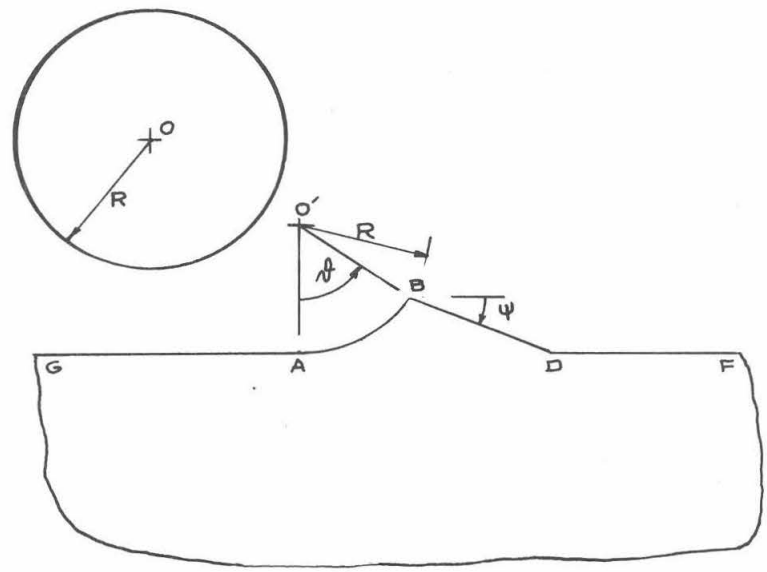

(b)

Fig. III-15. The instantaneous solution of the rolling problem.

III-2. Wedge indentation by a rigid smooth roller, the instantaneous solution of plane strain rolling

Consider the plane strain problem of a rigid smooth cylinder with radius R and a rigid-perfectly plastic wedge Fig.III-15-a, with the upper surface GABE. The portion GA is horizontal, BE is straight and makes a clockwise angle Ψ from the horizontal. Portion AB is a circular arc with the same radius R as that of the cylinder and a center of curvature O' which lies vertically above A. The angle between the two radii O'A and O'B is δ. The cylinder is to be fitted so that its center O coincides with O' and then an instantaneous horizontal velocity U, to the right, is given to O. Simultaneously an angular velocity ω is given to the cylinder about its center.

In the following part we present two failure mechanisms to the problem.

(1) A front failure pattern in which the plastic zone within the wedge lies ahead of the roller. It is an exact solution and will be proven to apply in the case when the surface of the wedge has the shape GABDF, Fig. III-15-b, which is the same as the previous problem but now DF is horizontal and $\overline{BD}$ is equal to $R\delta$. The latter problem will be used in chapter IV where the rolling theory is treated.

(2) A rear failure pattern in which although the stress and velocity fields are satisfied, the condition that the power of dissipation be positive everywhere is violated. From a

theoretical standpoint such a violation of a fundamental postulate is not permissible, nevertheless it will be presented as a first step towards a better solution without however using its results in subsequent applications.

Finally we present the general case where the front and rear pattern exist and give the criterion for the development of each. The validity of solutions including a rear failure pattern should be assessed in the light of the violation of the positive power of dissipation condition.

III-2-1. The front failure pattern

For the indentation problem shown in Fig. III-15-a and described earlier we now present a plastic field that lies ahead of the roller. Such a front failure pattern will be proven exact and later be shown to develop for any value of Ψ.

(1) The plastic and stress fields

A field of characteristics is shown in Fig. III-16. To describe the manner in which it was constructed Fig. III-17 was drawn. The main parameters are:

ζ is the radial angle, measured counterclockwise, from the vertical through the center of the cylinder O and the intersection of any α-line (such as IJKL) with the rim of the cylinder.

$\mathcal{S}$ is the maximum value of ζ when the α-line is degenerated into point B, the intersection of the free surface with the rim of the cylinder.

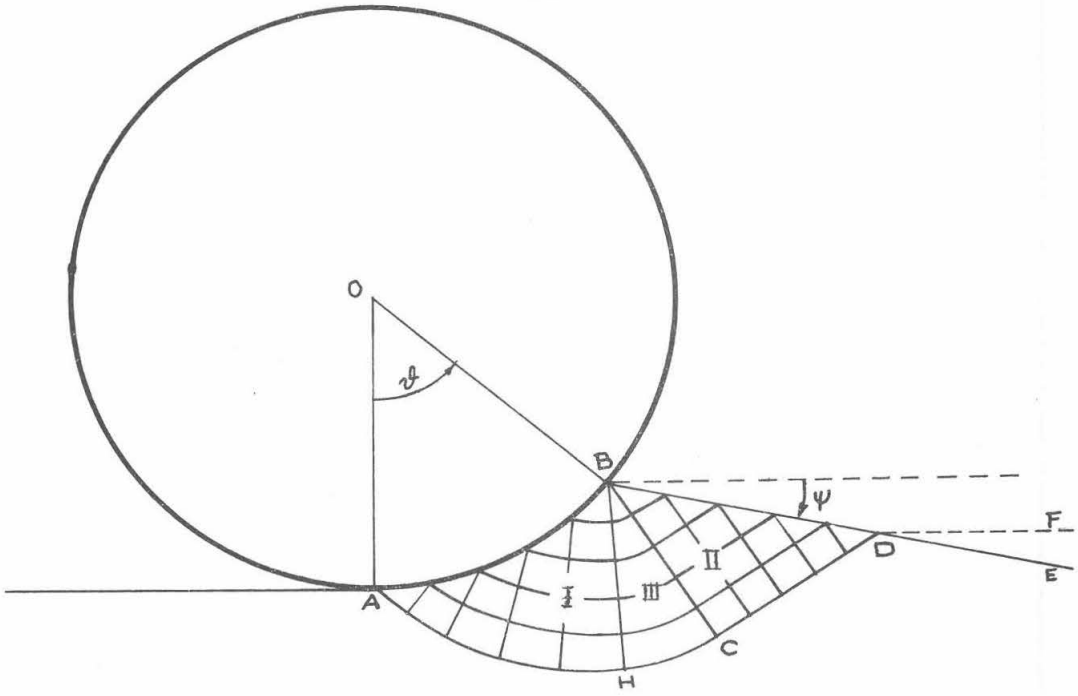

Fig. III-16. Typical field of characteristics for a front failure mode ($\vartheta = 50^{\circ}$, $\Psi = 10^{\circ}$).

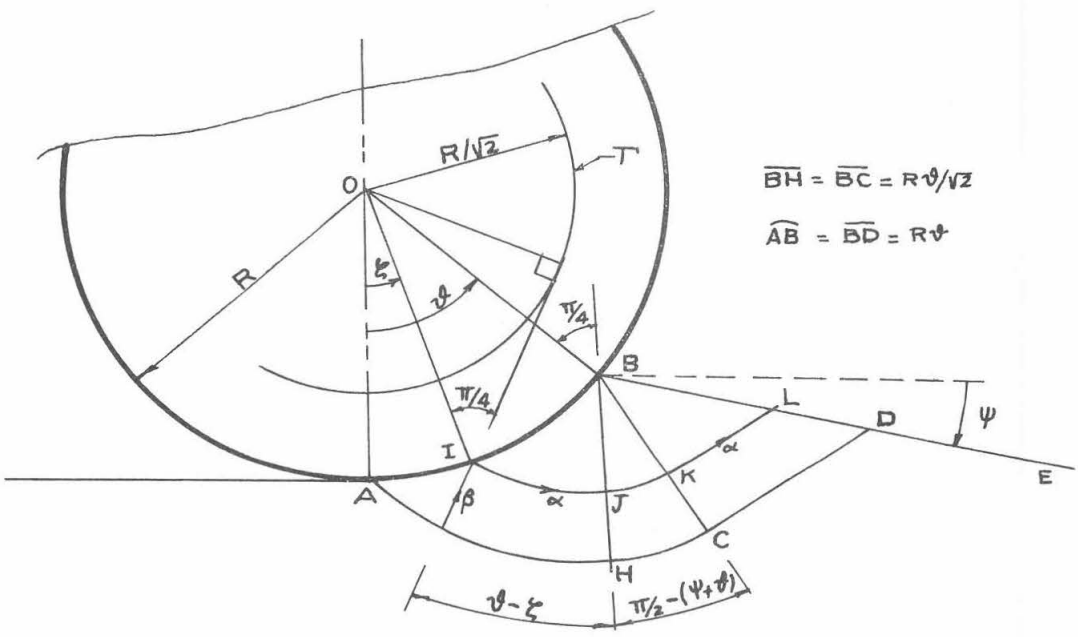

Fig. III-17. Details of the construction of the field of characteristics in a front failure mode.

Γ is a circle of radius $\frac{R}{\sqrt{2}}$ centered at O and is considered as the evolute of all α-lines.

Zone I is determined by AHBA, where

AH has Γ as an evolute

$\widehat{BA}$ is the circular arc along the cylinder surface

HB is straight

The zone has all β-lines straight and tangent to Γ. All α-lines are parallel and are formed by unwinding a taut string about Γ.

Zone II is determined by the triangle BCDB, and has both families straight.

Zone III is determined by the circular fan BHCB, and has the β-lines straight and the α-lines consisting of circular arcs.

For the typical α-line such as IJKL, we have IJ the involute of Γ; JK a circular arc centered at B and KL straight. A moment's thought shows that on one hand the field satisfies the "Hencky-Prandtl" net requirements and on the other hand satisfies the stress boundary conditions along $\widehat{AB}$ and $\overline{BD}$. The field is thus a solution to the problem.

To describe the stress field, instead of using the graphical technique, the analytical formulation was found simpler and hence will be used.

From the equilibrium of an element in the plastic zone , one may easily deduce that:

$$\left.\begin{array}{ll} \text{Along an } \alpha\text{-line} & \sigma + 2k\theta = C_\alpha \\ \text{Along a } \beta\text{-line} & \sigma - 2k\theta = C_\beta \end{array}\right\} \text{ Hencky's equations} \qquad \begin{array}{l} (16) \\ (16)' \end{array}$$

Where θ is the slope of the positive α-line to the horizontal at any point, $-\pi < \theta < \pi$, and the positive direction of θ being counterclockwise

σ is the compressive hydrostatic pressure at that point.

C_α and C_β are constants.

To satisfy the stress-free boundary condition along BD, we have at any point along LK:

$$\left.\begin{aligned} \theta &= \frac{\pi}{4} - \Psi \\ \sigma &= k \end{aligned}\right\} \qquad (17)$$

$$(17) \text{ into } (16) \rightarrow C_\alpha = k(1 + \frac{\pi}{2} - 2\Psi) \qquad (18)$$

$$(18) \text{ into } (16) \rightarrow \sigma + 2k\theta = k(1 + \frac{\pi}{2} - 2\Psi) \qquad (19)$$

In particular for point I where $\theta = \zeta - \frac{\pi}{4}$

$$\therefore (19) \rightarrow \sigma(\zeta) = k[1 + \pi - 2(\Psi + \zeta)] \qquad (20)$$

For $p(\zeta)$ the external pressure at I, then

$$p(\zeta) = \sigma(\zeta) + k \qquad (21)$$

$$(20) \text{ and } (21) \rightarrow p(\zeta) = k[2 + \pi - 2(\Psi + \zeta)] \qquad (22)$$

Notes:

1. Using the fact that all β-lines are straight, i.e., θ = constant, in (16)', together with (19), the stresses at any point in the plastic field are determined.
2. The pressure $p(\zeta)$ at the interface decreases with both Ψ and ζ. This means that for small ζ and

for small (or negative) Ψ the contact pressure becomes high. As will later be seen, these conditions cause a plastic zone behind the roller or a rear failure pattern to develop.

3. From the geometry of the field we have

$$\left.\begin{aligned} \overline{BH} = \overline{BC} &= \frac{R\mathcal{S}}{\sqrt{2}} \\ AB = \overline{BD} &= R\mathcal{S} \end{aligned}\right\} \qquad (23)$$

These values are important since they determine the size of the plastic domain.

(2) The velocity field

As described earlier, the surface of the wedge has the shape GABDE, Fig. III-15-a; then the cylinder is fitted such that the arc AB is the interface of contact.

A horizontal velocity U, to the right is instantaneously given to the center of the cylinder O together with clockwise angular velocity ω to the cylinder about O. The complete solution of the problem is given in Fig. III-18 and III-19. The origin of the hodograph lies at 00 and the heavy lines represent the jumps in velocities between points on the cylinder's rim, ($\overline{00}$, $\overline{11}$, $\overline{22}$, ..., etc.). All curves on the hodograph are circular arcs centered at the origin 00 except arc ($\overline{00}$, $\overline{11}$, $\overline{22}$, $\overline{33}$) which is centered at 0. The incompressibility condition is directly checked by the normality of corresponding images in both Figs. III-18 and III-19 along the characteristics. Noting that the jump at any point on the rim of the cylinder is parallel

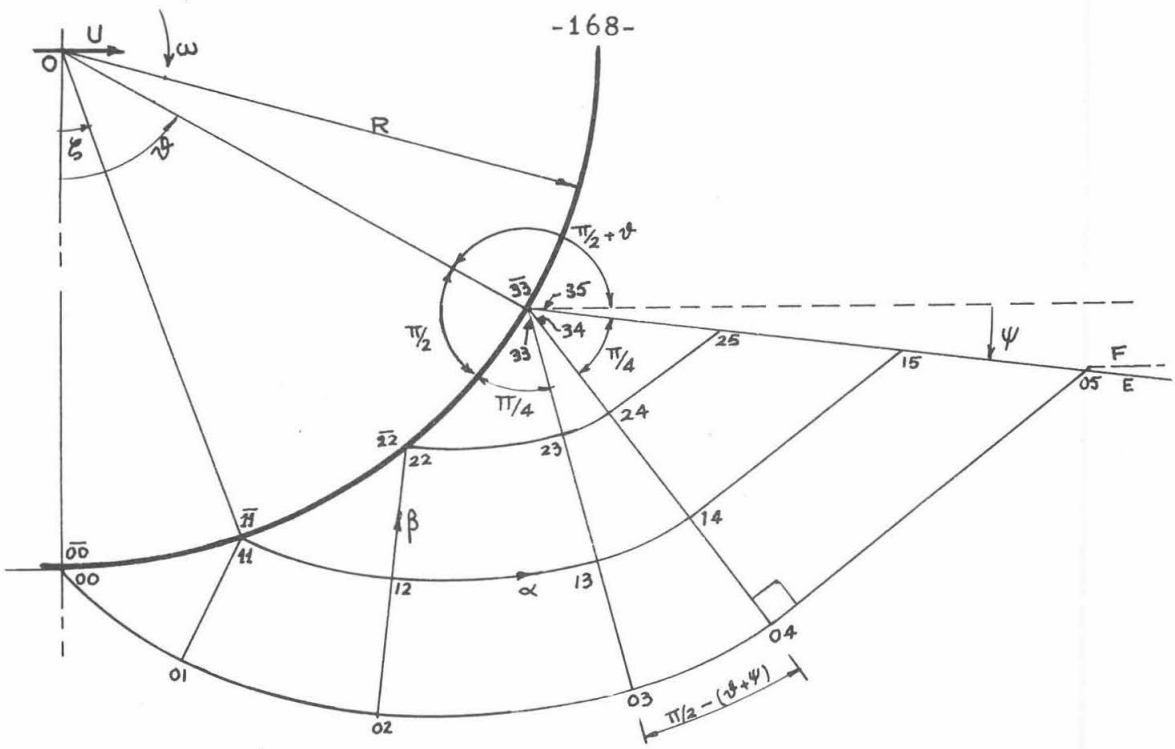

Fig. III-18. Physical plane for a front failure mode.

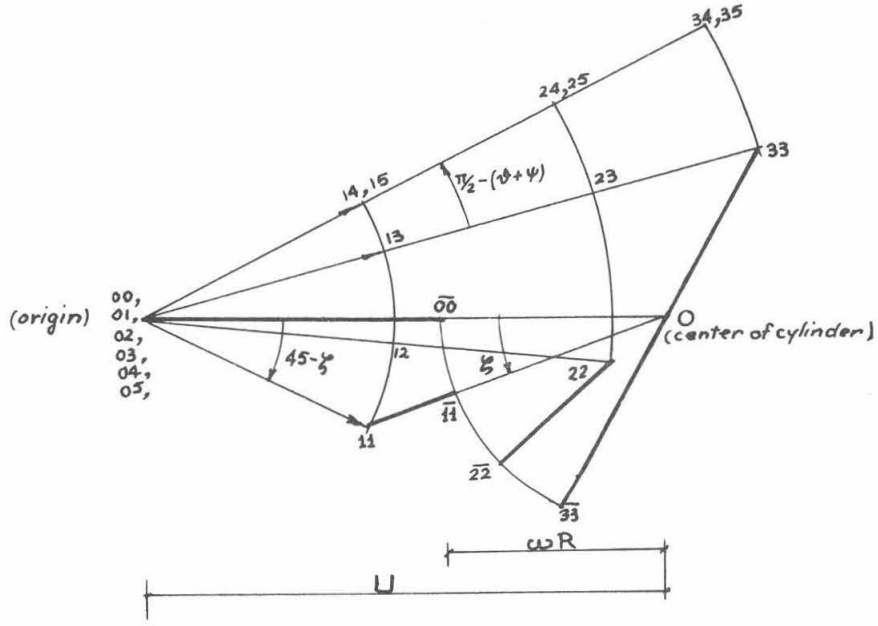

Fig. III-19. Hodograph of Fig. III-18.

to the tangent to the cylinder at that point; also that the velocity along any β-line is nil and the velocity along any α has a constant magnitude, the following results are emphasized.

1. The velocity boundary conditions are satisfied.
2. Suppose we increase ω while keeping U fixed; the only change in Fig. III-19 is the magnification of the radius of the circular arc $(\overline{00}, \overline{11}, \overline{22}, \overline{33})$ centered at 0. The directions of $(0,\overline{00})$, $(0,\overline{11})$, ... , etc., which are also the directions of the jumps, remain unchanged. The condition of zero velocity along β-lines implies that the direction of (00,11), (00,12), ... etc. must remain the same. It is thus clear that the location of 11, 12, 13, ... etc. is independent of ω. In other words, changing ω does not affect the velocity field in the plastic zone.
3. The shape of the region outside the plastic zone being immaterial to the present solution, we can consider either BDE straight or DF horizontal in Fig. III-15-a and III-15-b.
4. The direction of the shearing stresses and the shearing strain rates at any point in the plastic zone have the same sign, thus satisfying the positive power of dissipation condition.
5. Changing the value of U, keeping $U > 0$, causes only a change of the scale of the hodograph but the stress field remains unaltered.

III-2-2. The rear failure pattern

As a second solution to the problem of Fig. III-15-a, a rear failure pattern will now be presented. As mentioned earlier, the stress and velocity field equations will be proven satisfied but the power of dissipation is not positive everywhere.

(1) The plastic and stress fields

A field of characteristics is given in Fig. III-20. The manner in which it was constructed is shown in Fig. III-21. The details of construction are the same as for a front failure but with α and β interchanged.

To determine the stress field, we apply (16)' to the β-line IJKL at point L where $\theta = -\frac{3\pi}{4}$ and $\sigma = k$, then

$$C_\beta = k(1 + \frac{3\pi}{2})$$

Thus (16)' can be written in the form

$$\sigma - 2k\theta = k(1 + \frac{3\pi}{2}) \qquad (24)$$

For point I, where $\theta = \zeta - \frac{\pi}{4}$

(ix) becomes $\sigma(\zeta) = k[1 + \pi + 2\zeta]$

but since the interface pressure $p'(\zeta)$ is given by

$$p'(\zeta) = \sigma(\zeta) + k$$

then

$$p'(\zeta) = k[2 + \pi + 2\zeta] \qquad (25)$$

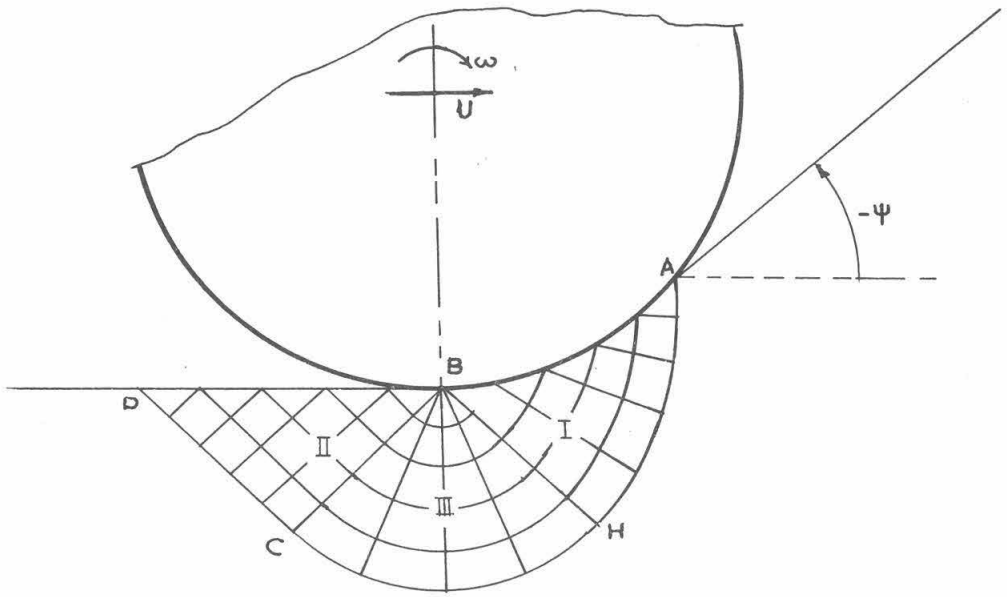

Fig. III-20. Typical field of characteristics for a rear failure mode.

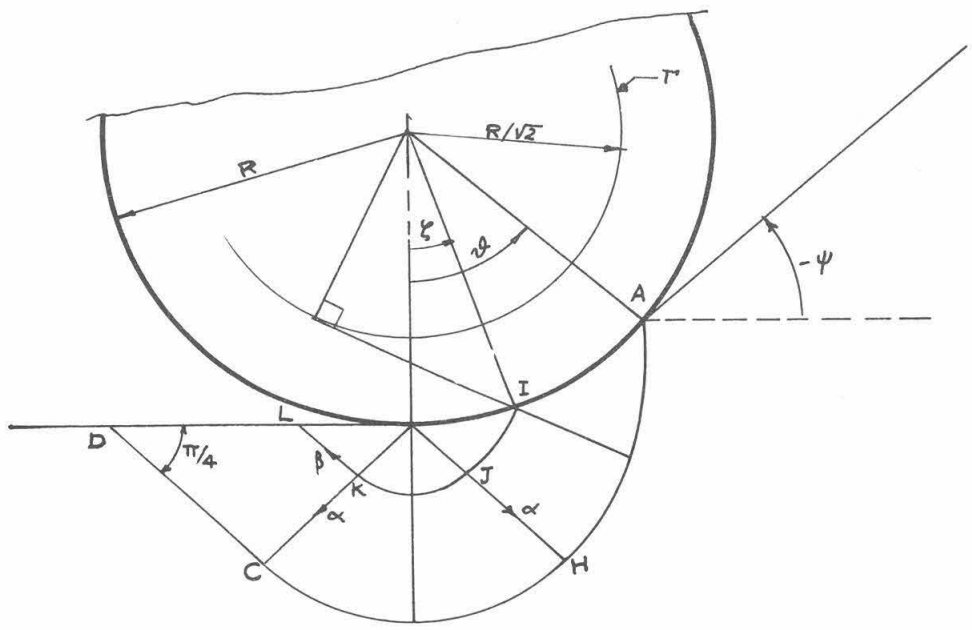

Fig. III-21. Details of the construction of the field of characteristics in a rear failure mode.

(2) The velocity field

Figs. III-22 and III-23 solve the problem completely. Details concerning the velocity field in the case of a front failure may be helpful to the reader noting the interchange of the α and β lines.

Again ω does not affect the velocity field in the plastic zone. Special attention should be given to the power of dissipation inside the plastic field since the shearing stresses and the rates of straining are opposite in direction.

III-2-3. The general case: two failure zones

From the front and rear failure patterns, the interface contact pressure is given by:

$$\left.\begin{array}{ll} \text{front failure} & p(\zeta) = k[\pi + 2 - 2(\Psi + \zeta)] \quad (22)\text{ bis} \\ \text{rear failure} & p'(\zeta) = k[\pi + 2 + 2\zeta] \quad (25)\text{ bis} \end{array}\right\} \Psi \geq \zeta \geq 0$$

Since a discontinuity of the contact pressure at the point where the front and rear failure zones meet the rim is unacceptable, as proven by Hill* , the contact pressure has to be a continuous function of ζ. For a minimum upper bound solution, the minimum of p or p' should be used.

Let ζ_{cr} denote the value of the critical point at which $p = p'$, i.e., the location where both zones meet the surface of the roller.

Equating (22) and (25) we get:

$$-(\Psi + \zeta_{cr}) = \zeta_{cr}$$

or $$\Psi = -2\zeta_{cr}$$

---

* See reference 30 in Chapter IV

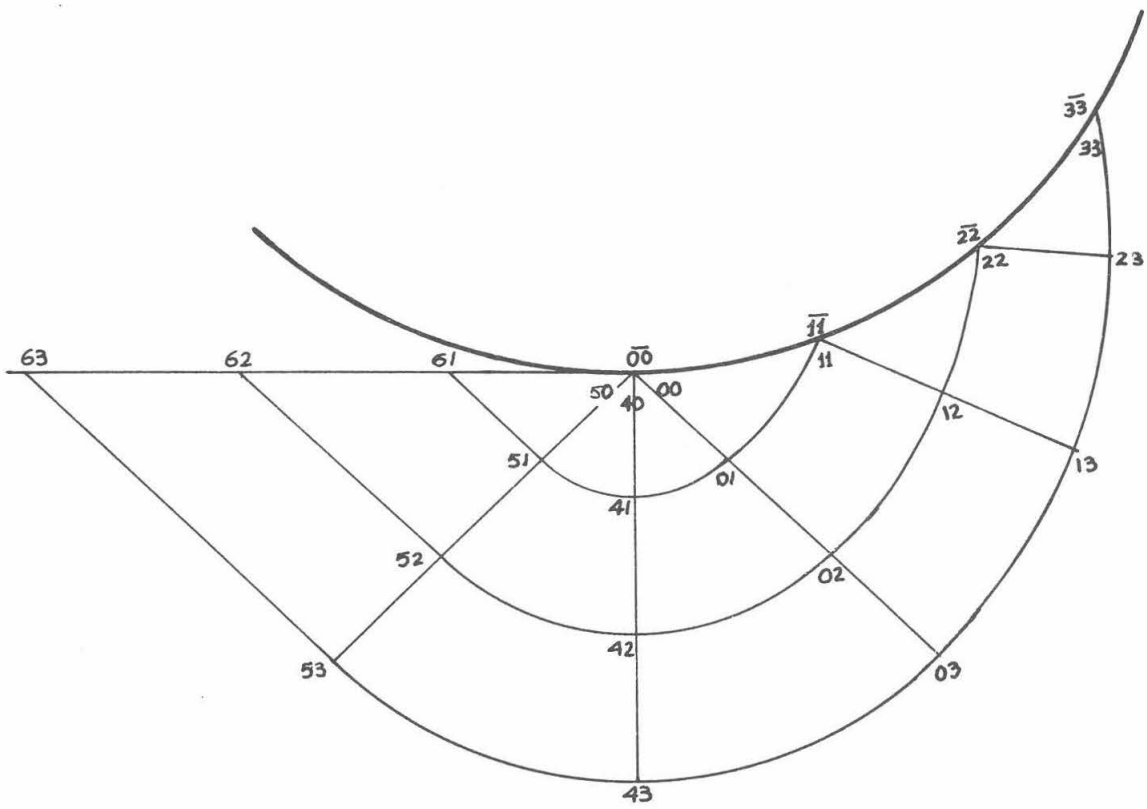

Fig. III-22. Physical plane for a rear failure mode.

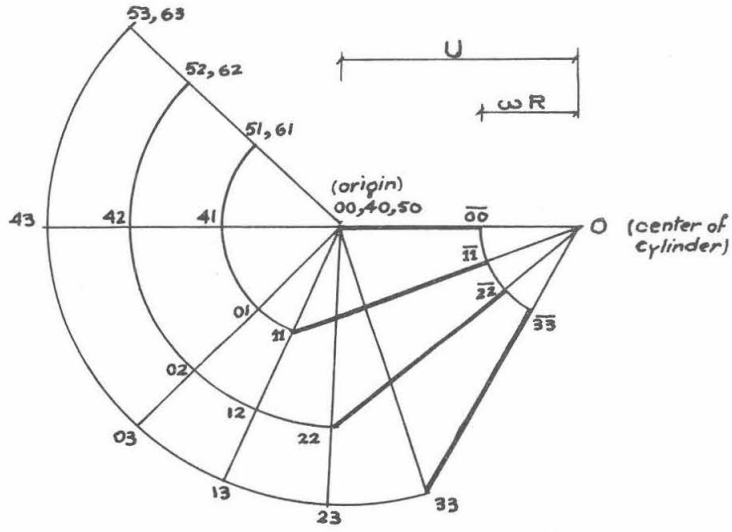

Fig. III-23. Hodograph of Fig. III-22.

for $\Psi < 0$

In Fig. (III-21), it is clear that to get a meaningful problem we must have $|\Psi| < \delta$. This implies that $0 < \zeta_{cr} \leq \delta/2$ and we get two failure zones.

for $\Psi = 0$

$\zeta_{cr} = 0$

for $\Psi > 0$

ζ_{cr} does not exist and we get only a front failure pattern. However for the present solution to hold we must have $\Psi \leq \pi/2 - \delta$.

It is now possible to extend the previous results to the case when the surface behind the wedge has a counterclockwise slope Ψ' to the horizontal, Fig. III-24. Only the contact pressure for a rear failure will be affected; equation (25) in a more general form becomes:

$$p'(\zeta) = k[\pi + 2 + 2(\zeta - \Psi')] \qquad (26)$$

We note that it reduces to equation (25) for the special case when $\Psi' = 0$.

Equations (22) and (26) are plotted in Fig. III-24 and an example clarifying its use now follows.

Example for the use of Fig. III-24

Suppose $\Psi = -10^{\circ}$, $\Psi' = 20^{\circ}$, $\delta = 40^{\circ}$ as shown in Fig. III-25. Corresponding to these values, the lines p'/k and p/k in Fig. III-24 intersect at $\zeta = \zeta_{cr} = 15^{\circ}$ and

$$p = p' = p_{max} = 5k$$

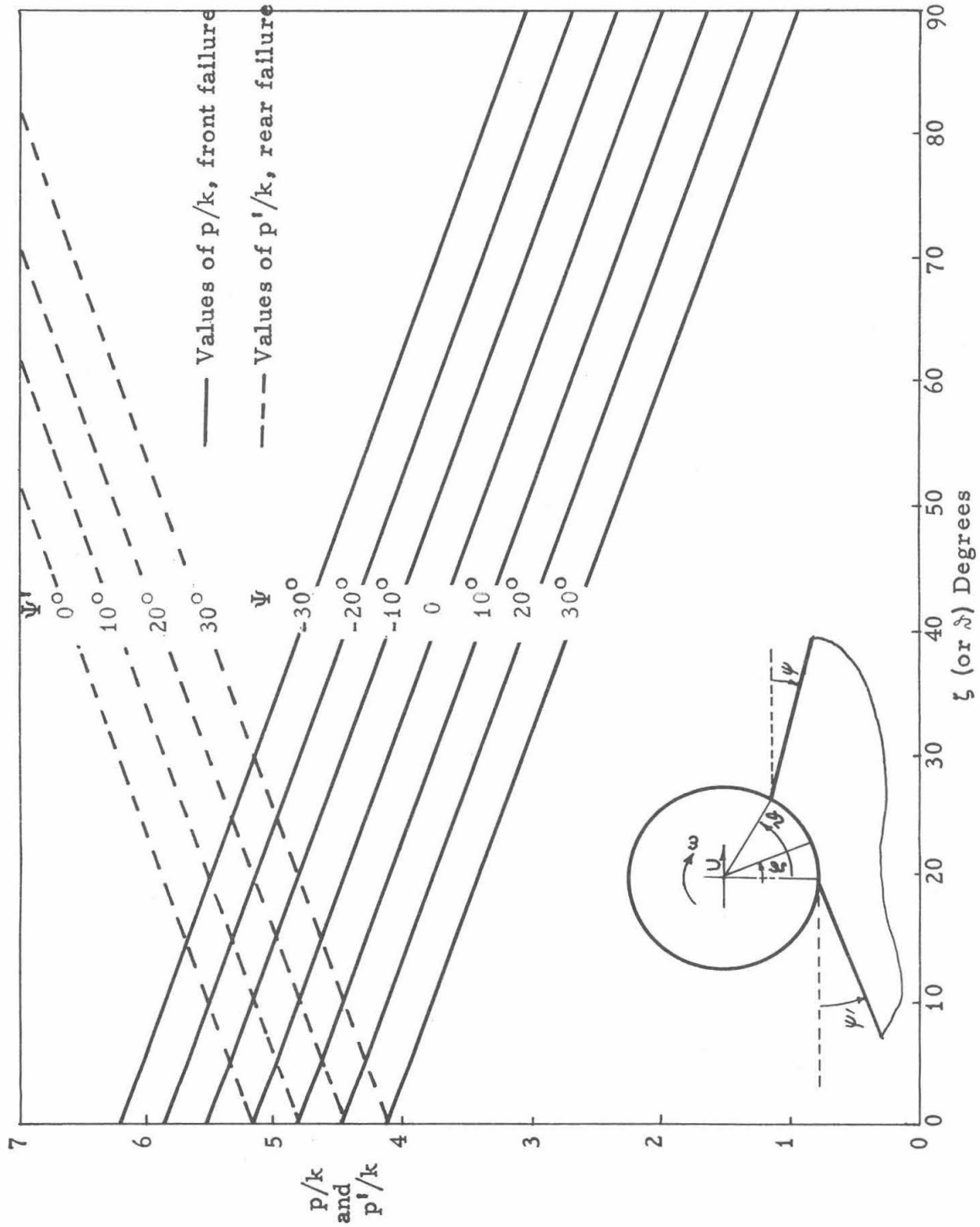

Fig. III-24. Pressure distribution along the rim of a rigid smooth roller, an instantaneous solution.

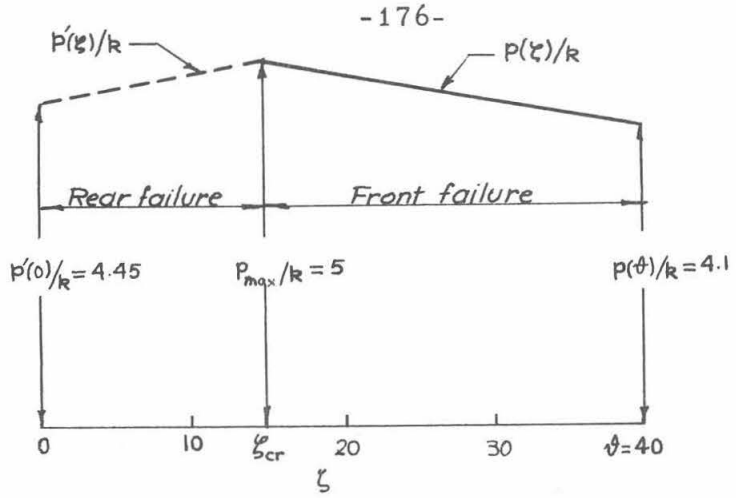

Pressure distribution along rim

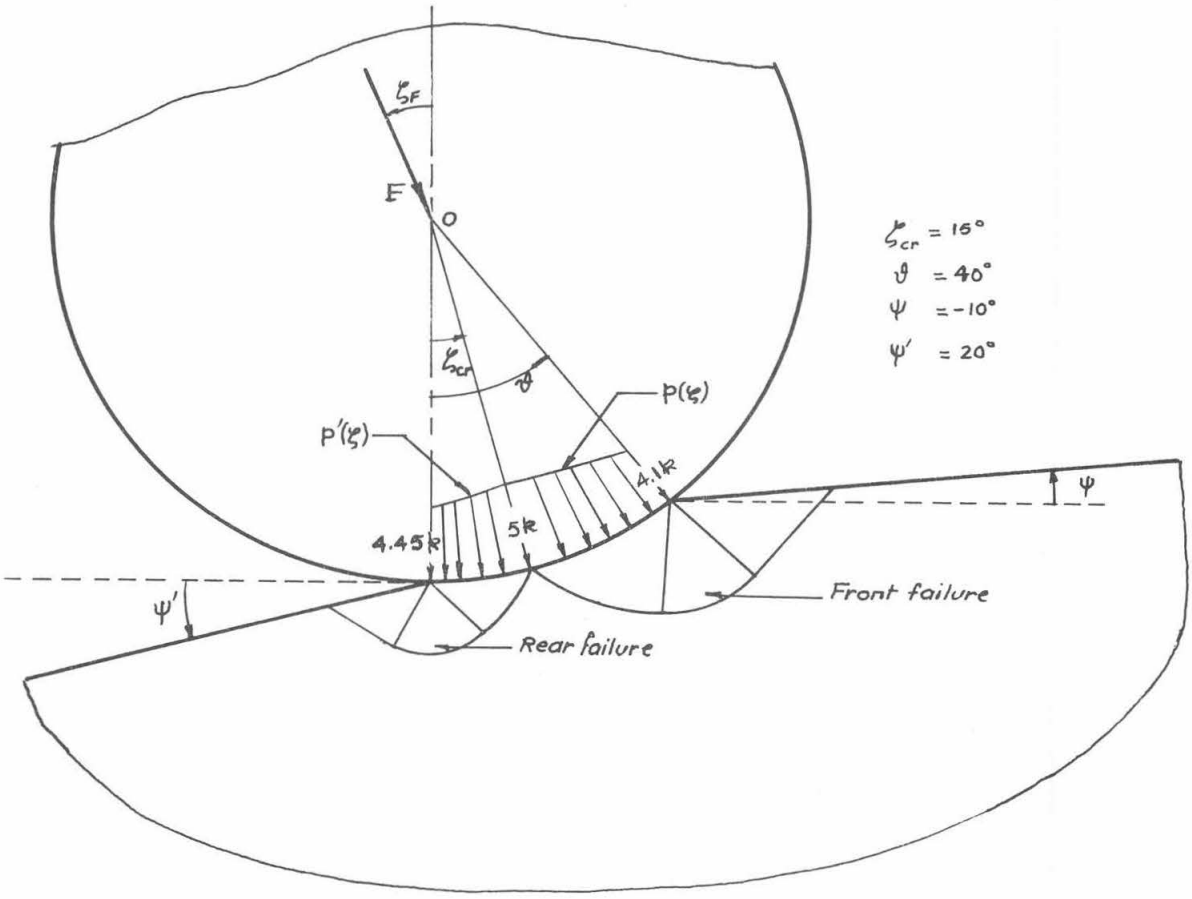

Fig. III-25. Example on the use of Fig. III-24 when $\Psi = -10^{o}$, $\Psi' = 20^{o}$ and $\vartheta = 40^{o}$.

The pressure distribution along the rim of the cylinder is shown in Fig. III-25.

For F denoting the resultant external force, then

$$F = \int_0^{\zeta_{cr}} p'R\, d\zeta + \int_{\zeta_{cr}}^{\vartheta} pR\, d\zeta$$

$$= R\left[\left(\frac{p_{max} + p'(0)}{2}\right)\zeta_{cr} + \left(\frac{p_{max} + p(\vartheta)}{2}\right)(\vartheta - \zeta_{cr})\right]$$

$$F = kR\left[\left(\frac{5 + 4.45}{2}\right)\frac{15\pi}{180} + \left(\frac{5 + 4.1}{2}\right)\frac{25\pi}{180}\right]$$

$$= kR\,[1.24 + 1.98]$$

$$= 3.22\ kR$$

Noting that the contact pressure is radial (smooth surface) and with ζ_F the inclination of F to the vertical, then

$$\zeta_F = \frac{1}{FR}\left[\int_0^{\zeta_{cr}} p'R\zeta\, d\zeta + \int_{\zeta_{cr}}^{\vartheta} pR\zeta\, d\zeta\right]$$

$$\simeq 19.7^{o} = 0.344\ \text{rad}$$

calling $\mu = \tan \zeta_F$

$$\mu \simeq 0.358$$

This is the ratio of horizontal to vertical forces to be applied at the center of the cylinder, to produce the assumed instantaneous motion.

CHAPTER IV

ON THE THEORY OF THE STEADY-STATE, FREE ROLLING OF RIGID CYLINDERS

IV-1. Introduction

Man has used the rolling process since the discovery of the wheel, yet study of the phenomenon did not start until 1712 when Varlo [1]* and later Coulomb in 1785 [2] began to perform tests on rollers. Eversince, numerous investigations have been made in the rolling on metals for its applications to bearings [3, 4, 5, 6, 7, 8, 15, 18, 19, 20, 21, 22, 23, 24, 25, 28, 29] and in the rolling on soils for its applications to land locomotion [9, 10, 11, 12, 13, 14, 31, 34]. The two fields progressed separately and although rolling on metals is presently fairly advanced, the literature on soils is rich in experimental results and empirical formulae but lacks the theory that would rationalize the process and would ultimately, with proper formulation, improve many engineering designs. The need for such a theory, which ordinarily is covered by carrying out more tests, was especially felt when a land rover was to be sent to the moon. No tests could have reasonably been performed on the moon's surface and the empirical formulae, without the proper understanding of the rolling mechanism, could hardly be relied upon in a project of such magnitude.

With its application to soils in mind, rolling is first considered a mechanism of energy dissipation. The history of development of

*Number in brackets refers to the bibliography at the end of the chapter.

the theory of rolling for metal applications is used to outline all available models that may account for the energy dissipated. The problem of the steady-state free rolling of a rigid cylinder is then properly formulated and ideal plasticity was chosen to account for the losses. An approximate solution is next derived for rolling under light loads; this was achieved by obtaining the exact solution of two problems that encompass the one of interest. The first is a steady-state solution of a problem with a geometry that is not exactly that of the cylinder, and the second is an instantaneous solution for the geometry of the cylinder but is not a steady-state. The combination of those two solutions together with that obtained by Marshall [26], using the perturbation technique developed by Spencer [27], which is another approximate solution to the rolling problem for applications to metals, provide a good estimate of what the exact solution should be. When checked with existing empirical formulae for the rolling of wheels on clays, the predicted rolling resistance compares favorably.

IV-2. Free rolling, the existing models for energy dissipation

By discovering the wheel, man found a means of reducing the energy required to move objects from one place to another. For a closer look at the subject, let us consider the plane strain steady-state free rolling shown in Fig. IV-1. The external force H, called the rolling resistance, moving with a constant velocity U dissipates energy at the rate of HU per unit time. For energy equilibrium, the study of the rolling problem requires the consideration of a

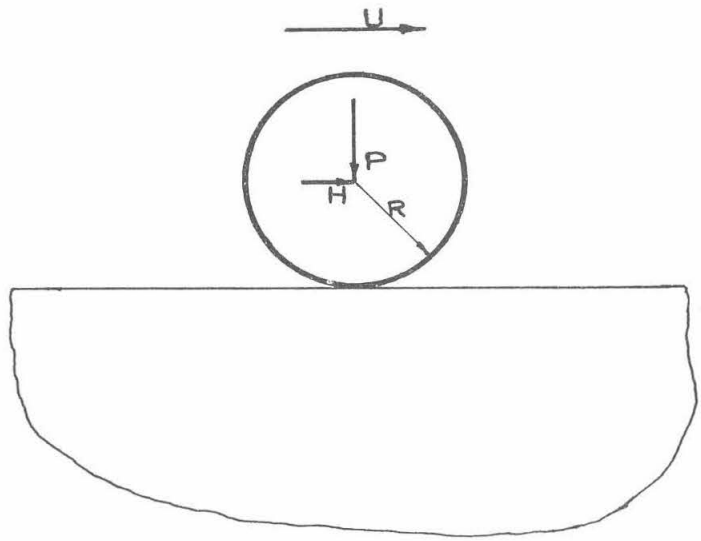

Fig. IV-1. Plane strain steady-state free rolling

system exhibiting some form of power dissipation ability.

The nature of the sink to absorb the power released by the external forces is no doubt a cornerstone for any theory dealing with the subject. Motivated by metal bearings research, all available theories for energy dissipation have been exploited, a brief summary of which follows:

(1) The surface phenomenon, or the friction model

The dissipated power, as explained by this model, is due to the interface stresses undergoing relative velocities between the rolling element and the base. Theoretically, the energy is dissipated in the form of heat at the interface alone, where discontinuities in velocities occur. Some theories based on this phenomenon are referred to as "Interfacial Slip theories."

Two types of slip are considered, the first called "Reynolds slip" which is present in part of the contact area and is due to the difference in elastic compliance between the rolling and static parts. The second is called "Heathcote microslip" and is only present for balls rolling in grooves (tracks), and is due to the non-conformity between the ball and the groove.

Another theory, due to Tomlinson, attributes losses to the energy required to break interfacial joints.

Experiments showed that the interface losses do contribute to the rolling resistance; however Eldredge and Tabor [3] established experimentally that this contribution is negligible in most practical cases, thus the friction model alone is considered to be inadequate for describing the rolling process.

(2) Plasticity

After its successful use in solid friction, plasticity seemed the natural substitute for the friction model.

Experiments on the rolling of a hard ball between flat parallel horizontal plates of a softer metal, led Eldredge and Tabor [3] in 1955 to derive an empirical formula giving the rolling resistance for the first traversal. The area of contact between the ball and the plate was assumed to consist of half a circle when projected on the horizontal, the center of the half circle lying directly below the center of the ball. Using this assumption and by measuring the applied forces, the average value of contact stress was calculated and was found to depend on the yield pressure of the softer metal.

To rationalize these results Eldredge and Tabor argued that the rolling resistance is primarily due to plastic displacement of the plate metal ahead of the ball. Thus the use of plasticity is first to account for the large permanent deformations of the plate material and second for the nearly uniform stress distribution at the contact. Evidently, because of the complexity of the problem, no real plasticity analysis was performed; nevertheless, the rolling resistance H claimed to be valid only for the first traversal, still holds a primary rank in the field of the rolling theory because of its reasonable prediction and its interpretation of the phenomenon.

Theoretically speaking, the plane strain problem of the roller is much simpler than the three-dimensional ball problem. However, the formula for ball resistance was not extended to the roller, presumably because of the absence of an exact plasticity analysis. By

increasing the number of traversals n, Tabor found that the rolling resistance H_n gradually decreased to approach a constant value H_∞ for large values of n. Simultaneously, the width of the track left behind the ball increases and approaches a constant value. Since for large n no more detectable permanent deformation was to be found, and because of the presumed connection between plasticity and large deformation, Tabor and followers rejected plasticity. The elastic hysteresis was thus introduced.

(3) Elastic hysteresis

Tabor [4] introduced a coefficient α of hysteresis loss to account for the energy dissipated in the rolling after a large number of traversals ($n \simeq \infty$). To convey the fact that no permanent deformation is observed, the term elastic was used and thus α was defined as the "coefficient of elastic hysteresis." With this ambiguous definition, it was assumed that all solids to which the theory applied, after a certain number of stress cycles, reach a state of imperfect elasticity where they dissipate energy without permanent deformation.

The difficulty in formulating the "imperfect elasticity" is clear from its definition; moreover, if α is considered as a distinct material property, the theory ends by finding this constant through rolling experiments. Unfortunately α is not only a material constant but depends on the loads and dimensions of the problem [4].

(4) Viscoelasticity

Although it may account for the effect of special parameters (such as the rolling speed) on the rolling resistance, viscoelasticity

has the serious disadvantage of being too complicated to yield closed form results of rolling resistance. Another deficiency of the model is that materials exhibiting non-viscoelastic properties under practical conditions and use and/or experiments, e.g., steel and sands, can hardly be expected to obey this model.

From the previously treated models it is clear that the subject of rolling on metals is far from being solved; all four models are still used to formulate the rolling resistence [17, 26, 33]. The total energy dissipated in actual rolling problems is the sum of the effect of these models (surface phenomenon, hysteresis, etc.). Each effect contributes to a different proportion depending upon the materials, loads, surface roughness, temperature, etc., characterizing the problem. An exact solution, including all the parameters, is not conceivable; on the other hand, a reasonable solution would be to consider the major factors contributing the most to the solution and to neglect the parameters of minor importance.

Off-the-road locomotion or the rolling of wheels on soils is a relatively new subject compared with metal bearings. Soils, as a half-space material, are weak and have complicated properties, thus it is natural to expect that the theory of rolling on soils is where it stands today, i.e., a tremendous amount of experimental results (see, for example, Bekker [14] for some), yet very little is known about the mechanism of rolling; especially that until the present, no link has been made between rolling on metals and that on soils.

In the rolling on soils, the large deformations near and at the surface of the half space represent a difficult problem, because they

can no longer be neglected. On the other hand, they give a clear insight as to what the rolling process is about and further lead us to believe,as most workers in the field do,that plastic flow in the upper layers of the half space is the main source of energy dissipation. The final check on the approach is clearly how close the predictions are to the experimental results. In this text we will refer rolling resistance to plasticity and expect the test results to conform (or disagree) with the predictions of the theory.

IV-3. Plane strain free rolling of a rigid wheel, general formulation and simplifying assumptions

Consider the problem of steady state free rolling of a rigid cylinder of radius R and infinite length on the surface of a half space. A force F, per unit length of the cylinder axis, acts at the center O and makes an angle $\tan^{-1}\mu$ with the vertical Fig. IV-2. The half-space material is a general solid of known properties; the surface roughness for both the roller and the half-space are also known.

It is required to find the solution to the problem, i.e., find U, ω, p, τ, the geometry and the velocity field in the half space where

U is the forward horizontal velocity of the center O of the roller

ω is the angular velocity of the roller about O

p and τ the normal and shearing stresses at the interface AB.

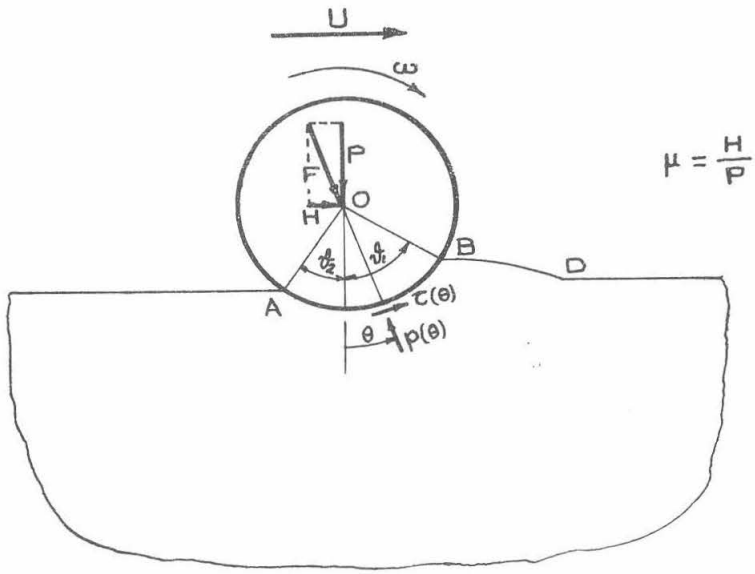

Fig. IV-2. Plane strain steady-state free rolling of a rigid cylinder

(1) Difficulties of the problem

The major difficulties encountered in solving the problem are:

i - Along the interface AB

The stresses and velocities along AB are on one hand part of the results and on the other hand represent the boundary conditions for the half space.

Of special interest are the shearing stresses $\tau(\theta)$. The factors affecting $\tau(\theta)$ are:

- The equilibrium of the roller; at the center O we have:

$$P = R\int_{-\vartheta_2}^{\vartheta_1} [\, p(\theta) \cos\theta + \tau(\theta) \sin\theta] \, d\theta$$

$$H = R\int_{-\vartheta_2}^{\vartheta_1} [\, p(\theta) \sin\theta - \tau(\theta) \cos\theta] \, d\theta$$

$$\text{Zero} = R^2 \int_{-\vartheta_2}^{\vartheta_1} r(\theta) \, d\theta$$

where P and H are the vertical and horizontal components of F respectively.

- The roughness of both surfaces.
- The velocity in the roller along AB, which is best described by

$$s = 1 - \frac{U}{\omega R}$$

From these factors only, P, H, R and the roughness of surfaces are known, while the velocity in the half space, s, ϑ_1 and ϑ_2 are all part of the solution.

ii - The free surface, BD, or the heap ahead of the roller. Being part of the geometry, BD is part of the result of the solution.

On the other hand, BD is an essential boundary condition for the half space.

By looking at the above points (i) and (ii) it becomes clear that, for any of the available models representing the half-space material, an exact solution in the applied mechanics sense is not available. The alternative is to try to get approximate results by using either of the two methods:

- Trial and error methods and numerical solutions. Even with the availability of computers, these techniques are not expected to yield useful results. The reason for this failure is the infinite variety of alternatives in the assumed values of stresses, velocities and geometry along the boundaries of the half-space.
- Additional assumptions, based on test results of steady state free rolling, that would eliminate the variables of secondary importance and make the solution possible.

The latter technique will be used to establish the boundary condition along the interface AB.

(2) Surface roughness of the roller

Experiments carried out by Halling [5] , Noonan and Strange [6] , and Eldredge and Tabor [3] in steady-state free rolling on metals, have shown that for a constant vertical force P, lubrication has little or no effect on the rolling resistance H. This evidence suggests one of two interpretations.

- The shearing stresses at the interface $\tau(\theta)$ exist and are substantially large. The lubricant, however, cannot pene-

trate the contact zone and is thus ineffective.

- The shearing stresses at the interface are small enough, such that when these stresses are reduced to zero by the lubricant, the rolling resistance is negligibly affected.

The second of these interpretations seems more reasonable, particularly that:

- From the third of (i), τ must change sign along the interface.
- Experiments by Bikerman [7], Halling [5] and Drutowski [8] in rolling on metals, show that reasonable changes in the surface roughness (say less than 100%) produced negligible changes in the rolling losses (less than 10%).

It will be thus assumed that the solution for a smooth roller ($\tau(\theta) \equiv 0$) represents an approximate solution for the general surface texture of the roller in the steady state free rolling.

IV-4. Steady-state rolling of a smooth rigid roller on a rigid-perfectly plastic half-space

The relevant properties of the half-space material now have to be specified; we postulate that plastic flow of the half-space material is the main source of energy dissipation; the validity and accuracy of the postulate in describing the free rolling on a certain solid can only be checked by its consequences compared with actual testing results. The elastic-plastic material, as a tool, is too complicated; instead, we will have to settle for the more restrictive material previously used in the half space of the plate problem and for convenience called rigid-perfectly plastic material.

The material being incompressible, the volume preservation condition implies that the surface of the half space far ahead and behind the roller be at the same level. The absence of elastic effects together with the fact that the stresses at the interface can only be compressive, suggest that the point A, representing the toe of the interface, should be directly below O; we will thus assume the geometry of the problem to be as in Fig. IV-3, with the free surface BD still unknown.

A complete solution in the half space, as it is understood in plasticity problems, consists mainly of finding a stress field together with a velocity field that would be permissible with respect to the material properties, and simultaneously satisfy the boundary conditions. Now with the curve BD still unknown, the problem remains unspecified in terms of plasticity. One way of avoiding this deadlock is to assume the curve BD. The technique, however, is faced with the infinite variety of alternatives in choosing BD, especially that actual roller testing shows it to be of a very complicated shape. (See, for example, Wong and Reece [9].) Also noting that, in solving any particular problem by this trial and error method, no generalization of the results seems possible; consequently, this tediuus method will not be used. The alternative is to specialize the problem further, and this will be done by treating only the special case when the angle δ is small, Fig. IV-3.

With less details, this string of simplifications were assumed by Marshall [26] who solves the presently reduced problem using the perturbation technique developed by Spencer [27]. A known

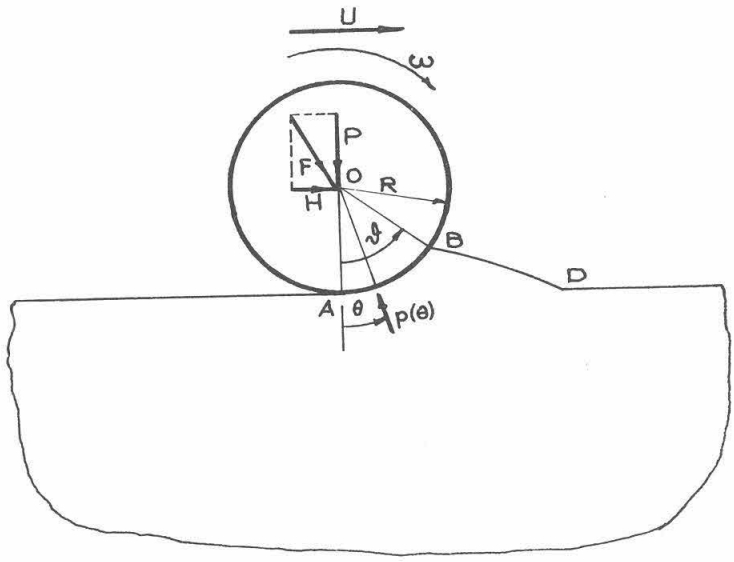

Fig. IV-3. Plane strain steady-state free rolling of a smooth rigid cylinder on a rigid-perfectly plastic half-space

exact solution (taken in this case to be the incipient failure of a half-space indented by a rigid smooth flat ended punch [32] at the limit state of zero velocity within the plastic field, Fig. IV-4-c) is perturbed to account for (1) the translation velocity U and (2) the difference in geometry between the cylinder and the punch. The values of the rolling resistance H and deformation of the surface of the half space δ_{max} are deduced and are accurate to order δ. This solution however requires the implicit assumption that the free surface BD ahead of the roller is a circular arc symmetrical to AB with respect to the vertical through B, Fig. IV-3-d. With no estimate of how this assumption affects the results and to get a clear picture of where the error in the stress and velocity fields occur and also because Marshall's solution breaks at the interface between the plastic and rigid domains (when $x/x_a = O(\delta)$) the present solution was found necessary. We essentially break the rolling problem into two problems and solve each exactly. The first problem (A) is the steady-state ironing plate shown in Fig. IV-4-a, which accounts for the translational velocity U but where the geometry of the roller is not there. The second problem (B) is an instantaneous solution, Fig. IV-4-b where the geometry of the roller is met but the steady state is not. Achieving in two steps what perturbation does in one, the approach is physically more attractive and one gets a clear picture of where the errors are. Moreover we find that H is not affected by the assumed shape of the free surface BD ahead of the roller while δ_{max} is.

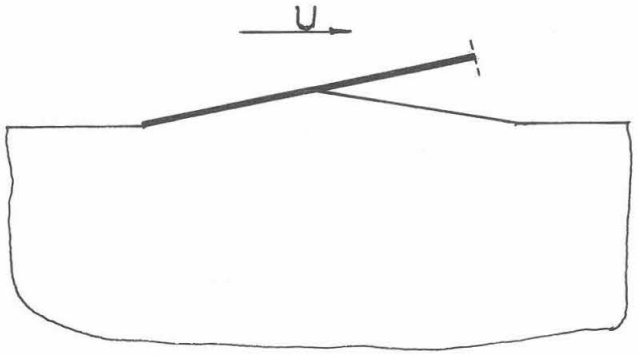

(a) Problem A, the ironing plate problem

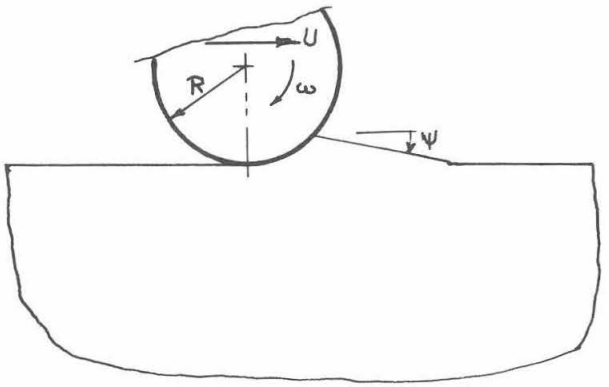

(b) Problem B, an instantaneous solution

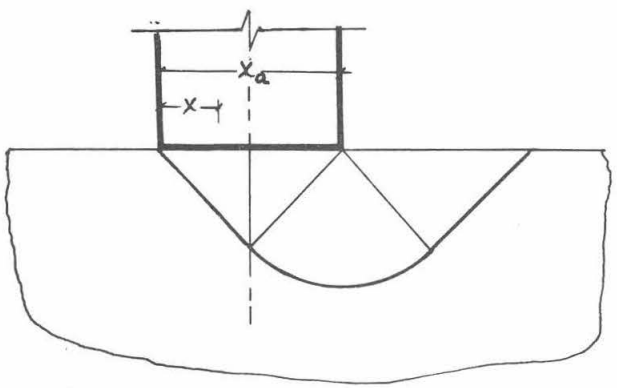

(c) Indentation of a half-space by a rigid punch

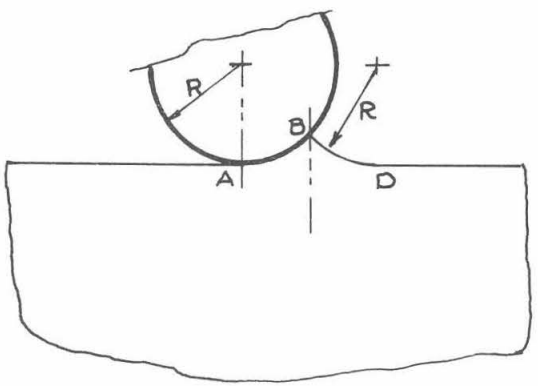

(d) Marshall's assumption regarding the free surface ahead of the roller

Fig. IV-4. Different idealizations of the rolling process

IV-4-1. Problem A - the ironing plate

Consider a rigid smooth plate moving with constant velocity U parallel to the surface of a half space as shown in Fig. IV-5-a. The lowest point of the plate is at the level of the surface of the half space. The shape of the heap ahead of the plate is by some means controllable and acts with the half-space as a continuum. The material of the half space is taken as rigid-perfectly plastic. It is required to find a steady state solution which would give a constant shape of the heap for all times. Compared with the problem of interest in Fig. IV-3, the difference between the two is that the arc AB is now replaced by straight line $\overline{AB}$.

An exact solution to problem A is given in detail in Chapter III when the heap ahead of the plate is an isosceles triangle Fig. IV-5-b. The results of interest are:

(i) The slip line field is shown in Fig. IV-5-b.

(ii) The stress distribution at the smooth plate/solid interface interface AB is uniform and given by

$$p = [\pi + 2 - 4\vartheta]\, k \quad \text{(compressive)} \tag{1}$$

where

k = yield constant of a material

$= Y/2$ for a Tresca material

$= Y/\sqrt{3}$ for a Von Mises material

with Y being the simple tension yield stress

ϑ = the inclination of the plate to the horizontal

the external force on the plate F is such that:

$F = [\pi + 2 - 4\vartheta]\, kL$ and acts at an angle ϑ to the vertical.

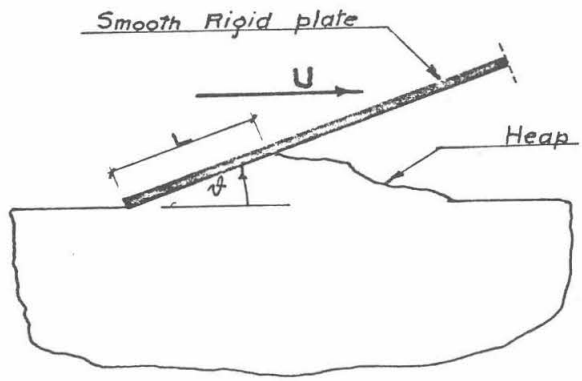

(a) Problem identification

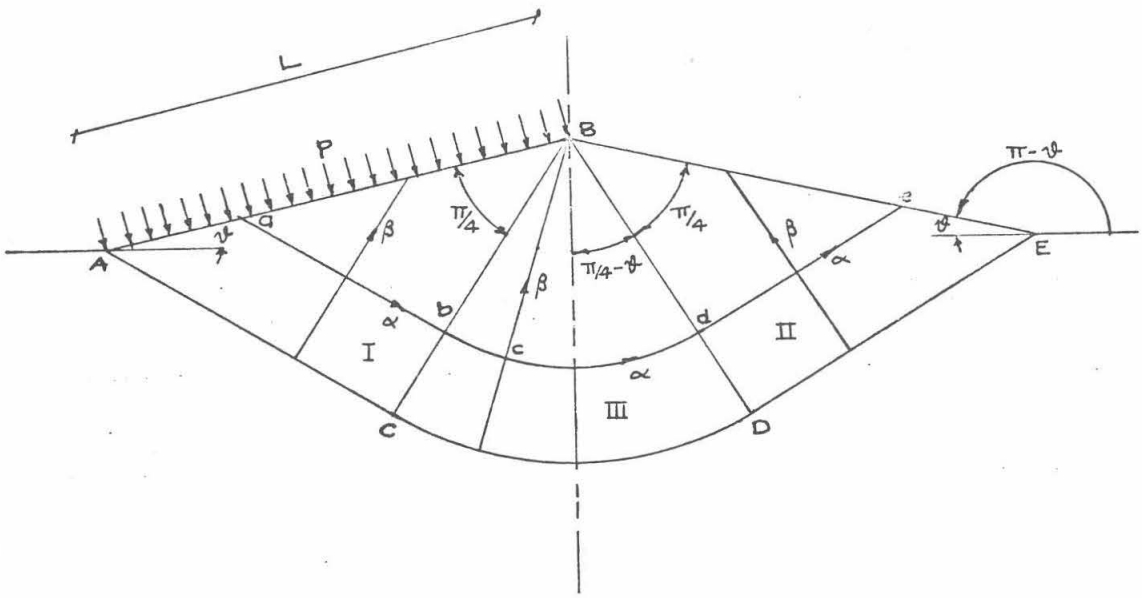

(b) Solution found for the free surface ahead of the plate

Fig. IV-5. The ironing plate problem

(iii) The maximum depth affected is

$$t_{max} = \frac{L}{\sqrt{2}} [1 - \sqrt{2} \sin \vartheta] \tag{2}$$

where L = length of contact.

(iv) For δ_n denoting the horizontal displacement of any point after n traversals by the plate with respect to its original position, we get:

$$\delta_n = n\delta_1 \quad (n = 1, 2, \ldots) \tag{3}$$

(v) The vertical displacement after any traversal is always equal to zero.

Now let $L = R\vartheta$

where R = a fundamental length

$\therefore$ (1) and (2) imply

$$\left.\begin{aligned} p &= [\pi + 2 - 4\vartheta]k \\ t_{max} &= \frac{R\vartheta}{\sqrt{2}} [1 - \sqrt{2} \sin \vartheta] \end{aligned}\right\} \tag{4}$$

and

$$F = [\pi + 2 - 4\vartheta] kR\vartheta$$

Consider the special case of ϑ small, equations (4) become:

$$\left.\begin{aligned} p &\simeq (\pi + 2)k \\ t_{max} &\simeq \frac{R\vartheta}{\sqrt{2}} \end{aligned}\right\} \tag{5}$$

and

$$F \simeq [\pi + 2] kR\vartheta$$

The horizontal permanent deformation, for small δ, is drawn in Fig. IV-6 . The maximum horizontal displacement δ_{max} occurs at the surface and for each traversal is given by:

$$\delta_{max} \simeq 2R\delta^2 \tag{6}$$

Noting that no permanent vertical deformation is present and that δ_{max}, from equation (6), is of the order of δ^2, we would thus expect that for small δ, the changes in the geometry due to the plate traversal cannot be easily observed by looking at the surface of the half space. Furthermore, if the connection, later established, between the free rolling process of a hard ball or roller and this plate problem, for small δ, is accepted, one can hardly agree with Tabor and followers that when no geometry changes are noticed, the plastic flow in the half space material ceases to exist.

IV-4-2. Problem B: An instantaneous solution to the rolling problem

Consider the plane strain problem of the rigid smooth cylinder with radius R and a wedge or half-space with the upper surface GABDF as shown in Fig. IV-7 . The curved part of the half space AB is a circular arc with the same radius R as that of the cylinder with center of curvature at O' vertically above A. The cylinder is to be fitted so that its center O coincides with O'. Then an instantaneous velocity $U > 0$, in the horizontal direction is given to the center O of the cylinder. Simultaneously an angular velocity ω is given to the cylinder about its center. Compared with the problem of interest and shown in Fig. IV-3, this solution does not satisfy the

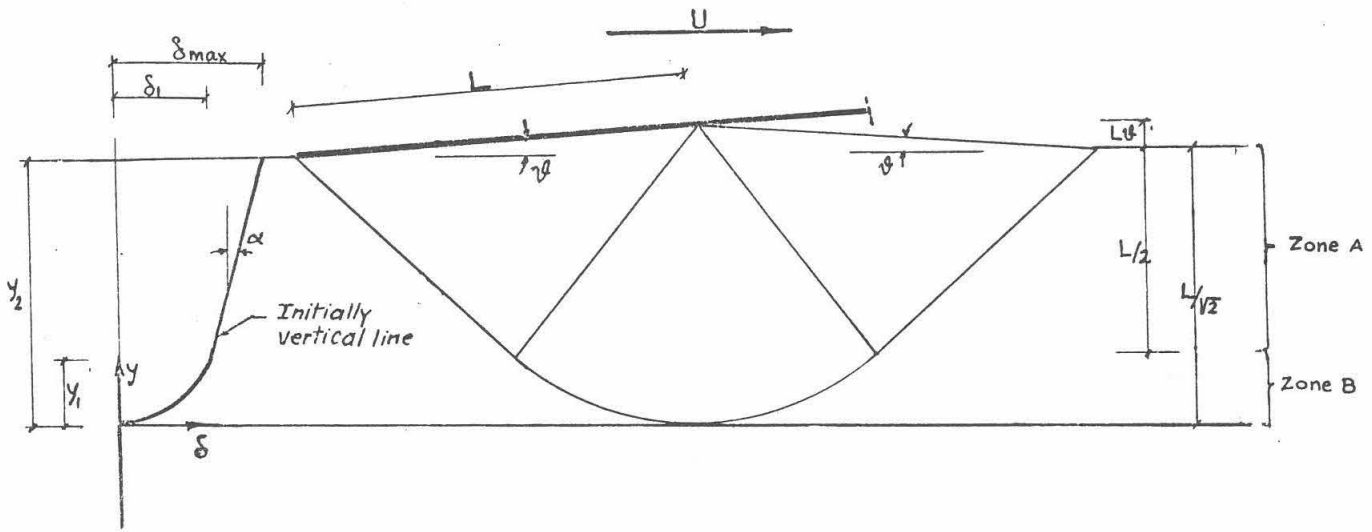

For small ϑ :

$\alpha \simeq 1.51\,\vartheta$

$y_1 \simeq 0.207\,L$ $\qquad \delta_1 \simeq 1.245\,L\vartheta$

$y_2 \simeq 0.707\,L$ $\qquad \delta_{max} \simeq 2\,L\vartheta$

Fig. IV-6. Summary of the computed distortion in the ironing plate problem for small values of ϑ

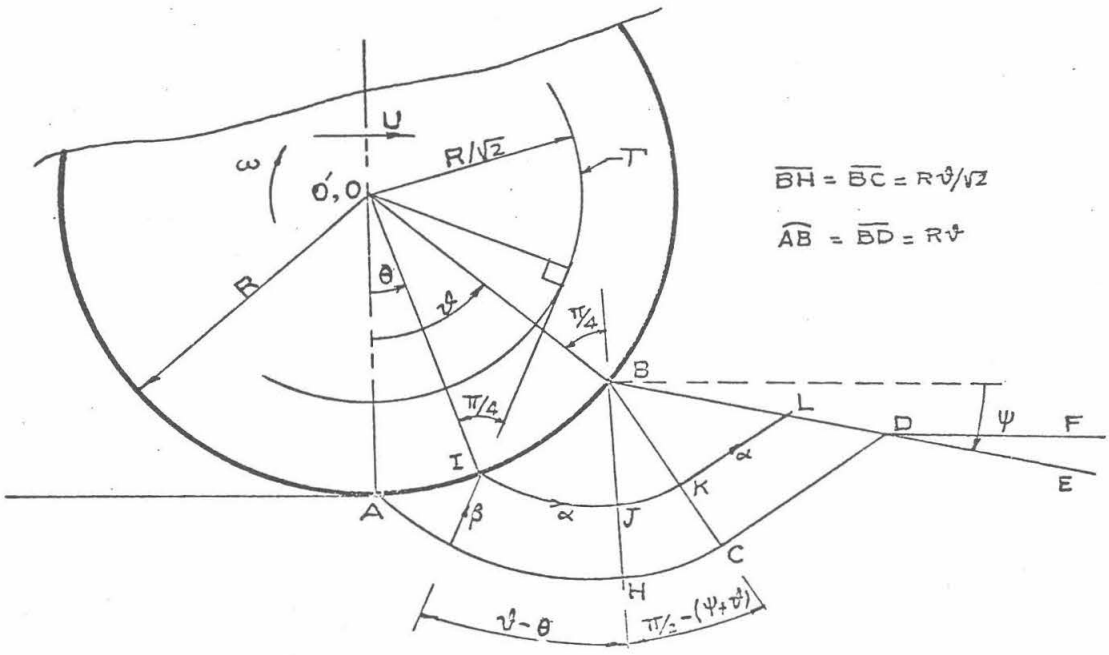

Fig. IV-7. Problem B, an instantaneous solution of the rolling process

steady-state condition. The exact solution of problem B is given in Chapter III by the front failure pattern. The results of interest are:

(1) The value of ω, as expected from the smoothness of the roller, is immaterial to the solution of both stress and velocity fields.

(2) A variation in the value of U changes only the scale of the velocity in the plastic field while the stress field and velocity directions remain unaltered.

(3) The velocity in the part BCD is not uniform; hence, the portion BD of the surface does not remain straight at subsequent times. The solution is thus valid only when motion is first started (instantaneous solution).

(4) Measuring the positive direction Ψ clockwise, we get for $\Psi < 0$ two failure zones - one ahead of the roller and the second behind it. For the case of $\Psi > 0$ we get only a front plastic zone.

(5) The pressure distribution along the circumference AB is given by:

$$p = [\pi + 2 - 2(\theta + \Psi)]\, k \tag{7}$$

where

$$0 \leq \theta \leq \delta, \quad \text{for all } 0 < \delta < \frac{\pi}{2}$$

(6) The same instantaneous solution is to be found if the half space had the surface DF instead of DE.

IV-4-3. Connection between problem B, problem A, and the rolling of a rigid cylinder

Suppose δ and Ψ are small, then from (7), by neglecting higher orders:

$$p \simeq (\pi + 2)k \tag{8}$$

Now by comparing (8) and the first of equations (5), we realize that the pressure distribution is the same as in the plate problem (for small δ). By decreasing δ the arc AB, Fig. IV-7 reduces to the straight line AB, Fig. IV-6. Furthermore by letting $\Psi = \delta$ it becomes clear that problem B approaches problem A. the latter having the advantage of being not only an instantaneous solution but also of an acceptable geometry for a steady state. From results previously obtained we deduce that for small δ:

(1) The pressure at the interface p is given by (8) and acts radially. The force F is thus inclined by an angle $\delta/2$ to the vertical and is given by:

$$F \simeq (\pi + 2)kR\delta \tag{9}$$

The coefficient of folling friction μ (the rolling resistance per unit weight) defined as the ratio H/P is thus given by:

$$\tan^{-1} \mu = \frac{\delta}{2} \tag{10}$$

Neglecting higher orders (for small δ), we substitute $P \sim F$ and $\mu \sim \tan^{-1} \mu$ in equations (9) and (10) to get:

$$\mu \simeq \frac{P}{2(\pi + 2)kR} \tag{11}$$

This result is the first term in the expansion solution derived by Marshall [26] assuming the free surface BD ahead of the roller to be a circular arc. This shows that the geometry of this free surface has no effect on μ (for small values of ϑ). The higher order terms in his expansion are incorrect because the stress field, in fact the whole solution, is only valid to the zero order of magnitude in ϑ.

(2) The maximum depth affected by the rolling process is given by

$$t_{max} \sim \sqrt{2\,\mu R} \tag{12}$$

In actual rolling, this value is expected to be exceeded because of the behavior of real materials. The rigid state assumed by the theory for points outside the plastic domain cannot be practically achieved.

(3) On the basis of results of the ironing plastic problem (the exact steady-state solution), the distribution of permanent horizontal deformation is given in Fig. IV-6 . The maximum deformation occurs at the surface and is given by

$$\delta_{max} \simeq 2R\vartheta^2 \tag{13}$$

This value is twice as large as the one found by Marshall [26]. However, referring to Fig. IV-8, if we calculate δ_{max} on the basis of results of problem B then, for small values of ϑ, we have:

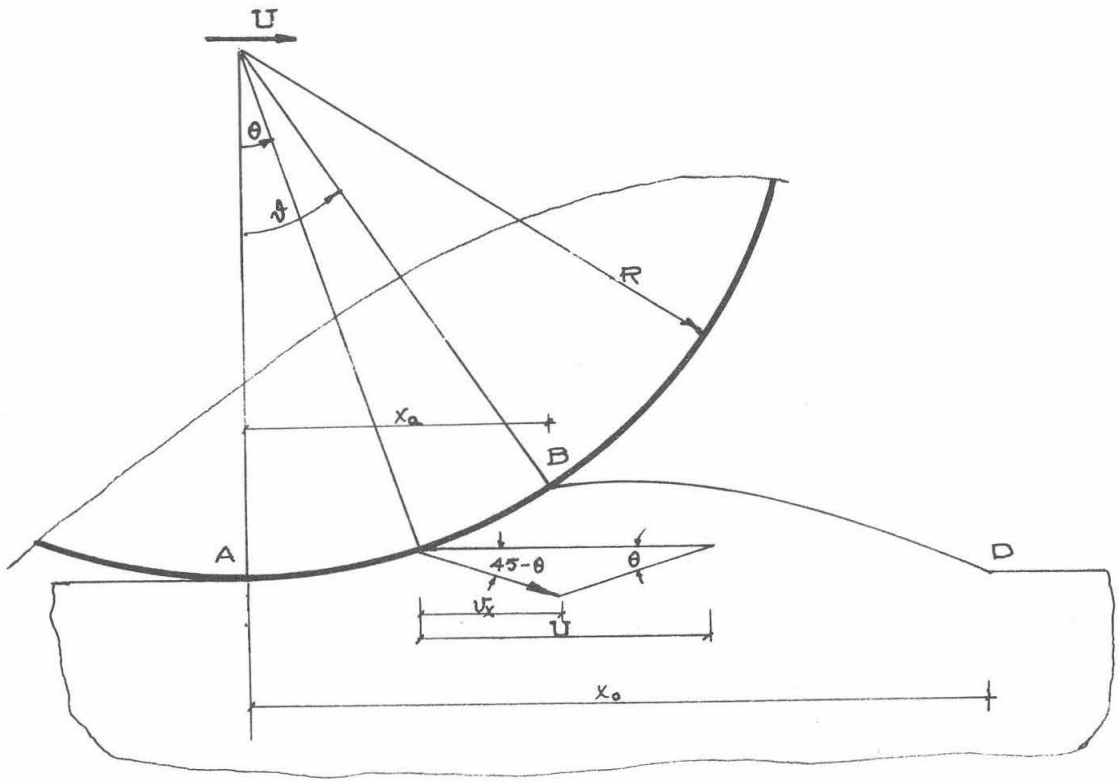

(a) Actual problem

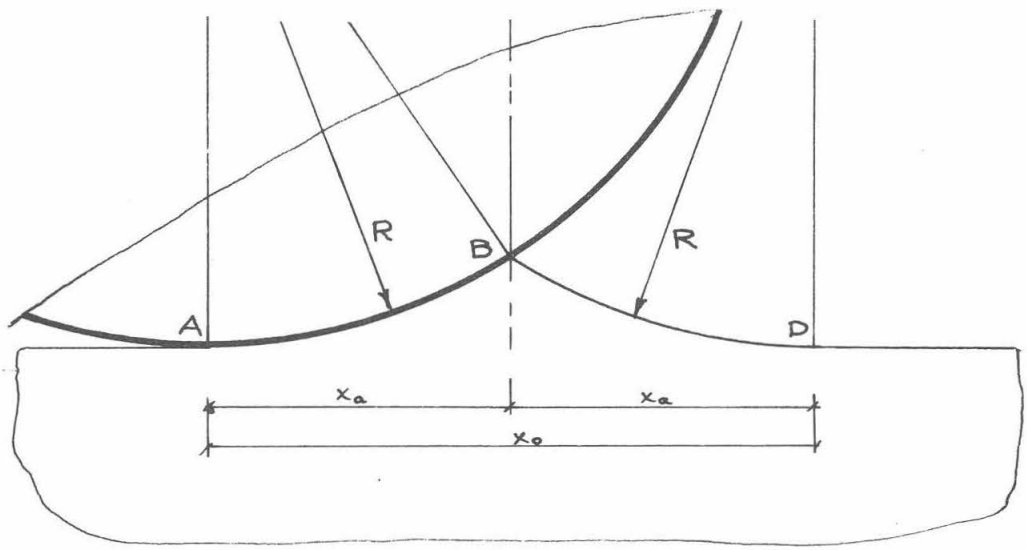

(b) Marshall's assumption

Fig. IV-8. Variables for evaluating the surface deformation due to rolling

$$\delta_{max} \simeq \int_0^{x_o} \frac{v_x(\xi)}{U} \, d\xi \qquad (14)$$

from the hodograph of Fig. III-19 . The value of $v_x(\xi)$ is given by

$$v_x \simeq \frac{U}{R} \xi \qquad (15)$$

If we now use the symmetry assumed by Marshall Fig. IV-8-b, then equations (14) and (15) imply:

$$\delta_{max} \simeq \frac{2}{R} \int_0^{R\vartheta} \theta \, d\theta \simeq R\vartheta^2 \qquad (16)$$

Equation (16) is the result obtained by Marshall [26]. It is thus clear that although assuming different shapes for the free surface BD ahead of the roller does not affect the rolling resistance, it does change the value of the deformation δ. This is caused by the change in the velocity field rather than the geometry of the problem. Values given by (13) and (16) are thus to be considered reasonable estimates to within the order of magnitude considered.

IV-5. Comparison with experimental results

In applications to the rolling of wheels on soils, the number of test results is beyond description, we will thus compare the empirical formulae currently in use for the rolling resistance with the theoretical expression in equation (11).

With P' the total vertical load of the wheel and d the width

of the wheel,

Gerstner, Schultz, Grandvoinet, Goriatchkin and Garbari propose

$$\mu = \frac{0.54}{M^{\xi}} \cdot \frac{1}{R^{\eta}} \cdot \left(\frac{P'}{d}\right)^{\xi} \quad \text{with} \quad \begin{matrix} \xi = 1/3 \\ \eta = 2/3 \end{matrix} \tag{17}$$

Bernstein proposes

$$\mu = \frac{0.57}{M^{\xi}} \cdot \frac{1}{R^{\eta}} \cdot \left(\frac{P'}{d}\right)^{\xi} \quad \text{with} \quad \begin{matrix} \xi = 1/2 \\ \eta = 3/4 \end{matrix} \tag{18}$$

Letoshnev proposes

$$\mu = \frac{1}{2M^{\xi}} \cdot \frac{1}{R^{\eta}} \cdot \left(\frac{P'}{d}\right)^{\xi} \quad \text{with} \quad \xi = \eta = 1 \tag{19}$$

The parameter M is a material property independent of P' and R but sometimes dependent on d.

After more than 20 years of rolling and pushing different objects on and in the ground, Bekker [14] proposes a general formula which for special types of soil reduces to (17), (18) and (19). His formula, restricted to small values of sinkage, for the free rolling of a rigid cylinder reads:

$$\mu = \frac{1}{(m+1)2^{\eta}} \left(\frac{3}{3-m}\right)^{2\eta} \frac{1}{M^{\xi}} \cdot \frac{1}{R^{\eta}} \left[\frac{P'}{d}\right]^{\xi} \tag{20}$$

where

$$\xi = \frac{1}{2m+1} \quad , \quad \eta = \frac{m+1}{2m+1}$$

Note: for $m = \begin{Bmatrix} 1 \\ 0.5 \\ 0 \end{Bmatrix}$ (31) reduces to $\begin{Bmatrix} (28) \\ (29) \\ (30) \end{Bmatrix}$

M and m are soil parameters to be determined from the relation

$$\sigma = My^m \tag{21}$$

where σ and y are the stress and sinkage respectively of a plate pushed vertically into the soil, see Fig. IV-9.

Equations (31) and (32) are the most widely tested and used in land locomotion. However, the parameter M is still a subject of controversy; Bekker [14] proposes

$$M = \frac{k_c}{d} + k_\Phi$$

and Reece [31] maintains that

$$M = \frac{k_1 + k_3 d}{d^m}$$

where k_c, k_Φ, k_1 and k_2 are soils constants. In any case, for a soil with properties similar to that of a rigid-perfectly plastic material, in the plate indentation Fig. IV-9, we expect to get $m \to 0$ and $\sigma \to M \simeq (\pi + 2)k$. The above value of M was deduced from the solution of a long rectangular plate, Hill [32] and that of a circular plate, Shield [16].

Substituting $m = 0$ (i.e. $\eta = \xi = 1$) and $M = (\pi + 2)k$ into (31), we get

$$\sigma = \frac{1}{2(\pi + 2)} \cdot \frac{P'}{kRd} \tag{22}$$

Comparing equation (22) and (11) and noting that $P'/d = P$, the two expressions are identical. Note: Bekker's restriction that the sinkage be small is covered in the present theory by μ being small.

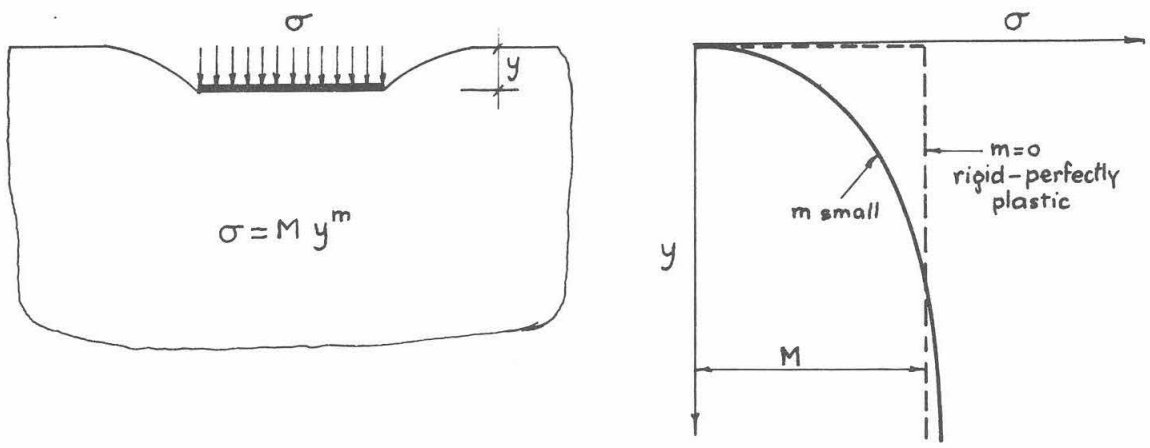

Fig. IV-9. Bekker's method to determine soil parameters

REFERENCES OF CHAPTER IV

1. Varlo, C., "Reflections upon friction ... ," printed for the author, London, 1772.

2. Coulomb, C. A., Mem. Math. Phys. Acad. Roy. Sci,, 161, 1785.

3. Eldredge, K. R., and Tabor, D., "Mechanism of Rolling Friction - Part I, the Plastic Range," Proceedings of the Royal Society, London, Series A., Vol. 229, 1955, pp. 181-198.

4. Tabor, D., "Mechanism of Rolling Friction - Part II, the Elastic Range," Proceedings of the Royal Society, London, Series A, Vol. 229, 1955, pp. 198-220.

5. Halling, J., "The relationship between surface texture and rolling friction," British Journal of Applied Physics, Vol. 9, 1958, pp. 421-428 - Vol. 10, 1959, pp. 172-176 - Journal of Scientific Instruments, Vol. 32, 1955, pp. 8-9.

6. Noonan, N. G., and Strange, W. H., "Tests on Rollers," Technical Memorandum No. 399, U.S. Department of Interior, Bureau of Reclamation, Sept. 1954 - Noonan, N.G., M.S. Thesis, University of Colorado, Boulder, Colo., 1951, 45 pp.

7. Bikerman , J. J., "Effect of Surface Roughness on Rolling Friction," Journal of Applied Physics, Vol. 20, 1949, pp. 971-975.

8. Drutowski, R. C., "Energy Losses of Balls Rolling on Plates," Journal of Basic Engineering, Trans. ASME, Vol. 81, Series D, 1959, pp. 233-238 - Friction and Wear, pp. 16-35, Davies, R., Ed., Elsevier, Amsterdam, 1959.

9. Wong, J. Y., and Reece, A. R., "Soil failure beneath rigid wheels," Second Int. Conf. for Terrain-Vehicle Systems, University of Toronto Press, 1966, pp. 425-445.

10. Yong, R. N., Boyd, C. W., and Webb, G. L., "Experimental study of behavior of sand under moving rigid wheels," Soil Mechanics Series, McGill University, Montreal, Report No. 20, 1967.

11. Yong, R. N. and Webb, G. L., "Energy considerations in wheel-clay soil interaction," Soil Mechanics Series, McGill University, Montreal, Report No. 25, 1969.

12. Frietag, D. R., Green, A. J., and Melzer, K. J., "Performance evaluation of wheels for lunar vehicles," (Summary report), U.S. Army Engineer Waterways Experimental Station, Vicksburg, Mississippi, Paper M-70-4, May 1970, pp. 36-37.

13. Yong, R. N., Fitzpatrick-Nash, J. D., and Webb, G. L., "Response behavior of clay soil under moving rigid wheels," Soil Mechanics Series, McGill University, Montreal, Report No. 23, 1968.

14. Bekker, M. G., "Introduction to terrain-vehicle systems," The University of Michigan Press, Ann Arbor, Michigan, 1969, p. 437, p. 463.

15. Johnson, K. L., "Tangential Tractions and Micro-slip in Rolling Contact," Rolling Contact Phenomena, Bidwell, J. B., Ed., Elsevier, Amsterdam, 1962, p. 17.

16. Shield, R. T., "On the plastic flow of metals under conditions axial symmetry," Proc. Roy. Soc. Lon. Series A, Vol. 233, 1955, p. 282.

17. Hunter, S. C., "The rolling contact of a rigid cylinder with a viscoelastic half space," Transactions of the ASME, Jour. of Applied Mechanics, Dec. 1961, p. 611.

18. Konvisarov, D. V., "Investigation of type II friction (Russian), Trudy Nauchnoi Konferentsii Sibirskogo Fiziko - Tekhnicheskogo Instituto, Vol. 28, Tomsk., 1949, p. 223 - Trudy Akademiya Nauk SSSR, Vol. 83, No. 3, 1952.

19. Root, L. E., "The Measurement of Pure Rolling Friction," Master of Science thesis, Department of Mechanical Engineering, M.I.T.

20. Hisada, T., and Tsugawa, K., "On the Rolling Friction," Journal of the Mechanical Laboratory, AIST, Sumiyoshido Suginami-ku, Tokyo, Vol. 4, Mar. 1950, pp. 9-21.

21. Hersey, M. D., "Rolling Friction III - Review of later investigations," Journal of Lubrication Technology, April 1969, pp. 269-275.

22. Sasaki, T., and Okino, N., "Rolling Friction at High Speed," Bulletin of the Japan Society of Mechanical Engineers, Vol. 5, No. 18, 1962, pp. 360-373.

23. Benton, W. A., "Some Aspects of Friction," The Engineer, Vol. 141, April 23, 1926, pp. 458-459.

24. Hamilton, G. M., "Plastic Flow in Rollers Loaded Above the Yield Point," Proceedings of the Institution of Mechanical Engineers, Vol. 177, 1963, pp. 676-690.

25. Merwin, J. E., and Johnson, K. L., "An Analysis of Plastic Deformation in Rolling Contact," Proceedings of the Institution of Mechanical Engineers, Vol. 177, 1963, pp. 676-690.

26. Marshall, E. A., "Rolling Contact with Plastic Deformation," Jour. Mech. Phys. Solids, Vol. 16, 1968, p. 243.

27. Spencer, A. J. M., Jour. Mech. Phys. Solids, Vol. 8, 1960, p. 362; Ibid., Vol. 9, 1961, p. 279; Ibid., Vol. 10, 1962, p. 17; Ibid., Vol. 10, 1962, p. 165; Ibid., Vol. 12, 1964, p. 231.

28. Bowden, F., and Tabor, D., The Friction and Lubrication of Solids, Clarendon Press, Oxford, 1964, pp. 277-319.

29. Rabinowicz, E., Friction and Wear of Materials, Wiley, New York, 1965, pp. 82-85.

30. Hill, R., "On the limits set by plastic yielding to the intensity of singularities of stress," Jour. Mech. Phys. Solids, Vol. 2, 1954, p. 278.

31. Reece, A. R., "Principles of Soil Vehicle Mechanics," Proc. Augo. Div. Instn. Mech. Engrs., Vol. 180, Pt. 2A, No. 2, p. 45, 1965-1966.

32. Hill, R., The Mathematical Theory of Plasticity, Oxford University Press, 1950, p. 254.

33. Kalker, J. J., "A Minimum Principle for the Law of Dry Friction, with Applications to Elastic Cylinders in Rolling Contact. Part I: Fundamentals - Application to Steady Rolling. Part II: Application to Nonsteadily Rolling Elastic Cylinders," Transactions of the ASME, Journal of Applied Mechanics, Dec. 1971, p. 875.

34. Janosi, Z., "Performance Analysis of a Driven Non-deflecting Tire on Soils," U.S. Army Land Locomotion Lab., ATAC, No. 8091, Warren, Michigan, 1963.

APPENDIX A

EXAMPLES OF PROBLEMS SOLVED BY THE MODIFIED WILSON TECHNIQUE

We present now two problems solved by the modified Wilson technique. The first is intended to emphasize the importance of choosing the proper convergence method according to the type of problem treated. This is done by comparing three convergence methods with the linear elasticity solution. The second problem, which is of the same nature as the rigid indenters problems of chapter II, stresses a more important point, namely the applicability of Wilson's technique to this class of problems with a reasonable degree of accuracy. This is done by comparing the finite element solution to both the linear elasticity and the perfect plasticity ones.

A-1. Short relatively thin cylinder under internal pressure

The problem with its dimensions and material properties is shown in Fig. A-1. It can either be considered as a short, thin cylinder under internal pressure, or a reinforcement web for a pipe also subjected to internal pressure.

In cylindrical coordinates (r,θ,z), the rotational symmetry makes all variables depend on r and z only. The internal pressure p is taken to be unity while the rest of the boundary is traction free, hence the problem falls into the second boundary value type for which the stress-controlled method of convergence should prove superior when solving for a bilinear material.

Material properties

Linear material

shear modulus	G = 1000
Poisson's ratio	ν = 10.4

Bilinear material

	G = 1000
	ν = 0.4
Ratio of plastic to elastic modulus	n = 0.01
One dimensional yield stress	Y = 1

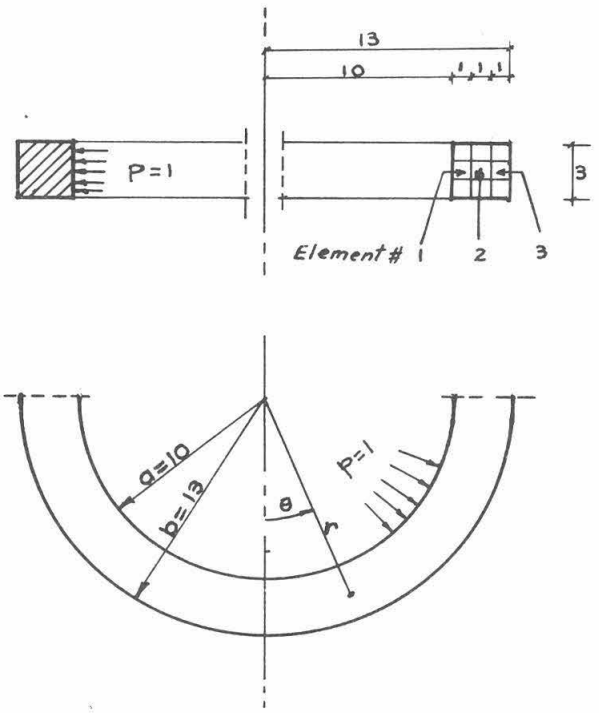

Fig. A-1. Cylinder under internal pressure

A-1-1. Linear elasticity solutions

Neglecting the variation with respect to z through a plane stress approximation, an exact solution may be found in Timoshenko and Goodier [1]. Here we give the values of σ_θ and σ_r:

$$\sigma_r = \frac{a^2 p}{(b^2 - a^2)} \left(1 - \frac{b^2}{r^2}\right)$$

$$\sigma_\theta = \frac{a^2 p}{(b^2 - a^2)} \left(1 + \frac{b^2}{r^2}\right)$$

a and b are the inner and outer radii respectively. On the other hand, the simplified analysis for thin-walled cylinders gives

$$\sigma_\theta = \frac{pa}{(b - a)}$$

Using the finite element mesh shown in Fig. A-1 and solving for a linear material, we first find that the variation of the inplane stresses and strains with respect to z are negligibly small (less than 0.5%). As for u_z and σ_z, they are less than 1% with respect to the inplane displacement and stresses; hence the plane stress assumption of the theory is justified to this order of magnitude. Moreover, by plotting σ_r and σ_θ results together with graphs of the theoretical results in Fig. A-3-a, it is seen that the F.E. method gives good results.

A-1-2. Solutions for bilinear material

With the same mesh shown in Fig. A-1 and for the properties given on the same Figure, we solve the problem for a bilinear material using three types of convergence methods, the strain-controlled

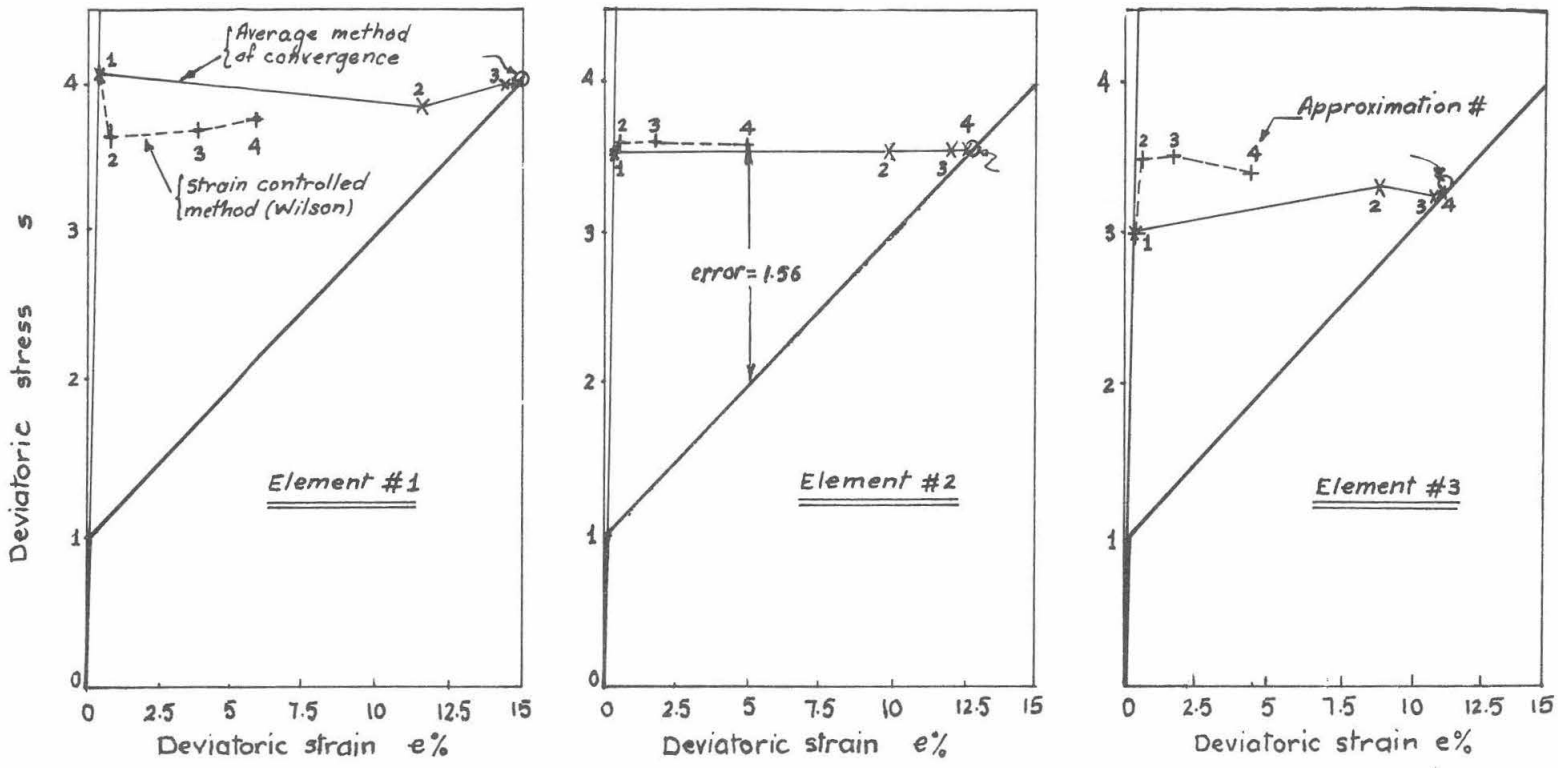

Fig. A-2. Comparison between different convergence methods

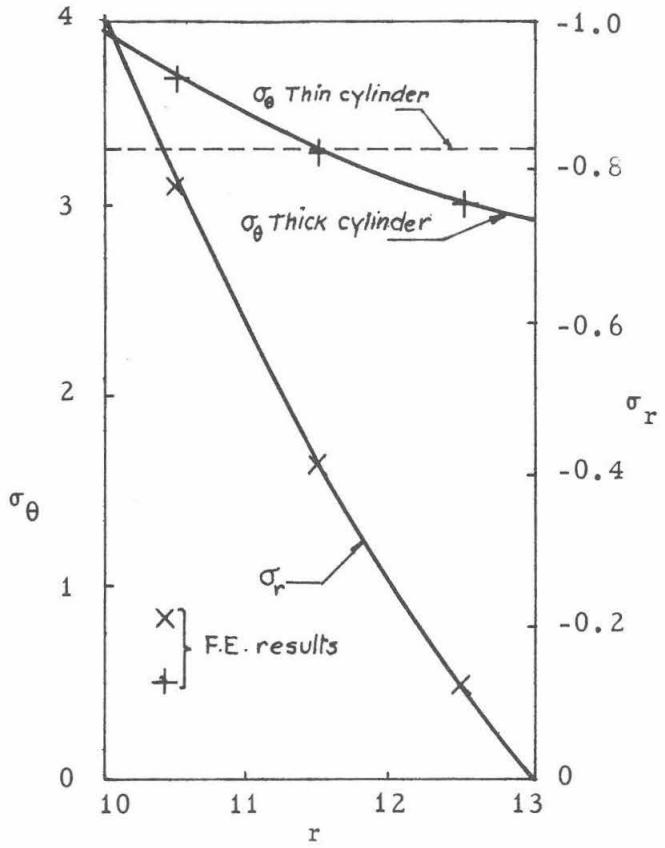

(a) σ_r and σ_θ for a linear material according to theory and finite element

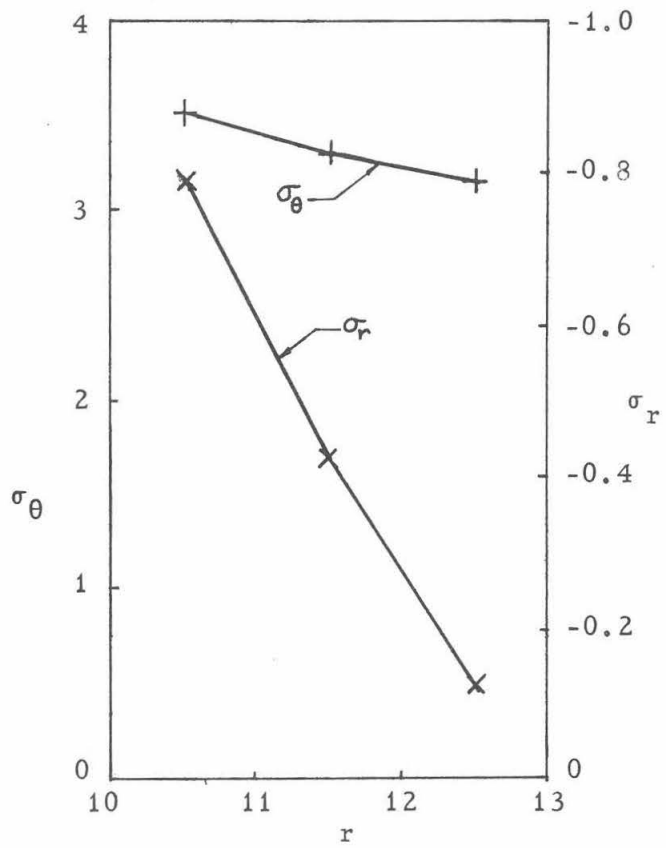

(b) σ_r and σ_θ for a bilinear material according to finite element

Fig. A-3. Distribution of stresses for a cylinder under internal pressure.

(Wilson), the stress-controlled and the average method. A comparison between the three methods is made in Fig. A-2 and in Tables A-1 and A-2.

For every element we draw the (s,e) state location in Fig. A-2 after each approximation for each convergence method. Joining the (s,e) states at successive approximations we get what we called the convergence curve, the intersection of which with the bilinear line should give the solution.

Consider element #2 say. All convergence curves start from the same point 1 which is the linearly elastic solution. The dotted line corresponding to Wilson's convergence, with each approximation, moves closer to the bilinear curve; however this is done much more slowly than the solid line corresponding to the average technique such that after four approximations the error in the strain-controlled solution is still very large ($\Delta s = 1.56$). As for the stress-controlled method, which is especially suitable to this problem, it gives (s,e) states, from the second approximation on, which are virtually on the bilinear curve. Its location is denoted by a small circle in Fig. A-2.

A further proof of the superiority of the stress-controlled method is given by Table A-1 in which values of the average error $\overline{\Delta s}$ appear (see eq. (9), chapter I). The $\overline{\Delta s}$ value is a measure of how far are the (s,e) states in the field from the bilinear curve.

Finally we compare the results of two different convergence techniques with each other in Table A-2 after four approximations. It can be seen that differences in results due to different convergence methods do not exceed 1% and are more like 0.4%.

TABLE A-1

Average error values $\overline{\Delta s}$ in the bilinear problem according to different convergence techniques

Approximation # / Convergence method	1 (elastic solution)	2	3	4
Stress-controlled	2.57	0.045	0.017	0.0068
Strain-controlled (Wilson)	2.57	2.47	2.19	1.56
Average method	2.57	0.56	0.085	0.0124

TABLE A-2

Comparison of results by different convergence methods after four approximations

Element #	Variable / Convergence type	Radial displacement u_r	Stresses σ_r	σ_z	σ_θ
1	stress-controlled	1.0781	-0.78853	-0.00925	3.4991
	Average method	1.0734	-0.78845	-0.00922	3.5005
2	stress-controlled	1.0265	-0.42108	-0.00587	3.2959
	Average method	1.0219	-0.42095	-0.00584	3.2969
3	stress-controlled	0.98715	-0.12897	-0.00978	3.1476
	Average method	0.98293	-0.12891	-0.00983	3.1455

A-2. Indentation of a half-space by a rigid smooth circular punch

The problem with its dimensions and material properties is shown in Fig. A-4. In cylindrical coordinates (r,θ,z), the rotational symmetry makes all variables depend on r and z only. The boundary conditions are:

$$\left.\begin{aligned} u_\nu &= u^* \\ s_\tau &= 0 \end{aligned}\right\} \quad \text{on } \partial_1 R'$$

$$s_\nu = s_\tau = 0 \text{ on } \partial_2 R$$

where

u_ν is the normal component of displacement

s_ν, s_τ are normal and tangential components of the surface tractions

$\partial_1 R'$ defined by $|r| < R, \quad z = 0$

$\partial_2 R$ defined by $|r| > R, \quad z = 0$

A-2-1. The linearly elastic solution

An exact solution may be found in Green and Zerna [2], from which we lift the results of interest here:

$$u^* = \frac{\pi}{2} p_{av} R \frac{(1 - \nu^2)}{E}$$

$$p(r) = \frac{p_{av}}{2\sqrt{1 - \left(\frac{r}{R}\right)^2}}$$

where

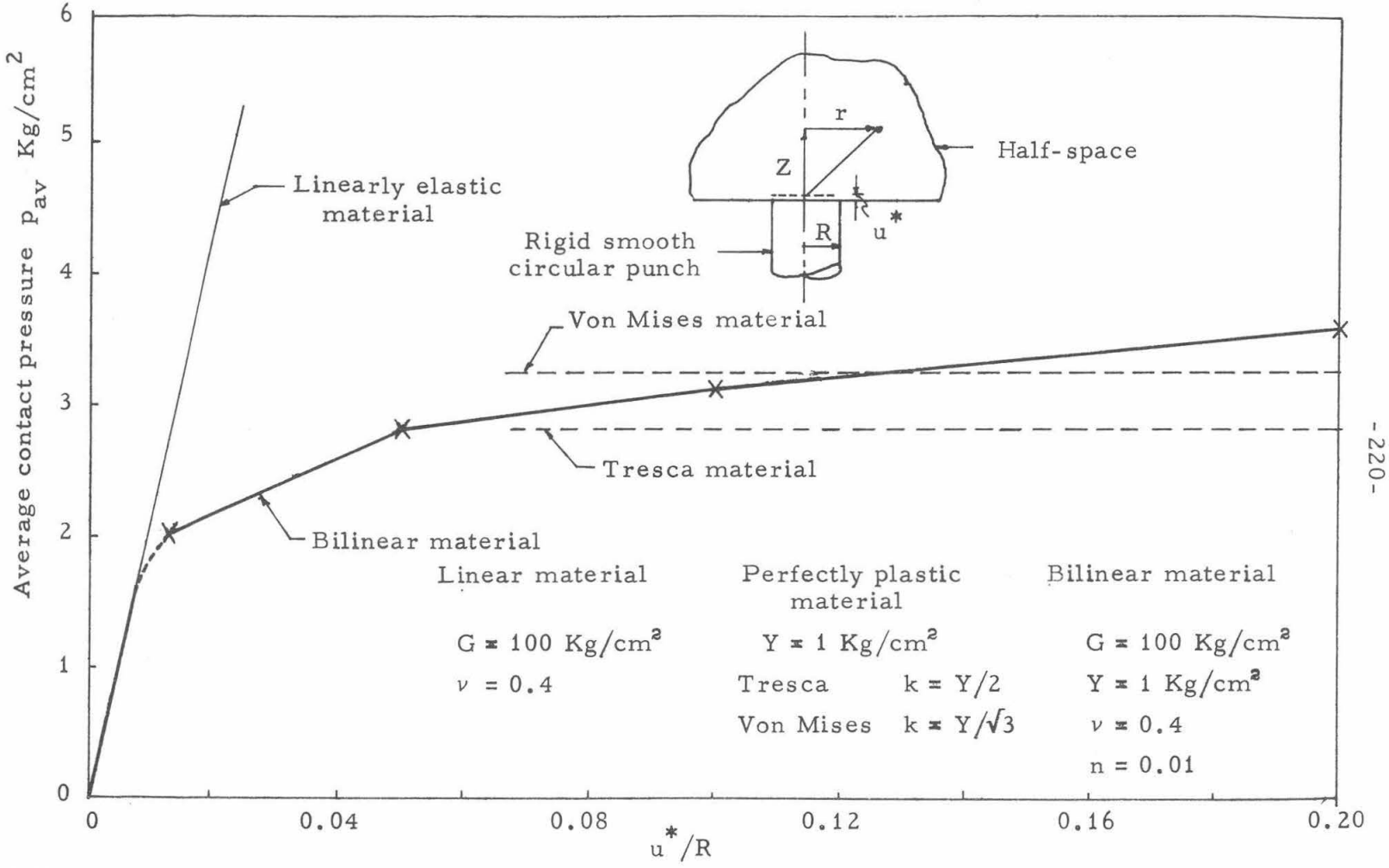

Fig. A-4. Comparison between p_{av} vs. u^* relationship for different material idealizations.

p_{av} is the average contact pressure at the interface between the punch and the half space

$p(r)$ the contact pressure distribution.

Graphs of these results are shown in Figs. A-4 and A-5 for the dimensions and material constants of our problem. Also in Fig. A-5 are plotted the results of the finite element solution for a linear material.

A-2-2. The perfect-plasticity solution

A solution to the problem for a Tresca material was derived by Shield [3] using the method of characteristics. The average contact pressure, for an incipient failure state, is given by

$$P_{av} = 5.69\ k$$

Although, rigorously speaking, the above result does not hold for a Von Mises material we assumed, for the sake of comparison, that it does and plot the results in Figs. A-4 and A-6. The incipient failure was interpreted as occurring after a sufficiently large value of u^*/R had been reached (say $u^*/R > 0.1$).

A-2-3. F.E. solutions for a bilinear material

The node points of the F.E. mesh used in the solution are shown in Fig. A-8. It consists of 248 nodes and 215 elements. Nodes along the boundary bc lie on a circular arc with a radius equal to 97 times the radius of the punch. For a closer look at the contact zone the dark part near the origin in Fig. A-8 was magnified 40 times and drawn in Fig. A-9.

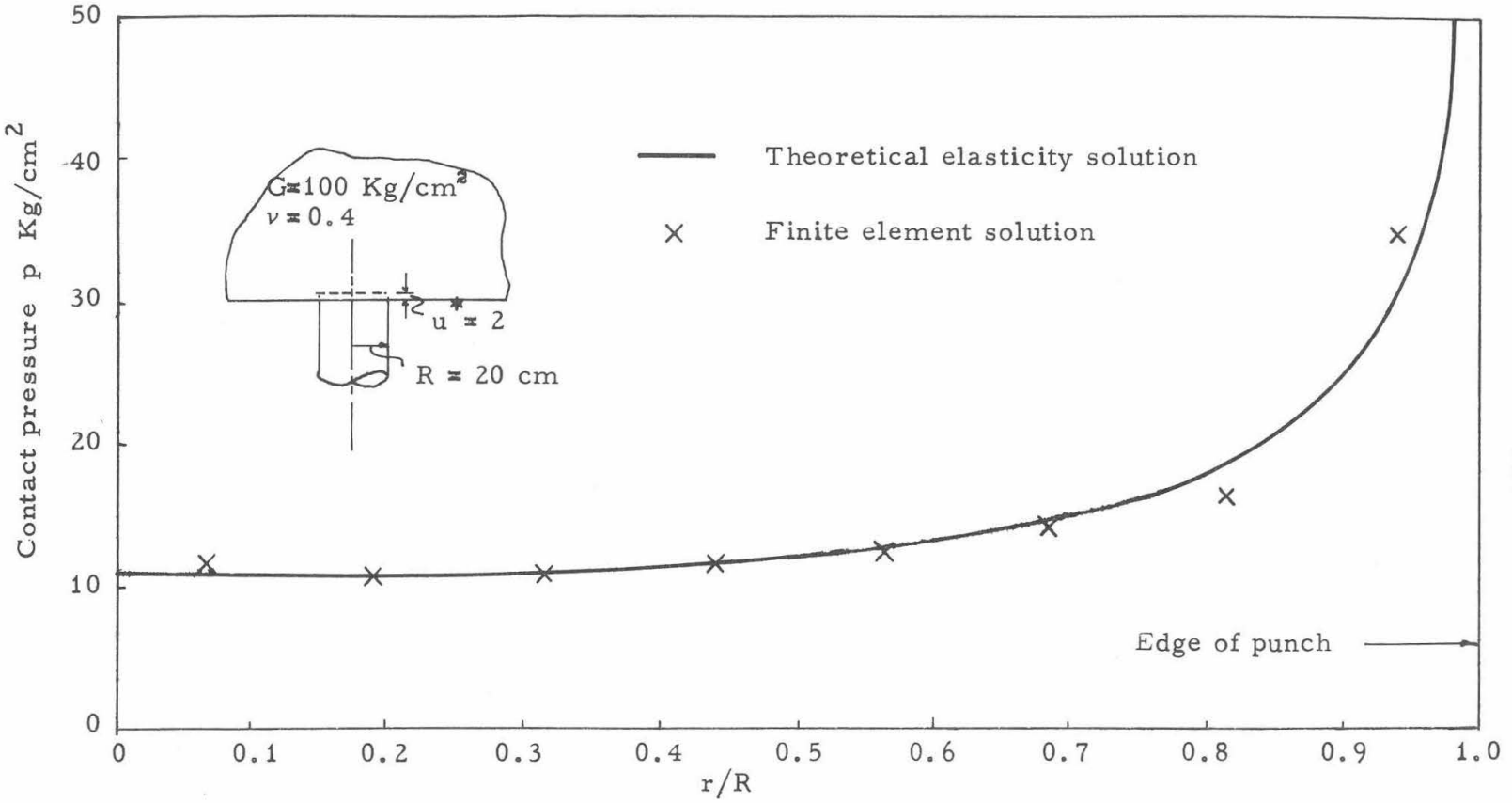

Fig. A-5. Contact pressure distribution for a linear material at $u^*/R = 0.1$.

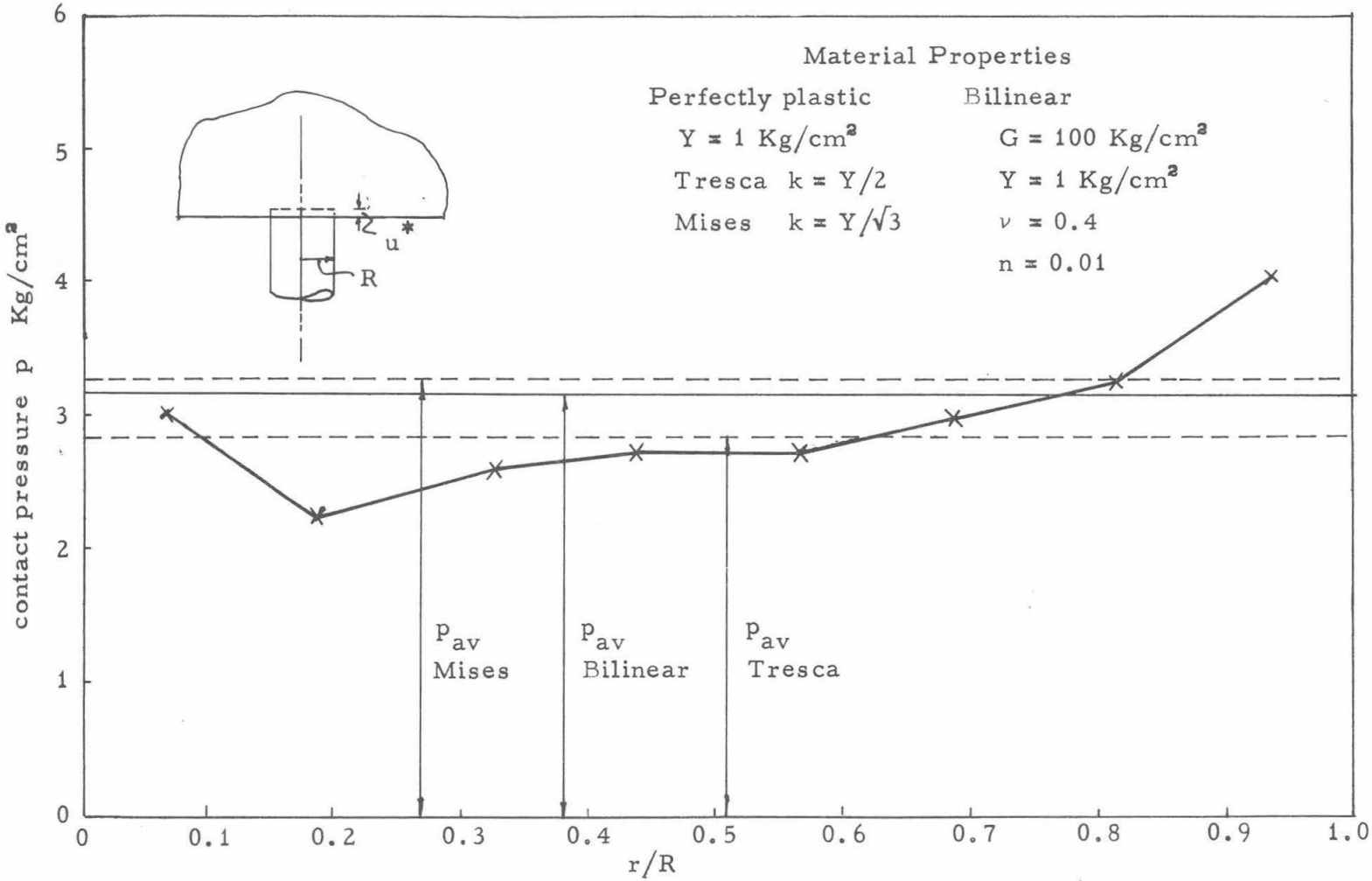

Fig. A-6. Contact pressure distribution for a bilinear material at $u^*/R = 0.1$.

With the bilinear properties shown in Fig. A-4, solutions were obtained for $u^*/R = 0.01, 0.05, 0.10, 0.20$ using four approximations in each case. The problem being of the mixed-mixed type a more sophisticated convergence method than the three described previously had to be used. After several trials it was found that, for this type of problem, faster convergence was achieved when the second approximation was made using the average method while the third and fourth approximations were made using the strain-controlled method. Some results are given in Figs. A-4, A-6 and A-7.

In Fig. A-4 one can clearly see that the bilinear material gives a load-deflection graph typical of the punching of a clay layer by a surface footing. The incipient failure values of the load are reached at $u^*/R \sim 0.1$. The use of such a diagram for critical designs is most valuable since it combines settlement and failure criteria in one figure. Usually the problem is divided into two parts, solved using linear elasticity and the second using perfect plasticity.

For $u^*/R = 0.2$, Fig. A-7 shows that the extent of the plastic zone is much larger than that found by perfect plasticity solutions. Moreover a transition zone between elastic and heavily strained domains proves to be of substantial dimensions; this seems to replace the boundary surfaces between the plastic and rigid domains found in the ideally plastic solution. Along these boundaries discontinuities in velocities are present in the theoretical case. This phenomenon of the spreading of surfaces of discontinuities into region of finite thickness is interesting since it reveals itself also in the test results.

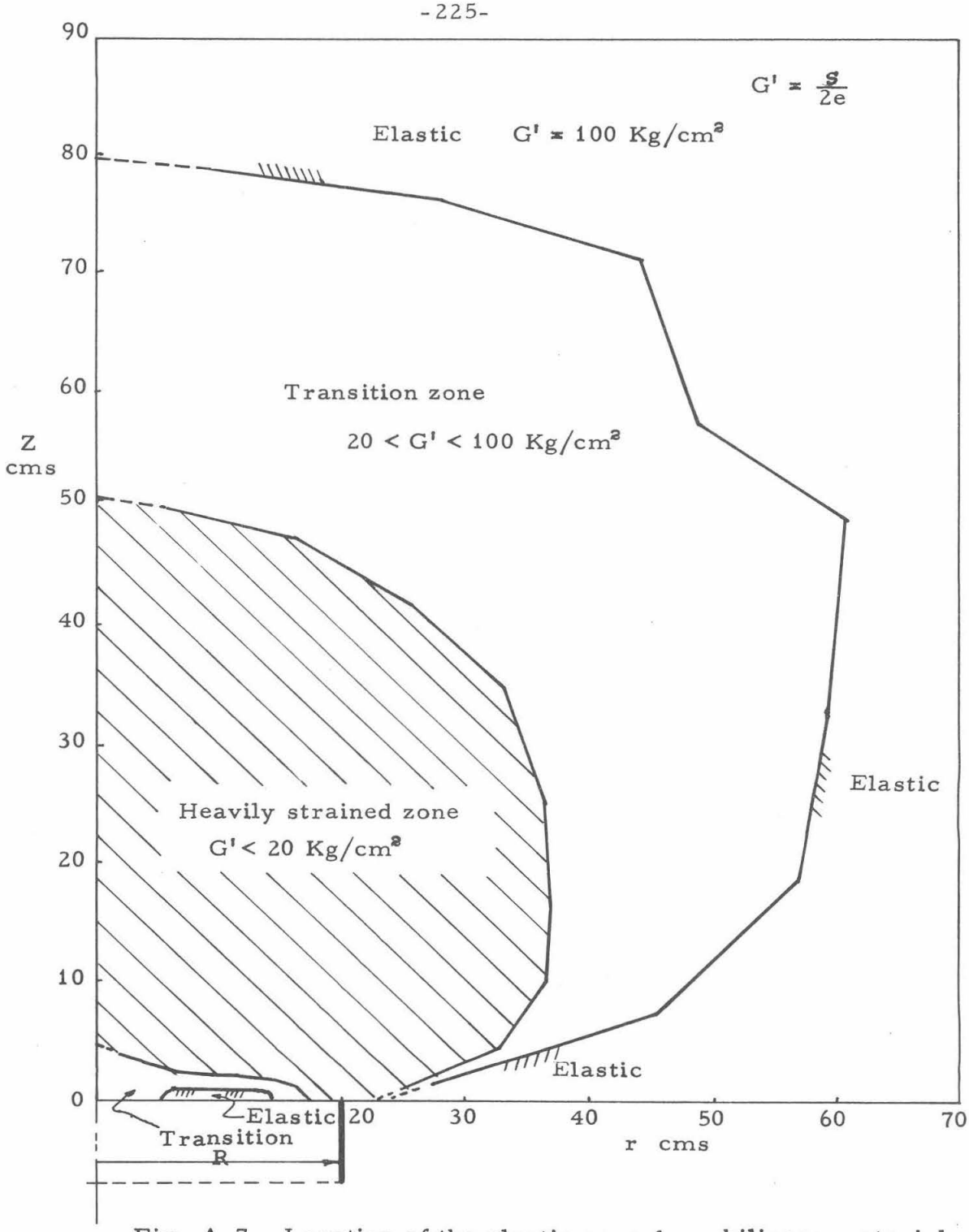

Fig. A-7. Location of the plastic zone for a bilinear material $u^*/R = 0.2$.

Boundary conditions :-

$\overline{ab}$: $u_r = s_z = 0$

$\widehat{bc}$: $u_r = u_z = 0$

$\overline{dc}$: $s_r = s_z = 0$

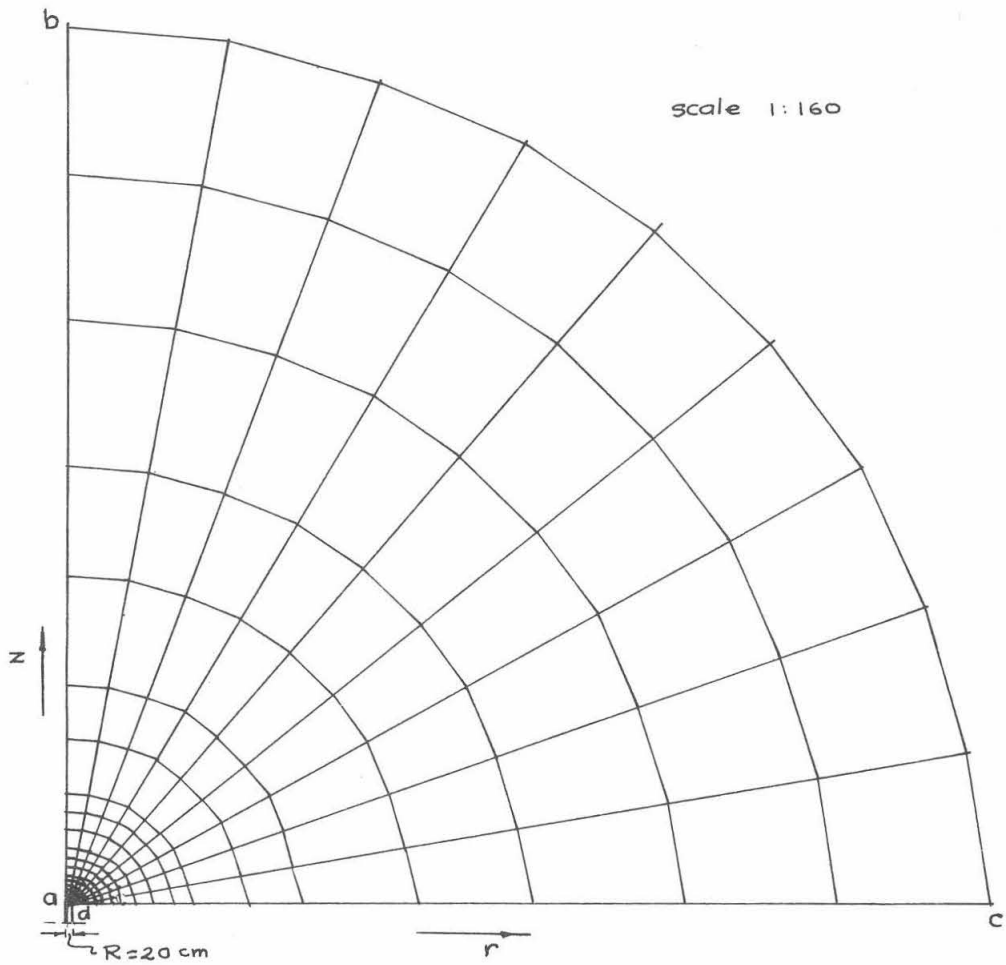

Fig. A-8. Finite element mesh for the punching problem

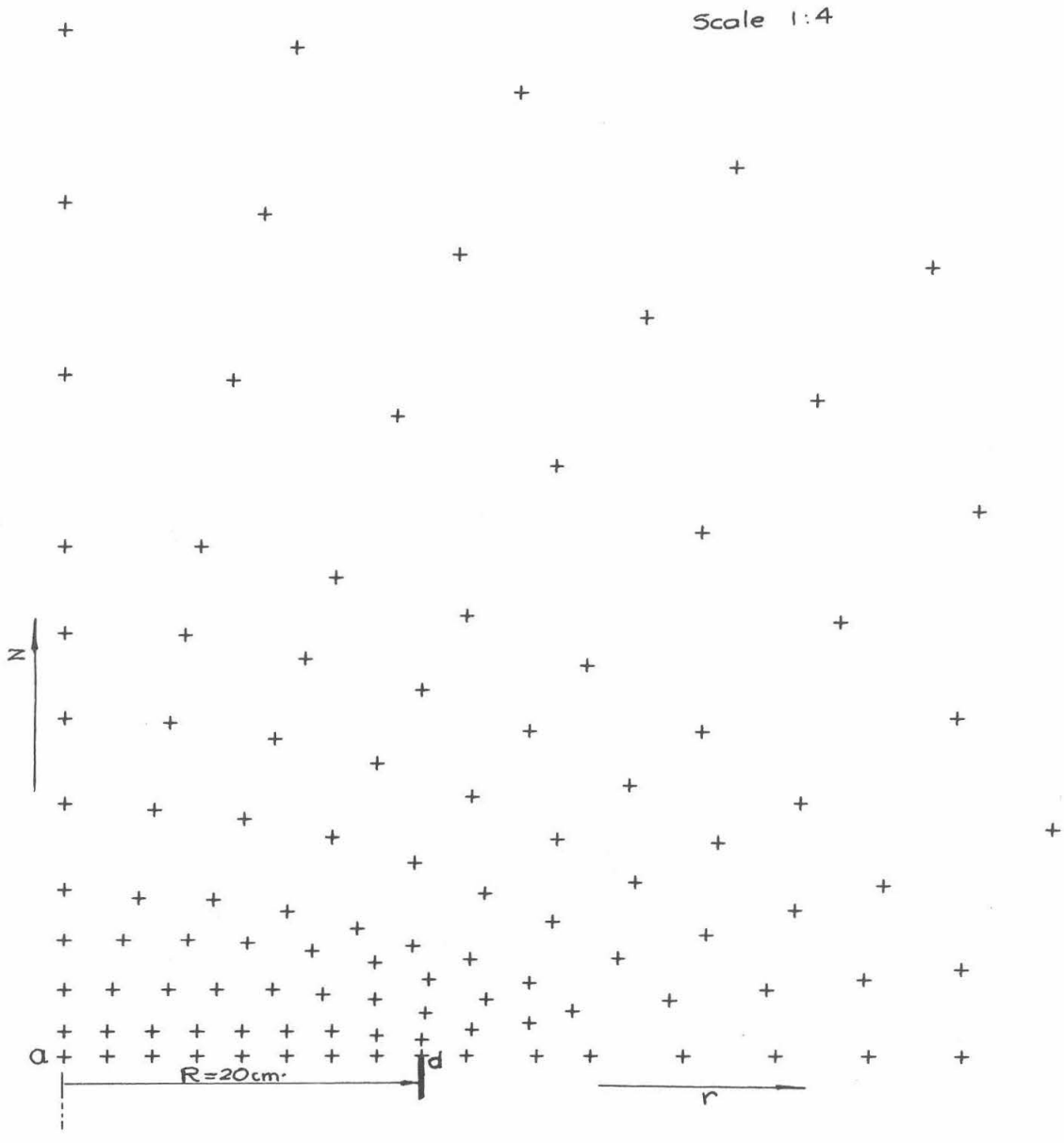

Fig. A-9. Finite element mesh near the punch surface

REFERENCES OF APPENDIX

1. Timoshenko, S. and Goodier, J. N., Theory of Elasticity, McGraw-Hill, Second ed., 1951, p. 356.

2. Green, A. E. and Zerna, W., Theoretical Elasticity, Oxford University Press, Second ed., 1968, p. 173.

3. Shield, R. T., "On the plastic flow of metals under conditions of axial symmetry," Proc. Roy. Soc. Lon. Series A, Vol. 233, 1955, p. 282.